DISCLAIMER
The publication of papers in International Journal of Engineering does not imply that the editorial board, reviewers or publisher accept, approve or endorse the data and conclusions of authors.

CONTENTS

Transactions C: Aspects

Dry Sliding Behaviour Study of Novel Low-metallic Friction Materials by using DoE-Taguchi Method

S. P. Jadhav*[a], S. H. Sawant[b]

[a] Department of Technology, Shivaji University, Kolhapur, Maharashtra, India
[b] Sant Gajanan Maharaj College of Engineering, Mahagaon, Gadhinglaj, Maharashtra, India

A B S T R A C T

With the plethora of automobiles introduced in the last 2 decades, brake emissions have been a notorious contributor to overall emissions. In the present work, the low-metallic friction material is developed (for 3 samples accounting for 10 different ingredients) to reduce non-exhaust emission. The friction materials are manufactured by the compression molding method and various samples are required for physical, mechanical and tribological characterization are prepared as per ASTM standards. The tribological performance is tested by a 'pin on disc' apparatus. The tribological parameters such as speed, load and sliding distance is selected by considering for the scooter application. Taguchi Design of Experiment (DoE) is used to find optimal operating parameters. Additionally, ANOVA and regression analysis are also done. Results reveal that the wear rate is minimum at the optimal operating parameters. The average wear rate obtained from sample 3 is less than samples 1 and 2. The higher and lower wear rate and coefficient of friction for sample 3 are 0.002 and 0.00033 mg/m and 0.462 and 0.301, respectively. The morphological behaviors are studied with the help of SEM. Moreover, Thermo gravimetric analysis (TGA) is carried out to explore the thermal behavior of friction material samples. Results illustrate that sample 3 proves to be a potential substitute as a novel brake friction material.

doi:10.5829/ije.2024.37.03c.01

1. INTRODUCTION

Development of low metallic eco-friendly friction material is a challenging task in front of researchers with concern environment and health. The brake pad composition contains several metallic and other ingredients in the form of binder, filler, reinforcement, abrasives, and lubricants (1-4). Some of the toxic elements in brake friction material pollutes the environment are Asbestos, Cu, Cd, Ni, Pb, Sb, Zn, etc. and responsible for human diseases like lung cancer, irritation to the respiratory system, kidney failure, liver cells, and the tissues damage. Environmental agencies of different countries in the world are found the bad effect of brake pads emitted pollutants on plants, animals, and human beings (5-7).

In non or low metallic and organic brake friction materials natural organic fibers like cotton, kapok, jute, sisal, abaca, pineapple, sun hemp, oil palm, kenaf, coir, banana, flax, wheat straw, bamboo, and inorganic fibers such as metals, steel wool, man-made vitreous fibers (MMVF) glass, carbon, ceramic fibers, etc. are reinforced with modified resins and rubber. The other constituents contain filler, abrasives and elastomer are added to enhance hardness, wear resistance, coefficient of friction, and shock-absorbing properties of friction material. In low metallic friction materials some of the binders used are phenolic, epoxy modified, COPNA, cyanate ester, silicon modified resins, etc (8). The researchers also made eco-friendly brake friction material from seashell and aagricultural waste to reduce non exhaust pollution (9, 10). The structural changes in brake friction material also effects on performance parameters (11).

Selection and deciding the percentage of ingredients play a crucial role in the formulation of friction material.

*Corresponding Author Email: spjadhav2112@gmail.com
 (S. P. Jadhav)

The trial and error method is generally obeyed for the formulation of brake composition that depends on the experience of the researcher. But a drawback of this method is very time-consuming. A lot of iteration has to be done for the formulation of the material. The important tool employed to overcome this difficulty is the design of experiment (DoE). Taguchi method is a design of experiment tool that tests a pair of combinations such as manufacturing and operating parameters instead of testing all possible combinations like factorial design (12). With DoE concern, design like Taguchi, factorial and response surface are the tools used to obtain the rank of influenced parameters on response. The combinations of parameters that influence the response are also studied in Taguchi design. ANOVA and multiple linear regression analysis models for wear rate are obtained. An optimum value of wear rate and coefficient of friction is obtained from signal to noise ratio by considering smaller is better and larger is the best quality criteria respectively. Results showed that wear rate is a function of load but decreases with an increase in speed. The percentage of reinforcement is also a major factor in the coefficient of friction (13, 14). The dry sliding behavior of composite is studied by making specimen hand layup technique or compression molding method. Most of the time authors are selected sliding distance, load, speed, percentage of reinforcement, and friction modifier as operating parameters with their two or three levels. The outputs of all experiments are to study performance parameters like coefficient of friction, wear rate, and specific wear rate (15, 16).

The present work aims to develop novel friction material from low metallic and more natural ingredients that reduces toxic producer metallic ingredients at sources and helps in reducing non-exhaust pollution. The friction material is prepared by the compression molding method and dry sliding tribological behavior is studied by using a wear test. The optimal combinations of operating parameters that have improved the performance of friction material are found by using the design of the experiment (Taguchi design). The S/N ratio quality characteristics are considered for wear rate. Regression analysis is used to prepare the model for a low wear rate. Morphological and thermal behavior of friction material is studied by scanning electron (SEM) and Thermo gravimetric analysis (TGA) method.

2. MATERIAL AND METHODS:

Friction material composition is made by varying four ingredients by volume percentage viz. Epoxy resin, boron carbide, cashew dust, and human nail nevertheless the volume percentage for vermiculate, sodium silicate, rubber crumb powder, zirconium dioxide powder, steel wool, and glass fiber ingredients are kept constant as displayed in Table 1. The flow chart of manufacturing method is shown in Figure 1.

The pin specimen of 12 mm diameter is fabricated by preparing mold followed by crushing, sieving, mixing, and compaction procedure. The compressive molding technique is used to fabricate pin specimens. The homogeneous mixture of all the ingredients is mixed and poured into the mold at room temperature. The mold is kept under a compression molding machine by compressing the mixture with pressure 17 MPa. For the post-curing, the mold is further kept in the furnace at 150^0C for 6 hours. The pin is withdrawn from the mold after 24 hours. To ready the pin for the test, the finishing of the pin is done to remove bur or any foreign matter by grit paper.

3. DESIGN OF EXPERIMENT

The Taguchi design of experiment (DoE) method is used to optimize various parameters or factors by considering

TABLE 1. Volume % of three different samples

Name of Ingredients	Sample 1	Sample 2	Sample 3
Epoxy resin	32	33	34
Cashew shell powder	31	26	21
Boron carbide	3	8	13
Human nail	3	2	1
Steel wool	3	3	3
Glass fiber	1	1	1
Vermiculate	12	12	12
Zirconium dioxide	5	5	5
Rubber crumb	3	3	3
Sodium silicate	7	7	7
Total	100	100	100
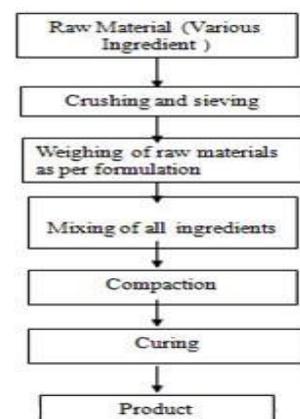
Figure 1. Flow chart of friction material manufacturing method
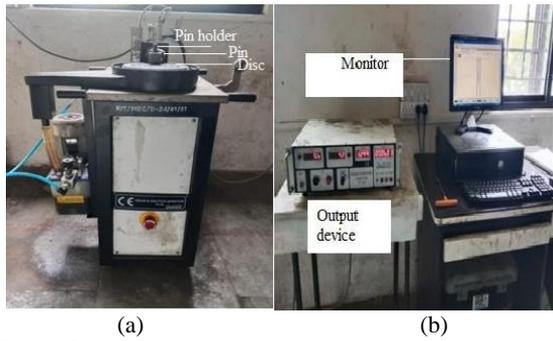
Figure 2. a) Pin on disc wear test rig, b) Output monitoring device

signal to noise ratio (S/N ratio). For the brake pad application coefficient of friction should be high and low wear rate. Signal-to-noise ratio considered for the coefficient of friction is larger is best while smaller is better is considered for wear rate. Equation 1 is used to calculate the S-N ratio smaller is better for the wear rate (17, 18).

$$\frac{S}{N} \; ratio = -10 log_{10} \; \frac{1}{n} \Sigma(y^2) \tag{1}$$

where, n is the number of experiments and y denotes response for wear rate The control factors and their levels are shown in Table 2.

4. DRY SLIDING WEAR TEST

Pin-on disc wear and friction monitor apparatus are shown in Figure 2 (a) and (b). (Ducom Instruments, Bangalore, India) is used to study dry sliding behavior of a sample pin according to ASTM G99 standard. The machine has a split hard jaw for clamping 3, 4, 6, 8, 10, and 12 mm cylindrical pins. The disc rotation range is between 200 rpm to 2000 rpm and the load range is 1 N to 200 N. The wear measurement capacity of tribo-tester is 2000 micrometers. In this study, a 12 mm diameter friction material pin is rubbed against a cast-iron disc having a diameter of 165 mm and 8 mm thickness. To uniform contact of the pin with the disc, the pin was ground with a SiC paper of 500 grits before starting the experiment. The time duration of each test is different according to sliding speed and sliding distance. The range of 900 rpm to 1300 rpm speed is selected by

TABLE 2. Control factors and levels

Factors Levels	Load (N)	Speed (rpm)	Sliding Distance (m)
1	9.81	900	1000
2	19.62	1100	2000
3	29.43	1300	3000

considering the friction material used for moped or scooter application having average speed of 30 to 40 Km/h. Before starting and after completing the experiments weight of each specimen is recorded by electronic balance up to 4 decimals. Weight loss is noted to obtain wear rate by the Equation 2 (19, 20). Also, specific wear rate of material is calculated by calculating wear volume.

$$Wear \; rate = \frac{\Delta w}{s} \tag{2}$$

where,
Wear rate in mg/m
Δw - Difference in weight of pin sample before and after test in mg
S - Sliding distance in meter

5. RESULT AND DISCUSSION

5. 1. Density Test   Samples experimental density is found by ASTM D792 standard by Archimedes principle. The digital balance is used to measure the dry weight of the friction specimen and volume is measured by the water displacement method. The results showed that among the 3 samples, the high density obtained from sample 2 is 2.246 g/cm³ are shown in Table 3.

5. 2. Friction and Wear Test   The results obtained from the pin on disc wear and friction monitor revealed that for sample 1, at low speed 900 rpm and high level of load 29.43 N the wear observed is 53 microns while at

TABLE 3. Comparative properties of three different pin samples (21)

Properties	Sample 1	Sample 2	Sample 3	Commercial friction material
Density (g/cm³)	1.566	2.246	1.735	1.89
Water absorption test (%)	5.7	4.07	4.99	NA
Oil absorption test (%)	6.4	5.12	5.74	NA
Rockwell hardness test (HRB)	61	80	89	101
Wear rate (mg/m)	0.0003-0.006	0.0003 - 0.003	0.0003-0.002	3.8
CoF	0.29-0.45	0.30 - 0.45	0.30 - 0.46	0.3-0.4
Specific wear rate * 10⁻¹²	0.014 - 0.130	0.007-0.045	0.006-0.057	NA
TGA at 200⁰C weight loss (%)	9	8.76	9.05	NA

low level of load and speed 9.81 and 900 rpm, respectively, it is 46.03 microns. At a load of 9.81 N and speed of 900 rpm, 1100 rpm, 1300 rpm, and sliding distances of 1000 m, 2000 m and 3000 m the average coefficient of friction value is 0.91 whereas at 19.62 N and 29.43 N for the same speeds and sliding distances the average value of coefficient of friction is 0.45 and 0.30, respectively. This reveals that as speed and load increases, the coefficient of friction decreases. This is because at higher speed only higher asperities are contact between a pin and disc that reduces contact area. The same behavior was observed in the case of sample 2, the average wear value is less as compared to sample 1 due to increase in boron and epoxy volume percentage. Sample 3 showed the average coefficient of friction 0.9 at 9.81 N load, 900, 1100, 1300 rpm speed and 1000, 2000, and 3000 m sliding distances whereas at 19.62 N and 29.43 N load for the same speeds and sliding distances the average coefficient of friction is 0.455 and 0.31, respectively. The average coefficient of friction values in sample 1 at the load of 19.62 and 29.43 is found 0.459 to 0.298, respectively while samples 2 and 3 show a slight increase in coefficient of friction 0.304 and 0.459 and 0.301 to 0.462, respectively are shown in Table 3.

5. 3. Taguchi Experiment   The DoE is carried out using the Taguchi method of optimization the levels and quality characteristics are shown in Table 2 and Equation 1. The design of the experiment is conducted using Minitab 17, the orthogonal array L27 is selected. The results showed that sliding distance is the dominant factor are shown in Table 4, having significant p-value of 0.001 whereas the speed and load are not significant illustrating

in Table 5. For the optimal operating parameters, 29.43 N load, 1100 rpm speed, and 1000 m sliding distance, the low wear rate obtained in 1, 2, and 3 samples are 0.006, 0.003, and 0.002 mg/m, respectively are shown in Table 6. The main effect plot for means and the main effect plot for the S-N ratio are shown in Figure 3. The regression equation for the wear rate is shown in Equation 3.

5. 4. Taguchi Confirmation Test   Taguchi confirmation test is conducted for sample 3 with optimal operating parameters 29.43 N load, 1100 rpm speed and 1000 m sliding distance. From the regression equation predicted wear rate of 0.021 is calculated. After the experiment, the wear rate for sample 3 is 0.002 mg/m. The percentage error between predicted and experimentation 4.76 is obtained. The results are shown in Table 7.

5. 5. Regression Equation

Wear rate = 0.00534 + 0.000001 Load - 0.000002 Speed - 0.000001 Sliding Distance   (3)

TABLE 4. S /N ratio response table for wear rate

Level	Load	Speed	Sliding Distance
1	58.15	57.02	51.76
2	60.89	61.54	61.42
3	58.95	59.43	64.81
Delta	2.74	4.52	13.05
Rank	**3**	**2**	**1**

TABLE 5. ANOVA result table showing significance levels of different parameters

Source	DF	Adj SS	Adj MS	F-Value	P-Value	level Significant
-Regression	3	-0.00002	-0.000007	5.47	0.005	Significant
Load (N)	1	0	0	0	0.98	Not Significant
Speed (rpm)	1	-0.000002	-0.000002	2	0.17	Not Significant
Sliding distance (m)	1	017-0.000	017-0.000	14.4	0.001	Significant
Error	23	-0.000028	-0.000001			
Total	26	-0.00004				

TABLE 6. Optimal operating parameters for wear rate

Parameters	Load (N)	Speed (rpm)	Sliding Distance (m)	Wear rate (mg/m)
Sample 1	29.43	1100	1000	0.006
Sample 2	29.43	1100	1000	0.003
Sample 3	29.43	1100	1000	0.002

5. 6. Optimal Combination Results Graph   The combined behavior pattern of coefficient of friction versus time and wear in micron versus time are shown in Figure 4. (a) and (b) at 29.43 N load, 1100 rpm speed and 1000 m sliding distance respectively. In Figure 4 (a), the slightly fluctuation in the coefficient of friction is observed due to stick and slip phenomena between tribo-
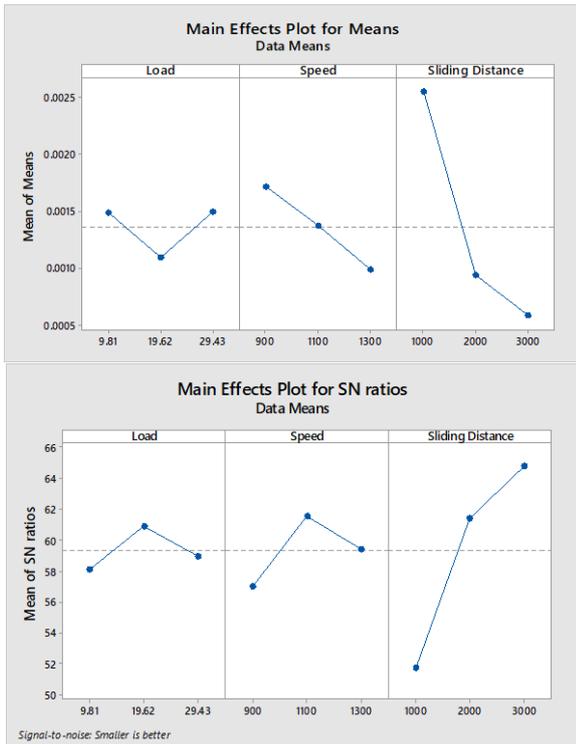
Figure 3. Main effect plot of means and Main effect plot of S-N ratio

TABLE 7. Taguchi experiment confirmation test result

| Sample No. | Test | Taguchi confirmation test results | | |
	Optimal operating parameter test	Wear rate (experimentally)	Wear rate (predicted)	Error %
Sample 1	29.43 N, 1100 rpm and 1000 m	0.0022	0.0021	-4.76
Sample 2		0.0019	0.0021	9.52
Sample 3		0.002	0.0021	4.76

pair. The wear in sample 3 is lower as compared to sample 1 and 2 is shown in Figure 4(b). This is due to increase in percentage of boron carbide (13%) and epoxy resin (34%) as compared to sample 1 and 2. Also hard particles of boron carbide increases primary plateaus that reduces rate of wear. Also at high speed 1300 rpm, the less asperities of tribo-pair are in contact that is responsible to reduce wear rate and coefficient of friction simultaneously.

5. 7. TGA Analysis   Thermo gravimetric analysis (TGA) of samples 1, 2 and 3 is shown in Figure 5. All samples show an average weight loss of 9 % at 200^0C that is linear weight loss with temperature. From 200^0C to 370^0C, progressive weight loss is found. The weight loss

rate increased in all three samples that are noted 30% in progressive weight loss region. After 370^0C, the sample 1, 2 and 3 lines differ and show a complete combustion region at temperatures 750^0C, 800^0C and 980^0C respectively (22).
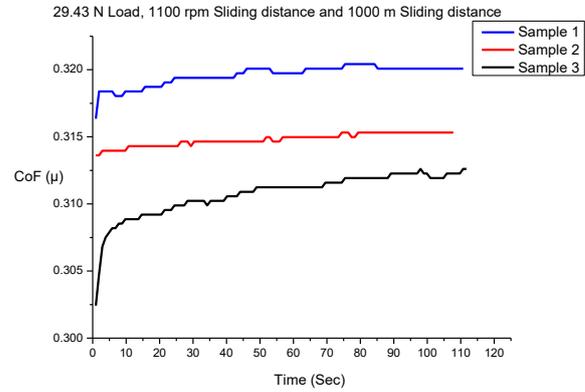
(a)
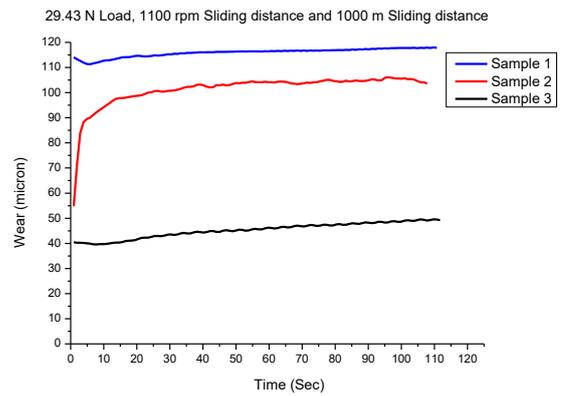
(b)

Figure 4. Optimal combination graph of sample 1, 2 and 3 a) Plot of coefficient of friction against time, b) plot of wear against time
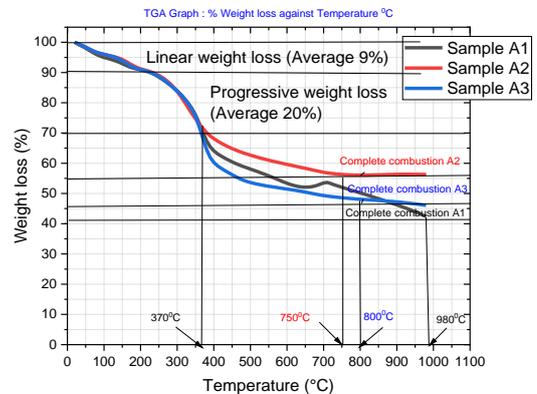
Figure 5. Thermo Gravimetric Analysis (TGA) of sample 1, 2 and 3

5. 8. SEM Analysis SEM are done for the wear test having operating parameters load, speed and sliding are shown in Figures 6-8(a) and (b) respectively. Scanning electron microscope (SEM) is used to study the wear of samples pin surface morphology of the friction material before and after the wear test. The micrograph reveals a wear debris pattern and the nature of surface appearance. The SEM is operated under high vacuum mode by providing grounding for earthling with carbon tape. On SEM image 4 nm resolution can be obtained. Two types of layers are formed, one is a loose granular type and another is a dense layer type. The primary plateaus are produced and served to adhere to fibers and flakes of ingredients that arrest fine wear debris in the tribe-pair interface. The primary Plateaus have a high load-bearing capacity and support the secondary plateaus. In the operation pin-on-disc test as the load increases, the load is first taken up by primary plateaus and then it is transmitted to secondary plateaus. Mostly loosely trapped hard particles of ingredients between pin and disc form the third body and are responsible for the generation of micro cracks. In the present work, hard particles of abrasive material such as boron carbide create a third body between the disc and pin surfaces and plough the material from the pin surface and form wear debris and pits on the contact surface of the pin. Also, there is a generation of active and passive debris, active debris is responsible for the supplementary wear mechanism that entrapped between tribe-pair surfaces and causes micro-

(a)

(b)

Figure 7. (a) SEM image before test (sample 2), (b) SEM image after test (sample 2)

(a)

(b)
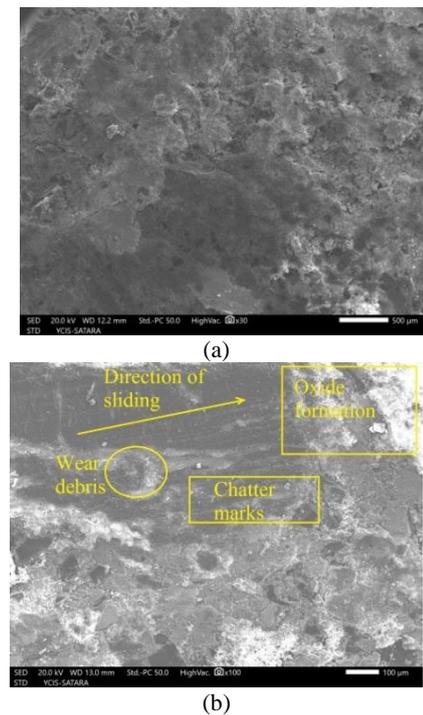
Figure 8. (a) SEM image before test (sample 3), (b) SEM image after test (sample 3)

(a)

(b)

Figure 6. (a) SEM image before test (sample 1), (b) SEM image after test (sample 1)

cutting. At high speed, only a few asperities are contacted between the tribe-pair that generates small debris. In all three samples 1, 2 and 3, the wear of the pattern is clearly shown by yellow marks which are in the sliding direction.

6. CONCLUSION

The dry sliding behavior of three samples of friction materials is studied on wear and friction monitor pin on disc apparatus. By conducting experiments with the help of the Taguchi method, the findings reveals that 29.43 N load, 1100 rpm sliding speed, and 1000 m sliding distance, are the optimal operating parameters possesses the least wear rate (0.002 mg/m). The S/N ratio response table reveals sliding distance is dominant parameters among three operating parameters. From ANOVA p-value is 0.005 and 0.001 which are significant by considering confidence levels of 95 %. Sample 1 possesses highest average-wear-rate whereas sample 3 has lowest average-wear-rate (0.00033 - 0.002 mg/m). The average coefficient of friction obtained in sample 3 is 0.301 to 0.462. The properties of parent friction materials are compared with commercial friction material and find better results. With morphological behavior concerns, all samples shows wear debris accumulated over the surface after wear test. Some chatter marks also observed in the sliding direction. The thermo gravimetric analysis has recorded 9 % average weight loss at 200^0C of all three samples. The complete decomposition temperatures for all 3 samples were 750^0C, 800^0C and 980^0C, respectively. With low metallic concern it is possible to develop brake friction material for low duty applications that helps to reduce non toxic pollution.

7. REFERENCES

1. Vasiljević S, Glišović J, Stojanovic B, Stojanovic N, Grujic I. Analysis of influencing factors on brake wear and non-exhaust emission with reference to applied materials in brake pads. Mobility and Vehicle Mechanics (MVM). 2021. https://doi.org/10.24874/mvm.2021.47.02.0

2. Kumar N, Bharti A, Goyal H, Patel KK. THE EVOLUTION OF BRAKE FRICTION MATERIALS: A REVIEW. Materials Physics & Mechanics. 2021;47(5). https://doi.org/10.18149/MPM.4752021_13

3. Kumar M, Kumar A. Thermomechanical analysis of hybrid friction composite material and its correlation with friction braking performance. International Journal of Polymer Analysis and Characterization. 2020;25(2):65-81. https://doi.org/10.1080/1023666X.2020.1746543

4. Mawuli SE, Anthony S, Akintunde DO. A Conceptual Review of Automobile Disc Brake Friction Materials. European Journal of Applied Sciences. 2022;10(6):492–505. https://doi.org/10.14738/aivp.106.13535

5. Ciudin R, Verma P, Gialanella S, Straffelini G. Wear debris materials from brake systems: environmental and health issues. WIT Transactions on Ecology and the Environment. 2014;191:1423-34. https://doi.org/10.2495/SC141202

6. Park S-H. Types and health hazards of fibrous materials used as asbestos substitutes. Safety and health at work. 2018;9(3):360-4. https://doi.org/10.1016/j.shaw.2018.05.001

7. Maiorana S, Teoldi F, Silvani S, Mancini A, Sanguineti A, Mariani F, et al. Phytotoxicity of wear debris from traditional and innovative brake pads. Environment international. 2019;123:156-63. https://doi.org/10.1016/j.envint.2018.11.05

8. Adekunle A, Okunlola M, Omoniyi P, Adeleke A, Ikubanni P, Popoola T, et al. Development and analysis of friction material for eco-friendly brake pad using seashell composite. Scientia Iranica. 2023;30(5):1562-71. https://doi.org/10.24200/sci.2022.59835.6454

9. Mgbemena CO, Esigie RU, Mgbemena CE, Ata CM. Production of low wear friction lining material from agro-industrial wastes. Journal of Engineering and Applied Science. 2022;69(1):74. https://doi.org/10.1186/s44147-022-00130-3

10. Ilie F, Cristescu A-C. Tribological Behavior of Friction Materials of a Disk-Brake Pad Braking System Affected by Structural Changes—A Review. Materials. 2022;15(14):4745. https://doi.org/10.3390/ma15144745

11. ÜNALDI M, Recai K. The determination of the effect of mixture proportions and production parameters on density and porosity features of Miscanthus reinforced brake pads by Taguchi method. International Journal of Automotive Engineering and Technologies. 2018;7(1):48-57. https://doi.org/10.18245/ijaet.438047

12. Uvaraja V, Natarajan N, Rajendran I, Sivakumar K. Tribological behavior of novel hybrid composite materials using Taguchi technique. Journal of tribology. 2013;135(2):021101. https://doi.org/10.1115/1.4023147

13. Saurabh A, Joshi K, Manoj A, Verma PC. Process Optimization of Automotive Brake Material in Dry Sliding Using Taguchi and ANOVA Techniques for Wear Control. Lubricants. 2022;10(7):161. 10.3390/lubricants10070161

14. Chavhan G, Wankhade L. Optimization of test parameters that influence on dry sliding wear performance of steel embedded glass/epoxy hybrid composites by using the taguchi approach. Tribology in Industry. 2020;42(4):556. https://doi.org/10.24874/ti.863.03.20.09

15. Kalhapure V, Khairnar H. Taguchi method optimization of operating parameters for automotive disc brake pad wear. Appl Eng Lett J Eng Appl Sci. 2021;6:47-53. https://doi.org/10.18485/aeletters.2021.6.2.1

16. Rochardjo H, Nawangsari P, Waskito A. Friction Modifiers Optimization on Tribological Properties of Non-asbestos Organic (NAO) Brake Pad by DoE-Taguchi Method. Tribology in Industry. 2021;43(2):310. https://doi.org/10.24874/ti.1044.01.21.04

17. Lee PW, Lee L, Filip P. Development of Cu-Free Brake Materials. SAE Technical Paper; 2012. Report No.: 0148-7191.

18. Renukappa N, Suresha B, Devarajaiah R, Shivakumar K. Dry sliding wear behaviour of organo-modified montmorillonite filled epoxy nanocomposites using Taguchi's techniques. Materials & Design. 2011;32(8-9):4528-36. https://doi.org/10.1016/j.matdes.2011.03.028

19. Saindane U, Soni S, Menghani J. Friction and wear performance of brake pad and optimization of manufacturing parameters using grey relational analysis. International Journal of Engineering, Transactions C: Aspects. 2022;35(3):552-9. https://doi.org/10.5829/ije.2022.35.03C.07

20. Saindane U, Soni S, Menghani J. Dry sliding behavior of carbon-based brake pad materials. International Journal of Engineering, Transactions B: Applications. 2021;34(11):2517-24. https://doi.org/10.5829/ije.2021.34.11b.14

21. Idris U, Aigbodion V, Abubakar I, Nwoye C. Eco-friendly asbestos free brake-pad: Using banana peels. Journal of King Saud University-Engineering Sciences. 2015;27(2):185-92. https://doi.org/10.1016/j.jksues.2013.06.006

22. Narasimha Reddy P, Ahmed Naqash J. Experimental study on TGA, XRD and SEM analysis of concrete with ultra-fine slag. International Journal of Engineering, Transactions B: Applications,. 2019;32(5):679-84. 10.5829/ije.2019.32.05b.09

Persian Abstract

چکیده

با انبوهی از خودروهای معرفی شده در 2 دهه گذشته، آلایندگی ترمز یکی از عوامل بدنام در انتشار کلی بوده است. در کار حاضر، مواد اصطکاک فلزی کم (برای 3 نمونه که
10 ماده مختلف را تشکیل می دهند) برای کاهش انتشار غیر اگزوز توسعه داده شده است. مواد اصطکاکی به روش قالب‌گیری فشاری تولید می‌شوند و نمونه‌های مختلفی برای
توصیف فیزیکی، مکانیکی و تریبولوژیکی طبق استانداردهای ASTM مورد نیاز است. عملکرد تریبولوژیکی توسط دستگاه "پین روی دیسک" آزمایش می شود. پارامترهای
تریبولوژیکی مانند سرعت، بار و فاصله لغزشی با در نظر گرفتن برای کاربرد اسکوتر انتخاب می شوند. طراحی آزمایش تاگوچی (DoE)برای یافتن پارامترهای عملیاتی بهینه
استفاده می شود. علاوه بر این، ANOVA و تجزیه و تحلیل رگرسیون نیز انجام می شود. نتایج نشان می دهد که نرخ سایش در پارامترهای عملیاتی بهینه حداقل است. میانگین
نرخ سایش به‌دست‌آمده از نمونه 3 کمتر از نمونه‌های 1 و 2 است. نرخ سایش و ضریب اصطکاک بالاتر و پایین‌تر برای نمونه 3 به ترتیب 0.002 و 0.00033 mg/m و
0.462 و 0.301 است. رفتارهای مورفولوژیکی با کمک SEM مورد مطالعه قرار می گیرند. علاوه بر این، تجزیه و تحلیل گرما وزنی (TGA)برای بررسی رفتار حرارتی
نمونه‌های مواد اصطکاکی انجام می‌شود. نتایج نشان می‌دهد که نمونه 3 به عنوان یک ماده اصطکاک ترمز جدید، جایگزینی بالقوه است.

International Journal of Engineering

Performance and Economic Analysis of the Utilization of Construction and Demolition Waste as Recycled Concrete Aggregates

N. Yadav*, R. Kumar

Department of Civil Engineering, Sardar Vallabhbhai National Institute of Technology, Surat, India

P A P E R I N F O	*A B S T R A C T*
	Construction and demolition (C&D) wastes are increasing continuously with intensified construction activities worldwide resulting in ecological concerns. Recycling of these waste products into recycled concrete aggregates (RCA) in base and sub-base layers of pavement is one of the solutions for the problem. Thus, the present study is an in-depth investigation of the utilization of the RCA in construction sector containing laboratory tests, microstructural characterization, and economic analysis. The experiment revealed that, for each mix proportion, the maximum dry density decreases and the ideal moisture content increases as the cement percentage is increased. The 7-day average ultimate compressive strength value for natural aggregates (NA) and recycled concrete (RCA) combined with additives met the requirements. The durability index for all the mix proportions was greater than 0.80. Finally, it was found that 17.86% of the material cost was saved with incorporation of RCA (50%)-NA (50%) for the construction of the sub-base layer of the pavement.

Graphical Abstract

---
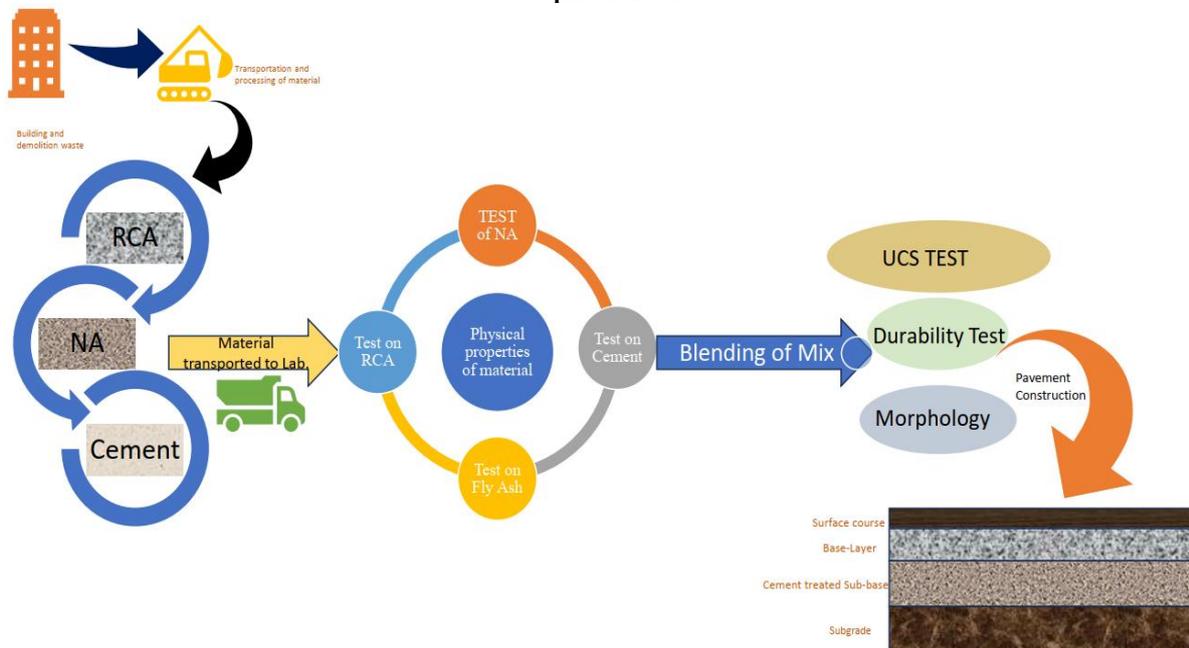
*Corresponding Author Email: neetuyadav403@yahoo.com (N. Yadav)

1. INTRODUCTION

The number of building projects is growing daily. And as a result, it leads to an increase in the production of C&D wastes. The leftovers from maintenance, rehabilitation, and revamping procedures are known as C&D wastes. It consists of steel, plastic, concrete blocks, broken bricks, recycled asphalt, and other building supplies. Additionally, the collection of demolition trash is a result of routine maintenance on the structures. Environmental issues are raised by the improper C&D waste disposal. However, just 1.3 percent of the C&D wastes that are produced overall are recycled. Therefore, C&D waste needs to be properly handled and recycled for its maximum utilization. Based on the volume of construction, C&D wastes come from a variety of sources. They fall into two categories: major and minor contributors. Roads, apartments, bridges, flyovers, malls, etc. are the major contributors, whilst low-rise residential structures are the minor ones. These factors therefore have an adverse influence on the soil's natural composition, threaten flora and animals, affect human health, etc. Figure 1 displays the C&D waste produced in India's main cities (1).

Before incorporating C&D waste into building procedures, it should be thoroughly processed via several steps such as breaking, removing, and crushing. There are no garbage, plastic, glass, or wood in these wastes. The unharmed bricks are separated from the others and set out on the tipping floor. Later, a crusher is used to reduce them to sizes between 20 and 40 mm. Then, to create recycled concrete aggregates, concrete fragments are sorted and put into the crusher (RCA). Comment 4 and 6 Concrete (45%), mortar (24%), masonry/crushed bricks (5%), wood/plastic/crushed glass (3%), and metal wires/marbles (1 percent) make up the majority of RCA, which is composed primarily of gravel (22%) (2, 3).

Various countries have developed specifications of implementation and classification of RCA based on their
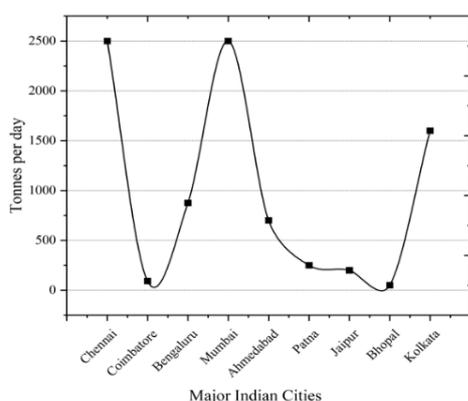
Figure 1. C&D waste generation in major cities in India [1]

composition. European (CEN) practice includes RCA in European (EN) standards; which comprises of natural aggregates (NA), manufactured aggregates, and recycled aggregates. British standards, UK-BS 8500-2:200628, have two variants namely RCA and recycled aggregate. The International Union of Laboratories and Experts in Construction Materials, Systems and Structures, (RILEM) have of aggregates as Type I, II, and III based on its constituents. There are numerous advantages of using RCA in construction sector. It mitigates shortage of raw material such as coarse aggregate, sand etc. Its availability is closer to the construction site; thus, transportation cost reduces. Sources of NA are conserved and dumping site requirement for C&D waste is reduced.

Various researchers have investigated on use of RCA in construction sector (4-6). The growth of India's road network after independence has led to NA depletion. Up to 40% of cement can be replaced in part by cementitious materials (by weight of concrete). This study of the literature addresses the use of artificial aggregates and demolished bricks as a partial replacement for cement (7-9). Fly Ash (FA) usage with RCA increased compressive strength, tensile strength and durability. Experiments on chloride ion penetration and drying shrinkage were carried out to investigate into the durability aspect (10-13). The mechanical properties and durability of concretes are greatly influenced by the size of FA particles. The compression resistance gain of the mortars increases as the FA particle size decreases. If there are any significant differences between the investigated properties, an analysis of variance (ANOVA) test was used to evaluate this (14). Researchers also examined C&D materials that had been hydrated with lime (HL) in concentrations ranging from 1% to 5%. Scanning electron microscopy (SEM) and energy-dispersive X-ray spectroscopy were used for micro-scale analysis (EDS) (15, 16). Utilizing waste materials in building will aid in reducing the rate of the depletion of natural resources (17). Two distinct waste kinds, FA and connected mortar clay brick, have their geo-polymeric potentials examined. Compared to attached mortar clay brick, the UCS value of FA + Fine Aggregates (C&D) raise by 10% over the course of 28 days (CBS) (18). It is explored if recycling C&D waste as aggregate in pavements with substantial traffic volumes is feasible. The mechanical behaviour of the aggregate material was improved by stabilising the C&D waste with Portland cement or lime, reducing mechanical response variability (19). Researchers looked more closely at using RHA to stabilise RCA. It was discovered that adding RHA increases the compressive strength value for blended mixtures. When added to the blended mixture, the hydrated lime raised the blend's crushed strength value (20, 21). Researchers compared several stabilised concrete mix designs (with and without the incorporation of the cooking oil) The blended mixes, consisting of 100 percent RCA plus 70 percent FA plus

30 percent L (by weight of aggregates) and 100 percent RCA plus 95 percent GGBS plus 5 percent L with cooking oil, respectively, were found to have strength of 2 MPa in just two days and 28 MPa after 56 days (22). According to the examined literature, researchers stabilised processed C&D wastes such RCA, bricks, mortar, broken concrete, etc. with the help of additives like FA, lime, RHA, and ground-granulated blast furnace slag (GGBFS). They did not, however, combine FA-L mixes with C&D wastes (for partial replacement of the cement). Additionally, just 1.3 percent of all C&D wastes are recycled on a marginal basis. Furthermore, only a few numbers of studies have used SEM, X-Ray diffraction (XRD), EDS, etc. to characterise the blends' microstructures. Therefore, further study is needed in the area of C&D waste use in the construction sector, specifically in terms of performance evaluation and economic analysis. This research has replaced the granulated sub-base of flexible pavement with a cementitious sub-base mix. Using recycled aggregate in place of natural aggregate can save natural resources and become cost-effective. (Comment 1& 2)

2. MATERIAL AND METHODS

For the present investigation, materials to be studied are selected and procured initially. Then, different types of tests are performed on these procured materials. After that, these materials are graded and blended as per required percentage. Further, laboratory tests are repeated on the blended mixture. Then, microstructural characterization of the blend is performed using SEM. Lastly, cost comparison of blend with original material is performed to check economic viability of the study.

2. 1. Selection of Materials   Crushed concrete, crushed bricks, demolition scrap, and scraped-off pavement are just a few examples of the various elements that are included in C&D wastes. C&D wastes have been treated & recycled prior to being used into the building of the pavement foundation or sub-base. Table 1 lists material used in the present research with their procurement sites. Stone, gravel, sand, silt, and clay are produced as a result of rock erosion and weathering in NAs. For the investigation, an ordinary Portland cement (OPC) of Grade 53 cement was employed, which met the IS: 12269: 1987 standard's specifications. To keep it safe from moisture, the cement was stored in an airtight container. FA is a kind of industrial waste that is created when coal is burned. Iron, silicon, and aluminium oxides make up the majority of fine particles. HL is a dry, white, crystalline powder that is produced when calcium oxide is treated with water. When HL and FA are combined, early strength is improved. Therefore, HL was utilized as an addition to enhance the pozzolanic capabilities of FA or the blended mix's ability to reach early age compressive strength. The materials used in this work are listed in Table 1 along with the locations where they were purchased. Table 2 lists the chemical make-up of Fly Ash "Class F" and Hydrated lime.

TABLE 1. Types of Materials and their procurement sites

Sr. No.	Material	Procurement site
1	RCS	Surat Green Precast Pvt. Ltd.
2	NA	From Stone Quary Site at Chikhli
3	OPC 53	Aditya Birla Company
4	FA (Class F)	From Hazira Industrial area
5	HL	Purchased from local market

TABLE 2. Chemical composition of Fly Ash "Class F" and Hydrated lime

Chemical Analysis	"Class F" Fly Ash (%)	Specifications as per ASTMC618 (%)	Hydrated Lime (%)	Specifications as per ASTM C977-18 (%)	Recycled Material	Test method
Al_2O_3	25.70	-	-	-	13.77	
Fe_2O_3	5.3	-	-	-	7.86	
$SiO_2+Al_2O_3+Fe_2O_3$	85.9	70	-	-	76.44	IS 1727 (2013)
CaO	5.6	-	72	CaO + MgO = 90%	10.65	
MgO	2.1	5	4		1.98	
TiO_2	1.3	-	-	-	-	-
K_2O	0.6	-	-	-	-	-
Na_2O	0.4	1.5	-	-	-	-
SO_3	1.4	5	-	-	-	-
Loss on Ignition	1.9	6	24	-	7.28	IS 1727 (2013)

2. 2. Tests on Materials   The Los Angeles abrasion test is used to determine how much wear is caused by the abrasive action between the aggregates and the steel balls used as abrasive charges. The specific gravity of coarse aggregates is regarded to be a better indicator of the strength and quality of materials used in construction while the water absorption test gives information on the coarse aggregates' capacity to hold water or, to put it another way, their strength. For coarse aggregates, the Ministry of Road Transport and Highways (MoRTH) 5th revision has established an acceptable limit for the combined flakiness and elongation index. According to MoRTH, the sub-base and base layers of the pavement might suffer negative effects from the presence of flaky and elongated pebbles. To assess the durability and resilience of the coarse aggregates under heavy traffic loads, an aggregate impact test was conducted. Only aggregates that pass 12.5 mm and are retained on a 10 mm Indian Standard (IS) screen are subjected to this test.

3. RESULT AND DISCUSSION

3. 1. Gradation and Blending of Aggregates
For better evaluation of the laboratory tests, the current study effort has integrated a varied percentage of the relevant materials, including RCA, FA, and HL. Cement was mixed in the following proportions: 3%, 4%, 5%, and 6% (by weight of aggregates) with RCA in the following proportions: 25%, 50%, 75%, and 100% by partially substituting NA. In addition to using RCA, it's crucial to minimize cement usage by partially substituting it with affordable pozzolanic materials like FA and HL blends in the proportions of 10%, 15%, and 20% (by weight of cement), respectively, when creating blended mixes.

3. 2. Tests on Blended Mix   Executing the tests required for evaluating the physical properties of the NA and RCA was the first step in the relevant research endeavour (according to the standards as indicated in respective IS codes and MoRTH: 5th Revision). Regarding the strength and durability properties of the blended mixes, the recommended tests as explained in detail in the following sections, meeting the requirements of IS Code and IRC: SP:89 specifications, conducted in the lab.

3. 2. 1. Modified Proctor Test   On the mix proportions specified in IS:2720 (Part-8): 1983, a modified Proctor test was conducted in the lab. The test was conducted using a sample that weighed 30 kg and passed through a 37.5 mm IS Sieve. With a 4.9 kg rammer, each layer received 55 hits. Figures 2 and 3 displays the OMC-MDD plot for the RCA (100 percent).
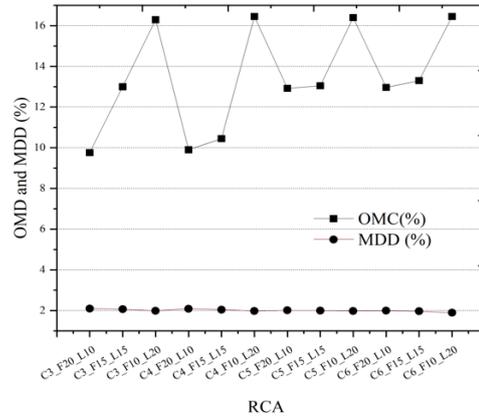
Figure 2. OMC-MDD plot for RCA (100%)
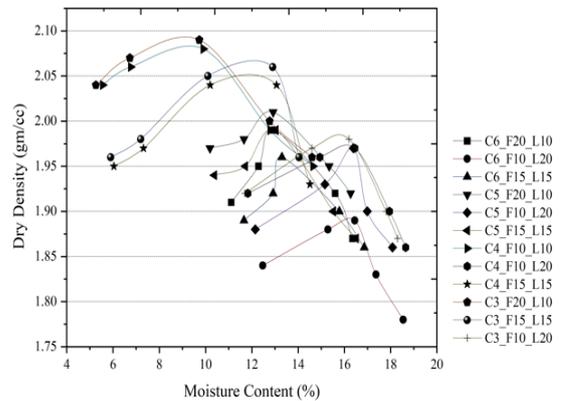
Figure 3. Variation in OMC-MDD with changes % of binder

The findings indicate that, for each mix proportion, the maximum dry density (MDD) decreases and the ideal moisture content (OMC) rises as cement percentage, notwithstanding the trend observed following the integration of the combinations of the used additives, i.e. For FA and HL combined, the lime content increased to 30% of the cement weight (partially replaced), which led to an upward trend in the OMC. For MDD, an increase in the lime content would have led to an upward trend. The water-absorbent property of RCA is another factor contributing to the rising trend of OMC. OMC rises in tandem with an increase in RCA %. The RCA's MDD (100%) turned out to be lower than the NA's (100 percent). This is the reason why the MDD has decreased: attached cement mortar over the surface of the RCA created a porous, considerably weaker fractured layer. The RCA was crushed into considerably finer fractions than NA during the compaction process, which led to a fall in dry density and an increase in water content. This was the other factor.

3. 2. 2. UCS Test The pozzolanic action of the FA and Lime with cement is the primary factor contributing to the development of strength in FA-L blended mixtures. The production of calcium silicate hydrate (CSH) gel and calcium aluminosilicate hydrate (CASH) gel occurred as a result complementing the lime's greater calcium content. The of the silica and alumina rich FA possibly mix-proportions produce an unconstrained compressive strength as a result of the binding gels' pozzolanic reaction. Since FA was present, which slows down the hydration process of pozzolanic materials, greater strength at 7 days could not be reached. However, the UCS value significantly rises if the mixture is cured for a lengthy period of time, such as 28 days. Moreover, the required unconfined compressive strength (UCS) of the sub-base layer, according to the IRC:SP:89, is 1.5 to 3 MPa (comments 3 and 4).

The usage of RCA in the sub-base layer of the pavement was the subject of the most recent study. Therefore, the computed average UCS values of the mixed fraction with RCA content are the major emphasis. It was found that the 50/50 blend of RCA and NA, along with 6 percent C, 10 percent FA, and 20 percent L, produced a 7-day average UCS value (3.57 MPa) that met the requirements of IRC 37:2018. For successful application in the sub-base layer of the pavement, all other mix proportions of 50% RCA and 50% NA readily obtained the average UCS values at 7 days and 28 days, respectively. However, for cement contents of 5% and 6%, the obtained UCS values for the mix-proportion were less than NA (100%) (by weight of aggregates).

3. 2. 3. Durability Test Two like sets (Set 01 and Set 02) of UCS specimen have been made for the observed OMC. Both sets had been dried out in a humidity chamber with a fixed moisture level. For aggregates coarser than 20 mm, Method 2 cannot be used.

Figure 4 shows the Change in UCS with binder % and curing period and Figure 5 shows the Durability Index plot for the RCA (75%)-NA (25%) combination.

To assess the effects of HL and FA when utilized in the stabilization of RCA under various curing conditions, the Durability test was carried out. The main purpose of the test was to determine if blends were durable or resistant to the effects of water on strength under various curing circumstances. This particular aspect was calculated using the Durability Index. This indicator displays the resistance to the strength's impact from water. If the result is less than 0.80, it should be assumed that the stabilizer content is low and that the value for the stabilizer should be adjusted.

3. 2. 4. Beam Load Test To determine the degree of stiffness of the sub-base layer of the flexible pavement, an elastic modulus test was conducted. Three beam specimens measuring $700 \times 150 \times 150$ mm have been cast out for the combined RCA-NA percentage of 50%. Table 3 lists the E-value calculations for the RCA (50%)-NA (50%) pair. Figure 6 depicts a beam load test specimen and specimen testing.

The explanation for the discrepancy in the E-value is that the UCS specimen had a higher surface area under load, but in a beam load test, the area under stress is lower, hence a smaller weight would have a greater influence on the specimen. As the E-value completely depends on the load value, it represents the specimen's stiffness. As a result, this can be one of the causes of the lower number seen during the Beam Load test. However, the ECTSB found in the Beam Load test is within the parameters specified in IRC:37:2018.

3. 3. SEM The SEM technique can be employed to gather data on the specimen's crystallinity, microstructural composition, and surface topography.

TABLE 3. Calculation of E-value for RCA (50%)-NA (50%)

Sample No.		1	2	3
Failure Load (P) kN		9.88	9.92	9.94
Corresponding Disp. (d) mm		6.221	6.29	6.31
	700	700	700	700
Dimension of Beam	150	150	150	150
	150	150	150	150
Effective Length of Beam (L) mm		600	600	600
Moment of Inertia (mm^4)		42187500.00	42187500.00	42187500.00
a=L/3 (mm)		200	200	200
E value (MPa)		2556.60	2566.95	2572.13
Average E-value (MPa)			2565.23	
Modulus of Rupture (MPa)		2.049	2.057	2.061
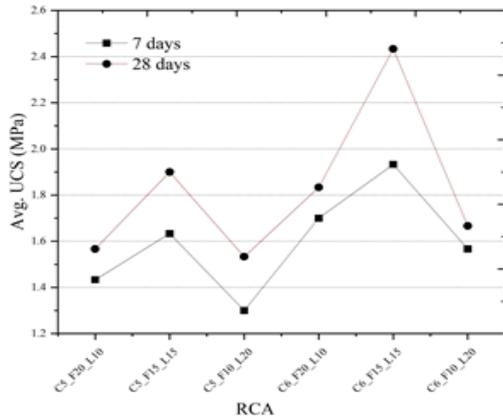
Figure 4. Change in UCS with binder % and curing period
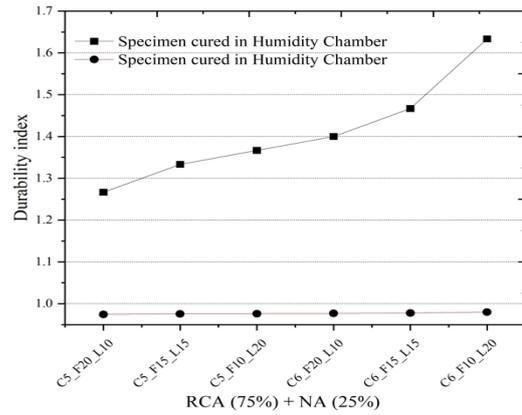
Figure 5. Durability Index plot for RCA (75%)-NA (25%)

Magnification in SEM reaches up to 400X to 30000X resolution. The resolution of a microscope is its capacity to effectively discern two nearby spots. The pores, ettringite gel formation, and microcracks on the aggregate surface have all been investigated using SEM. With a resolution of 1000X, the SEM image shown in Figure 7 for microscopically characterized analysis. The major elements in this specific SEM picture, including the pores, Ettringite gel formation, Calcium Hydroxide, CASH, hydrated cement, and microcracks on the aggregate surface, have all been examined. Tricalcium Silicate, Dicalcium Silicate, and Tricalcium Aluminate are the primary components of cement (C3A). Gypsum and C3A react over the first 24 hours of the hydration process, resulting in the formation of Calcium-Alumino Sulfate ettringite gel. The hydrated lime and fly ash's pozzolanic interaction with the cement is what increases strength. Fly ash, which is rich in silica and alumina, might possibly complement the lime's greater calcium content, resulting in the creation of gels called CSH and CASH. The mix-proportions produce an unconstrained compressive strength as a result of the binding gels' pozzolanic reaction. Since Fly Ash delayed the hydration process of pozzolanic materials, greater strength at 7 days could not be attained because of its presence. However, the UCS value significantly rises if the mixture is cured for a lengthy period of time, such as 28 days. The cementitious materials that were used to fill the tiny holes on the surface of the RCA prevented the electrons from being backscattered, giving the pores a darker appearance.

The development of UCS strength was aided by the significant HL presence with FA. There would have been less microcracks and unreacted Fly ash present. The structure under examination was made visible using a 3000X resolution magnification of the SEM pictures. The spike-like ettringite particles were seen when the SEM picture was again enlarged at a resolution of 10,000X.

Figure 6. Testing of specimen

The initial stage of the hydration process is when this ettringite gel developed. And it continues to react to create CSH and CASH, which causes the strength to develop (Figure 7) (23-25).
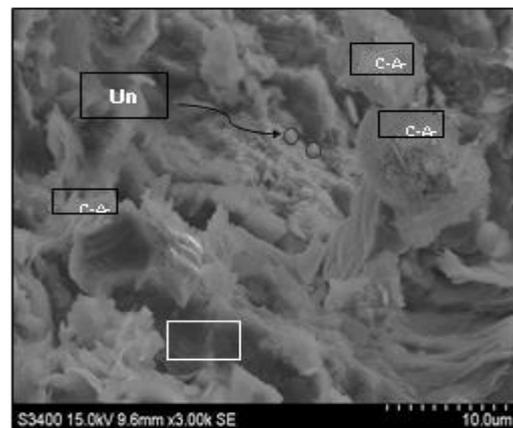
Figure 7. SEM image showing of RCA (50%)-NA (50%) sample Micro cracks, Unreacted Fly Ash, and C-A-S-H

3. 6. Cost Comparison   Cost comparison for the present study is performed as per current market price of various materials and binders. The cost of various materials per m3 is calculated for a conventional mix with RCA (50%) and NA (50%) applied. It was determined that if the RCA (50%)-NA (50%) were used in the building of the sub-base layer of the pavement, 17.86% of the material cost (per m^3) would be saved.

4. CONCLUSION

In the present study, an investigation of utilization of RCA in construction sector has been performed using laboratory tests, microstructural characterization, and economic analysis. Following are important findings of the study-

- For each mix proportion, the maximum dry density drops as the cement % rises, but the ideal moisture content rises. The maximum dry density of the RCA (100%) was lesser than the NA (100%).
- The 7 days average ultimate compressive strength value for 50% RCA and 50% NA blended with additives satisfied the specifications.
- All mix proportions had durability indices that were higher than 0.80. The E-value for the mix ratio of RCA (50%)-NA (50%) was calculated to be 2565.23 MPa. SEM study has been done on the aggregate surface's pores, ettringite gel formation, calcium hydroxide, calcium aluminosilicate hydrate, hydrated cement, and microcracks.
- Economic analysis found that employing RCA (50%)-NA (50%) for the construction of the pavement's sub-base layer reduced material costs by 17.86%.

5. REFERENCES

1. Jain MS. A mini review on generation, handling, and initiatives to tackle construction and demolition waste in India. Environmental Technology & Innovation. 2021;22:101490. 10.1016/j.eti.2021.101490

2. Thang V, Cung L, Nguyen D. An Application of Artificial Neural Network to Predict the Compressive Strength of Concrete using Fly Ash and Stone Powder Waste Products in Central Vietnam. International Journal of Engineering, Transactions B: Applications. 2022;35(5):967-76. 10.5829/IJE.2022.35.05B.12

3. Sumardi D, Rochman T, Riskiyah I. High-contribution of strip glass waste in buckling-strengthening of slim GLARC columns at once avoiding ASR deterioration problems in concrete materials. International Journal of Engineering, Transactions B: Applications. 2021;34(11):2452-66. 10.5829/ije.2021.34.11b.09

4. Mohsin MS, Alwash NA, Kadhum MM. Comparative Study on Structural Behavior of Reinforced Concrete Straight Beam and Beams with out of Plane Parts. International Journal of Engineering, Transactions A: Basics. 2021;34(10):2280-93. 10.5829/ije.2021.34.10a.09

5. Gunasekaran K, Choudhury S. Experimental Study on Single Bay Reinforced Coconut Shell Concrete Portal Frame under Lateral and Cyclic Load. International Journal of Engineering, Transactions B: Applications. 2021;34(8):1905-12. 10.5829/ije.2021.34.08b.12

6. Beiram A, Al-Mutairee H. Effect of using waste rubber as partial replacement of coarse aggregate on torsional strength of square reinforced concrete beam. International Journal of Engineering, Transactions B: Applications. 2022;35(2):397-405. 10.5829/IJE.2022.35.02B.16

7. Malhotra V. Durability of concrete incorporating high-volume of low-calcium (ASTM Class F) fly ash. Cement and Concrete Composites. 1990;12(4):271-7. 10.1016/0958-9465(90)90006-J

8. Woolley G, Coombs R. The significance of improvements in fly ash quality. Waste Management. 1996;16(1-3):7-13. 10.1016/S0956-053X(96)00025-6

9. Zakaria M, Cabrera J. Performance and durability of concrete made with demolition waste and artificial fly ash-clay aggregates. Waste Management. 1996;16(1-3):151-8. 10.1016/S0956-053X(96)00038-4

10. Kou SC, Poon CS, Chan D. Influence of fly ash as a cement addition on the hardened properties of recycled aggregate concrete. Materials and structures. 2008;41:1191-201. 10.1617/s11527-007-9317-y

11. Barbhuiya S, Gbagbo J, Russell M, Basheer P. Properties of fly ash concrete modified with hydrated lime and silica fume. Construction and Building Materials. 2009;23(10):3233-9. 10.1016/j.conbuildmat.2009.06.001

12. Kou S, Poon CS. Enhancing the durability properties of concrete prepared with coarse recycled aggregate. Construction and building materials. 2012;35:69-76. 10.1016/j.conbuildmat.2012.02.032

13. Anastasiou E, Filikas KG, Stefanidou M. Utilization of fine recycled aggregates in concrete with fly ash and steel slag. Construction and Building Materials. 2014;50:154-61. 10.1016/j.conbuildmat.2013.09.037

14. da Silva SR, de Oliveira Andrade JJ. Investigation of mechanical properties and carbonation of concretes with construction and demolition waste and fly ash. Construction and Building Materials. 2017;153:704-15. 10.1016/j.conbuildmat.2017.07.143

15. Mohammadinia A, Arulrajah A, Haghighi H, Horpibulsuk S. Effect of lime stabilization on the mechanical and micro-scale properties of recycled demolition materials. Sustainable Cities and Society. 2017;30:58-65. 10.1016/j.scs.2017.01.004

16. Arulrajah A, Mohammadinia A, D'Amico A, Horpibulsuk S. Effect of lime kiln dust as an alternative binder in the stabilization of construction and demolition materials. Construction and Building Materials. 2017;152:999-1007. 10.1016/j.conbuildmat.2017.07.070

17. Cristelo N, Fernández-Jiménez A, Vieira C, Miranda T, Palomo Á. Stabilisation of construction and demolition waste with a high fines content using alkali activated fly ash. Construction and Building Materials. 2018;170:26-39. 10.1016/j.conbuildmat.2018.03.057

18. Das SK, Shrivastava S. A study on the viability of fly ash and construction and demolition waste as geopolymerized masonry mortar and their comparative analysis. Materials Today: Proceedings. 2020;32:574-83. 10.1016/j.matpr.2020.02.402

19. Marathe S, Shetty TS, Mithun B, Ranjith A. Strength and durability studies on air cured alkali activated pavement quality concrete mixes incorporating recycled aggregates. Case Studies in Construction Materials. 2021;15:e00732. 10.1016/j.cscm.2021.e00732

20. Jethy B, Paul S, Naik B. Effect of utilization of rice husk ash on hardened properties of recycled concrete aggregate. Materials

Today: Proceedings. 2022;59:1625-35. 10.1016/j.matpr.2022.03.322

21. Hemalatha T, Ramaswamy A. A review on fly ash characteristics–Towards promoting high volume utilization in developing sustainable concrete. Journal of cleaner production. 2017;147:546-59. 10.1016/j.jclepro.2017.01.114

22. Bun P, Cyr M, Laniesse P, Bun KN, Idir R. Concrete made of 100% recycled materials-Feasibility study. Resources, Conservation and Recycling. 2022;180:106199. 10.1016/j.resconrec.2022.106199

23. Imtiaz T, Ahmed A, Hossain MS, Faysal M. Microstructure analysis and strength characterization of recycled base and sub-base materials using scanning electron microscope. Infrastructures. 2020;5(9):70. 10.3390/infrastructures5090070

24. Evangelista L, Guedes M, Ferro A, de Brito J. Microstructure of concrete prepared with construction recycled aggregates. Microscopy and Microanalysis. 2013;19(S4):147-8. 10.1017/S1431927613001359

25. Pawluczuk E, Kalinowska-Wichrowska K, Jimenez JR, Fernández-Rodríguez JM, Suescum-Morales D. Geopolymer concrete with treated recycled aggregates: Macro and microstructural behavior. Journal of Building Engineering. 2021;44:103317. 10.1016/j.jobe.2021.103317

Persian Abstract

چکیده

زباله های ساخت و ساز و تخریب با تشدید فعالیت های ساخت و ساز در سراسر جهان به طور مداوم در حال افزایش است که منجر به نگرانی های زیست محیطی می شود. بازیافت این ضایعات به سنگدانه های بتن بازیافتی (RCA) در لایه های پایه و زیر پایه روسازی یکی از راه حل های این مشکل است. بنابراین، مطالعه حاضر یک بررسی عمیق از استفاده از RCA در بخش ساخت‌وساز است که شامل تست‌های آزمایشگاهی، خصوصیات ریزساختاری و تحلیل اقتصادی است. آزمایش نشان داد که برای هر نسبت مخلوط، حداکثر چگالی خشک کاهش می‌یابد و با افزایش درصد سیمان، رطوبت ایده‌آل افزایش می‌یابد. میانگین مقاومت فشاری نهایی ۷ روزه برای سنگدانه های طبیعی (NA) و بتن بازیافتی (RCA) همراه با مواد افزودنی الزامات را برآورده می کند. شاخص دوام برای تمام نسبت های مخلوط بیشتر از 0.80 بود. در نهایت، مشخص شد که ۱۷.۸۶٪ از هزینه مواد با ادغام (٪50) NA - (٪50) RCA برای ساخت لایه زیرین روسازی صرفه جویی گردید.

International Journal of Engineering

Journal Homepage: www.ije.ir

Synthesis, Characterization, and Evaluation of an Eco-friendly Demulsifier for Crude Oil Emulsion Treatment Using Waste Corn Oil

M. M. Abed*, T. M. Naife

Department of Chemical Engineering, College of Engineering, University of Baghdad, Baghdad, Iraq

A B S T R A C T

Despite the diversity of energy sources at the present time, they have not been able to be a real alternative to crude oil, as it is still considered the primary source of energy in the world and will remain so for many years. As is known, the petroleum industry consists of an interconnected series of operations, starting with extracting crude oil from wells and ending with its refining process. As is known, the petroleum industry consists of an interconnected series of operations, starting with extracting crude oil from wells and ending with its refining process. These operations vary in degree of difficulty, cost, and challenges they face. Crude oil emulsion is one of the most costly issues in this important industry. In the current study, a novel environmentally friendly bio-demulsifier synthesized from corn oil waste has been introduced. The unique characteristics of this novel bio-demulsifier were diagnosed using several tests, including: Fourier transform infrared spectroscopy (FTIR), gas chromatography-tandem mass spectrometry (GC-MS), proton nuclear magnetic resonance (1HNMR), and thermogravimetric analysis (TGA). The demulsification activity has been evaluated using a bottle test method as a function of settling time, water content, and temperature. The maximum separation ratio was 69.3% at a dose of 1000 ppm for 5 hours and 70 °C, while the water-oil ratio was 30/70. The obtained results demonstrate that bio-demulsifier could be used as a safe and environmentally friendly alternative in initial demulsification units, which will reduce the environmental hazards and financial costs associated with the oil industry when using traditional demulsification methods.

doi: 10.5829/ije.2024.37.03c.03

Graphical Abstract
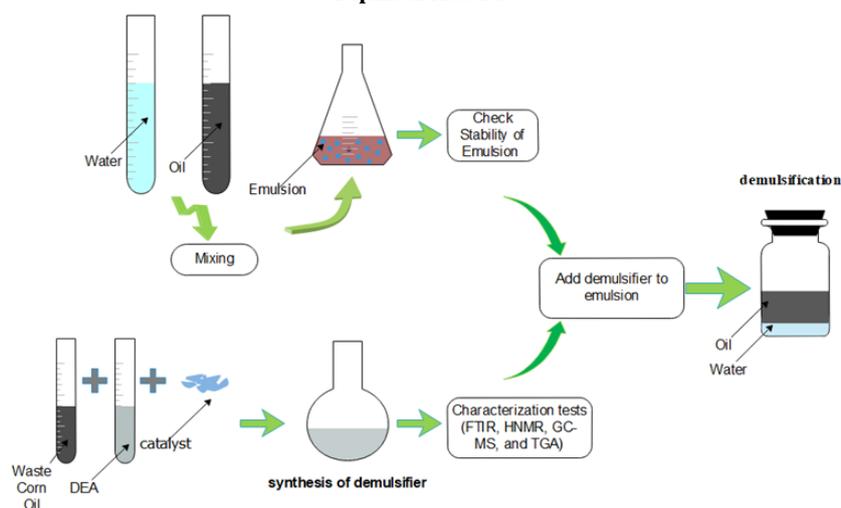
Corresponding Author Email: mohammed.abd2107m@coeng.uobaghdad.edu.iq (M. M. Abed)

1. INTRODUCTION

The oil industry is still the largest supplier of the global energy sector, and the rest of the energy industries have not risen to compete with this industry despite making great strides in development and growth. Reaching the stage of serious competition between renewable energy sources and those provided by the oil industry will take a long time. Therefore, it is necessary to continue developing the oil industrial sector and make it as safe and environmentally friendly as possible (1, 2). In order to achieve the aim of sustainability in the oil industry, attention must be paid to the issue of chemicals that enter the process of preparing crude oil emulsions. Crude oil emulsions can be defined as systems with two or more immiscible liquids distributed as droplets with the assistance of an emulsifying agent (3). The continuous phase surrounds the droplets, which represent the internal phase. The emulsifying agent stabilizes the emulsion and separates the dispersed droplets from the continuous phase (4, 5). The most common types of crude oil emulsions found in petroleum production are oil-in-water emulsions (O/W), water-in-oil emulsions (W/O), and more complex water-in-oil emulsions (W/O/W) (4, 6). Water-in-oil emulsions affect oil production and processing. Hydrocarbon reserves, production, refineries, and pipelines can generate emulsions (4, 7). Crude oil may include water droplets for many reasons. Due to its composition, crude oil contains less than 50 μm water droplets. Drilling causes turbulent mixing and agitation that disperse water droplets in the oil system (8, 9). Since water is considered one of the causes of corrosion in oil pipelines crude oil viscosity, and catalyst poisoning during refining (10-12). Therefore, it requires the removal of emulsified water during the process of transporting and refining crude oil. The process by which dispersed water is separated from the crude oil phase is called demulsification (13). Different techniques, such as electrical, thermal, membrane filtration, microwave, and physical/chemical methods, can be applied to process oil emulsions (14-16). Chemical demulsifiers/heating are the most efficient approaches to water dehydration. Demulsifiers work by diffusing chemicals into emulsions, replacing the asphaltene layer around water droplets with a soft film that encourages droplet coalescence, and allowing gravity to separate emulsified water (4, 14). Fermentation, transesterification, and methanation are examples of biotechnology procedures that may be used efficiently in waste biorefineries that use waste oil. Industrial production of biodiesel and biogas from waste oil can create value-added products (17). Biosurfactants have shown superior performance compared to chemical surfactants, where they exhibit high stability at higher pH and temperature. The most critical parameter is that these materials are biodegradable, biocompatible, and less toxic. Compared to conventional surfactants, biosurfactants can recover more oil, and they are both economical and ecologically friendly (18, 19). Commercial oils like maize oil (20), castor oil (21, 22), linseed oil, and soybean oil (23) can be used to make demulsifiers. Waste corn oil, a popular vegetable oil that is inexpensive, non-toxic, and abundantly renewable, has promise as a suitable material. The ultimate aim of this study is to develop a novel, eco-friendly, and cost-effective demulsifier derived from corn waste oil for separating water-in-oil emulsions (W/O). FTIR, GC-MS, TGA, and 1HNMR methods will be used to characterize the produced surfactant. The bottle test technique will be used to evaluate its demulsification effectiveness as a biodemulsifier.

2. MATERIALS and METHOD

2. 1. Materials
The materials used in this study included the following:
1. Waste corn oil for frying: This material was obtained from local vegetable oil factories.
2. Diethanolamine (DEA): has a purity of 98%. DEA was supplied by Thomas Baker, India.
3. P-Toluensulphonic Acid Monohydrate: with a purity of 98.5%, is supplied by HIMEDIA, India.
4. Sodium chloride: is supplied by Alpha Chemika, India, with 99.5% purity.
5. Ether Petroleum, 40–60 °C: with 98% purity. This material was supplied by Alpha Chemika, India.
6. Sour crude oil: The sour crude oil sample was taken from Al-Dura refinery, which was extracted from Basrah crude oil in Iraq. The properties of this sample are listed in Table 1.

2. 2. Demulsifier Synthesis
The demulsifier preparation process consists of four steps, which procedures have been completed according to the reference (20):
1. First step: waste corn oil has been filtered to eliminate impurities and solid carbonous particles.
2. Second step: involved reacting waste corn oil with diethanolamine at a ratio of 2:1 (v%) using the base catalyst p-toluene sulfonic acid monohydrate. The reaction occurred in a 500 mL flask fitted with a reflux

TABLE 1. Physical properties of sour crude oil

Property	Value
Sp.Gr. at 15.6ºC	0.88490
API	28.40
Viscosity (cp) at 20 °C	19.4
Sediment and Water content (%vol.)	0.050
Asphaltenes (%wt.)	2.220

condenser, thermometer, and magnetic stirrer. Initially, the waste corn oil (66.6 mL) and catalyst (0.83 g) were heated to 140 °C while stirring until the catalyst dissolved, which took approximately 1 hour. Diethanolamine (33.3 mL) was gradually added, and the temperature was increased to 180 °C for one hour. The reaction was then allowed to proceed for an additional 2 hours with continuous stirring, during which water (8 mL) was collected as an indicator of the chemical reaction. The resulting product was collected and allowed to cool to room temperature.

3. Third step: an excess of petroleum ether was added to the product and mixed thoroughly for 20 minutes.

4. Fourth step: involved purification, where the solvent, along with contaminants and unreacted materials, was removed using the evaporation technique via a rotary evaporator under vacuum conditions at a temperature of 50 °C and a rotation speed of 100 rpm.

2. 3. Emulsion Preparation　　　　In order to create conditions similar to those found in the crude oil industry, a simulated crude oil emulsion was prepared by mixing a brine solution with a 3% concentration (0.5M NaCl solution) with crude oil in a volumetric ratio of 30/70. The brine solution was chosen as an imitation of the aqueous solution commonly employed in the field of crude oil. The crude oil emulsion was homogenized at 10000 rpm for 30 minutes at ambient temperature. The stability of the emulsion was evaluated through visual observation and the analysis of droplet size distribution using an optical microscope.

2. 4. Demulsification Experiments　　　　The bottle test was performed to evaluate the demulsifier's performance. The demulsifier was added in various amounts, ranging from 1000 ppm to 6000 ppm, to each 100 mL of the emulsion. Using a graduated measuring container and the measured volume of water in milliliters, Equation 1 was used to compute the water separation efficiency (WSE%):

$$WSE\,\% = \frac{\text{volume of separated water (ml)}}{\text{Total volume of water in the sample (ml)}} * 100\% \qquad (1)$$

The graph illustrates three distinct dispersion rates. In addition, the different parameters were determined to reach the optimum conditions.

3 .RESULTS AND DISCUSSION

3. 1. structure and Bonding Characterization
3. 1. 1. Fourier Transform Infrared Spectroscopy (FTIR)　　　　This test was done to detect the bonding of the demulsifier.The range of wavelength of FTIR spectra was between 400 and 4000 cm^{-1} using liquid cells. The

test was done via FTIR type 8400S manufactured by Shimadzu/ Japan). This test was done to detect the bondings of the demulsifier.

The FTIR spectra of the synthesized demulsifier (WMF) in Figure 1 show a broad peak at 3375 cm^{-1} sequentially, which, according to its classification as secondary aliphatic alcohols, indicates O-H stretching. The two stretching peaks of NH$_2$ disappearance at 3375cm^{-1} had confirmed interactions of hydroxyl groups with amine groups (24).

TIR spectra show NH$_2$ stretching peaks at 3100-3400 cm^{-1}. These peaks represent amine group N-H stretching vibrations. N-H stretching peaks may shift, expand, or disappear due to amine-hydroxyl group interactions. Hydrogen bonds between hydroxyl and amine groups weaken the N-H bond, lowering its vibrational frequency and shifting or eliminating the peak (24).

Sharp absorption peaks at 3008–2855 cm^{-1} are given to both symmetrical and asymmetrical alkane stretching (–CH$_3$) and alkenes (=CH$_2$) in the aliphatic hydrocarbon groups (20).

The peaks at 1739 and 1165 cm^{-1} refer to the presence of fatty acids (C=O) stretching of esters. This is clear evidence of ester formation (25). The band at 1053 cm-1 is the major group of aliphatic alcohols (C-OH) (20). As illustrated in Figure 1, several functional groups in surfactants, such as hydroxyl, carboxyl, fats, aliphatic alcoholic, and alkane compounds, were found by the examination of the FTIR spectrum data.

3. 1. 2. Gas Chromatography-mass Spectrometry (GC-MS)　　　　Gas chromatography-mass spectrometry (GC-MS) is a powerful analytical technique used to identify and quantify chemical components in complex mixtures. The GC can separate compounds in a mixture according to their physical qualities, whereas the mass spectrometer can identify them based on their structure and molecular weight (14). GC-MS has the ability to
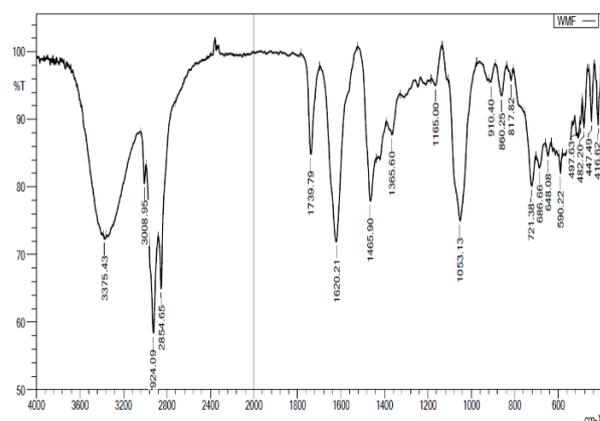
Figure 1. The demulsifier FTIR

detect and quantify a vast variety of chemical substances, even at very low concentrations, making it a valuable tool for the characterization of the demulsifier.

As shown in Table 3, the analysis of the GC mass results reveals that the demulsifier is a complex mixture of various compounds. The most abundant compound found in the demulsifier is 1,4-Bis(2-Hydroxyethyl)-Piperazine (BHEP), with an area percentage of 24.77%. BHEP has properties that make it effective in breaking emulsions and aiding in the separation process. In general, hydroxyethyl piperazine is intermediate in the manufacture of corrosion inhibitors, polyurethane catalysts, synthetic fibers, surfactants, and pharmaceutical.

Phenyl-3-methylpenta-1,2,4-triene with an area percentage of 17.47 %, also known as isopropenylbenzene or alpha-methylstyrene. It is an aromatic compound that belongs to the class of styrenes and could have a positive effect. It is widely believed that demulsifiers containing aromatic groups exhibit exceptional speed and performance. This can be attributed to the similarity between the aromatic groups in demulsifiers and those found in asphaltenes, which are known to generate the least stable oil film. Therefore, it is advantageous to have aromatic compounds in demulsification breakers, as an example methsuximide, flupentixol, 2-Cyclopropen-1-one, 2-cyclopropyl-3-(dichlorocyclopropyl methyl)-(CAS), and 5,8-dibromo-2-phenyl-1-aza-azulene, as they may improve the efficiency and effectiveness of the demulsification process (26).

On the other hand, there is a group of different compounds that have been found to assist in the process of breaking emulsions due to the existence of hydroxyl and amine groups (27), such as Ethanol, 2-[(2-aminoethyl) amino]-, and ribitol. Due to the absence of hydroxyl and amine groups, the remaining components are thought to have no influence on demulsification.

TABLE 2. Technical requirements for GC/MS operation

Gas Chromatograph	
Analytical Column	Agilent HP 5 MS/USA (30 m x 0.25 mm x 0.25 μm)
Injector-Port	Split (80:1)
GC Inlet Temp	260℃
Carrier-Gas	Helium
Injection Volume	1μl
Oven Program	
Temperature	60 ℃
Hold Time	4 min
Rate	3 ℃
Temperature	100 ℃
Rate	4 ℃
Temperature	260 ℃
Mass Spectrometer	
Auxiliary heat	280 ℃
Mass Variation via Full Scan Method	50-500

TABLE 3. Surfactant chemical composition as identified by GC-MS

No.	RT (min)	Name	chemical formula	Area (Ab*s)	Area%	CAS Number
1	9.083	Ethanol, 2-[(2-aminoethyl) amino]-	$C_4H_{12}N_2O$	409458786	3.73	000111-41-1
2	10.033	Ribitol	$C_5H_{12}O_5$	442973316	4.04	000488-81-3
3	17.702	1,4-BIS(2-HYDROXYETHYL)-PIPERAZINE	$C_8H_{18}N_2O_2$	2716336661	24.77	000122-96-3
4	22.615	Methsuximide	$C_{12}H_{13}NO_2$	724236388	6.60	000077-41-8
5	27.638	Linoleic acid, methyl ester	$C_{18}H_{32}O_2$,	295894561	2.70	000112-63-0
6	29.174	Flupentixol	$C_{23}H_{25}F_3N_2OS$	561733856	6.12	002709-56-0
7	34.861	Methimazole	$C_4H_6N_2S$	635394394	5.79	000060-56-0
8	36.915	Heptanoic acid, 7-bromo-, methyl ester	$C_{11}H_{21}BrO_2$	514522050	4.69	054049-24-0
9	37.061	Methyl 9,10-dichlorooctadecanoate	$C_{19}H_{36}Cl_2O_2$	512381414	4.67	033094-27-8
10	40.236	2-Cyclopropen-1-one, 2-cyclopropyl-3-(dichlorocyclopropylmethyl)- (CAS)	$C_{20}H_{27}Cl_2NO_3S$	374996861	3.42	062688-80-6
11	42.317	5,8-dibromo-2-phenyl-1-aza-azulene	$C_{15}H_9Br_2N$	353097888	3.22	121505-50-8
12	42.654	1-phenyl-3-methylpenta-1,2,4-triene	$C_{12}H_{12}$	1917606567	17.47	093247-38-2

3. 1. 3. ¹H NMR Spectroscopy

The ^{1}HNMR (Proton Nuclear Magnetic Resonance) test looks at how hydrogen atoms move in a magnetic field to figure out the shape and chemical surroundings of molecules. It offers valuable insights into molecular connectivity, functional groups, and stereochemistry and finds applications in fields like chemistry, pharmaceuticals, and biochemistry. In this study, 1H nuclear magnetic resonance spectroscopy (^{1}H NMR) using a BioSpin GmbH Bruker spectrometer/ Germany was performed to verify the WMF synthesized chemical structure.

The compound's structure was assessed using ^{1}H NMR. The chemical shifts, multiplicities, coupling constants, and correlations of the NMR peaks, together with any other relevant information, were accurately measured.

Figure 2 shows the demulsifier structure. on the basis of the chemical components ^{1}H NMR (DMSO, 500 MHz) spectra, Demulsifier spectra show amine groups (NH$_2$ and NH) as a single peak and double peak at 0.84-1.5 ppm (28). At the same time, the (CH$_2$)n peaks of the alkyl group show up many times at 2.01 ppm and the -OH proton of WMF at 2.52 ppm (9). The chemical shift value of 3.46-5.35 typically indicates the presence of a proton signal in the region of aliphatic protons. It is less commonly associated with aromatic protons, as they typically appear in a higher chemical shift range (28).

3. 1. 4. Thermal Gravimetric Analysis (TGA)

A thermogravimetric analyzer (TGA) from TA Instruments (SDT Q600 model/ USA) was used to determine the thermal stability of the synthesized demulsifier. TGA measures the amount of demulsifier mass lost when the temperature changes. The test was conducted in an Argon environment, with temperatures ranging from 25 to 800 degrees Celsius and a heating rate of 20 degrees Celsius/min.

Figure 3 presents the results of a thermal stability investigation of the WMF demulsifier. There were two stages of mass reduction. The first zone relates to the loss of weakly linked water molecules and has a mass loss of 7.584% from room temperature to 150 °C .

The second zone, from 150 to 800 °C, saw a dramatic decrease in mass (89.73%), indicating that at temperatures above 150 °C, WMF molecules begin to decompose. At 800 °C, the ash content is about 3%, and this indicates that the majority of the compounds in WMF are light ones.

The average temperature of a reservoir is between 50 and 120 degrees Celsius (13). WMF thermal stability is good because the water content makes it lose less than 5% of its weight. This can be fixed by adding a drying step at the end of the manufacturing process.

3. 2. Emulsion Stability

The droplet size distribution of the simulated emulsion was characterized using an optical microscope (BVH340, Altay Scientific, Belgium)

The stability of the emulsion is a very crucial factor specified in the demulsification process. In this study, two approaches were used to specify the stability of simulated crude oil emulsions. The first one is visual observation. The duration observation continued for 72 hours after the synthesis process, and the separation ratio was recorded with time.

The second technique involved using an optical microscope to measure the droplet sizes of a drop-off generated emulsion (Figure 4 depicts the average droplet size and droplet size dispersion).

According to the emulsion stability determined by optical microscope methods, the emulsion can be classified according to the mean diameter. In this study, the mean diameter was 27.15μm, which means that the emulsion is stable, where the range of macro-emulsions is (0.5-100 μm) (29).

Figure 2. The demulsifier H NMR spectroscopy

Figure 3. The demulsifier Thermal Gravimetric Analysis

Figure 4. Images of the droplet dispersion in an emulsion, captured using a microscope.

3. 3. Assessment of Parameters Influencing the Demulsification Process

3. 3. 1. Impact of Settling Time and Demulsifier Doses on Water Separation Efficiency (WSE)

Figure 5 depicts the average separation efficiency achieved at various concentrations of WMF (1000-6000 ppm) for the Basrah emulsion. The results indicate that water separation improves with longer settling times. This is because the presence of sufficient time increases the chance of oil droplets colliding with one another, increasing the phenomena of flocculation and coalescence of the oil into larger droplets. Demulsification and phase separation are both improved as a result (28). After 5 hours, the average separation efficiency reached 69.3% when the dose was 1000 ppm. Different responses were observed for other doses compared to the emulsion without the addition of WMF. So, the optimum separation time of the demulsification process was 5 h.

It was found, based on the outcomes, that increasing the concentration of demulsifier WMF led to a decrease in water separation efficiency (WSE), indicating an overdosing effect. Overdosing demulsifiers can lead to the restabilization of emulsions. Demulsifier lipophilicity or hydrophilicity and molecular mass determine the ideal demulsification quantity (15). This study found 1000 ppm optimal.

A decrease in demulsification efficiency can be traced to the production of a back emulsion, which is then labeled as a w/o/w emulsion because of the influence of shearing rate and temperature (25).

3. 3. 2. Effect of Temperature on Water Separation Efficiency (WSE)

Experiments were run at varying temperatures of 50, 60, and 70 degrees Celsius, According to experts, demulsifiers are best studied at this temperature (20, 30). Oil, water, interfacial films, and the
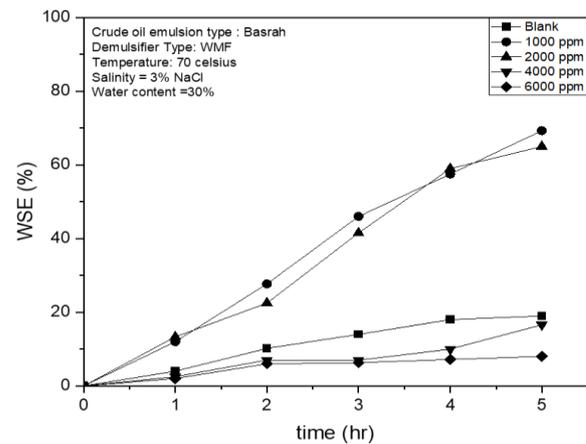
Figure 5. Demulsifier doses and emulsion separation efficiency
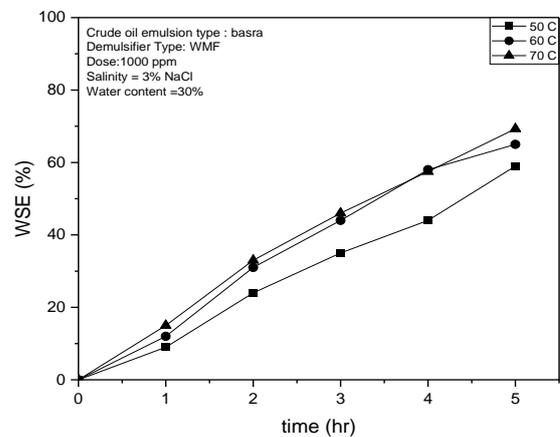
Figure 6. Temperature and emulsion separation efficiency.

solubility of surfactants in both the oil and water phases are all impacted by temperature. Another key effect of temperature on emulsions is the decrease in viscosity that occurs as temperatures rise.

This is because the thermal energy of the droplets increases as the temperature rises (15, 31). For these reasons, investigating how temperature affects the stability of W/O emulsions is important. For varying concentrations of demulsifiers, rising temperatures were clearly associated with rising WSE. WMF performed best at 50, 60, and 70 degrees Celsius with a dosage of 1000 ppm and 5 hours of separation time, and the results are clarified in Figure 6 (57.2, 65, and 69.3%, respectively). As the temperature of the oil rises, its density and viscosity fall, allowing the water droplets to settle more quickly. So, the optimum temperature was 70 °C in this work.

3. 3. 3. Effect of Water Content

The main factors affecting water-in-oil emulsion separation efficiency and

stability are water and oil content. A series of experiments were conducted to investigate the impact of water content and demulsifier concentration on water separation efficiency (WSE). The water content levels examined included 10%, 30%, and 50%, while the demulsifier employed was WMF. In Figure 7, it is observed that when WMF is present at 1000ppm, a temperature of 70°C, and a duration of 5 hours, Demulsification efficiency improves from 10% to 50% of the amount of water. Since the interface layer becomes thinner as the water content increases, the attraction of water droplets increases. The rate of coalescence consequently increases (7). However, due to the limited quantity of asphaltenes that can be adsorbed at the water-oil interface, the system tends to be inherently unstable. Specifically, As water content rises, the amount of asphaltene distributed per water molecule falls (23).
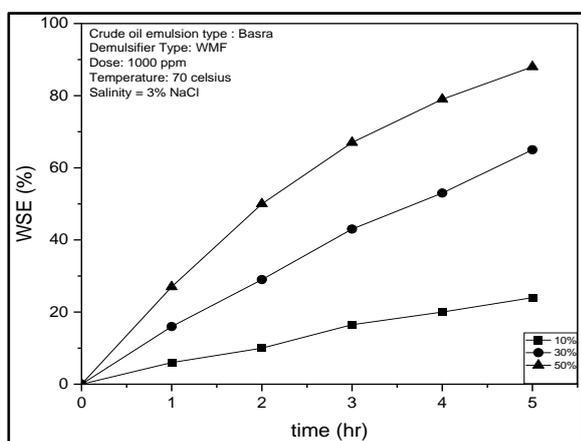

Figure 7. Water content and emulsion separation efficiency

4. CONCLUSIONS

The following conclusions may be drawn based on the study's findings:

1. The bio-demulsifier synthesized from waste corn oil shows promise as a potential and environmentally friendly alternative to chemical demulsifiers.

2. The synthesized bio-demulsifier has the potential to lessen the environmental impact associated with traditional demulsifiers. However, more research and development is needed to optimize the effectiveness of this novel bio-demulsifier, and achieve 100 percent water separation efficiency.

3. The characterization tests proved their efficiency in specifying and describing the bio-demulsifier.

4. Besides, these tests can be used to determine the types of functional groups they possess.

The maximum demulsification ratio was 69.3% at 1000 ppm, 5 hours of settling time, 70 °C, and 30% water

content, all of which are operation factors with significant influence on the demulsification process.

5. REFERENCES

1. Shakir F, Hussein HQ, Abdulwahhab ZT. Influence of Nanosilica on Solvent Deasphalting for Upgrading Iraqi Heavy Crude Oil. Baghdad Science Journal. 2023;20(1):0144-.

2. Jiad MM, Abbar AH. Treatment of petroleum refinery wastewater by an innovative electro-Fenton system: Performance and specific energy consumption evaluation. Case Studies in Chemical and Environmental Engineering. 2023;8:100431.

3. Admawi HK, Mohammed AA. A comprehensive review of emulsion liquid membrane for toxic contaminants removal: An overview on emulsion stability and extraction efficiency. Journal of Environmental Chemical Engineering. 2023:109936.

4. Raya SA, Mohd Saaid I, Abbas Ahmed A, Abubakar Umar A. A critical review of development and demulsification mechanisms of crude oil emulsion in the petroleum industry. Journal of Petroleum Exploration and Production Technology. 2020;10:1711-28.

5. Mohammed AA, Selman HM. Liquid surfactant membrane for lead separation from aqueous solution: Studies on emulsion stability and extraction efficiency. Journal of environmental chemical engineering. 2018;6(6):6923-30.

6. Majeed NS, Mohammed MA. Demulsification of remaining waste (water in oil emulsions) after removal of phenol in emulsion liquid membrane process. Journal of Engineering. 2016;22(9):83-102.

7. Maddah ZH, Naife TM. Demulsification of water in Iraqi crude oil emulsion. Journal of Engineering. 2019;25(11):37-46.

8. Yasir AT, Hawari AH, Talhami M, Baune M, Thöming J, Du F. The impact of electric field on the demulsification efficiency in an electro-coalescence process. Journal of Electrostatics. 2023;122:103796.

9. Shilliday E, Ling N, Fridjonsson E, Graham B, Johns M. Destabilisation of water-in-crude oil emulsions using inorganic acids: The role of counter-ions and malonic acid. Geoenergy Science and Engineering. 2023;229:212076.

10. Roshan N, Ghader S, Rahimpour M. Population Balance Equation Modeling of Crude Oil Demulsification Considering Demulsifier: Modification of Collision Frequency Function Based on Thermodynamic Model. International Journal of Engineering. 2017;30(10):1434-42.

11. Mohammed SA, Salih WK. Microwave assisted demulsification of iraqi crude oil emulsions using tri-octyl methyl ammonium chloride (TOMAC) ionic liquid. Iraqi Journal of Chemical and Petroleum Engineering. 2014;15(3):27-35.

12. Mohammed SA, Maan SD. The Effect of Asphaltene on the Stability of Iraqi Water in Crude Oil Emulsions. Iraqi Journal of Chemical and Petroleum Engineering. 2016;17(2):37-45.

13. Abdulredha MM, Aslina HS, Luqman CA. Overview on petroleum emulsions, formation, influence and demulsification treatment techniques. Arabian Journal of Chemistry. 2020;13(1):3403-28.

14. Abdullah MM, Al-Lohedan HA. Demulsification of arabian heavy crude oil emulsions using novel amphiphilic ionic liquids based on glycidyl 4-nonylphenyl ether. Energy & Fuels. 2019;33(12):12916-23.

15. Yonguep E, Kapiamba KF, Kabamba KJ, Chowdhury M. Formation, stabilization and chemical demulsification of crude oil-in-water emulsions: A review. Petroleum Research. 2022;7(4):459-72.

16. Amid M, Nabian N, Delavar M. Functionalized Halloysite Nanotubes and Graphene Oxide Nanosheets Fillers Incorporated in UF Membranes for Oil/Water Separation. International Journal of Engineering. 2023;36(7):1201-10.

17. Liepins J, Balina K, Soloha R, Berzina I, Lukasa LK, Dace E. Glycolipid biosurfactant production from waste cooking oils by yeast: Review of substrates, producers and products. Fermentation. 2021;7(3):136.

18. Bayee P, Amani H, Najafpour G, Kariminezhad H. Experimental investigations on behaviour of rhamnolipid biosurfactant as a green stabilizer for the biological synthesis of gold nanoparticles. International Journal of Engineering. 2020;33(6):1054-60.

19. Jain P, Yadav PK, Raghav S. Application of biosurfactant in the refinery of crude oil. Green sustainable process for chemical and environmental engineering and science: Elsevier; 2021. p. 235-54.

20. Saad M, Abdurahman N, Yunus RM. Synthesis, characterization, and demulsification of water in crude oil emulsion via a corn oil-based demulsifier. Materials Today: Proceedings. 2021;42:251-8.

21. Babu K, Maurya N, Mandal A, Saxena V. Synthesis and characterization of sodium methyl ester sulfonate for chemically-enhanced oil recovery. Brazilian Journal of Chemical Engineering. 2015;32:795-803.

22. Alves RS, Maia DL, de Oliveira PH, Maia LC, Alves Filho EG, Fernandes FA, et al. Molecular optimization of castor oil maleate as demulsifier for water-in-crude oil emulsions. Fuel. 2022;322:124204.

23. Al-Sabagh A, El-Kafrawy AF, Noor El-Din M, El-Tabay A, Fakher E. Some factors affecting the demulsification efficiency of modified alkyl benzene sulfonic acid in petroleum industry. Indian Chemical Engineer. 2016;58(1):61-78.

24. Pretsch E, Bühlmann P, Affolter C, Pretsch E, Bhuhlmann P, Affolter C. Structure determination of organic compounds: Springer; 2000.

25. Sar P, Saha B. Potential application of Micellar nanoreactor for electron transfer reactions mediated by a variety of oxidants: A review. Advances in Colloid and Interface Science. 2020;284:102241.

26. Kang W, Yin X, Yang H, Zhao Y, Huang Z, Hou X, et al. Demulsification performance, behavior and mechanism of different demulsifiers on the light crude oil emulsions. Colloids and Surfaces A: Physicochemical and Engineering Aspects. 2018;545:197-204.

27. Wang D, Yang D, Huang C, Huang Y, Yang D, Zhang H, et al. Stabilization mechanism and chemical demulsification of water-in-oil and oil-in-water emulsions in petroleum industry: A review. Fuel. 2021;286:119390.

28. Abdullah MM, Al-Lohedan HA, Faqihi NA. Synthesis and Performance of Two New Amphiphilic Ionic Liquids for Demulsification of Water-in-Crude Oil Emulsions. ACS omega. 2023.

29. Al-Gburi AKI. Demulsification of water/crude oil emulsions using functionalised PolyHIPEs in an electrostatic field: Newcastle University; 2020.

30. Al-Sabagh A, Nasser N, Khamis E, Abd-El-Raouf M. Resolution of water in crude oil emulsion by some novel aromatic amine polyesters. Egyptian Journal of Petroleum. 2015;24(3):363-74.

31. Roshan N, Ghader S, Rahimpour MR. Application of the response surface methodology for modeling demulsification of crude oil emulsion using a demulsifier. Journal of Dispersion Science and Technology. 2018;39(5):700-10.

Persian Abstract

چکیده

علیرغم تنوع منابع انرژی در حال حاضر، آنها نتوانسته اند جایگزین واقعی نفت خام باشند، زیرا هنوز هم منبع اولیه انرژی در جهان محسوب می شود و تا سالیان دراز باقی خواهد ماند. همانطور که مشخص است، صنعت نفت شامل یک سری عملیات به هم پیوسته است که با استخراج نفت خام از چاه ها شروع می شود و به فرآیند پالایش آن ختم می شود. همانطور که مشخص است، صنعت نفت شامل یک سری عملیات به هم پیوسته است که با استخراج نفت خام از چاه ها شروع می شود و به فرآیند پالایش آن ختم می شود. این عملیات از نظر درجه سختی، هزینه و چالش هایی که با آن روبرو هستند متفاوت است. امولسیون نفت خام یکی از پرهزینه ترین مسائل در این صنعت است. در مطالعه حاضر، یک بیودمولسیفایر دوستدار محیط زیست جدید سنتز شده از ضایعات روغن ذرت معرفی شده است. ویژگی‌های منحصربه‌فرد این دمولسیفایر زیستی جدید با استفاده از چندین آزمایش تشخیص داده شد، از جمله: طیف‌سنجی فروسرخ تبدیل فوریه(FTIR) ، کروماتوگرافی گازی–طیف‌سنجی جرمی (GC-MS)، تشدید مغناطیسی هسته‌ای پروتون ۱(HNMR)، و آنالیز وزنی گرما (TGA) فعالیت غیر امولسیون با استفاده از روش آزمایش بطری به عنوان تابعی از زمان ته نشینی، محتوای آب و دما ارزیابی شده است. حداکثر نسبت جداسازی ٦۹.۳٪ در دوز ۱۰۰۰ ppm به مدت ۵ ساعت و ۷۰ درجه سانتیگراد بود، در حالی که نسبت آب به روغن ۷۰/۳۰ بود. نتایج به‌دست‌آمده نشان می‌دهد که دمولسیفایر زیستی می‌تواند به‌عنوان یک جایگزین ایمن و سازگار با محیط‌زیست در واحدهای امولسیون‌زدایی اولیه مورد استفاده قرار گیرد که باعث کاهش مخاطرات زیست‌محیطی و هزینه‌های مالی مرتبط با صنعت نفت در هنگام استفاده از روش‌های دمولسی‌سازی سنتی می‌شود.

International Journal of Engineering

Design and Performance Analysis of High-k Gate All Around Fin-field Effect Transistor

K. Rohith Sai, K. Girija Sravani, K. Srinivasa Rao, B. Balaji*, V. Agarwal

Department of Electronics and Communication Engineering, Koneru Lakshmaiah Education Foundation, Green Fields, Vaddeswaram, Andhra Pradesh, India

P A P E R   I N F O

A B S T R A C T

This paper introduces and investigates a symmetrical structural design centered around a Nanoscale Fin Field-Effect Transistor (Fin-FET). Employing advanced tcad simulation techniques, the study discusses the characteristics of the Fin-FET. Here, a comprehensive exploration of the device performance across a spectrum of parameters, including drain current, electric field distribution, surface potential variations, energy band configurations, carrier concentration behaviors, and the Ion/Ioff ratio. Through rigorous analysis, the research sheds light on the symmetrical design's impact on these fundamental aspects of the Fin-FET's operation. The insights gained from this study hold the potential to enhance our understanding of device behavior, paving the road for refined designs and optimized utilization of Fin-FET technology in advanced semiconductor applications. Several types of engineering's are applied to test the device under various aspects. Gate engineering, doping engineering, and work function engineering were applied to test the device drain current characteristics. Therefore, this proposed has been widely adopted in modern Nano scale semiconductor devices.

Graphical Abstract
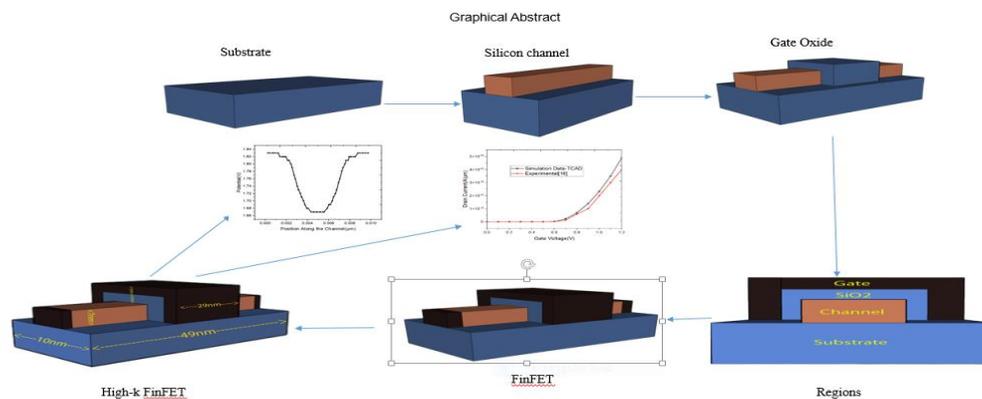
NOMENCLATURE

eV	Energy bands	SS	Sub-threshold slope
SiO_2	Silicon dioxide	Ion	On state current
Ioff	Off state current	I_d	Drain Current
Vgs	Gate to source voltage	V_{ds}	Drain to source voltage

*Corresponding Author Email: vahividi@gmail.com (B. Balaji)

1. INTRODUCTION

Last few years, the relentless demand for smaller, faster, and more energy-efficient electronic devices has driven semiconductor manufacturers to continually advance transistor technology. The traditional device such as planar metal oxide-semiconductor field-effect transistor (MOSFET) designs in the nano scale semiconductor field, which had served well for many years, faced insurmountable physical limitations as feature sizes shrank into the nanometer range. Challenges such as leakage currents, power dissipation, and gate control complexities became significant barriers to sustaining the continuous scaling predicted by Moore's Law (1).

The emergence of Fin Field-Effect Transistor (Fin-FET) technology marked a transformative moment in semiconductor design, providing a departure from the conventional planar MOSFET structure. This innovation reinvigorated the possibilities for performance scaling and energy efficiency improvements. The origin of Fin FET technology can be traced back to the early 2000s, when semiconductor engineers and researchers embarked on a quest to develop new transistor designs capable of overcoming the inherent limitations of planar MOSFETs. This quest led to the concept of the Fin FET architecture, characterized by its distinctive three-dimensional channel structure resembling fins. This novel architecture not only offers improved control over current flow but also effectively reduces undesirable leakage paths (2, 3). A significant milestone in the adoption of Fin FET technology was Intel's introduction of the Tri-Gate transistor in 2011. This event marked a crucial step, showcasing the practical application of Fin FETs in modern microprocessors and validating their potential to outperform traditional transistor designs. The introduction of Fin FETs has been instrumental in advancing semiconductor technology and enabling the development of more powerful and energy-efficient electronic devices (4, 5).

The operating principle of Fin FETs is deeply rooted in their distinctive structure, where the channel region is raised vertically above the substrate, resembling a fin. This structural configuration results in elevated gate control achieved by surrounding the fin with gate material. This arrangement enhances electrostatic control, leading to reduced leakage and more efficient operation. The Fin FETs offer several significant advantages, including reduced leakage currents, faster switching speeds, higher packing densities, and lower power consumption. These attributes collectively empower electronic devices with enhanced computational capabilities and energy efficiency, making them well-suited for advanced applications in consumer electronics, data centers, and emerging technologies like the Internet of Things (IoT). However, despite the transformative impact of Fin FET technology on the semiconductor industry, it is not without its challenges. The intricacies of manufacturing the intricate fin-like structures introduce complexities that could affect yields and production costs. Furthermore, as transistor dimensions continue to shrink into the nanoscale, new phenomena like quantum tunneling and variability become more prominent, necessitating innovative solutions to maintain the projected gains in performance. However, despite the transformative impact of Fin FET technology on the semiconductor industry, it is not without its challenges. The intricacies involved in manufacturing the intricate fin-like structures introduce complexities that could affect yields and production costs (6-10).

In the domain of nano-scale semiconductor technology, Fin FET have emerged as a groundbreaking solution that transcends the limitations inherent in traditional planar MOSFET designs. As transistor dimensions continue to shrink towards the nanometer scale, the challenges stemming from quantum mechanical effects, leakage currents, and power dissipation become increasingly acute (11). In response, FinFETs present an innovative three-dimensional architecture, wherein the channel takes on the form of a vertically protruding fin from the substrate. This distinctive arrangement not only enhances gate control but also effectively mitigates issues tied to short-channel effects, enabling precise modulation of current flow at an atomic scale (12, 13). The incorporation of Fin FETs within the nano-scale domain has inaugurated a novel epoch in semiconductor innovation, underpinning the development of exceptionally efficient and high-performance integrated circuits that serve a diverse spectrum of applications – ranging from portable devices to cutting-edge computing systems (14, 15).

This research paper introduces a study focused on a symmetrical structural design involving a Fin Field-Effect Transistor (FIN-FET) as shown in section 2. Through advanced TCAD simulation techniques, the investigation delves into the intricate characteristics of the FIN-FET, exploring parameters like drain current, electric field distribution, surface potential variations, energy band configurations, carrier concentration behaviors, and the Ion/Ioff ratio as shown in section 3. The research sheds light on how this symmetrical design influences these fundamental aspects of the FIN-FET's operation. The insights gained hold the potential to refine device designs and optimize the application of FIN-FET technology in advanced semiconductor contexts. Additionally, the paper evaluates the impact of gate engineering, doping engineering, and work function engineering on the device's drain current, contributing to a comprehensive understanding of its performance under various aspects.

The High-k GAA-FinFET device has been widely adopted in modern semiconductor technology,

particularly in advanced integrated circuits. This proposed device offers better electrostatic control over the channel, resulting in improved performance compared to traditional planar transistors. This is crucial for achieving higher speed and lower power consumption in electronic devices. The three-dimensional FinFET design helps mitigate leakage current issues prevalent in smaller transistor sizes. This reduction in leakage current contributes to lower power consumption and improved energy efficiency. The manufacturing process for Fin FET is more complex compared to traditional planar transistors. This complexity can result in increased production costs and challenges in fabrication.

2. STRUCTURE OF PROPOSED DEVICE

The schematic view of the proposed device Fin-FET is shown in Figure 1. The 3-D ATLAS simulator is utilized to conduct device simulations. These parameters define the characteristics of the device under consideration. The gate length of 29 nm, fin thickness of 9 nm, and fin width of 10 nm determine the physical dimensions of the transistor. The channel thickness of 7 nm refers to the thickness of the conducting channel in the transistor. The gate oxide thickness (Tox) of 1 nm represents the thickness of the oxide layer between the gate and the channel (16-18). The source and drain length (Source and Drain) are both set at 10 nm. The source/drain doping level is $1x10^{20}$ atoms/cm^3, indicating the concentration of dopant atoms in the source and drain regions. The gate work function is 4.9 eV, signifying the energy level required to extract an electron from the gate and introduce it into the channel, influencing the transistor's behavior. These parameters collectively define the operational characteristics and behavior of the proposed device (19).

In the design and analysis of the Fin FET device, a comprehensive set of advanced simulation models has been employed to accurately capture its electrical and physical behavior (20, 21). The chosen models include Schrödinger-Poisson solver (Schro), Non-Equilibrium Green's Function with multisubband (NEGF_MS), Oxide Schrödinger (Ox. Schro), semi-classical particle-based transport (sp. fast), and two-dimensional geometry representation (sp. geom=2dyz) as shown in Figure 2.


(b)

(c)
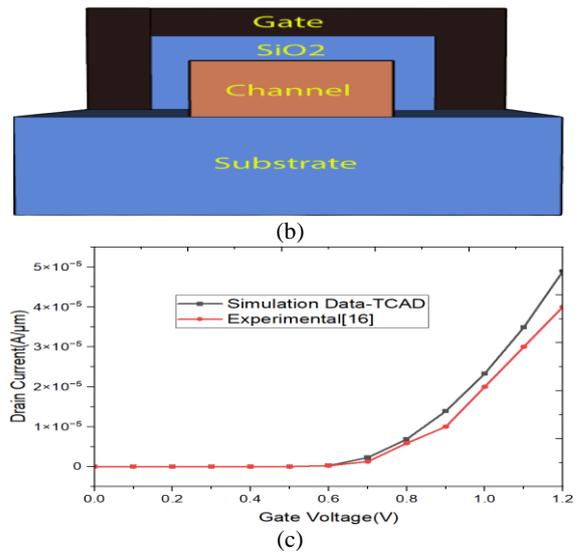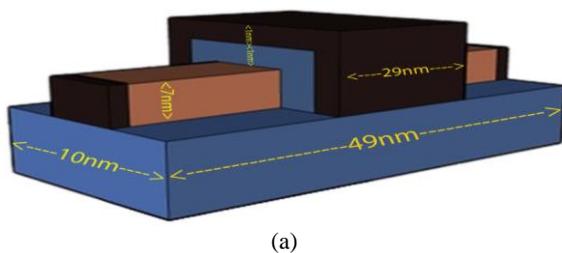
Figure 1. The structure of *the* proposed device (a) Dimensions of the device (b) Regions of the device (c) Calibrated Drain Currents


(a) Silicon Substrate

(b) Implementation of the silicon channel

(c) Adding Gate Oxide

(d) Adding Metals
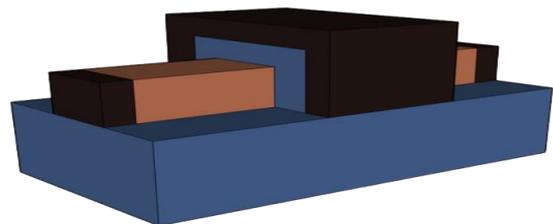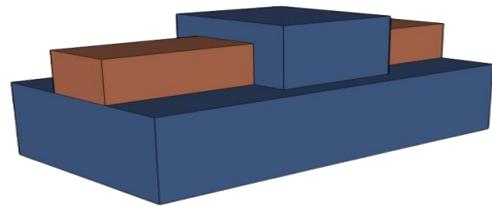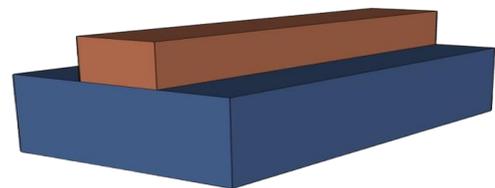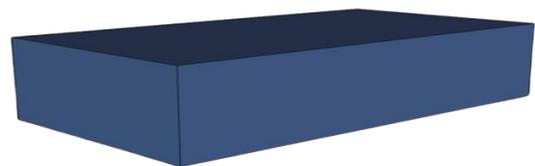
Figure 2. The Tentative Fabrication Process Flow of the proposed FinFET device

(a)

FinFET is designed in a three-dimensional structure, where the channel is a raised fin surrounded by the gate on all sides. This design allows for better electrostatic control of the channel and mitigates short-channel effects. In contrast, planar transistors have a two-dimensional structure, and as transistor sizes shrink, controlling the channel becomes more challenging. The three-dimensional FinFET design helps to reduce leakage current significantly. Leakage current is a critical concern in smaller transistor sizes due to increased quantum tunneling effects.

The parameters used for the simulation of the proposed device and performance parameters are shown in Table 1 and the comparison table is shown in Table 2.

3. RESULTS AND DISCUSSIONS

3. 1. Gate Engineering   Modifying the gate thickness in FinFET devices has a significant impact on their performance characteristics. Specifically, - reducing the gate thickness plays a crucial role in enhancing the device's performance. Decreasing the gate thickness allows for better electrostatic control over the channel. This results in more precise regulation of the transistor's behavior. Thinning the gate effectively manages short-channel effects, which can be a challenge in nanoscale transistors.

This improvement is critical for maintaining reliable transistor operation. The reduction in gate thickness increases gate capacitance. This increased capacitance provides greater control over the channel's behavior, enabling more effective gate regulation. Thinner gates lead to a decrease in the threshold voltage required for transistor activation. This is beneficial for achieving higher on-currents, which are essential for faster and more efficient transistor operation. Addressing concerns related to power leakage is a crucial aspect of modern semiconductor design. Thinner gates help in reducing power leakage, which is essential for energy-efficient device operation. Augmenting the gate thickness in Fin

TABLE 2. The comparison of the proposed Fin FET Device of its electric parameters with previous works

Parameters	Proposed Device	(9)	(22)	(23)
Ion	$5.79e^{-05}$	$2.05e^{-05}$	$2.24e^{-05}$	$1.11e^{-05}$
Ioff	$1.43e^{-18}$	$5.2e^{-11}$	$1.08e^{-11}$	$6.9e^{-13}$
Ion/Ioff	$4.05e^{+13}$	$2.5e^{+06}$	$1.85e^{+06}$	$1.61e^{+07}$
SS	55mV/D	---	75mV/D	61.97mV/D

FETs introduces divergent consequences. A thicker gate diminishes gate capacitance, introducing complexities in the effective modulation of the channel's conductance. While this adjustment could aid in reducing off-state leakage current, it could concurrently lead to sluggish switching speeds and sub-optimal electrostatic dominance over the channel (24).

Figure 3 shows the variation in drain current for different gate thickness. A reduction in gate thickness brings about a notable increase in drain current. As such, the decision to manipulate the gate thickness necessitates meticulous consideration, weighing the desired trade-offs between performance, power efficiency, and switching speed. This evaluation should align with the distinctive application and design requisites of the FinFET device (25).

3. 2. Effect of Changing Doping Concentration The doping concentration within FinFET structures yields significant changes in the drain current, revealing a direct correlation between doping levels and device performance. Elevated doping concentrations in the source and drain regions lead to an increased pool of charge carriers primed for conduction. This surplus of carriers translates into a higher drain current, facilitated by the amplified availability of charge carriers for seamless transport between the source and drain terminals. In contrast, reducing doping concentrations curtails the available carriers, subsequently diminishing the overall drain current. This controlled manipulation of

TABLE 1. The dimensions of the proposed FinFET device

Parameters	Values
Gate Length	29 nm
Fin Thickness	9 nm
Fin Width	10 nm
Channel thickness	7nm
Tox	1nm
Source	10nm
LDrain	10nm
S/Doping	1E20
Gate work function	4.9ev
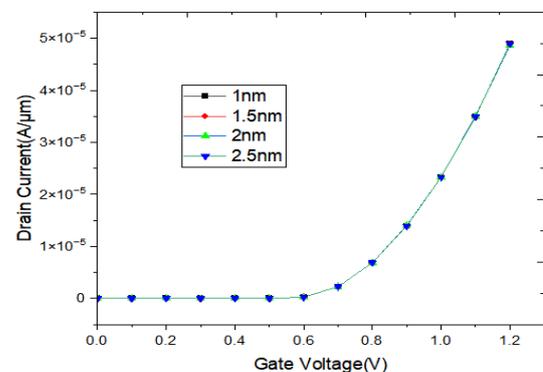
Figure 3. The Drain current characteristics of the proposed device for different gate thickness (1, 1.5, 2, 2.5nm)

doping concentration emerges as a potent strategy for tailoring the electrical traits of FinFETs. Through deliberate adjustments in doping levels, a fine equilibrium can be achieved, optimizing conduction efficiency while simultaneously curbing leakage currents. This dynamic tuning of doping concentration stands as a versatile approach for refining the performance characteristics of the device to meet specific application demands (26).

Figure 4, shows the variation in drain current for different doping concentrations. With a rise in doping concentration within the source and drain regions of FinFET structures, the abundance of available charge carriers for conduction experiences a significant surge. This excess of charge carriers plays a pivotal role in driving a substantial increase in the drain current. This augmentation is facilitated by the heightened availability of charge carriers, enabling efficient transportation between the source and drain terminals (27). Consequently, this heightened carrier concentration contributes to an elevated level of conductivity, thereby enhancing the overall performance of the device. By elevating the doping concentration, the device's suitability for facilitating current flow is enhanced, leading to an amplification of its capacity to manage electrical signals.

3. 3. Effect of Changing Work Functions

The work function within the Fin FET framework across the range of 4.9 to 5.3 introduces noticeable alterations in the drain current, uncovering a direct correlation between work function values and the device's operational prowess. As the work function progressively increases from 4.9 to 5.3, a transformation occurs in the energy barrier situated at the gate-channel interface. This evolution in the energy barrier has a direct impact on how charge carriers respond to the gate voltage's influence—altering the balance between attraction and repulsion. With a higher work function, the energy barrier becomes narrower, facilitating a more efficient regulation of

charge carrier flow between the source and drain regions. This heightened gate control culminates in an amplified drain current, as charge carriers encounter reduced resistance during their traversal (28).

Figure 5 shows the relationship between drain current and gate voltage for varying work functions ranging from 4.9eV to 5.3eV in the FinFET device. As the work function increases, the modulation of drain current becomes more pronounced, highlighting the pivotal role of work function in influencing device behavior and performance (29).

3. 4. The Optimization of the Proposed Device

Incorporating modifications to the device based on the analysis of drain current, we have established fixed values for the gate thickness, doping concentration, and the work function of the gate metal. The parameters such as electric field, surface potential, energy bands, and carrier concentration have been analyzed for the suggested device.

In Figure 6, we have observed the spatial profile of the electric field of this proposed device within the channel of a FinFET. Understanding the energy bands within a FinFET is pivotal for comprehending its electronic behavior.
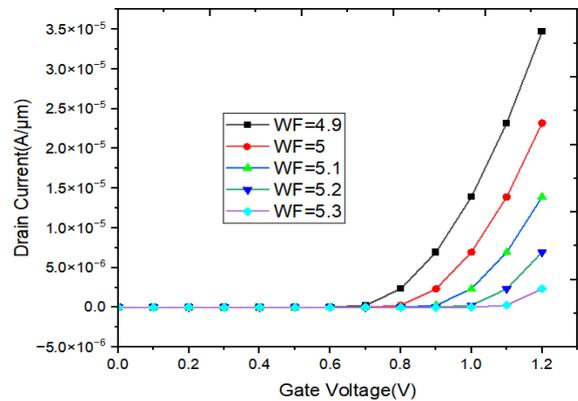
Figure 5. The variation in drain current with respect to gate voltage for different work functions (4.9-5.3)

Figure 4. The drain current for gate voltage for different doping concentration (1e17, 1e18, 1e19, 1e20)
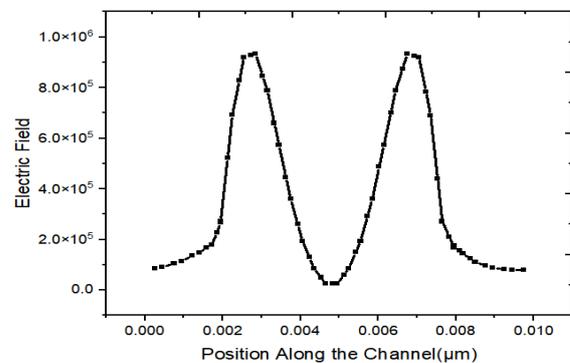
Figure 6. The electric field concerning position along the channel for the proposed device

Figure 7 is a comprehensive visualization of the energy bands across the channel length within a Fin FET device. Consequently, this graphical representation enhances our understanding of the interplay between spatial positioning and energy distribution, a pivotal factor in shaping the device's overall performance characteristics.

Figure 8 is a visual depiction that effectively showcases the distribution of potential across the length of the channel within a Fin FET device. This provides valuable insights into the progressive changes in potential as they relate to spatial position within the channel. Notably, the unique three-dimensional structure of the fin-like channel introduces intricate variations in potential along both the vertical and lateral dimensions.

Figure 9 is a visual portrayal that offers insight into the alteration of carrier concentration across the channel's length within a Fin FET (Fin Field-Effect Transistor) device. This representation sheds light on the transformation of charge carrier density—whether electrons or holes—relative to the spatial location within the channel. The concentration undergoes subtle shifts as one traverses from the source to the drain region. The channel's distinct three-dimensional fin-like design introduces complex changes in carrier concentration, encompassing both vertical and lateral dimensions.
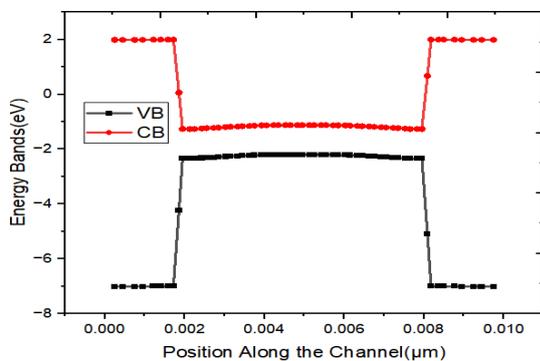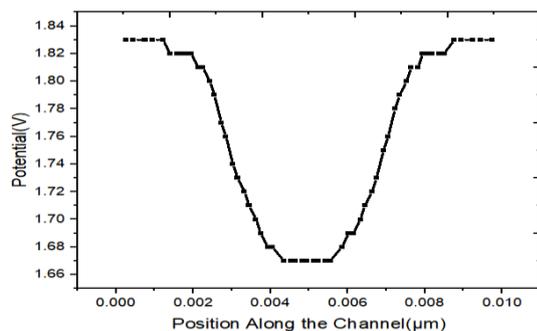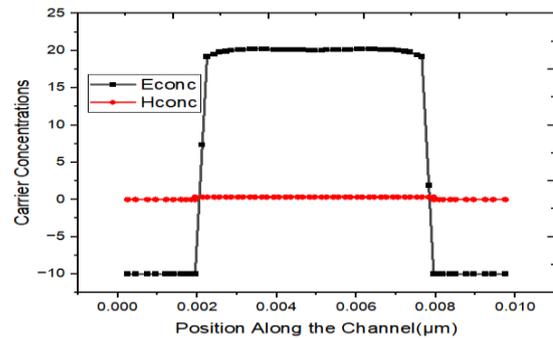
Figure 9. The carrier concentration with respect to position along the channel for the proposed device

4. CONCLUSION

This paper presents a comprehensive investigation into a symmetrical structural design centered around the Fin Field-Effect Transistor (Fin-FET). Through the utilization of advanced TCAD simulation techniques, the study delves deeply into the intricate characteristics of the Fin-FET, analyzing a wide array of crucial parameters such as drain current, electric field distribution, surface potential variations, energy band configurations, carrier concentration behaviors, and the Ion/Ioff ratio. The symmetrical design's impact on these fundamental operational aspects of the Fin-FET has been rigorously examined, providing valuable insights into its behavior. The findings of this research contribute significantly to our understanding of the Fin-FET's behavior and performance. These insights hold substantial promise for the advancement of semiconductor technology, as they can guide the development of refined designs and optimized utilization of Fin-FETs in advanced applications.

5. REFERENCES

1. Kumar ES, Kumar P S, Vignesh NA, Kanithan S. Design and Analysis of Junctionless FinFET with Gaussian Doped for Non-polar Structure. Silicon. 2022:1-9. 10.1007/s12633-021-01626-y

2. Gowthami Y, Balaji B, Srinivasa Rao K. Performance Analysis and Optimization of Asymmetric Front and Back Pi Gates with Dual Material in Gallium Nitride High Electron Mobility Transistor for Nano Electronics Application. International Journal of Engineering, Transactions A: Basics. 2023;36(7):1269-77. 10.5829/ije.2023.36.07a.08

3. Radhamma E, Vemana Chary D, Krishnamurthy A, Venkatarami Reddy D, Sreenivasa Rao D, Gowthami Y, et al. Performance analysis of high-k dielectric heterojunction high electron mobility transistor for rf applications. International Journal of Engineering, Transactions C: Aspects. 2023;36(9):1652-8. 10.5829/ije.2023.36.09c.09

4. Howldar S, Balaji B, Srinivasa Rao K. Design and Qualitative Analysis of Hetero Dielectric Tunnel Field Effect Transistor Device. International Journal of Engineering, Transactions C: Aspects. 2023;36(6):1129-35. 10.5829/ije.2023.36.06c.11

Figure 7. The energy bands concerning position along the channel for the proposed device

Figure 8. The potential concerning position along the channel for the proposed device

5.   Karimi G, Shirazi S. Ballistic (n, 0) Carbon Nanotube Field Effect Transistors\'IV Characteristics: A Comparison of n= 3a+ 1 and n= 3a+ 2. International Journal of Engineering, Transactions A: Basics. 2017;30(4):516-22. 10.5829/idosi.ije.2017.30.04a.09

6.   Dixit A, Gupta N. A compact model of gate capacitance in ballistic gate-all-around carbon nanotube field effect transistors. International Journal of Engineering, Transactions A: Basics. 2021;34(7):1718-24. 10.5829/IJE.2021.34.07A.16

7.   Prakash MD, Nelam BG, Ahmadsaidulu S, Navaneetha A, Panigrahy AK. Performance analysis of ion-sensitive field effect transistor with various oxide materials for biomedical applications. Silicon. 2021:1-11. 10.1007/s12633-021-01413-9

8.   Chakrabarty R, Roy S, Pathak T, Kumar Mandal N. Design of Area Efficient Single Bit Comparator Circuit using Quantum dot Cellular Automata and its Digital Logic Gates Realization. International Journal of Engineering. 2021;34(12):2672-8. 10.5829/ije.2021.34.12c.13

9.   Howldar S, Balaji B, Srinivasa Rao K. Design and Analysis of Hetero Dielectric Dual Material Gate Underlap Spacer Tunnel Field Effect Transistor. International Journal of Engineering, Transactions C: Aspects. 2023;36(12):2137-44. 10.5829/IJE.2023.36.12C.01

10.   Mehrabani AH, Fattah A, Rahimi E. Design and Simulation of a Novel Hetero-junction Bipolar Transistor with Gate-Controlled Current Gain. International Journal of Engineering, Transactions C: Aspects 2023;36(03):433. 10.5829/ije.2023.36.03c.01

11.   Prakash MD, Krsihna BV, Satyanarayana B, Vignesh NA, Panigrahy AK, Ahmadsaidulu S. A study of an ultrasensitive label free silicon nanowire FET biosensor for cardiac troponin I detection. Silicon. 2022;14(10):5683-90. 10.1007/s12633-021-01352-5

12.   Meriga C, Ponnuri R, Satyanarayana B, Gudivada A, Panigrahy A, Prakash M. A novel teeth junction less gate all around FET for improving electrical characteristics. Silicon. 2021.

13.   Rafiee A, Nickabadi S, Nobarian M, Tagimalek H, Khatami H. Experimental investigation joining al 5083 and high-density polyethylen by protrusion friction stir spot welding containing nanoparticles using taguchi method. International Journal of Engineering, Transactions C: Aspects. 2022;35(6):1144-53. 10.5829/ije.2022.35.06c.06

14.   Kumar S, Sahoo G. A random forest classifier based on genetic algorithm for cardiovascular diseases diagnosis (research note). International Journal of Engineering, Transactions B: Applications. 2017;30(11):1723-9. 10.5829/ije.2017.30.11b.13

15.   Kamal N, Singh J. A highly scalable junctionless FET leaky integrate-and-fire neuron for spiking neural networks. IEEE Transactions on Electron Devices. 2021;68(4):1633-8. 10.1109/TED.2021.3061036

16.   Im K-S, An SJ, Theodorou CG, Ghibaudo G, Cristoloveanu S, Lee J-H. Effect of gate structure on the trapping behavior of GaN junctionless FinFETs. IEEE Electron Device Letters. 2020;41(6):832-5. 10.1109/LED.2020.2991164

17.   Cadareanu P, Gaillardon P-E. A TCAD simulation study of three-independent-gate field-effect transistors at the 10-nm node. IEEE Transactions on Electron Devices. 2021;68(8):4129-35. 10.1109/TED.2021.3089671

18.   Hu L, Lou H, Li W, Chang K-C, Lin X. Suppression of statistical variability in Junctionless FinFET using accumulation-mode and charge plasma structure. IEEE Transactions on Electron Devices. 2020;68(1):399-404. 10.1109/TED.2020.3040137

19.   Sehgal HD, Pratap Y, Gupta M, Kabra S. Performance analysis and optimization of under-gate dielectric modulated Junctionless FinFET biosensor. IEEE Sensors Journal. 2021;21(17):18897-904. 10.1109/JSEN.2021.3090263

20.   Jung S-G, Park E, Shin C, Yu H-Y. LER-induced random variation–immune effect of metal-interlayer–semiconductor source/drain structure on N-type Ge Junctionless FinFETs. IEEE Transactions on Electron Devices. 2021;68(3):1340-5. 10.1109/TED.2021.3050031

21.   Sehgal HD, Pratap Y, Gupta M, Kabra S. Performance Investigation of Novel Pt/Pd-SiO 2 Junctionless FinFET as a High Sensitive Hydrogen Gas Sensor for Industrial Applications. IEEE Sensors Journal. 2021;21(12):13356-63. 10.1109/JSEN.2021.3067801

22.   Kumar M, Aditya K, Dixit A. A junctionless accumulation mode NC-FinFET gate underlap design for improved stability and self-heating reduction. IEEE Transactions on Electron Devices. 2020;67(8):3424-30. 10.1109/TED.2020.2997848

23.   Kumar PK, Balaji B, Rao KS. Design and analysis of asymmetrical low-k source side spacer halo doped nanowire metal oxide semiconductor field effect transistor. International Journal of Electrical and Computer Engineering (IJECE). 2023;13(3):3519-29. 10.11591/ijece.v13i3.pp3519-3529

24.   Gowthami Y, Balaji B, Rao KS. Design and Analysis of a Symmetrical Low-κ Source-Side Spacer Multi-gate Nanowire Device. Journal of Electronic Materials. 2023;52(4):2561-8. 10.1007/s11664-023-10217-z

25.   Manasawi D, Srinivasa Rao K. Design and Analysis of Charge Plasma Junction Less TFET Biosensing Applications. Transactions on Electrical and Electronic Materials. 2023;24(1):65-72. 10.1007/s42341-022-00419-3

26.   Harika P, Kondavitee GS, Rao KS, editors. Design and Analysis of Dielectrically Modulated Tunnel FET Embedded Nanocavity for BreastCancer Cells. 2023 IEEE Devices for Integrated Circuit (DevIC); 2023: IEEE. 10.1109/DevIC57758.2023.10134925

27.   Fouladinia F, Gholami M. Decimal to excess-3 and excess-3 to decimal code converters in QCA nanotechnology. International Journal of Engineering, Transactions C: Aspects. 2023;36(9):1618-25. 10.5829/ije.2023.36.09c.05

28.   Balaji B, Sravani SS, Rao KS. Qualitative Analysis of DG-TFET Structures with Gate material Engineering. Journal of Integrated Circuits and Systems. 2022;17(3):1-6. 10.29292/jics.v17i3.635

29.   Balaji B, Srinivasa Rao K, Girija Sravani K, Bindu Madhav N, Chandrahas K, Jaswanth B. Improved drain current characteristics of hfo2/sio2 dual material dual gate extension on drain side-tfet. Silicon. 2022;14(18):12567-72. 10.1007/s12633-022-01955-6

Persian Abstract

چکیده

این مقاله یک طراحی ساختاری متقارن را با محوریت ترانزیستور اثر میدانی باله نانومقیاس (Fin-FET) معرفی و بررسی می‌کند. این مطالعه با استفاده از تکنیک‌های شبیه‌سازی tcad پیشرفته، ویژگی‌های Fin-FET را مورد بحث قرار می‌دهد. در اینجا، یک کاوش جامع از عملکرد دستگاه در طیفی از پارامترها، از جمله جریان تخلیه، توزیع میدان الکتریکی، تغییرات پتانسیل سطحی، پیکربندی‌های باند انرژی، رفتارهای غلظت حامل و نسبت یون / یون است. از طریق تجزیه و تحلیل دقیق، این تحقیق تأثیر طراحی متقارن را بر این جنبه‌های اساسی عملکرد Fin-FET روشن می کند. بینش‌های به‌دست‌آمده از این مطالعه، پتانسیل افزایش درک ما از رفتار دستگاه، هموار کردن راه را برای طراحی‌های دقیق و استفاده بهینه از فناوری Fin-FET در کاربردهای نیمه‌رسانای پیشرفته دارد. چندین نوع مهندسی برای آزمایش دستگاه در جنبه های مختلف اعمال می شود. مهندسی گیت، مهندسی دوپینگ و مهندسی عملکرد کار برای آزمایش ویژگی‌های جریان تخلیه دستگاه استفاده شد. بنابراین، این پیشنهاد به طور گسترده ای در دستگاه های نیمه هادی در مقیاس نانو مدرن پذیرفته شده است.

International Journal of Engineering

Investigation of Laser Cutting of Thin Polymethyl Methacrylate Sheets by Response Surface Methodology

M. Safari*, J. Joudaki, M. Rezaei

Department of Mechanical Engineering, Arak University of Technology, Arak, Iran

P A P E R I N F O	*A B S T R A C T*
	Laser cutting is a precise, powerful, and low-cost tool for cutting different sheets of metals and polymers. The literature survey shows that the quality of cutting (surface roughness and kerf geometry) is a sophisticated parameter and conventional approaches cannot describe the quality of cutting for thin sheets of polymers very well. Statistical tools can help to interpret the effect of process variables. In this article, the laser cutting of Polymethyl methacrylate (PMMA) is experimentally investigated. The effect of process variables of laser cutting including the scanning speed, laser power, and laser beam diameter on the kerf width and surface roughness by Response Surface Methodology design investigated. The results revealed that increasing the laser power leads to increasing the surface roughness and decreasing the taper angle, while the kerf width at the top and bottom surface of the sheet decreases at first, then increases (for higher laser power than 90W). Also, increasing the scanning speed causes increasing surface roughness while the taper angle and the kerf width at the top and bottom surface increase at first, then it decrease. By increasing the laser beam diameter, the surface roughness will increase while the taper angle and the kerf width at the top and bottom surface decrease at first and then increase. The sophisticated effect of the main process variables and their interactions determines that finding the optimum condition of process parameters is hard and multi-objective optimization approaches are needed to find local minimum surface roughness and kerf geometry.

1. INTRODUCTION

Laser cutting is a non-contact process that produces precise cutting along a defined curve with minimum heat affected zone (HAZ) and minimum distortion of the sheet while no external load is applied to the sheet. This process is mostly utilized for the precise cutting of metals, especially steel alloys. However, in recent years, the use of low-power laser beams to cut different types of polymers has spread. The laser cutting process can be carried out for different purposes. Cutting and producing a blank workpiece is the most convenient. But by performing the cutting at low laser power, microchannel with very low surface roughness (as low as 110 nm) can be fabricated for microfluidic studies (1-3).

One of the most convenient polymers is Polymethyl Methacrylate (PMMA). PMMA is one of the most appropriate thermoplastics for laser cutting. PMMA has

a high melting point (160°C) and high absorptivity of the laser wavelength, 2.914 GPa elastic modulus, 79.16 MPa tensile strength, and 0.40 strain at failure (4). Choudhury and Shirley (5) studied the quality of surface roughness, formation of heat affected zone (HAZ), and dimensional accuracy during laser cutting of different materials (polymethyl methacrylate (PMMA), polypropylene (PP), and polycarbonate (PC)). The results show that surface roughness is improved in laser cutting of PMMA polymer compared to PP and PC. The width of HAZ decreased in PMMA compared to PP and PC polymers. Moreover, similar dimensional accuracy was achieved despite different material properties.

Eltawahni et al. (6) studied the kerf width variation and surface roughness variation during the laser beam cutting of ultra-high molecular weight polyethylene (UHMWPE) material. A design of experiments has been done and the effect of process variables including laser

*Corresponding Author Email: m.safari@arakut.ac.ir (M. Safari)

power, cutting speed, and focal point position is discussed by performing 17 different experiments. The levels of laser power were very high (800-1150 W) due to the property of UHMWPE. The results show that the kerf at the upper surface was reduced by decreasing the laser power and increasing the cutting speed and the focal position. In addition, the kerf at the bottom decreases by decreasing the laser power and focal position and increasing the cutting speed. Also, Eltawahni et al. (7) discussed the advantage of CO_2 laser for cutting four different thicknesses of PMMA by employing a Box-Behnken design of the experiments.

Response Surface Methodology (RSM) and the Taguchi method are two of the approaches for the design of experiments (8-10). Khoshaim et al. (11) investigated the laser cutting of PMMA sheets by a continuous CO_2 laser. A design of experiments based on Taguchi L18 design was planned and the effect of input variables (cutting speed, laser power, sheet thickness, and assisting gas pressure) on output variables responses has been investigated. The output variables of the study were kerf deviation, maximum surface roughness, heat-affected zone (HAZ), and rough area. Regression equations were derived according to the effectiveness of each process input. The results show that by increasing the laser power and gas pressure, the kerf deviation and roughness increase. The kerf deviation increases and the roughness decreases by increasing the cutting speed. The results show that for obtaining the best surface roughness and decreased HAZ, lower laser power, and higher cutting speed were experimentally implemented. Unfortunately, high kerf deviation is inevitable at higher cutting speeds. Elsheikh et al. (12)studied the formation of kerf during the cutting of PMMA by a pulsed CO_2 laser machine. The effect of process variables including cutting speed, laser power, assisted gas pressure, and sheet thickness was investigated using Taguchi L18 orthogonal array. Using the analysis of variance technique (ANOVA), the effect of process variables has been determined. The results show that the top and the bottom kerf widths decrease by increasing the laser power, cutting speed, and gas pressure. The kerf taper angle increases by increasing the cutting speed. The effect of laser power and gas pressure on the kerf taper angle is almost negligible. Increasing the thickness leads to a decrease in the top and the bottom kerf width and kerf taper angle. Genetic Algorithm (GA) and random vector functional link network with equilibrium optimizer (RVFL-EO) algorithm (13) were used to optimize the quality of cutting. Yang et al. (14) developed a combined strategy called the progressive Taguchi neural network model for assessing the kerf taper angle during laser cutting of PMMA sheets by combining the artificial neural network and Taguchi method. The results show that a higher precision can be obtained by the proposed method while the number of experiments decreased with using the L9 orthogonal array instead of the L18 or L27 orthogonal array.

Ninikas et al. (15) studied the influence of the cutting speed and laser power, and the position and orientation of the samples, on the dimensional accuracy and surface roughness of laser cutting of PMMA sheets. A mixed fractional factorial design (36 measurements) was carried out and the dimensional accuracy and surface roughness were measured. The ANOVA results showed that the cutting speed is the most influential process parameter for both dimensional accuracy and surface roughness. Also, the surface roughness improves and minimizes for samples aligned in the travel direction. Also, the authors proposed a neural network-based approach to predict the kerf geometry in laser cutting of PMMA sheets (16) and 3D-printed Polylactic Acid (PLA) (17). Varsi and Shaikh (18) studied the effect of process variables (power, cutting speed, and the number of passes) on the kerf taper angle during the drilling of cylindrical holes in PMMA sheets by the laser beam. The full factorial methodology was used for data analysis and the results show that the kerf taper angle decreases by increasing the laser power and number of passes and decreasing the cutting speed. Several researches have been done in the field of laser cutting. Mushtaq et al. (19) discussed the latest advances in laser cutting of polymers. Hashemzadeh et al. (20) also studied the effect of workpiece vibration in the vertical direction (parallel to the laser beam) at different frequencies. The thickness of the PMMA sheet was 6 mm and cutting was carried out by 70 W laser power. The results show that the laser beam cut through the depth at lower scanning speeds (in the range of 0.2 to 0.4 m/s) while a groove will be formed at higher scanning speeds (0.4 to 2 m/s). the depth of cut increases by increasing the vibration frequency. The authors also published research about the utilization of laser beams and their different applications in industries (21-23).

The literature survey shows that laser cutting is a complicated phenomenon and based on the attitude of the researchers it can be carried out in different ways. Each of the researchers specified some aspect of the cutting process that was novel. Analyzing the published research shows that some researchers only focused on the surface quality and improving it while others explored the kerf formation (width of the kerf, taper angle). However, parameters improving the surface roughness lead to higher kerfs and vice versa. The main challenge in the laser cutting of PMMA sheets is the different behavior of scanning speed and laser beam diameter at high and low laser power. The design of Experiments by RSM helps to find a second-order regression equation to assess the effect of parameters. In this research, the authors attempt to investigate the effect of influencing process variables to optimize the surface roughness and kerf geometry

simultaneously. In this article, the laser cutting of PMMA thin sheets (2.8 mm thickness) will be investigated by using a low power laser beam machine. A design of experiments according to RSM has been scheduled and the surface roughness and kerf width at the top and bottom of the surface was measured. The effect of process variables and their interactions will be discussed by ANOVA. The main difference between current work and other published research is the range of parameters and discussion about the effect of the interaction of process variables in laser cutting of thin sheets that has a negligible effect in laser cutting of thick sheets. Finally, a discussion about the optimization of parameters with different attitudes (cost function) will be added.

In this article, firstly an experiment planning will be carried out and the geometry of kerf due to laser cutting will be measured. Then, the effect of –process parameters and their interactions will be investigated by ANOVA and statistical tools of Minitab software. Finally, the optimization of the process variables will be carried out.

2. EXPERIMENTAL WORKS

The experimental works have been carried out on a PMMA sheet prepared by an approved supplier. The sheet thickness was 2.8 mm. The laser beam irradiated the surface of the sheet. Based on the literature survey, it was decided that the effect of three more important process variables (laser power, scanning speed, and laser beam diameter) will be investigated. For determining the levels of process parameter variation, some pre-tests have been carried out. The aim was to find proper process parameters that melt and cut the sheet without over-melting. In this way, the levels of process parameter variations are determined in Table 1. It should be noted that proper selection of the range of process variables is very important. For example, if the sheet did not cut under one of the designed tests, the statistical analysis cannot be completed and the regression equations cannot be obtained. In this circumstance, all of the implemented tests should be repeated with new levels of process variables which have considerable cost. So, some pre-tests have been carried out and the levels of parameters determined.

The important object in laser cutting is the effect of simultaneous variation of process parameters. For this purpose, the design of experiments (DOE) techniques have been utilized. Because the aim is the identification of the role of parameters, the RSM has been utilized. The list of experiments (15 tests) is shown in Table 2. The tests were determined according to the Box-Behnken approach in Minitab Software.

The laser beam was produced by a Ressi laser beam (RT1310U) machine which is a CO_2 source, continuous wave machine. The PMMA sheet was placed on the table

TABLE 1. The levels of process parameters variation in laser cutting of PMMA

Process Parameters	Value	Unit
Laser Power	72 90 108	W
Scanning Speed	10 20 30	mm/s
Laser Beam Diameter	0.2 0.6 1	mm

TABLE 2. List of experiments according to RSM

Run Order	Power (W)	Scanning speed (mm/s)	Beam diameter (mm)
1	90	30	0.2
2	90	10	0.2
3	72	10	0.6
4	90	30	1.0
5	72	20	1.0
6	90	20	0.6
7	90	20	0.6
8	90	10	1.0
9	108	20	0.2
10	108	30	0.6
11	108	10	0.6
12	90	20	0.6
13	72	20	0.2
14	108	20	1.0
15	72	30	0.6

of the laser machine and after irradiation of the laser beam for 40 mm length, the cutting process stopped and after moving the laser gun laterally, the next groove with new cutting parameters will be machined. Figure 1 shows a schematic view of the cutting cross-section of the laser beam. At ideal conditions, a square cross-section should be created but due to the small angular divergence of the laser beam, a trapezoidal cross-section will be formed. The kerf geometry consists of two parameters: the top kerf width (W_t) and the bottom kerf width (W_b). Therefore, the conical angle of the kerf (α) is defined as Equation 1.

$$a = \tan^{-1}\left(\frac{W_t - W_b}{2t}\right) \tag{1}$$

where t is the thickness of the sheet.
The roughness was measured by a SURFSCAN200 surface roughness tester machine. The probe of the roughness tester machine moves along a path on the surface and measures the profile of the surface. The average arithmetic roughness Ra is calculated by the
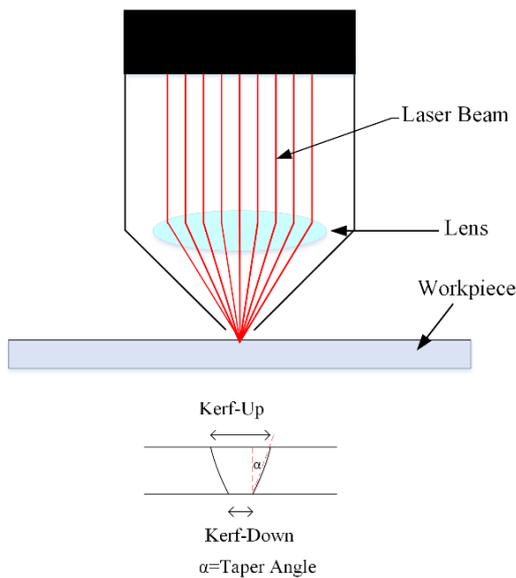
Figure 1. Schematic of laser beam kerf

machine and reported as the result of measurement. Some of the cutting of the PMMA sheet is shown in Figure 2(a). In addition, the cut specimens were observed by a DP73 OLYMPUS optical microscope, and the kerf width was measured by the calibrated software of OM. Figure 2(b) shows some images of kerfs (50X magnification). After that, the surface roughness was measured at three different locations along the laser travel direction, and the average of them is reported as the final result of the surface roughness. Figure 3 shows the surface roughness measurement apparatus. The resolution of the machine is 0.001 μm. The experiments were conducted in 2023 at the Laser Processing Laboratory of Arak University of Technology.

3. RESULTS AND DISCUSSION

3. 1. Surface Roughness Variation   After measuring the width of the kerf and surface roughness, the analysis of results has been carried out by Minitab software. Table 3 shows the results of ANOVA for surface roughness designed based on response surface methodology. The P-Value column (less than 0.05) shows the significance or effectiveness of each process parameter. The results show that the scanning speed and beam diameter are influencing parameters and the power parameter is not affecting the surface roughness. Equation 2 shows the fitted equation for the prediction of surface roughness. The determination factor R^2 for surface roughness is 90.85 % which is a good quality curve fitting. Figure 4 shows the main effect plot for the roughness of the cut surface. As can be seen in Figure 4, the beam diameter is a very important parameter of the
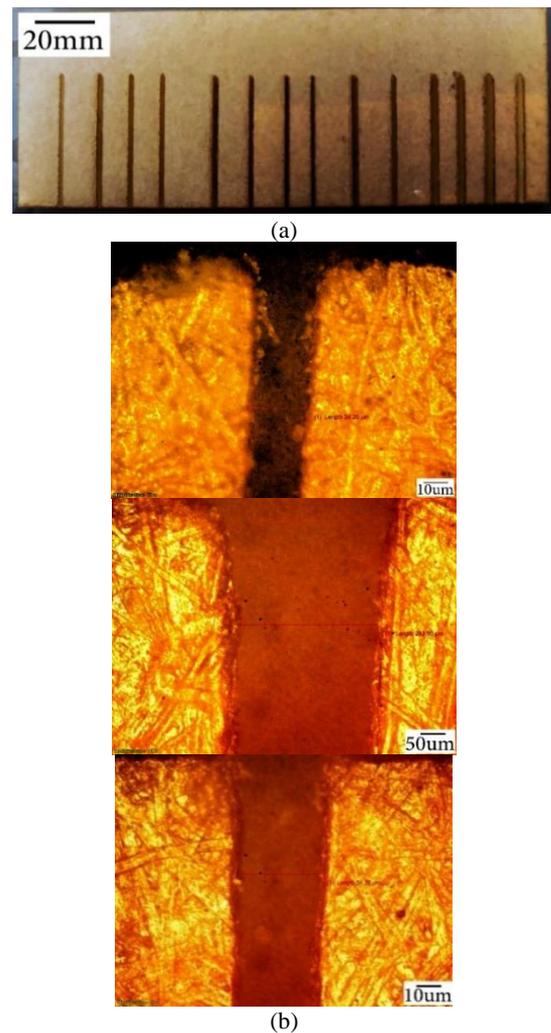
Figure 2. The laser cutting of PMMA sheet a) top view b) side view (observed by OM)

Figure 3. SURFSCAN200 roughness measurement machine

quality of roughness. Minimum surface roughness is obtained in 0.3 mm beam diameter and surface roughness is almost constant in the range of 0.2 to 0.4 mm. The

TABLE 3. ANOVA results for surface roughness

| Source	DF	Adj SS	Adj MS	F-Value	P-Value
Model	7	15.5210	2.2173	9.93	0.004
Linear	3	12.4175	4.1392	18.54	0.001
Power (W)	1	0.2450	0.2450	1.10	0.330
Scanning Speed (mm/s)	1	1.3613	1.3613	6.10	0.043
Beam Diameter (mm)	1	10.8112	10.8112	48.42	0.000
Square	1	2.1910	2.1910	9.81	0.017
Beam Diameter (mm)*Beam Diameter (mm)	1	2.1910	2.1910	9.81	0.017
2-Way Interaction	3	0.9125	0.3042	1.36	0.330
Power (W)*Scanning Speed (mm/s)	1	0.2500	0.2500	1.12	0.325
Power (W)*Beam Diameter (mm)	1	0.6400	0.6400	2.87	0.134
Scanning Speed (mm/s)*Beam Diameter (mm)	1	0.0225	0.0225	0.10	0.760
Error	7	1.5630	0.2233		
Lack-of-Fit	5	0.6030	0.1206	0.25	0.908
Pure Error	2	0.9600	0.4800		
Total	14	17.0840			
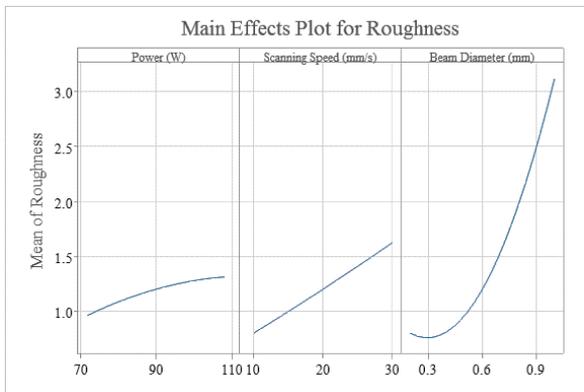
Figure 4. Main effect plot for surface roughness

surface roughness increases rapidly for beam diameters higher than 0.5 mm. The surface roughness increases by increasing the scanning speed (with a constant slope line). The laser power has the least effect on the surface roughness. The surface roughness increases with laser power too. Because all of the process parameters increase the surface roughness, the interaction of process parameters is always positive and increases the surface roughness. More details about the ANOVA results term can be found by Montgomery (24).

$$Roughness = -0.27 \ + 0.0042\,P + 0.178\,S \ -7.46\,D$$
$$+ 4.79\,D^2 - 0.00139\,P \times S \qquad (2)$$
$$+ 0.0556\,P \times D - 0.0188\,S \times D$$

A similar study was implemented by Huang et al. (3)on PMMA material. The thickness was 2 mm which is near the thickness of the current study. The surface roughness was reported in the range of 0.75 to 3 Ra surface roughness. The laser power was very low (15-45 W) and the surface roughness increased by increasing the laser power. However, the results of the current study show that better surface roughness can be obtained at higher laser power. The surface roughness also was in the range of 0.55 to 2.5 for scanning speed varying from 10 to 50 mm/s and the surface roughness increased by increasing the scanning speed linearly. However, the results of the current study show that better surface roughness can be obtained at higher scanning speeds. As can be seen, the trends are similar, but this study shows that laser beam diameter is a key factor (most influencing factor) on the surface roughness and a good quality surface can be obtained by decreasing the laser beam diameter. Huang et al. (3) studied the effect of process parameters (laser power and scanning speed) by varying one factor at a time and keeping constant the other parameters while RSM helps to better interpret the effect of main process parameters and their interactions.

3. 2. Kerf Width Variation The kerf width at the top and bottom surface behaves a little differently. Tables 4 and 5 show the ANOVA results for kerf width at the top (Kerf-up) and bottom (Kerf-down) surfaces. The results of ANOVA were illustrated as a graphical image in Figure 5 (Pareto chart). It is evident that the laser power and laser beam diameter are the influential process parameters and scanning speed is an unimportant parameter on the kerf width at the top surface. All of the square terms of process parameters influence process variables. The interaction of laser power with laser beam diameter and scanning speed with laser beam diameter are also important in process parameters on the kerf width of the top surface. As can be seen, the only insignificant process parameters are scanning speed and the interaction of scanning speed with laser power. The Pareto chart for the kerf width of the bottom surface shows that the square of laser power is the only significant process parameter and other process parameters, interactions, and squares are insignificant. Equations 3 and 4 show the regression equation for Kerf-up and Kerf-down width as a full quadratic equation. The determination factor R2 for Kerf-up and Kerf-down width is 98.72 and 82.32 % which shows that the equations can predict the kerf width at the top and bottom surface with adequate precision.

$$Kerf - up = 3830 \; -67.96\,P + 22.64\,S - 2137\,D$$
$$+0.3375\,P^2 - 0.4674\,S^2 + 608.1\,D^2 \qquad (3)$$
$$-0.1079\,P \times S + 13.48\,P \times D + 7.34\,S \times D$$

$$Kerf - Down = 1953 - 36.3\,P + 11.6\,S - 810\,D$$
$$+0.1880\,P^2 - 0.505\,S^2 + 342\,D^2 \qquad (4)$$
$$+0.049\,P \times S + 2.76\,P \times D$$
$$+5.00\,S \times D$$

The main effect plot for Kerf-up and Kerf-down width is shown in Figure 6. The kerf width at the top surface decreases by increasing the laser power at first, then it increases such that the local minimum happens at about 90 W laser power and 0.6 mm beam diameter. The kerf width increases by increasing the scanning speed at first, then it decreases. The minimum kerf width at the top surface happens at 30 mm/s scanning speed. Similar

TABLE 4. ANOVA results for Kerf-up

Source	DF	Adj SS	Adj MS	F-Value	P-Value
Model	9	138877	15430.8	42.97	0.000
Linear	3	8650	2883.5	8.03	0.023
Power (W)	1	4248	4247.7	11.83	0.018
Scanning Speed (mm/s)	1	1489	1488.9	4.15	0.097
Beam Diameter (mm)	1	2914	2913.9	8.11	0.036
Square	3	87616	29205.3	81.32	0.000
Power (W)*Power (W)	1	44151	44151.2	122.94	0.000
Scanning Speed (mm/s)*Scanning Speed (mm/s)	1	8066	8066.0	22.46	0.005
Beam Diameter (mm)*Beam Diameter (mm)	1	34953	34953.2	97.32	0.000
2-Way Interaction	3	42611	14203.7	39.55	0.001
Power (W)*Scanning Speed (mm/s)	1	1509	1509.3	4.20	0.096
Power (W)*Beam Diameter (mm)	1	37652	37651.5	104.84	0.000
Scanning Speed (mm/s)*Beam Diameter (mm)	1	3450	3450.4	9.61	0.027
Error	5	1796	359.1		
Lack-of-Fit	3	1499	499.6	3.37	0.237
Pure Error	2	297	148.4		
Total	14	140673			

TABLE 5. ANOVA results for Kerf-down

| Source	DF	Adj SS	Adj MS	F-Value	P-Value
Model	9	44110.2	4901.1	2.59	0.154
Linear	3	4717.5	1572.5	0.83	0.532
Power (W)	1	98.6	98.6	0.05	0.829
Scanning Speed (mm/s)	1	1291.3	1291.3	0.68	0.447
Beam Diameter (mm)	1	3327.6	3327.6	1.76	0.242
Square	3	35900.7	11966.9	6.31	0.037
Power (W)*Power (W)	1	13703.1	13703.1	7.23	0.043
Scanning Speed (mm/s)*Scanning Speed (mm/s)	1	9427.5	9427.5	4.97	0.076
Beam Diameter (mm)*Beam Diameter (mm)	1	11051.8	11051.8	5.83	0.061
2-Way Interaction	3	3491.9	1164.0	0.61	0.635
Power (W)*Scanning Speed (mm/s)	1	306.3	306.3	0.16	0.704
Power (W)*Beam Diameter (mm)	1	1582.4	1582.4	0.83	0.403
Scanning Speed (mm/s)*Beam Diameter (mm)	1	1603.2	1603.2	0.85	0.400
Error	5	9476.2	1895.2		
Lack-of-Fit	3	7747.7	2582.6	2.99	0.261
Pure Error	2	1728.5	864.2		
Total	14	53586.4			
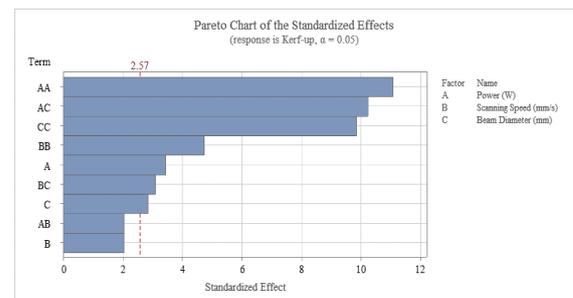
(a)
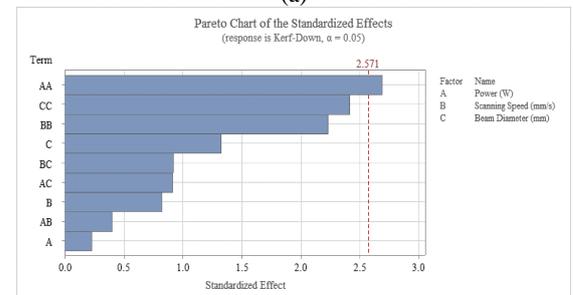
(b)

Figure 5. The Pareto chart for Kerf width at (a) top and (b) bottom surface

trends have been observed for kerf width at the bottom surface. The vertical axis of Figure 6 (a) and (b) is the magnitude of kerf width. As can be seen, the kerf-up width value is higher than the kerf-down value which shows the formation of kerf taper angle as shown in Figure 1.

Figure 7 shows the contour plot and surface plot of kerf width at the top surface. The interaction of process parameters shows that the kerf-up width decreases by increasing the laser power at constant scanning speed, then it increases and a saddle shape was observed as the surface response. The interaction of laser beam diameter with laser power shows that the kerf-up width decreases by simultaneously decreasing both the laser beam diameter and laser power and then it increases as shown in Figure 7 (c). The response surface is like a bowl-shaped surface which determines a local minimum at 90 W laser power and 0.6 mm laser beam diameter. The interaction of scanning speed with laser beam diameter shows that the effect of scanning speed is almost constant at low and high levels of laser beam diameter (0.2 mm and 1mm) while the kerf-up width increases at first and then decreases at 0.6 mm laser beam diameter. The shape of the response surface of the kerf-down width is similar to the kerf-up width. The formation of kerf at the top and bottom surfaces of the sheet are unwanted phenomena

and finding the behavior of the process output is very difficult. The statistical analysis of kerf width helps to determine this sophisticated phenomenon.

(a)

(b)

(c)

(d)
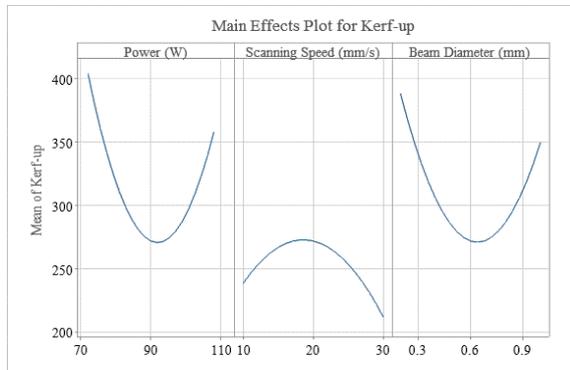
(a)
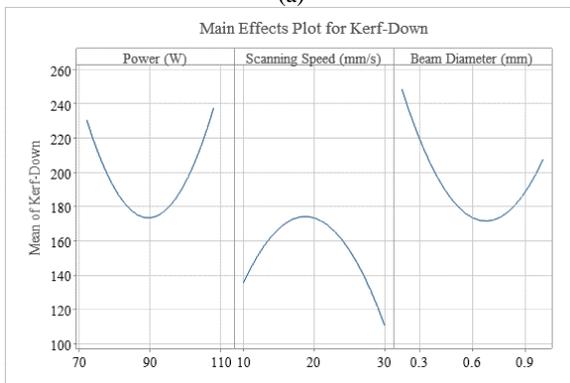
(b)

Figure 6. Main effect plot for kerf width at a) top and b) bottom surface

(e)

(f)
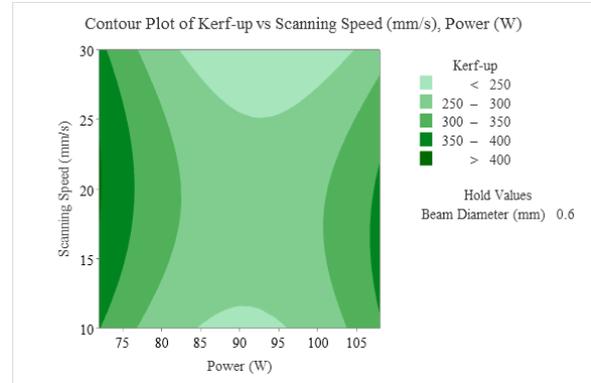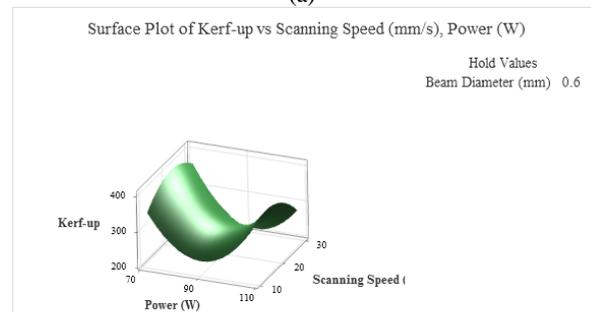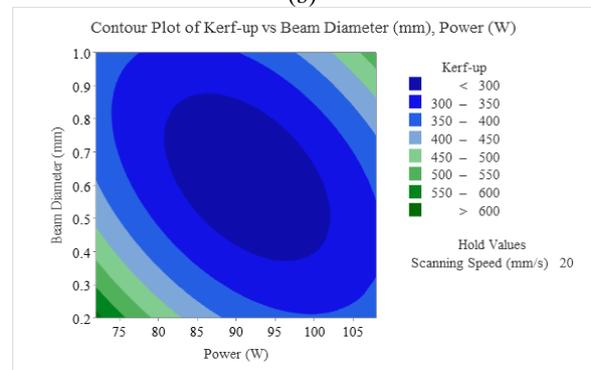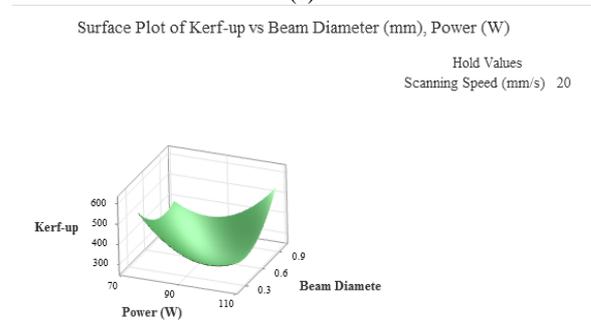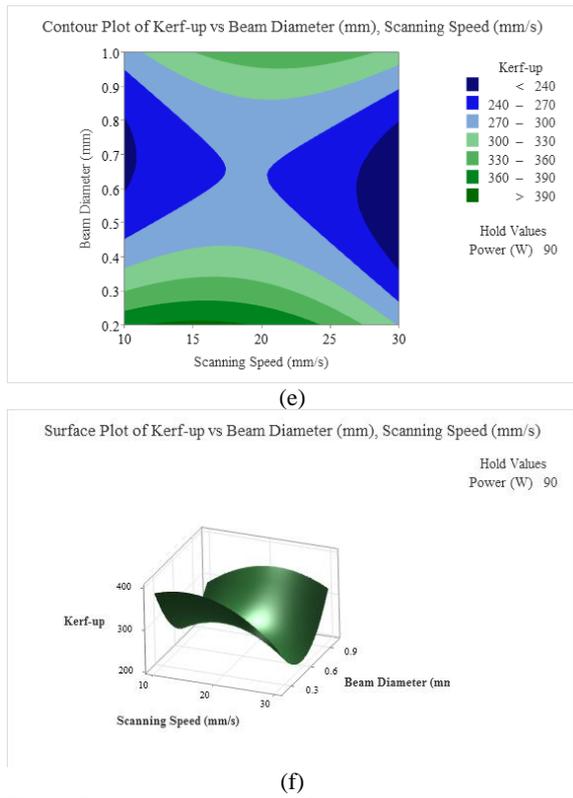
Figure 7. Contour plot and surface plot of kerf width at the top surface for the interaction of a, b) scanning speed with laser power, c, d) laser beam diameter with laser power, e, f) laser beam diameter with scanning speed

3. 3. Taper Angle Variation   Analysis of variance had been carried out and the effect of process variables was determined. The taper angle can be predicted by Equation 5. Based on ANOVA results, the main effect plot is shown in Figure 8. The taper angle decreases by increasing the laser power. The taper angle increases at first and then it decreases by increasing the scanning speed. The taper angle decreases at first and then it increases by increasing the beam diameter. Comparing Figure 6 with Figure 8, that shows the scanning speed and laser beam diameter have similar trends in kerf width at the top and bottom surface and taper angle. But the laser power is different. Despite increasing the kerf width at the top and bottom surface, the taper angle decreases. Increasing the laser power causes a higher material removal rate (higher melting and evaporating rate) and in this condition, the surface roughness will increase due to higher energy absorption.

$$
\begin{aligned}
Taper\ Angle = {} & 11.39 - 0.146\,P + 0.112\,S - 12.93\,D \\
& + 0.000382\,P^2 - 0.00332\,S^2 \\
& + 2.20\,D^2 - 0.00000\,P \times S \\
& + 0.1095\,P \times D + 0.0239\,S \times D
\end{aligned}
\tag{5}
$$
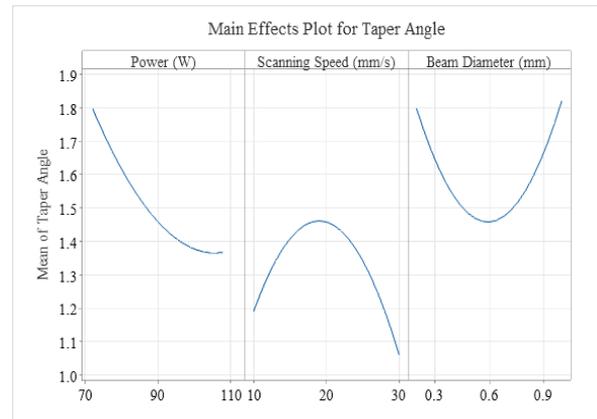
Figure 8. Main effect plot for taper angle

Figure 9 shows the contour plot and surface plot of the kerf taper angle. The results show that the taper angle increases at first then it decreases at different scanning speeds. Also, the taper angle decreases slightly by increasing the laser power. Maximum taper angle obtained at low laser power and moderate scanning speed. The taper angle decreases by increasing the laser power at a low beam diameter, but the taper angle increases by increasing the laser power at a high beam diameter. Minimum taper angle obtained at high laser power and low beam diameter. The interaction of laser beam diameter and scanning speed forms a saddle-shaped surface. Increasing the scanning speed increases at first, then it decreases. By increasing the beam diameter, the taper angle decreases at first, then it increases. Minimum taper angle obtained at high scanning speed and moderate beam diameter. The contour plot and surface plot show the complex interaction of the process variables and the minimum should be determined by optimization. Optimization by the Minitab software shows that the minimum bending angle will be obtained at high laser power (108W), high scanning speed (30 mm/s), and low beam diameter (0.2 mm) if the taper angle is the only target of optimization.
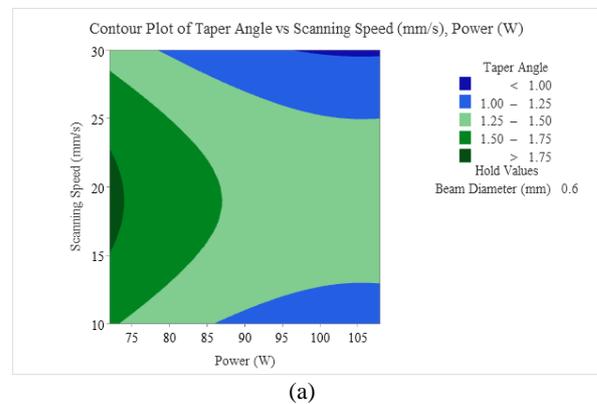
(a)
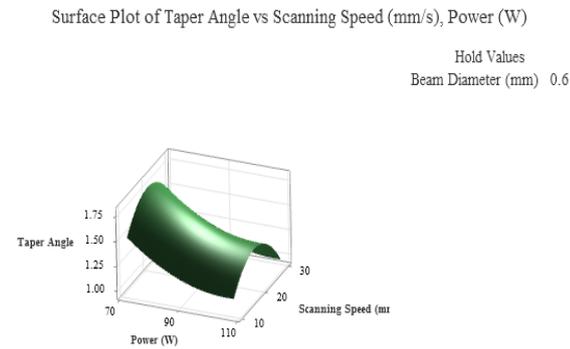
(b)
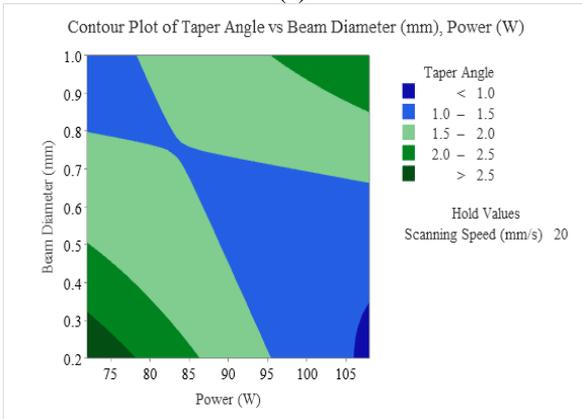
(c)
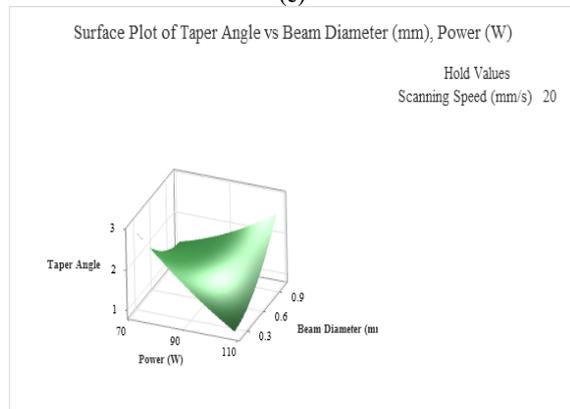
(d)
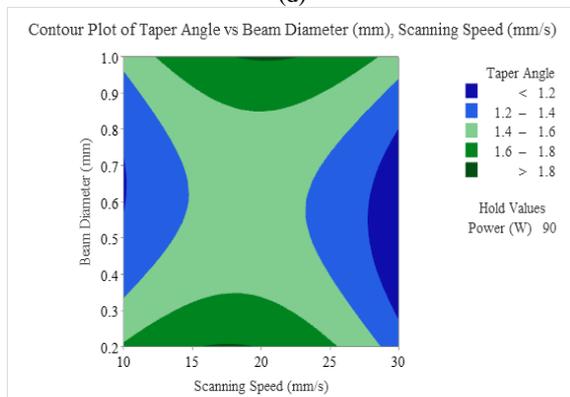
(e)
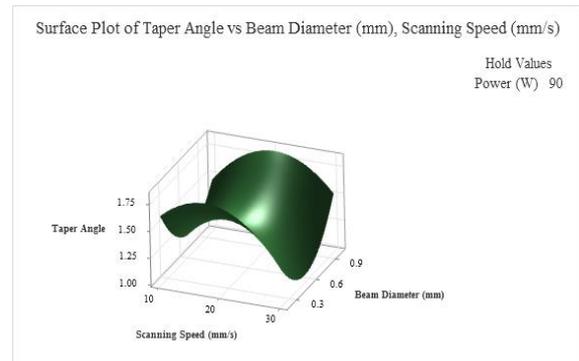
(f)

Figure 9. Contour plot and surface plot of kerf taper angle by a, b) scanning speed with laser power, c, d) laser beam diameter with laser power, e, f) laser beam diameter with scanning speed

At last, it should be noted that using RSM helps to interpret the results of statistical analysis better than the full-factorial design of experiments. In the full-factorial data analysis, the trend of variation should always be positive or negative (increasing or decreasing functions). But, as we can see in Figures 4, 6, and 8, the process output mostly increases at first, then it decreases or vice versa. So, using RSM can better predict the variation of the process output. While the number of experiments (15 experiments) is also lower than the full-factorial design (27 experiments). It should be noted that the data analysis by statistical tools helps the researchers to introduce a semi-empirical semi-analytical equation that is reliable in the range of the process parameters variation. In other words, regardless of the non-linear behavior of the process output, a quadratic equation can describe the trends of output change.

3. 4. Optimized Process Conditions   The effect of process variables is complicated in laser cutting. The effect of each variable and the interaction of the process variables is discussed in the previous section. Finding the optimum condition needs special considerations. The taper angle is calculated according to the value of kerf width at the top and bottom surfaces. So, the minimum taper angle will not happen at the minimum kerf width at the top surface (kerf-up) and kerf width at the bottom surface (kerf-down). Figure 10 shows the condition of minimum kerf-up and kerf-down width. The results show that if the laser power was 88 W, the scanning speed was 30 mm/s, and the beam diameter was 1 mm, the minimum kerf-up and kerf-down width would be obtained. In these conditions, the kerf-up, kerf-down width, and kerf taper angle will be 215.7 µm, 109.5 µm, and 1.07 °, respectively. The average surface roughness Ra will be 1.23 µm which is a coarse surface roughness. The taper angle of the kerf will not be the minimum. Figure 11 shows the optimized condition for obtaining minimum

surface roughness and minimum kerf taper angle simultaneously. The optimized condition for minimum surface roughness and minimum kerf taper angle is 106.5 W laser power, 10 mm/s scanning speed, and 0.2 mm beam diameter. The surface roughness and kerf taper angle at optimized conditions will be 0.38 µm and 0.809 ° respectively. In this situation, the kerf-up and kerf-down width will be 383.7 and 258.8, respectively.

Different attitudes can be selected in the optimization of process variables. Minimizing all four parameters leads to a narrow kerf but the surface roughness will be coarse comparatively. One of the best choices for optimization is minimizing the kerf-up and kerf-down width and minimizing the surface roughness (Figure 12). The results show that the process variables should be set as 87 W laser power, 10 mm/s scanning speed and 0.54 mm beam diameter to optimize the surface roughness (0.570 µm), kerf-up width (250 µm) and kerf-down width (143 µm). In this condition, the taper angle will be 1.25°.
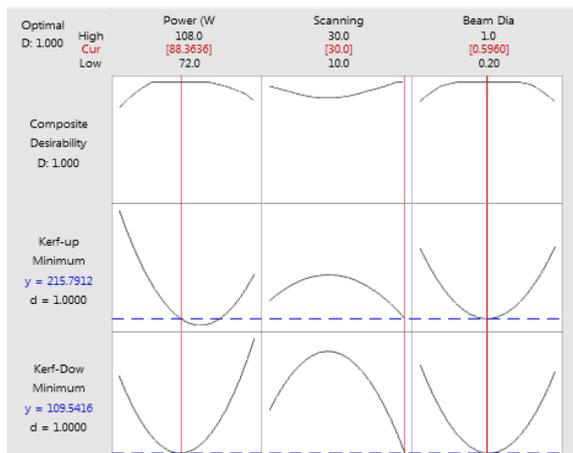
Figure 10. Optimized condition of kerf width at the top and bottom surfaces
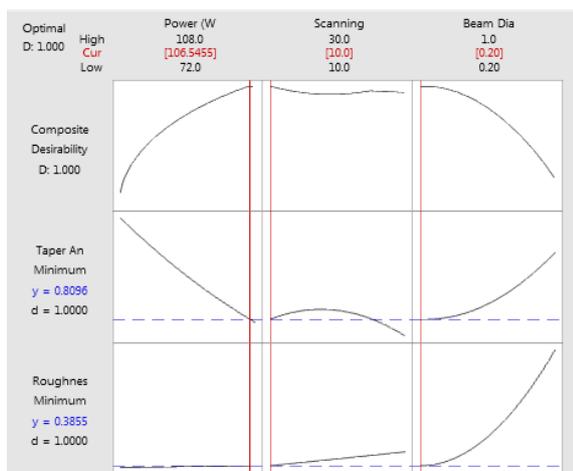
Figure 11. Optimized condition of surface roughness and kerf taper angle
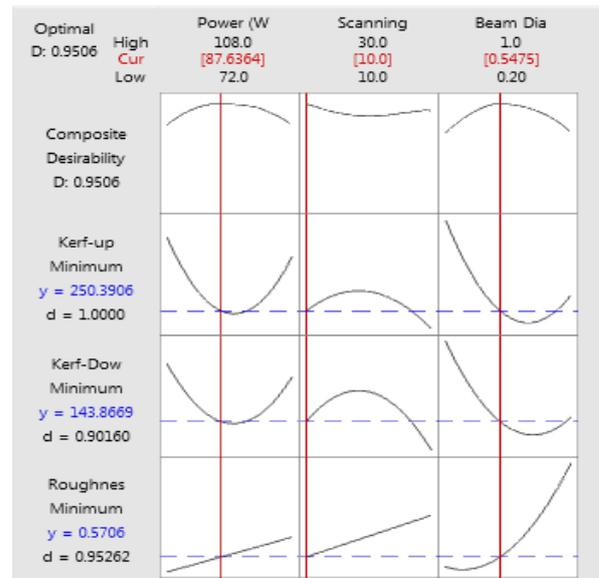
Figure 12. Optimized condition of surface roughness, kerf-up width, and kerf-down width

At the end, it should be noted that the attitude of this research was to find a regression equation between the process parameters and output parameters. ANOVA helps to identify the trend of variation and this was a cognitive process. So, no improvement existed to be discussed quantitatively. The main achievement of this article is finding the equations of output variables and determining the effect of the main and interactions of the process variables.

4. CONCLUSION

In this study, the laser cutting of thin PMMA sheets has been investigated using RSM. The analysis of variance has been utilized to investigate the effect of process variables and their interactions on surface roughness, kerf width, and taper angle. The results show that the beam diameter is the most influential process variable on surface roughness and minimum surface roughness will be obtained at 0.3 mm beam diameter. The minimum kerf-up and kerf-down width were obtained at about 90W laser power, 0.6 mm beam diameter, and 30 mm/s scanning speed. Increasing the laser power reduces the kerf taper angle of the cut surface and the minimum taper angle can be obtained at 0.6 mm beam diameter and 30 mm/s scanning speed. The surface roughness decreases by decreasing the laser power and scanning speed. Multi-objective optimization shows that the optimized condition for minimum surface roughness, kerf-up, and kerf-down width was obtained by setting the process parameters as 87 W laser power, 10 mm/s scanning speed, and 0.54 mm beam diameter.

5. REFERENCES

1. Li H, Fan Y, Kodzius R, Foulds IG. Fabrication of polystyrene microfluidic devices using a pulsed CO 2 laser system. Microsystem technologies. 2012;18:373-9. 10.1007/s00542-011-1410-z

2. Chen X, Li T, Zhai K, Hu Z, Zhou M. Using orthogonal experimental method optimizing surface quality of CO 2 laser cutting process for PMMA microchannels. The International Journal of Advanced Manufacturing Technology. 2017;88:2727-33. 10.1007/s00170-016-8887-7

3. Huang Y, Liu S, Yang W, Yu C. Surface roughness analysis and improvement of PMMA-based microfluidic chip chambers by CO2 laser cutting. Applied surface science. 2010;256(6):1675-8. 10.1016/j.apsusc.2009.09.092

4. Mosalman S, Rashahmadi S, Hasanzadeh R. The effect of tio2 nanoparticles on mechanical properties of poly methyl methacrylate nanocomposites (research note). International Journal of Engineering, Transactions B: Applications. 2017;30(5):807-13. 10.5829/idosi.ije.2017.30.05b.22

5. Choudhury IA, Shirley S. Laser cutting of polymeric materials: an experimental investigation. Optics & Laser Technology. 2010;42(3):503-8. 10.1016/j.optlastec.2009.09.006

6. Eltawahni H, Olabi A-G, Benyounis K. Effect of process parameters and optimization of CO2 laser cutting of ultra high-performance polyethylene. Materials & Design. 2010;31(8):4029-38. 10.1016/j.matdes.2010.03.035

7. Eltawahni H, Olabi A, Benyounis K, editors. Assessment and optimization of CO 2 laser cutting process of PMMA. AIP conference proceedings; 2011: American Institute of Physics. 10.1063/1.3552409

8. Ratnawati R, Wulandari R, Kumoro AC, Hadiyanto H. Response surface methodology for formulating PVA/starch/lignin biodegradable plastic. Emerging Science Journal. 2022;6(2):238-55. 10.28991/esj-2022-06-02-03

9. Safari M, Joudaki J, Ghadiri Y. A comprehensive study of the hydroforming process of metallic bellows: investigation and multi-objective optimization of the process parameters. International Journal of Engineering, Transactions B: Applications. 2019;32(11):1681-8. 10.5829/ije.2019.32.11b.19

10. Obinna AC, Mbah GO, Onoh MI. Optimization and process modeling of viscosity of oil based drilling muds. Journal of Human, Earth, and Future. 2021;2(4):412-23. 10.28991/hef-2021-02-04-09

11. Khoshaim AB, Elsheikh AH, Moustafa EB, Basha M, Showaib EA. Experimental investigation on laser cutting of PMMA sheets: Effects of process factors on kerf characteristics. journal of materials research and technology. 2021;11:235-46. 10.1016/j.jmrt.2021.01.012

12. Elsheikh AH, Deng W, Showaib EA. Improving laser cutting quality of polymethylmethacrylate sheet: experimental investigation and optimization. Journal of Materials Research and Technology. 2020;9(2):1325-39. 10.1016/j.jmrt.2019.11.059

13. Elsheikh AH, Shehabeldeen TA, Zhou J, Showaib E, Abd Elaziz M. Prediction of laser cutting parameters for polymethylmethacrylate sheets using random vector functional link network integrated with equilibrium optimizer. Journal of Intelligent Manufacturing. 2021;32:1377-88. 10.1007/s10845-020-01617-7

14. Yang C-B, Deng C-S, Chiang H-L. Combining the Taguchi method with artificial neural network to construct a prediction model of a CO 2 laser cutting experiment. The International Journal of Advanced Manufacturing Technology. 2012;59:1103-11. 10.1007/s00170-011-3557-2

15. Ninikas K, Kechagias J, Salonitis K. The impact of process parameters on surface roughness and dimensional accuracy during CO2 laser cutting of PMMA thin sheets. Journal of Manufacturing and Materials Processing. 2021;5(3):74. 10.3390/jmmp5030074

16. Kechagias JD, Ninikas K, Stavropoulos P, Salonitis K. A generalised approach on kerf geometry prediction during CO2 laser cut of PMMA thin plates using neural networks. Lasers in Manufacturing and Materials Processing. 2021;8(3):372-93. 10.1007/s40516-021-00152-4

17. Kechagias J, Ninikas K, Petousis M, Vidakis N, Vaxevanidis N. An investigation of surface quality characteristics of 3D printed PLA plates cut by CO2 laser using experimental design. Materials and Manufacturing Processes. 2021;36(13):1544-53. 10.1080/10426914.2021.1906892

18. Varsi AM, Shaikh AH. Experimental and statistical study on kerf taper angle during CO2 laser cutting of thermoplastic material. Journal of Laser Applications. 2019;31(3). 10.2351/1.5087846

19. Mushtaq RT, Wang Y, Rehman M, Khan AM, Mia M. State-of-the-art and trends in CO2 laser cutting of polymeric materials—a review. Materials. 2020;13(17):3839. 10.3390/ma13173839

20. Hashemzadeh M, Voisey K, Kazerooni M. The effects of low-frequency workpiece vibration on low-power CO 2 laser cutting of PMMA: an experimental investigation. The International Journal of Advanced Manufacturing Technology. 2012;63:33-40. https://doi.org/10.1007/s00170-011-3881-6

21. Safari M, Alves de Sousa R, Joudaki J. Recent advances in the laser forming process: A review. Metals. 2020;10(11):1472. 10.3390/met10111472

22. Safari M, Alves de Sousa R, Joudaki J. Comprehensive assessment of laser tube bending process by response surface methodology. steel research international. 2023;94(2):2200230. 10.1002/srin.202200230

23. Safari M, Rabiee AH, Joudaki J. Developing a Support Vector Regression (SVR) Model for Prediction of Main and Lateral Bending Angles in Laser Tube Bending Process. Materials. 2023;16(8):3251. 10.3390/ma16083251

24. Montgomery DC. Design and analysis of experiments: John wiley & sons; 2017.

Persian Abstract

چکیده

برش لیزری یک ابزار دقیق، قدرتمند و با هزینه پایین برای برش ورق های مختلف از چنس فلز و پلیمرها است. بررسی مقالات چاپ شده نشان می‌دهد که کیفیت برش (زبری سطح و هندسه شیار برش) یک پارامتر پیچیده است و روش‌های مرسوم نمی‌توانند کیفیت برش ورق‌های نازک پلیمرها را به خوبی توصیف کنند. ابزارهای آماری می توانند برای تفسیر متغیرهای تأثیر فرآیند مورد استفاده قرار گیرند. در این مقاله به بررسی برش لیزری پلی متیل متاکریلات (PMMA) به صورت تجربی پرداخته خواهد شد. اثر متغیرهای فرآیند برش لیزری شامل سرعت اسکن، توان لیزر و قطر پرتو لیزر بر روی عرض شیار برش و زبری سطح با کمک روش سطح پاسخ مورد بررسی قرار گرفت. نتایج نشان داد که افزایش توان لیزر منجر به افزایش زبری سطح و کاهش زاویه مخروطی شدن شیار می‌شود، در حالی که عرض شیار برش در سطح بالا و سطح پایین ورق، ابتدا کاهش و سپس افزایش می‌یابد (برای توان لیزر بالاتر از ۹۰ وات). همچنین افزایش سرعت اسکن باعث افزایش زبری سطح می شود در حالی که زاویه مخروطی و پهنای عرض شیار برش در سطح بالا و سطح پایین ابتدا افزایش یافته و سپس کاهش می یابد. با افزایش قطر پرتو لیزر، زبری سطح افزایش می یابد، در حالی که زاویه مخروطی و عرض شیار برش در سطح بالا و سطح پایین ابتدا کاهش و سپس افزایش می یابد. بررسی اثر متغیرهای فرآیند اصلی و برهمکنش‌های آنها نشان داد که یافتن شرایط بهینه پارامترهای فرآیند کار سختی است و باید از روشهای بهینه‌سازی چند هدفه برای یافتن حداقل زبری سطح و عرض شیار برش استفاده نمود.

International Journal of Engineering

Traffic Scene Analysis and Classification using Deep Learning

Z. Dorrani*

Department of Electrical Engineering, Payame Noor University (PNU), Tehran, Iran

A B S T R A C T

In this study, we aim to use new deep-learning tools and convolutional neural networks for traffic analysis. ResNeXt architecture, one of the most potent architectures and has attracted much attention in various fields, has been proposed to examine the scene, and classify it into three categories: cars, bikes (bicycles/motorcycles), and pedestrians. Previous studies have focused more on one type of classification and reported only human-facial recognition or vehicle detection. In contrast, the proposed method uses precise architecture to perform the classification of three classes. The proposed plan has been implemented in several steps: the first stage is to divide the critical objects. In the next step, the characteristics of the obtained objects are extracted to classify the process into three classes. Experiments have been conducted on different and essential datasets such as high-traffic, low-quality, real-time scenes. Essential evaluation criteria such as accuracy, sensitivity, and specificity show that the performance of the proposed method has improved compared to the methods being compared. The accuracy criterion reached more than 92%, sensitivity about 89%, and specially to 90.25%. The proposed method can be used to implement intelligent cities, public safety, and metropolitan decisions and use the results in urban management, predictive modeling of lost data management, sequential data management, and generalizability.

Graphical Abstract
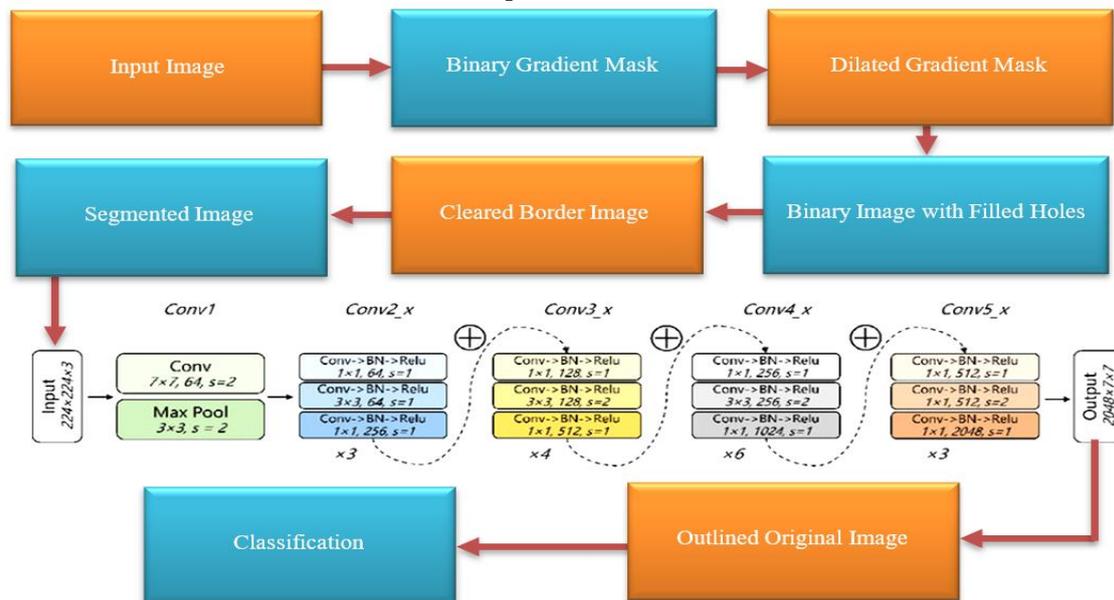
*Corresponding Author Email: dorrani.z@pnu.ac.ir (Z. Dorrani)

NOMENCLATURE

TP	true positive samples	**Greek Symbols**	
TN	true negative samples	η	Specially
FP	false positive samples	φ	Sensitivity
FN	false negative samples		

1. INTRODUCTION

The goal of machine vision is to imitate the capabilities of the human vision system (1). Computers do not have unique minds like humans, and human's previous knowledge makes them superior in this comparison. The significant weakness of the machine's vision compared to humans is the lack of extensive information and its flexibility in the real world. There are different ways to solve this challenge. One of these methods is deep learning based on Convolutional Neural Network (CNN) (2), which performs very well, especially for classification, and can reduce the error rate. The CNN can achieve end-to-end supervised training, without the need for unsupervised pre-training (3), and its various architectures have become the best tools for real-time object classification from image data (4).

Artificial neural networks, composed of many layers, drive deep learning. Deep Neural Networks (DNNs) are networks where each layer can perform complex operations such as representation and inference that make sense of images, audio, and text. Deep learning is the fastest-growing field in machine learning. Deep learning is used in a wide range of applications, such as the detection of researchers' communities (5), the detection of automatic modulation in radar signals (6), the monitoring of intelligent cities using facial recognition robots (7), and efficient classification of facial features (8). Deep learning has helped in image classification, language translation, and speech recognition. Deep learning can solve all pattern recognition problems without human intervention. Deep learning is used in object detection. Kurdthongmee et al. (9) used a YOLOv3 detector to detect parawood cross-sectional. This research seeks to solve the problem of needing data for detector training. It has a weakness due to the testing of the proposed method on specific data and the lack of comparison with previous methods.

Kurdthongmee et al. (10) studied the YOLOv7 method which was proposed for detection in cross-sectional images of a parawood log and pupil datasets. This study aims to identify critical points in these images.

Therefore, in this article, one of the robust architectures (ResNeXt) of this field is used to classify the images obtained from a street. The contribution of this study is the introduction of a scene analysis method and the diagnosis of the number of cars, pedestrians, and bikes based on the deep neural network. By using deep learning and pre-processing techniques, the proposed method performs better than existing methods. In this work, the identification of important goals in the traffic scene has been carried out in previous research, with limited and one-dimensional attention, and an essential gap in this field can be filled. The proposed method offers valuable insights and improvements in traffic scene analysis methods and offers potential applications for urban intelligence.

The pre-processing steps in the proposed method can lead to performance improvement so that it can be implemented for low-quality videos, and videos from high-traffic streets where there is much overlap between objects. In the following, the proposed method is explained first. In the results section, the performance of the proposed method has been checked on different videos, and the characteristics, sensitivity, and accuracy criteria have been calculated.

2. RELATED WORKS

To create a intelligent city, there is a need to control traffic congestion so that city officials have real-time analysis of traffic flow information. Much research has been done in this regard. Using deep learning, traffic analysis has been done. In the research conducted by Zhzng et al. (11), the simulation is based on drone-based videos, where the moving objects of the film are identified. This process uses a pre-trained, real-time model for traffic analysis.

You Only One Once (YOLO) v5 model is proposed by Sharma et al. (12) to detect cars, traffic lights, and pedestrians in lousy weather conditions. Several different classifications have been done for video scenes.

CNN, One of the deep learning models, has been used to identify and classify objects on images taken by drones, including pedestrians, cars (13), and motorcycles/bicycles (14). Two data sets have been evaluated using three GoogleNet, VggNet, and ResNet50 architectures in this research, and the highest level of accuracy has been obtained with the ResNet50 architecture. Through object classification with sensors, the model of the object or location can be recognized more accurately (15). An optimal approach to improve face recognition with and without a mask is proposed using machine learning and deep learning techniques, which use three classifiers: SVM, KNN, and DNN. A network search with meta-parameter adjustment, and nested cross-validation is proposed in this method (16). According to the review of previous research, the difference in the current research includes several items.

- ResNeXt architecture has not been used for traffic scene analysis and classification.
  - The data set used in previous research mainly was images obtained from drones.
  - In this research, actual data, including low-quality and high-traffic videos, have been used.
- In the proposed scheme, pre-processing has been done on the examined data set, which plays a significant role in improving performance.
  - The simulation results show improved characteristics, sensitivity, and accuracy parameters.

3. PROPOSED METHOD

The flowchart of the proposed method is shown in Figure 1.

In the proposed method, the image is segmented first. Image segmentation (17), or object separation, is one of the critical processes in analyzing essential features in each segment. Segmentation can be divided into two parts: general segmentation and partial segmentation. The goal of general segmentation is to determine non-connected points in an image related to target objects. General segmentation algorithms are used in cases where the characteristics of the desired area are uniform and homogeneous. On the other hand, partial segmentation deals with distant points that are not directly related to the desired object. In this type of segmentation, the background segments can be separated from the image. The purpose of removing the background is to create a distinction between the desired object and the scene; it divides the image into structural points, such as background and foreground. In other words, removing the background should be done in such a way that the structure of the desired objects is not destroyed. The constancy of the background color usually makes a big difference with the desired object, which reduces the complexity of the processes.

The gray level threshold is one of the simple and widely used methods for removing the background of images. This method uses general information and is computationally fast and low-cost. This method converts a gray image into binary parts, including background and foreground. This process is done using Equation 1:

$$E_{k.l} = \begin{cases} 1 & p_{k,l}^{(N)} \geq T^s \\ 0 & p_{k,l}^{(N)} \leq T^s \end{cases} \tag{1}$$

where, $p_{k,l}^{(N)}$, and T^s are the value of pixel k,l, and threshold, respectively. The method used for segmenting the background is that the pixels whose values are within a specific range are selected and kept as the background, and the rest of the pixels are assumed to be the background. It ignores the context.

After segmentation, feature extraction (18) is done using deep learning. At this stage, ResNeXt architecture, one of the most complete object recognition techniques, is used. The set of combined transformations can be signified as:

$$\digamma(x) = \sum_{i=1}^{c} \tau_i(x) \tag{2}$$

where, $\tau_i(x)$ can be an arbitrary function. This architecture builds upon the inception and ResNet architectures (19) to provide a new and improved architecture. The inception module is a significant change from sequential architectures. In one layer, there are several types of feature extractors, layers that receive input values, and convert them into some kind of data for calculations, in a network that is learning itself and has to use different options to solve tasks, this type of layering indirectly helps the network to perform better. This module can use the inputs directly in its calculations, or sum them directly. Pre-training works like a transfer learning model so that patterns learned from Inception data can be transferred to a program that has its own set of training data samples. The retraining process uses existing parameters learned as part of the Inception classifier, and its use saves significant training time. In addition, with the help of this module, a high-accuracy classifier is built with less training data by exploiting the transfer learning paradigm. It is possible to classify vehicles, including cars and bikes, using physical characteristics and visual characteristics. These characteristics include visual distance from the ground, vehicle height, and the distance between the license plate and the rear bumper, which is extracted from the input using CNN.

It is possible to recognize pedestrians using methods based on the human body model using two-dimensional and three-dimensional information of different body parts. Among this information, can mention the location and movements of different parts of the body. In fact, in
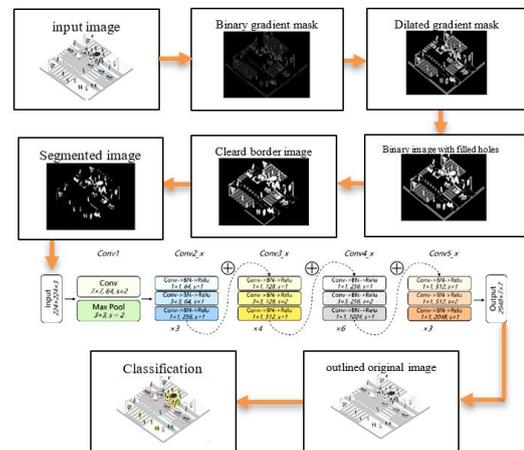

Figure 1. The flowchart of the proposed method

this method, the way the human body stands is recognized by estimating the posture, and different parts of the body, and checking the connection points. In order to strengthen the proposed method against the change in the camera angle, and the change in the environment, a two-point perspective has been used based on the tracking of body connection points.

Therefore, The contributions of this paper can be expressed in a few cases: First, a proposed method that will achieve superior performance in scene analysis. Secondly, its application in public management plays a significant role in analyzing governance policies and features of intelligent cities and understanding the changing needs of intelligent cities. Thirdly, deep learning is vital in designing, decision-making, and implementation by understanding data patterns, classification, and prediction.

4. RESULTS

The use of deep learning in the proposed method makes it possible to consider environmental and background conditions with a higher degree of accuracy, which in turn helps to improve the accuracy of detection, localization, and classification. Camera images are converted to pixel-level data, which are processed to remove the foreground. These image data are segmented, and then all the segmented data are structured in the form of a tensor. This composite tensor is then further processed to optimize the bounding box. The obtained data use the deep learning algorithm through CNN. The work steps are shown in Figure 2.

The first stage is an image that includes cars, bikes (bicycles/motorcycles), and pedestrians. In the second step, objects are segmented. The object to be segmented is very different from the background image. Contrast changes can be detected by operators that calculate the gradient of an image. In the third stage, the binary gradient mask (20) of high-contrast lines is shown in the image. These lines do not entirely define the outline of the subject of interest, and compared to the original image, there are gaps in the lines around the object in the gradient mask, and the linear gaps should be removed. In the fourth stage, the internal gaps are filled, but there are still holes inside the cell that need to be filled. In the fifth step, the connected objects on the border are removed. In the sixth step, the object is smoothed, and finally, to make the segmented object look natural, the object is smoothed by eroding the image twice with a diamond structure element. In the seventh step, an alternative method to represent the segmented object is to place the outline around the image. In the eighth step, classification is done using CNN architecture, and three different classes are shown with red, green, and yellow boxes.

An accurate sample of street videos was also analyzed to check the proposed method, and the obtained results are shown in Figure 3. In this figure, the proposed method has been checked on three different videos. Video A (21) contains 23435 frames with a low resolution of 480×320 pixels. This dataset is in an urban location. Video B shows the traffic of a three-way street in an urban area. Video C is a high-traffic city area where objects overlap a lot.
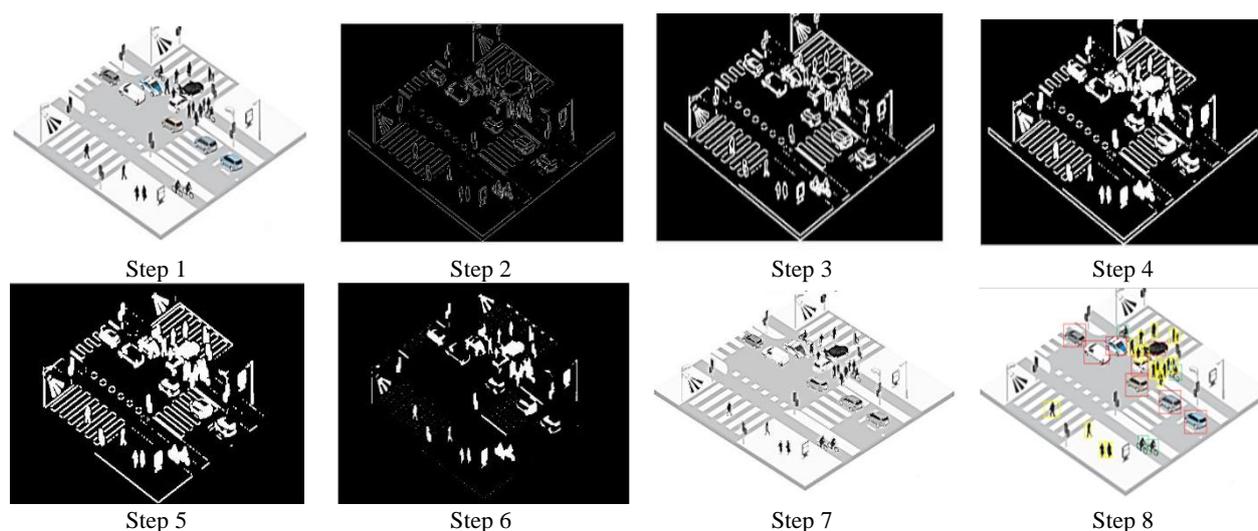
Figure 2. Proposed method teps: Step 1: Input; Step 2: Binary gradient mask; Step 3: Dilated gradient mask; Step 4: Binary image with filled holes; Step 5: Cleard border image; Step 6: Segmented image; Step 7: Outlined original image; Step 8: Classification
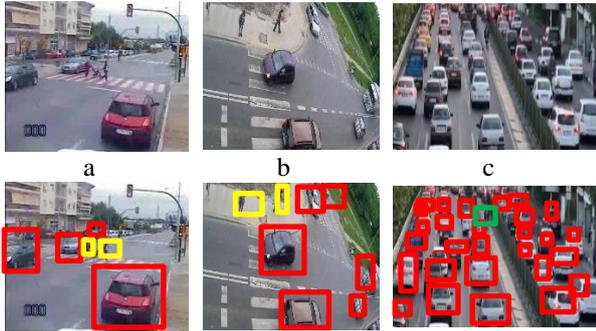
Figure 3. Traffic scene analysis and classification on the dataset

The evaluation of the proposed method is done using the existing criteria. Two critical criteria in order to recognize the correct classification, criteria The sensitivity and specially of classification, are obtained using the relations (2):

$$\varphi = \frac{TP}{TP+FN} \tag{3}$$

$$\eta = \frac{TN}{TN+FP} \tag{4}$$

where, TP is positive cases whose category is correctly diagnosed as healthy, TN is negative cases whose category is correctly diagnosed. FP is positive cases whose category is not correctly recognized, and FN is negative cases whose category is wrongly recognized.

In evaluating the proposed method, TP and TN, are the most critical important values that should be maximized in a problem. As summarized in Table 1, these two criteria are close to 0.9 for cars and bikes and lower than 0.9 for pedestrians. Considering the low quality of video a and the high density and traffic in video

c, acceptable results have been obtained. These results show that even for videos with high traffic and low quality, the performance of the proposed method is favorable. On the other hand, since the results were obtained from real samples, they can be used for actual applications.

Another vital criterion is accuracy, which is obtained by thefollowing relationship (19):

$$Accuracy = \frac{TP + TN}{TP + TN + FP + FN} \tag{5}$$

Accuracy is one of the most important criteria to determine the efficiency of a classification method. This criterion is the most famous and most common efficiency calculation criterion. It is a classification algorithm that shows how many percent of the entire set of test records is correctly classified. Table 2 shows a comparison between the proposed method and the combined method.

Table 2 shows the comparison of accuracy. From this table, it can be concluded that the classification accuracy for cars, and bicycles is above 90%, while for pedestrians, it is below 90%. The average accuracy for the combined method is 85.8% and for the proposed method is 90.2%, which is a significant improvement.

5. DISCUSSION

The proposed solutions to the research questions and discussion of the traffic scene analysis are as follows:
Can preprocessing improve the performance? The performed pre-processing leads to the removal of additional information, restoration of extraction objects, and, as a result, increasing the segmentation quality. Due to the large number of calculations, CNN can be a good moderator for this purpose.

TABLE 1. Sensitivity and specially values

	Video a	Video b	Video c	Total	φ	η
Car	125	41	223	389	0.91	0.89
Bike	9	7	86	102	0.95	0.92
Pedestrian	16	18	23	57	0.85	0.87
Total	150	66	332	53	0.9	0.89

TABLE 2. Accuracy values

	Car	Bike	Pedestrian	Total	Accuracy (%)	
					Ref. (5)	Proposed Method
Car	20	0	0	20	90.9	**92.4**
Bike	0	0	16	16	100	**100**
Pedestrian	0	5	12	17	66.7	**78.2**
Total	20	5	28	53	85.8	**90.2**

Can ResNeXt architecture increase the accuracy of the proposed method? One of the essential features of this architecture is its very high accuracy, and this has been proven in Pre-processing. This precise architecture contributes significantly to increase accuracy, sensitivity and specificity.

6. CONCLUSION

Traffic scene analysis is one of the essential components of intelligent cities. In traffic scenes, there are cars, bikes, and pedestrians in the street. The correct identification of each object in the scene, and then their correct classification can provide essential information to city managers and people who travel on that route. In this article, the classification is based on a robust ResNeXt architecture that contributes to increasing accuracy and improving diagnostic and classification performance. The preprocessing process makes these goals more attainable and helps to improve the performance. It shows the essential criteria for evaluating the calculation performance and the improvement results of the accuracy criterion. The proposed method reached over 90% on different data such as urban points, high traffic points, and actual data of implementation and evaluation criteria.

Deep learning has significant advantages, but its disadvantages cannot be easily overcome. One of its disadvantages is the high computational cost, and future research can try to reduce it by using creative methods. Another aspect of research can be adding other applications to the proposed method, Such as classifying cars separately, separating bicycles and motorcycles, and separating pedestrians into adults and minors. Tracking is another important application that can be considered after classification.

7. REFERENCES

1. Al-Mallahi A, Natarajan M, Shirzadifar A. Development of robust communication algorithm between machine vision and boom sprayer for spot application via ISO 11783. Smart Agricultural Technology. 2023;4:100212. https://doi.org/10.1016/j.atech.2023.100212

2. Dorrani Z. Road Detection with Deep Learning in Satellite Images. Majlesi Journal of Telecommunication Devices. 2023;12(1):43-7. https://doi.org/10.30486/mjtd.2023.1979006.1024

3. Long F, Yao T, Qiu Z, Li L, Mei T, editors. PointClustering: Unsupervised Point Cloud Pre-Training Using Transformation Invariance in Clustering. Proceedings of the IEEE/CVF Conference on Computer Vision and Pattern Recognition; 2023.

4. Ranjith CP, Hardas BM, Mohideen MSK, Raj NN, Robert NR, Mohan P. Robust deep learning empowered real time object detection for unmanned aerial vehicles based surveillance applications. Journal of Mobile Multimedia. 2023:451–76-–76. https://doi.org/10.13052/jmm1550-4646.1925

5. Torkaman A, Badie K, Salajegheh A, Bokaei M, Fatemi Ardestani S. A Hybrid Approach to Detect Researchers' Communities Based on Deep Learning and Game Theory. International Journal of Engineering, Transactions B: Applications. 2023;36(11):2052-62. 10.5829/IJE.2023.36.11B.10

6. Aslinezhad M, Sezavar A, Malekijavan A. A noise-aware deep learning model for automatic modulation recognition in radar signals. International Journal of Engineering, Transactions B: Applications. 2023;36(8):1459-67. 10.5829/IJE.2023.36.08B.06

7. Medjdoubi A, Meddeber M, Yahyaoui K. Smart City Surveillance: Edge Technology Face Recognition Robot Deep Learning Based. International Journal of Engineering, Transactions A: Basics. 2024;37(1):25-36. 10.5829/IJE.2024.37.01A.03

8. Rohani M, Farsi H, Mohamadzadeh S. Deep Multi-task Convolutional Neural Networks for Efficient Classification of Face Attributes. International Journal of Engineering, Transaction B: Applications. 2023;36(11):2102-11. 10.5829/IJE.2023.36.11B.14

9. Kurdthongmee W, Suwannarat K, Kiplagat J. A Framework to Create a Deep Learning Detector from a Small Dataset: A Case of Parawood Pith Estimation. Emerging Science Journal. 2022;7(1):245-55. 10.28991/ESJ-2023-07-01-017

10. Kurdthongmee W, Suwannarat K, Wattanapanich C. A Framework to Estimate the Key Point Within an Object Based on a Deep Learning Object Detection. HighTech and Innovation Journal. 2023;4(1):106-21. 10.28991/HIJ-2023-04-01-08

11. Zhang H, Liptrott M, Bessis N, Cheng J, editors. Real-time traffic analysis using deep learning techniques and UAV based video. 2019 16th IEEE International Conference on Advanced Video and Signal Based Surveillance (AVSS); 2019: IEEE. 10.1109/AVSS.2019.8909879

12. Sharma T, Debaque B, Duclos N, Chehri A, Kinder B, Fortier P. Deep learning-based object detection and scene perception under bad weather conditions. Electronics. 2022;11(4):563. 10.3390/ELECTRONICS11040563

13. Dorrani Z, Farsi H, Mohammadzadeh S. Edge Detection and Identification using Deep Learning to Identify Vehicles. Journal of Information Systems and Telecommunication (JIST). 2022;3(39):201. 10.52547/JIST.16385.10.39.201

14. Cengiz E, Yilmaz C, KAHRAMAN H. Classification of human and vehicles with the deep learning based on transfer learning method. Düzce Üniversitesi Bilim ve Teknoloji Dergisi. 2021;9(3):215-25. 10.29130/DUBITED.842394

15. Dheekonda RSR, Panda SK, Khan N, Al-Hasan M, Anwar S. Object detection from a vehicle using deep learning network and future integration with multi-sensor fusion algorithm. 2017. https://doi.org/10.4271/2017-01-0117

16. Thanathamathee P, Sawangarreerak S, Kongkla P, Nizam DNM. An Optimized Machine Learning and Deep Learning Framework for Facial and Masked Facial Recognition. Emerging Science Journal. 2023;7(4):1173-87. 10.28991/ESJ-2023-07-04-010

17. Fooladi S, Farsi H, Mohamadzadeh S. Segmenting the lesion area of brain tumor using convolutional neural networks and fuzzy k-means clustering. International Journal of Engineering, Transaction B: Applications. 2023;36(8):1556-68. 10.5829/IJE.2023.36.08B.15

18. Lu S, Ding Y, Liu M, Yin Z, Yin L, Zheng W. Multiscale feature extraction and fusion of image and text in VQA. International Journal of Computational Intelligence Systems. 2023;16(1):54. 10.1007/S44196-023-00233-6

19. Dorrani Z, Farsi H, Mohamadzadeh S. Deep Learning in Vehicle Detection Using ResUNet-a Architecture. Jordan Journal of Electrical Engineering. 2022;8(2):166-78. 10.5455/JJEE.204-1638861465

20. Dorrani Z, Farsi H, Mohamadzadeh S. Image edge detection with fuzzy ant colony optimization algorithm. International Journal of Engineering, Transactions C: Aspects 2020;33(12):2464-70. 10.5829/IJE.2020.33.12C.05

21. Wang Y, Ban X, Wang H, Wu D, Wang H, Yang S, et al. Detection and classification of moving vehicle from video using multiple spatio-temporal features. IEEE Access. 2019;7:80287-99. 10.1109/ACCESS.2019.2923199

Persian Abstract

چکیده

در این مطالعه، هدف ما استفاده از ابزارهای جدید یادگیری عمیق و شبکه عصبی کانولوشن برای تجزیه و تحلیل ترافیک است. معماری ResNeXt که یکی از قدرتمندترین معماری‌هاست وتوجهات زیادی را در عرصه‌های مختلف به خود جلب کرده، برای بررسی صحنه و طبقه‌بندی آن در سه دسته‌ی ماشین، موتور (موتورسیکلت/دوچرخه) و عابر پیاده پیشنهاد شده است. مطالعات قبلی بیشتر روی یک نوع طبقه‌بندی متمرکز شده و فقط تشخیص انسان و چهره، یا فقط تشخیص وسایل نقلیه را گزارش کردند. در مقابل، روش پیشنهادی از معماری دقیقی استفاده کرده تا دسته‌بندی سه کلاسه را انجام دهد. طرح پیشنهادی شامل چند مرحله است: مرحله اول بخش‌بندی است که اشیاء مهم جدا می‌شوند. در مرحله‌ی بعد ویژگی‌های اشیای بدست آمده استخراج می‌شود تا فرآیند دسته‌بندی به سه کلاس موردنظر انجام گیرد. آزمایش‌هایی روی مجموعه داده‌های مهم و متفاوتی مانند صحنه‌های پرترافیک، کیفیت پایین و واقعی انجام شده است. معیارهای مهم ارزیابی مانند دقت، حساسیت و ویژگی به دست آمده، نشان می‌دهد عملکرد روش پیشنهادی نسبت به روش‌های مورد مقایسه بهبود یافته است. معیار دقت به بیش از ٪۹۲، حساسیت حدود ۸۹٪ و ویژگی به ٪۹۰.۲۵ رسیده است. روش پیشنهادی می‌تواند برای اجرای هوشمندسازی شهرها، ایمنی عمومی، تصمیمات کلان شهری و استفاده از نتایج بدست آمده در مدیریت شهری، مدل‌سازی پیش‌بینی کننده از مدیریت داده‌های از دست رفته، مدیریت داده‌های متوالی و تعمیم‌پذیری مورد استفاده قرار گیرد.

International Journal of Engineering

Natural and Artificial Fibre Reinforced Concrete: A State-of-art Review

P. Hait*[a], R. Karthik[b], R. Mitra[c], R. Haldar[d]

[a] JSPM University Pune- 412207, India
[b] CVR College of Engineering, Hyderabad-501510, India
[c] Swami Vivekananda University, Kolkata - 700121, India
[d] Veltech University, Chennai- 600062, India

ABSTRACT

The Fibre reinforced concrete (FRC) has become popular in construction industry in last few decades. Various natural and artificial fibres are added in concrete to enhance the crack resistance property by developing some bonding between fibre and concrete. FRC is not only performs better than conventional concrete but also the fibre reinforced concrete (FRC) has become popular in construction industry in last few decades. FRC is not only performs better than conventional concrete but also it reduces environmental pollution. Actually in many rural area, people are not concerned about the pollution and hygiene. The unused portion of sugarcane fibre, banana fibre, jute fibre are thrown into pond/ lake. After few days they decompose and rotten, that causes pollution in waterbody and disturb the ecosystem. The fibres can be used as additive in concrete to enhance their overall performance as well as to reduce environmental pollution. In this paper, a state-of-art review has been investigated on FRC and its different benefits. Different fibres such as jute fibre, coconut fibre, polypropylene, basalt, areca leaf, glass, mask, plastic, carbon and steel fibre were incorporated in concrete by several researchers in the past decades that have been highlighted in detail in this paper. The performance has been evaluated in terms of load displacement hysteretic pattern, stiffness, ductility, energy dissipation, crack resistance, durability and workability of FRC. The virtue and limitations of FRC have also been discussed. From the existing literature, it is found that the performance of FRC under dynamic load, Damage assessment, Time dependent assessment of damage, Effect of fibre in high-performance concrete (HPFRC) and Life cycle assessment are found as major literature gap that needs to be fulfilled. A case study on damage assessment of FRC has also been conducted in this paper. From the result it is found that the Carbon fibre reinforced concrete (CFRC), Steel fibre reinforced concrete (SFRC) and Areca leaf sheath fibre reinforced concrete (ALSFRC) are experiencing lesser damage in compared to normal concrete without fibre. Based on the existing literature the future scope and probable direction of research of FRC have also been highlighted.

doi: 10.5829/ije.2024.37.03c.07

Graphical Abstract
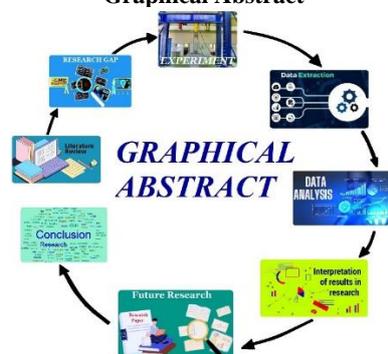
*Corresponding Author: pritamhait15@gmail.com (P. Hait)

1. INTRODUCTION

Concrete is a popular choice for construction purposes, typically combined with deformed steel reinforcing bar (rebar) due to its high compressive strength. Steel reinforcements are utilized only in regions where there is a chance of tensile or shear stress, resulting in the development of reinforced concrete (RC). These types of concrete have improved tensile and shear resistance, making them ideal for structural elements subjected to quasi-static loading conditions. However, in recent times, structures have been exposed to harsh loading conditions like blasts, and fire from various sources, including terrorist attacks. While reinforced concrete (RC) and Prestressed concrete (PSC) structures are efficient under static conditions, they prove inadequate under extreme loads due to concrete's poor energy absorption capacity and brittle nature, which causes it to break apart.

Fibre Reinforced Concrete (FRC) is a type of composite material that enhances the structural strength and integrity of concrete by incorporating fibrous materials. According to ACI, FRC refers to concrete that contains randomly dispersed fibres. Due to its inherent brittleness and poor tensile strength, concrete tends to crack easily, resulting in issues such as freeze-thaw damage, scaling, discoloration, and steel corrosion. To address these problems, fibres are added to concrete to control the formation and growth of cracks. Various synthetic and natural fibres are commonly utilized in concrete to manage cracking and its propagation caused by plastic and drying shrinkage.

Suresh et al. (1) investigated the strength of concrete infused with glass and jute fiber as a natural and artificial fiber combination. The workability and compressive strength of the concrete with 1% of fiber content with cement weight is more than 2% of fiber content. However, it reduces the crack width under different loading (1). Chloride diffusivity is reduced when the concrete is infused with PPF, and the diffusivity of chloride is increased when the concrete is infused with steel fibre. However, the mixture of these two fibres shows improvement in the concrete properties and decreases the drying shrinkage (2). The physical characteristics of fresh and durability properties of dried concrete made with PPF concrete and compared with conventional concrete. The result shows that the usage of fiber quantity affects the properties of fresh concrete. Among different volume fractions of fiber used in the concrete, 0.8% of fiber utilized mix shows a positive effect in durability aspect. An increment of the volume fraction of fiber exhibits the heterogeneous dispersion of fibers in concrete. Due to this, floccule formed in the mixes, leading to more voids forming (3). The mechanical and physical properties of concrete infused with steel fibre were compared with conventional concrete. Under loading, the conventional concrete

shows a typical advancement crack pattern, but on the contrary, in FRC, the crack ceased due to the ductile property of steel fibre. The compressive strength of the concrete increases as SF increases; on the contrary, the workability decreases when SF increases (4). The workability and mechanical property of the self-compacting HPC with PPF and M-sand was studied. Results show that around 25% increment was found in compressive strength compared to self-compacting PPC (5). Krishna et al. (6) have investigated the ductility and load-carrying capability of concrete made with coir and sisal fiber. The coir fiber in concrete controls the tensile crack and improves the ductility energy absorption capacity. Microstructural morphology of PPF concrete was carried out by using non-destructive technology. It is evident that the micro-crack develops during hydration are emerges on the interfacial zone along the close vicinity of aggregates. The maximum voids were found at the interfacial transition between cement paste and fibre or coarse aggregate. It is evident from the result that the volume of pores is proportionate to the fibre volume fraction (7). The durability of concrete made with polypropylene, glass, and hybrid fibre was studied by rapid chloride penetration and rapid chloride migration test. From the result, it is evident that the hybrid fibre shows better mechanical and durability properties. Compared to glass fibre, polypropylene fibre depicts better strength and durability (8). The effect of the fraction of polypropylene fibre and its geometry effect on ultra-high performance concrete (UHPC). It was evident that the length and dosage of fibre strongly influence permeability. The permeability does not increase once the fibre aspect ratio is less, even though the fibre dosage is increased. However, the authors proposed a mathematical model to select and optimize the fibre content to avoid the spalling of concrete (9). The mechanical, rheological, and microstructure of self-compacting lightweight concrete (SCLC) is analyzed by incorporating the combination of steel, PPF fibre, and silica fume. It is evident that a significant improvement in the mechanical properties by adding fibre and silica fume. Different mixes of SCLC show good flowability, passing ability, and viscosity (10). A study on the effect of the length of PPF on the emerging stage in High-Performance Concrete (HPC) was performed. Autogenous shrinkage value, temperature drop at a cracking time, and the value of specific tensile creep are reduced when the PPF length is increased. The ratio of cracking stress to axial tensile strength and the value of stress reserve is also reduced when the length of PPF increases. From the study, it was evident that the length of the fibre is another critical parameter (11). It was concluded that PPF did not alter cement's density, rheology, and free water property when infused with cement. The cement thickening time was reduced significantly. The 0.5% of PPF from the total weight of

cement added to the cement can enhancement in compressive stress is 17.8%, and the PPF of 0.75% of the total weight of cement increases the tensile strength of concrete by around 18% (12). The mechanical, durability, and microstructure of PPF concrete was studied with different utilization ratio. The fiber volume fraction varied from 0 to 0.5%; among this, the specimen with 0.3% PPF showed the highest flexural strength. The result of dry-wet cycles shows that the specimen with 0.1% of PPF is the lowest water absorption among others, and it is evident that the optimum fiber content helps to improve the compactness of concrete, thus helping to reduce the porosity. In the freeze-thaw test, the specimen with 0.5% PPF shows better resistance against salt freezing. However, in a chloride environment, the specimen with 0.1% PPF performs better in the freeze-thaw and wet-try tests (13). Jia et al. (14) confirmed that the interfacial adhesive strength between the cement matrix to PPF was increased when PPF was mixed with Micro-silica (MSi), which acts as a hydrophilic modifier. The effect of the inclusion of hybrid fibre, including PPF and Latex powder have been studied in concrete to evaluate their mechanical properties. The specimen at the initial days of the drying period shows significant shrinkage deformation; however, the shrinkage rate after 45 days of drying periods decreased. The shrinkage model shows a strong interrelation between shrinkage rate to polymer latex fibre. The optimum utilization value of fibrous materials to develop overlay materials for CC pavement is 0.2% of 9 mm length PP fibre with 2.5% of both latex and silica powder (15). The tribological and rheological properties of fresh concrete made with PPF were studied by Bentegri et al. (16). The effect of fibre, such as shape (fibrillated twist and wave fibre), length, and dosage in the fresh concrete with superplasticizers, was analyzed. The fibre length does not affect the plastic viscosity. However, the plastic viscosity and segregation (tribological) of the concrete show a negative effect when the fibre dosage increases, but it could improve with superplasticizers. The rheological and tribological properties and workability were improved for the concrete with superplasticizers. Combining fibres reduces plastic viscosity and constant viscosity compared to a single fibre (16). The mechanical and durability of hybrid fiber reinforced foam concrete (HFRFC) was investigated by Raj et al. (17). Flexural and split strength, the compressive strength of the concrete infused with fiber is improved compared to plain foam cement concrete; however, the synthetic fiber (ploy vinyl alcohol) shows better results than the natural (Coir) fiber. The chemical and physical properties of concrete infused with polypropylene fibre were discussed in detail. The amount of fibre is another critical parameter. If it is added more than its requirement, it may reduce the workability of the concrete. Adding polypropylene fibre can enhance the strength of the concrete, but it can produce negative results if it is more than the optimum dosage (18). The

durability of concrete can be increased when it is infused with polypropylene fibres (PPF), as it optimizes the opening of the pores in concrete. It helps to reduce the entry of ions and water, which is detrimental. When the combination of PPF and steel fibre is mixed in concrete, further enhancement in the durability of concrete is achieved. PPF shows weak bonding with cement matrix and does not disperse completely in concrete; however, it can be overcome when the fibre is treated with the chemical (19). Moreover, the abrasion and impact resistance of concrete are improved in addition to other mechanical properties. However, the hybrid fiber shows better results than the mono fiber. The researchers found the optimum dosage of hybrid fiber as 0.3% of PVA and 0.2% coir (20). Islam et al. (21) have investigated the mechanical and rheological properties of concrete with nylon, iron, and coir as steel, synthetic and natural fiber. The result shows that the addition of fiber causes a significant reduction in the workability of concrete. Among these three fibers, steel fiber shows a significant increment of compressive and flexural strength. However, these three fiber shows lower compressive strength at the beginning (3-7 days) days due to weak bonding of materials. From the study, it was evident that the addition of fiber enhanced the ductility after the crack and the capacity of energy absorption (21). The physical, mechanical, and durability properties of different natural and synthetic fiber-infused concrete were examined by More and Subramanian (22). The results show that water absorption of natural fiber is more than that of artificial fiber. However, the artificial fiber is more efficient compared to natural fiber. Under acidic exposure, the weight loss of fiber concrete is higher, but the weight loss is less under an alkaline environment. Split tensile strength, ductility, and post-cracking resistance were improved (22). Amir et al. (23) have analyzed flexural capacity by static analysis. The result shows that compared to conventional shear reinforcement, spiral reinforcement increases flexural performance. The crack pattern, punching shear, and load displacement of slap with steel fiber were analyzed. Ahmed et al. (24) have reviewed the mechanical, physical, and durability of coir fiber concrete. The flexural strength of concrete with coir fiber is significantly improved compared to compressive strength, as mentioned by previous researchers. Ahmed et al. (24) mentioned that the optimum dosage of coir fiber was 2 to 3%. However, Krishna et al. (6) mentioned that the optimum percentage of coir fiber was 1.5%. Effiong and Ede (25) have reviewed the techniques of Near Surface Mounted (NSM) and Externally Bonded (EB) for strengthening reinforced concrete beams by using natural fiber polymer composite. In the NSM technique, synthetic fiber shows failure by flexural rupture, pull-out driven by intermediate crack, and end pull-out. However, these failure mechanisms of the concrete beam with natural fiber reinforcement still need to be explored fully. Burst cycles and break solidity of

sisal fiber need to be studied mentioned that more data is needed for the design and performance of steel fiber concrete (25-27).

From the literature it has been observed that Performance of FRC under dynamic load, Damage assessment of FRC, Time-dependent assessment of damage of FRC, Effect of fibre in high performance concrete (HPFRC), life cycle assessment of FRC have not been performed. In the above literature review a detailed scenario on FRC has been presented. Different virtue and limitations are found from the literature and portrait in this paper. Based on the literature the research gap has been discussed. The probable future research direction has been explained based on the existing review.

2. RESEARCH SIGNIFICANCE

The natural and artificial fibres have their own properties based on which they help to improve the performance of concrete. On the other way the fibre also reduce the workability of concrete. A state-of-art review on FRC have been highlighted on existing literature in this paper. It shows different properties of fibre and their performance in concrete in terms of load displacement hysteretic pattern, stiffness, ductility, energy dissipation, crack resistance, durability and workability. This review also reveals the virtue and limitations of FRC. Based on the existing literature the research gap and probable future direction of research have been highlighted in this paper.

3. CLASSIFICATION OF FIBRE REINFORCED CONCRETE

Different types of natural and artificial fibres are available for FRC shown in Figure 1

(a)   (b)   (c)

(d)   (e)   (f)

(g)   (h)   (i)

(j)   (k)   (l)
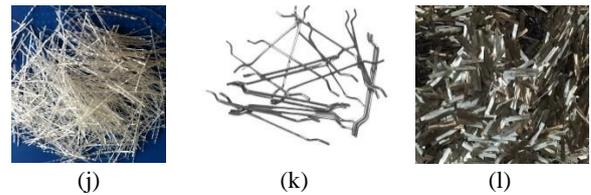
Figure 1. Different types of fibre (a) Coconut fibre (b) Jute fibre (c) Nylon fibre (d) Glass fibre (e) Polypropylene fibre (f) Carbon fibre (g) ALS fibre (h) Banana fibre (i) Sugarcane fibre (j) Plastic fibre (k) Steel fibre (l) Basalt fibre

4. CLASSIFICATION OF FIBRE

There are several types of fibres are available round the globe. They can be classified as per the following Figure 2 (28). A flow chart has been presented in Figure 3.

5. PROS AND CONS OF FRC

In this study an overview of commonly used fibres are discussed. The FRC has virtue and limitations have been discussed in Table 1.
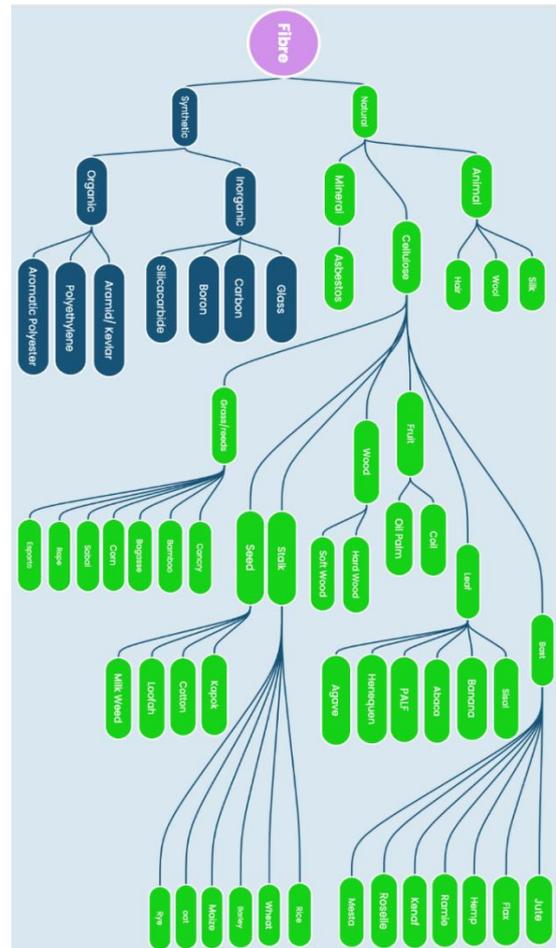
Figure 2. Classification of existing fibre [28]
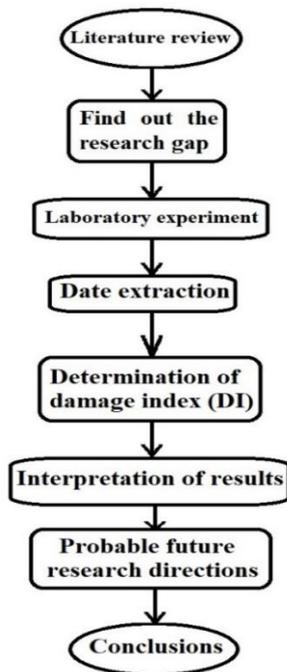
Figure 3. Flow chart of the research

TABLE 1. The virtue and limitations of FRC

Sl. No.	Virtue	Limitations
1.	From the above literature it is found that the FRC has many pros and cons. Firstly, the FRC is highly crack resistance while it is incorporated in concrete. Secondly, it increases tensile strength, compressive strength, shear capacity, ductility, stiffness, impact load resistance capacity, freeze-thaw resistance, shrinkage crack resistance.	Apart from many pros, there are few cons are associated with FRC. Firstly fibre reduces the workability of concrete, especially with steel fibre. Moreover there is a chance of fibre ball formation in concrete that may affect adversely. Secondly, due to corrosion the steel FRC may deteriorate early. Moreover, maximum FRC is costly with compared to normal concrete although the extra cost can be set off by reducing the cement consumption or other factors.

6. CASE STUDY

A case study has been conducted on fibre reinforced beam-column joint under cyclic load. In this study an uncommon natural fibre i.e. Areca leaf sheath (ALS) fibre, steel and carbon fibre have been used. For this purpose an Areca leaf sheath fibre reinforced concrete (ALSFRC) beam-column joint (BCJ), steel fibre BCJ and carbon fibre BCJ have been casted and tested under cyclic load in actuator shown in Figure 4. The performance has been assessed by Ghobarah et al. (29) stiffness damage index (DI). A beam-column joint without fibre has been tested as control specimen to compare the performance of FRC. The estimated DI is

compared with Park-Ang DI in Figure 5. It has been observed that the present study estimates the similar DI with Park et al. (30) DI.

$$DI = 1 - \frac{K_f}{K_i} \tag{1}$$

where, DI = Damage index of the member, K_i = Initial stiffness, K_f = final stiffness

The performance of the specimens are determined in terms of DI. Using the Eq. 1 the DI of the BCJs are determined. The DI is plotted with different displacement level to compare the performance among ALSFRC, Steel FRC (SFRC), Carbon FRC (CFRC) and BCJ without fibre presented in Figure 5. In this figure the ALSFRC, SFRC and CFRC are experiencing lower damage with compared to the BCJ without fibre. Moreover the CFRC achieved lowest DI due to its highest strength.

7. RESULTS AND DISCUSSIONS

In this article the state-of-art review has been examined. The performance of FRC have been discussed in terms of tensile strength, compressive strength, dissipated hysteretic energy, stiffness, ductility, crack resistance, creep and shrinkage. Apart from the existing research there are many other important aspects are required to discuss given below.
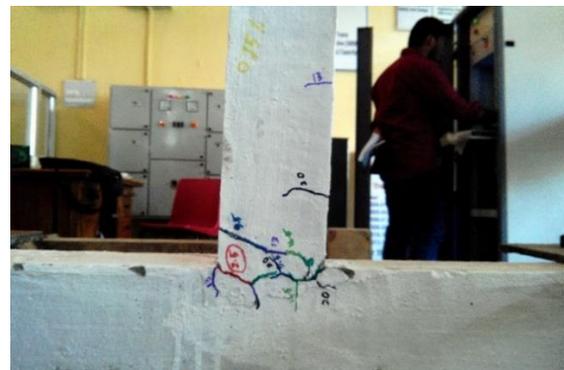
(a)

(b)

Figure 4. (a) ALSFRC BCJ (b) BCJ without fibre
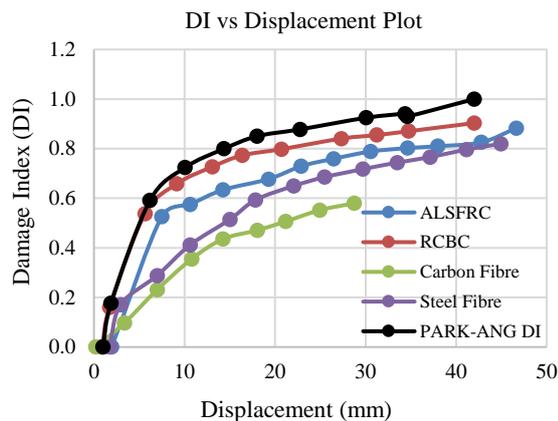
Figure 5. Comparison of DI between ALSFRC and BCJ without fibre

7. 1. Performance under Dynamic Load   From the existing literature it is found that the performance of concrete has been carried out under static load. Whereas non-linear dynamic analysis of FRC is not explored yet. The performance of FRC under seismic and wind load may reveal new outcomes and it may introduce new direction of research.

7. 2. Damage Assessment   The structural damage assessment of FRC has not been explored yet. It is very essential to determine the damage index (31-38) of FRC for different percentage of fibre under different types of static and dynamic load. The investigation results from damage assessment may explore new important direction of research.

7. 3. Time-dependent Assessment of Damage
Ageing, operational circumstances, materials utilization, geometric shape, repeated loads, increased mean load, and environmental factors all are responsible for structural degradation. Other factors that contribute to the slow decay of structures include humidity and chemical substances like sulphur and chloride. Environmental consequences and structural deterioration have not been explored significantly. Future research will compare various environmental elements and degradation mechanisms for hazard function.

7. 4. Effect of Fibre in High Performance Concrete (HPFRC)   The fibres are generally used in normal concrete found from literature. A few literature are available on HPFRC. It is necessary to know the effect of fibre in high performance concrete and its performance.

7. 5. Life Cycle Assessment   The life cycle assessment (LCA) is one of the important aspect in sustainable development. The LCA of FRC is essential to know its safety and serviceability. This investigation may help the future probable direction of research.

8. CONCLUSIONS

In this paper a detailed review has been discussed. The virtue and limitations of FRC have been discussed. The probable future scope of FRC has also been highlighted. Although several researchers have explored the properties and utilities of various types of FRC still it is not yet commercialized in large scale. The following conclusions can be drawn from this study:
1. The CFRC is experiencing lowest DI and RCBC is experiencing highest DI among all the specimens.
2. The structural damage assessment of FRC is essential to know the performance in high seismic region and its range of application.
3. FRC deteriorates due to ageing, operational circumstances, materials utilization, geometric shape, repeated loads, increased mean load, and environmental substances. This deterioration is called time-dependant damage assessment that is essential for FRC.
4. The effect of fibre in high performance concrete and LCA may be another important future direction of research.
5. Incorporation of fibre improves the mechanical properties of concrete such as tensile strength, compressive strength, ductility, stiffness and energy absorption capacity significantly and reduces the workability of concrete.
6. The creep deformation decreases and crack resistance property increases with higher aspect ratio and higher length of fibre.
7. Similarly, irregular, hooked or crimped shaped fibres perform better than regular shaped fibres due to better grip.

8. REFERENCES

1.   Suresh S, Charan MS, Ikkurthi S. Strength and Behaviour of Concrete by Using Natural and Artificial Fibre Combiations. Technology. 2017;8(4):1652-8. https://shorturl.at/cuxOR.A

2.   Afroughsabet V, Biolzi L, Monteiro PJ. The effect of steel and polypropylene fibers on the chloride diffusivity and drying shrinkage of high-strength concrete. Composites Part B: Engineering.   2018;139:84-96. 10.1016/j.compositesb.2017.11.047

3.   Mardani-Aghabaglou A, Özen S, Altun MG. Durability performance and dimensional stability of polypropylene fiber reinforced concrete. Journal of Green Building. 2018;13(2):20-41. 10.3992/1943-4618.13.2.20

4.   Mishra A, Chandraul K, Singh MK. Experimental study on steel fiber reinforced concrete. International Research Journal of Engineering   and   Technology.   2017;4(11):895-8. https://shorturl.at/lzBIW

5.   Bhaskar R, Nallanthel M, Teja K. A review on polypropylene fiber reinforced self-compacting concrete. International Journal of Pure and Applied Mathematics. 2018;119(17):2751-62. https://shorturl.at/nADP6

6.   Krishna NK, Prasanth M, Gowtham R, Karthic S, Mini K. Enhancement of properties of concrete using natural fibers. Materials   Today: Proceedings.   2018;5(11):23816-23. 10.1016/j.matpr.2018.10.173

7. Qin Y, Wu H, Zheng Y, Wang W, Yi Z. Microscopic texture of polypropylene fiber-reinforced concrete with X-ray computed tomography. Advances in Civil Engineering. 2019;2019:1-9. 10.1155/2019/2386590

8. Liu J, Jia Y, Wang J. Experimental study on mechanical and durability properties of glass and polypropylene fiber reinforced concrete. Fibers and Polymers. 2019;20:1900-8. 10.1007/s12221-019-1028-9

9. Li Y, Zhang Y, Yang E-H, Tan KH. Effects of geometry and fraction of polypropylene fibers on permeability of ultra-high performance concrete after heat exposure. Cement and Concrete Research. 2019;116:168-78. 10.1016/j.cemconres.2018.11.009

10. Liu X, Wu T, Yang X, Wei H. Properties of self-compacting lightweight concrete reinforced with steel and polypropylene fibers. Construction and Building Materials. 2019;226:388-98. 10.1016/j.conbuildmat.2019.07.306

11. Shen D, Liu X, Zeng X, Zhao X, Jiang G. Effect of polypropylene plastic fibers length on cracking resistance of high performance concrete at early age. Construction and Building Materials. 2020;244:117874. 10.1016/j.conbuildmat.2019.117874

12. Elkatatny S, Gajbhiye R, Ahmed A, Mahmoud AA. Enhancing the cement quality using polypropylene fiber. Journal of Petroleum Exploration and Production Technology. 2020;10:1097-107. 10.1007/s13202-019-00804-4

13. Wang C, Guo Z, Niu D. Influence of the fiber volume content on the durability-related properties of polypropylene-fiber-reinforced concrete. Sustainability. 2020;12(2):549. 10.3390/su12020549

14. Jia E, Mou H, Liu Z, Wang J, Zeng L, Yang X, et al. Surface hydrophilic modification of polypropylene fibers and their application in fiber-reinforced cement-based materials. Journal of Macromolecular Science, Part B. 2020;60(4):286-98. 10.1080/00222348.2020.1846953

15. Yang J, Wang R, Zhang Y. Influence of dually mixing with latex powder and polypropylene fiber on toughness and shrinkage performance of overlay repair mortar. Construction and Building Materials. 2020;261:120521. 10.1016/j.conbuildmat.2020.120521

16. Bentegri I, Boukendakdji O, Kadri E, Ngo T, Soualhi H. Rheological and tribological behaviors of polypropylene fiber reinforced concrete. Construction and Building Materials. 2020;261:119962. 10.1016/j.conbuildmat.2020.119962

17. Raj B, Sathyan D, Madhavan MK, Raj A. Mechanical and durability properties of hybrid fiber reinforced foam concrete. Construction and Building Materials. 2020;245:118373. 10.1016/j.conbuildmat.2020.118373

18. Blazy J, Blazy R. Polypropylene fiber reinforced concrete and its application in creating architectural forms of public spaces. Case Studies in Construction Materials. 2021;14:e00549. 10.1016/j.cscm.2021.e00549

19. Liu Y, Wang L, Cao K, Sun L. Review on the durability of polypropylene fibre-reinforced concrete. Advances in Civil Engineering. 2021;2021:1-13. 10.1155/2021/6652077

20. Madhavi K, Harshith V, Gangadhar M, Kumar VC, Raghavendra T. External strengthening of concrete with natural and synthetic fiber composites. Materials Today: Proceedings. 2021;38:2803-9. 10.1016/j.matpr.2020.08.737

21. Islam A, Shuvo AK, Chowdhury SA, Sharmin S, Hasan M. A comparative study on the properties of natural, synthetic and steel fibre reinforced concrete. Journal of Civil Engineering and Construction. 2021;10(4):216-24. 10.32732/jcec.2021.10.4.216

22. More FMDS, Subramanian SS. Impact of fibres on the mechanical and durable behaviour of fibre-reinforced concrete. Buildings. 2022;12(9):1436. 10.3390/buildings12091436

23. Amir A, Rahman A, Opirina L, Idris F. Performance Flexural of RC Beams Without Concrete at Tension Cross-section. Civil Engineering Journal. 2022;8(11):2560-72. 10.28991/CEJ-2022-08-11-014

24. Ahmad J, Majdi A, Al-Fakih A, Deifalla AF, Althoey F, El Ouni MH, et al. Mechanical and durability performance of coconut fiber reinforced concrete: a state-of-the-art review. Materials. 2022;15(10):3601. 10.3390/ma15103601

25. Effiong JU, Ede AN. Experimental Investigation on the Strengthening of Reinforced Concrete Beams Using Externally Bonded and Near-Surface Mounted Natural Fibre Reinforced Polymer Composites—A Review. Materials. 2022;15(17):5848. 10.3390/ma15175848

26. Mohammed AH, Mubarak HM, Hussein AK, Abulghafour TZ, Nassani DE. Punching Shear Characterization of Steel Fiber-Reinforced Concrete Flat Slabs. HighTech and Innovation Journal. 2022;3(4):483-90. 10.28991/HIJ-2022-03-04-08

27. Ahmeti M, Kryeziu D, Ramadani M. Effect of Steel Fibers on the Mechanical Strength of Concrete. Civil Engineering Journal. 2022;8(9):1890-905. 10.28991/CEJ-2022-08-09-010

28. Bajpai PK, Singh I, Madaan J. Development and characterization of PLA-based green composites: A review. Journal of Thermoplastic Composite Materials. 2014;27(1):52-81. 10.1177/0892705712439571

29. Ghobarah A, Abou-Elfath H, Biddah A. Response-based damage assessment of structures. Earthquake engineering & structural dynamics. 1999;28(1):79-104. 10.1002/(SICI)1096-9845(199901)28:1%3C79::AID-EQE805%3E3.0.CO;2-J

30. Park Y-J, Ang AH-S, Wen YK. Seismic damage analysis of reinforced concrete buildings. Journal of Structural Engineering. 1985;111(4):740-57. 10.1061/(ASCE)0733-9445(1985)111:4(740)

31. Hait P, Sil A, Choudhury S. Overview of damage assessment of structures. Current Science. 2019;117(1):64-70. 10.18520/cs/v117/i1/64-70

32. Hait P, Sil A, Choudhury S. Quantification of damage to RC structures: A comprehensive review. Disaster Adv. 2018;11(12):41-59. https://shorturl.at/yG245

33. Hait P, Mitra R, Farsangi EN, editors. Experimental investigations of resilient hybrid fiber reinforced SCC beam-column subassemblies under cyclic loadings. Structures; 2022: Elsevier. 10.1016/j.istruc.2022.05.026

34. Hait P, Sil A, Choudhury S. Modified Damage Assessment Method for Reinforced Concrete Buildings. Practice Periodical on Structural Design and Construction. 2021;26(4):04021039. 10.1061/(ASCE)SC.1943-5576.0000605

35. Hait P, Sil A, Choudhury S. Damage assessment of reinforced concrete buildings considering irregularities (research note). International Journal of Engineering, Transactions A: Basics 2019;32(10):1388-94. 10.5829/ije.2019.32.10a.08

36. El Yassari S, El Ghoulbzouri A. Numerical simulation of fiber-reinforced concrete under cyclic loading using extended finite element method and concrete damaged plasticity. International Journal of Engineering, Transactions A: Basics. 2023;36(10):1815-26. 10.5829/ije.2023.36.10a.08

37. Jabbar AM, Mohammed DH, Hasan QA. A numerical study to investigate shear behavior of high-strength concrete beams externally retrofitted with carbon fiber reinforced polymer sheets. International Journal of Engineering, Transactions B: Applications. 2023;36(11):2112-23. 10.5829/ije.2023.36.11b.15

38. Altalib F, Tavakoli H, Hashemi S. The Post-fire Behavior of Lightweight Structural Concrete is Improved by Nano-SiO2 and Steel Fibers. International Journal of Engineering, Transactions B: Applications. 2023;36(11):1942-60. 10.5829/ije.2023.36.11b.01

Persian Abstract

چکیده

بتن مسلح با الیاف (FRC) در چند دهه اخیر در صنعت ساختمان سازی رایج شده است. الیاف طبیعی و مصنوعی مختلفی به بتن اضافه می شود تا با ایجاد پیوند بین الیاف و بتن، خاصیت مقاومت در برابر ترک را افزایش دهد. FRC نه تنها عملکرد بهتری نسبت به بتن معمولی دارد، بلکه بتن مسلح با الیاف (FRC)نیز در چند دهه اخیر در صنعت ساختمان سازی رایج شده است. FRC نه تنها عملکرد بهتری نسبت به بتن معمولی دارد بلکه باعث کاهش آلودگی محیط زیست نیز می شود. در واقع در بسیاری از مناطق روستایی، مردم نگران آلودگی و بهداشت نیستند. بخش استفاده نشده از الیاف نیشکر، فیبر موز، فیبر جوت در حوضچه/دریاچه ریخته می شود. پس از چند روز تجزیه شده و پوسیده می شوند که باعث آلودگی آب و اختلال در اکوسیستم می شود. الیاف را می توان به عنوان افزودنی در بتن برای افزایش عملکرد کلی آنها و همچنین کاهش آلودگی محیط زیست استفاده کرد. در این مقاله، یک بررسی پیشرفته در مورد FRC و مزایای مختلف آن بررسی شده است. الیاف مختلفی مانند الیاف جوت، الیاف نارگیل، پلی پروپیلن، بازالت، برگ آرکا، شیشه، ماسک، پلاستیک، کربن و الیاف فولادی توسط چندین محقق در دهه‌های گذشته در بتن گنجانده شده‌اند که در این مقاله به تفصیل مورد اشاره قرار گرفته‌اند. عملکرد از نظر الگوی هیسترتیک جابجایی بار، سختی، شکل پذیری، اتلاف انرژی، مقاومت در برابر ترک، دوام و کارایی FRC ارزیابی شده است. مزیت و محدودیت های FRC نیز مورد بحث قرار گرفته است. از ادبیات موجود، مشخص شده است که عملکرد FRC تحت بار دینامیکی، ارزیابی خسارت، ارزیابی آسیب وابسته به زمان، اثر الیاف در بتن با عملکرد بالا (HPFRC)و ارزیابی چرخه حیات به عنوان شکاف اصلی ادبیات یافت می‌شوند که نیاز به برآورده شود. یک مطالعه موردی در مورد ارزیابی آسیب FRC نیز در این مقاله انجام شده است. از نتایج مشخص شد که بتن مسلح با الیاف کربن (CFRC)، بتن مسلح با الیاف فولادی (SFRC) و بتن مسلح با الیاف غلاف برگ Areca (ALSFRC) در مقایسه با بتن معمولی بدون الیاف آسیب کمتری را تجربه می‌کنند. بر اساس ادبیات موجود، دامنه آینده و جهت احتمالی تحقیق FRC نیز برجسته شده است.

International Journal of Engineering

J o u r n a l H o m e p a g e : w w w . i j e . i r

Effect of Crushing Process Parameters on Quality of Fly Ash Aggregates Produced After Crushing High Strength Fly Ash Blocks: A Laboratory Investigation

S. Singh*, S. Patel

Department of Civil Engineering, S. V. National Institute of Technology, Surat, Gujarat, India

P A P E R I N F O	*A B S T R A C T*
	The demand for aggregates for civil engineering construction is high in the market. The broad adoption of fly ash for producing fly ash aggregate is the best sustainable solution to fulfill aggregate demand and utilization of unused fly ash. Crushing is an essential step for producing angular-shaped aggregate. In this paper, an experimental study using a laboratory-scaled impact crusher was carried out to investigate the effect of crushing process parameters (feed block size, crusher speed and outlet sieve size) on the quality (particle size distribution, flakiness-elongation index and mechanical properties) of angular-shaped fly ash aggregates produced after crushing high-strength fly ash blocks. Particle size distribution and flakiness-elongation index were found to be changed with crushing parameters. Higher crushing speed resulted in small-size fly ash aggregates. Better particle size distribution of crushed fly ash aggregate was produced using a 60 mm outlet sieve compared to a 30 mm one. Well-graded fly ash aggregates with good particle shape (less flaky and less elongated) for the subbase layer of the road were obtained after crushing fly ash blocks of one-third feed size in a laboratory-scaled impact crusher at a crushing speed of 527 rpm and an outlet sieve of 60 mm. Mechanical properties (impact, crushing and abrasion values) of the fly ash aggregate were not much affected by crushing process parameters. The findings of this study will help in optimizing the crushing operation of the industrial impact crusher to produce high-quality angular-shaped fly ash aggregate on a large scale. *doi: 10.5829/ije.2024.37.03c.08*

Graphical Abstract
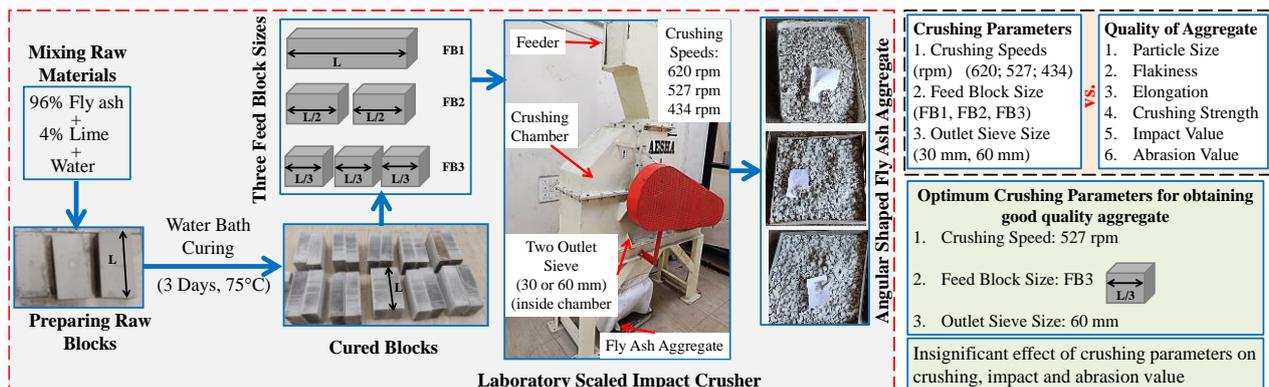
1. INTRODUCTION

Aggregate is the primary material required for making roads. India has the second biggest road network globally, covering more than 5.6 million kilometers (1). The road ministry had planned to build 12000 km of roadways in 2022. One of the biggest challenges in this field is fulfilling the demand for road aggregates, which

Corresponding Author Email: ssinghcivil11@gmail.com (S. Singh)

results in the consumption of natural rocks. Continuous consumption of natural rocks adversely affects the environment (2). Extraction of rocks from the earth causes habitat destruction, soil erosion, water pollution, air pollution, greenhouse gas emissions and land disturbance.

Conversely, the massive generation of fly ash by thermal power plants has caused many problems, including a lack of disposal areas and threats to public health and the environment (3). In 2020, 7575 million tons of coal ash was produced globally (4). In 2020–2021, India produced 232 million tons of fly ash with a utilization rate of 92.4% (5). There is still a gap between the production and utilization of fly ash. Due to the presence of significant amounts of silica and alumina in fly ash, it is quite useful for producing construction materials (6). The Indian government promotes the use of fly ash in the production of building materials and construction activities. The above data shows that a surplus amount of fly ash is available and has a broad scope for civil engineering applications.

Worldwide aggregates market value was $507.46 billion in 2021 and will likely be $837.3 billion by 2030 (7). Governments and industry stakeholders typically engage in strategic planning, resource management and infrastructure development to mitigate the adverse effects of a shortage in stone aggregates. Implementing policies and investing in sustainable practices may mitigate the negative impacts of rock consumption and unutilized fly ash. These may include reducing rock consumption through recycling and exploring alternative materials (i.e., waste composites) with a lesser environmental footprint (8, 9). The broad adoption of fly ash for producing fly ash aggregates as pavement material will prevent the rapid depletion of natural resources and the destruction of valuable land due to fly ash dumps (10, 11). Pelletization and compaction are the two primary agglomeration techniques used to combine fly ash particles into larger shapes. In the method of pelletization, agglomerated fly ash granules are formed using centrifugal forces, while in the compaction method, agglomerated fly ash blocks are formed using compacting forces (12). Sintering, autoclaving and cold bonding are the three most common methods for hardening agglomerated fly ash granules or blocks. The pelletization-sintering process is complicated as it requires high energy and more time to produce fly ash aggregates. Furthermore, pelletized aggregates are round in shape, leading to low interlocking and load-bearing capacity. These drawbacks limit the production and utilization of pelletized-sintered aggregates in the construction industry.

Shahane and Patel (13) developed angular-shaped fly ash aggregate using compaction and cold-bonding processes to overcome the problems related to pelletized aggregate, which is simple and requires less energy and time. Fly ash blocks were prepared using a fly ash-binder mix. These blocks were cured in a hot water bath. Then, cured high-strength fly ash blocks (HSFB) were crushed manually to produce angular-shaped fly ash aggregate. It was concluded that the developed aggregate is angular in shape and also fulfills the requirement of the Ministry of Road Transport and Highways (MoRTH), India, for its application in pavement construction.

Stone aggregates are produced by crushing rocks in crushers. The most common types of crushers in use are ball mills, jaw crushers, and gyratory crushers. Impact crushers are the most recent type of crusher in use. They are widely used because of their superiority in reducing particle size (14). Generally, rocks are crushed in two or more steps in a heavy crusher to obtain stone aggregates. Single crushing stages and jaw crushers are generally used for producing coarse aggregates for unbound applications, whereas two or more crushing stages and other crushers are used for producing aggregates for bound applications like concrete or asphalt. A heavy crusher with a multi-crushing stage requires more energy, space and time. Local aggregates are produced using portable crushing and screening machines, which require a simple setup due to cost and space constraints. Räisänen and Mertamo (15) produced good-shaped aggregates using a laboratory crusher. Eloranta (16) investigated the crushing operation and found that the feed gradation and crusher stroke are the most important properties for producing aggregates with good particle shape. The operating parameters of the crusher significantly impact the final shape of the aggregate (17). Particle shape in cone crusher output is influenced by crusher setting, feed size and crusher speed. The flakiness index rises with increasing feed size and decreasing crusher speed (18). It was concluded that larger aggregates are generally better in shape.

Literature proves that producing angular-shaped fly ash aggregate has several advantages over pelletized-sintered fly ash aggregate and can potentially replace natural aggregates in the subbase layer of roads. Bulk production of good-quality angular-shaped fly ash aggregate is highly needed to meet market demand for aggregate. Several studies have focused on producing good-quality stone aggregates from rocks after optimizing the crushing operations. Also, previous research has focused on the mix proportions, hardening process and enhancement of angular-shaped fly ash aggregate properties. Crushing of high-strength fly ash blocks (HSFB) in a crusher is required for the bulk production of these aggregates. The effect of the crushing process parameters on the quality of crushed fly ash aggregates is unknown. None of the presented research had focused on fly ash aggregates after crushing high-strength fly ash blocks in an impact crusher.

The aim of the current study was to produce high-quality angular-shaped fly ash aggregate after crushing

HSFB in a laboratory-scale impact crusher in a single crushing stage. The gradation, flakiness, elongation and mechanical properties of aggregate were used to assess the quality of fly ash aggregates. Feed block size, crusher speed and outlet sieve size were used as the operating crusher parameters. This paper presents the effect of crusher parameters on the gradation, flakiness, elongation and mechanical properties of fly ash aggregate. The findings of the present study will help in optimizing the crushing operation of an industrial impact crusher to generate high-quality angular-shaped fly ash aggregate on a large scale.

2. MATERIALS

The fly ash was procured from Reliance Industries Limited, Surat. The specific gravity of 2.01 was found for the present fly ash. This study used hydrated lime with 68.4% CaO as a binder. The chemical composition of fly ash is presented in Figure 1. Based on CaO content, the fly ash was classified as Class F, as per ASTM C-618 (19). The fly ash had a CaO content of 10.6% and 75.7% of combined silica, alumina and iron. Fly ash and lime percentages adopted were percentage by weight. A 91.2% of fly ash particles were found to be less than 0.075 mm IS sieve size. This shows that most of the fly ash particles were less than 0.075 mm. Using a modified proctor test (20), optimum moisture content (OMC) of 26.9% and 27.1% and maximum dry unit weight of 13.83 kN/m^3 & 13.87 kN/m^3 were found for only fly ash (100F) & 96% fly ash + 4% lime (96F+4L), respectively.

The mix proportion, pressing force and water bath curing technique were adopted following Shahane and Patel (13). Identical blocks were prepared by homogeneously mixing 96% fly ash, 4% lime, and 27.1% (=OMC) water. Blocks of size 200mm×100 mm×60mm with dry unit weight (= maximum dry unit weight determined using modified proctor test) were prepared after pressing the wet mix in a brick pressing machine. Raw blocks were cured at 75°C for 3 days and then cured high-strength fly ash blocks (HSFB) were crushed

in an impact crusher after 24 hours to obtain angular-shaped fly ash aggregate. The compressive strength of HSFB was in the range of 22 MPa to 24 MPa. Before being fed to the crusher, HSFB of 200mm×100mm×60mm (Full size: FB1), 100mm×100mm×60mm (Half size: FB2) and 67mm×100mm×60mm (One-third size: FB3) sizes were prepared. Small sizes (FB2 and FB3) of blocks were prepared by breaking FB1. The average weight of one HSFB (FB1) was found to be about 2.1 kg.

3. METHODOLOGY

Figure 2 shows the process flow sheet followed for studying the effects of crusher parameters on aggregate quality in the laboratory. FB1, FB2 and FB3 were used as feed material sizes. Samples of FB1, FB2 and FB3 were dropped into the feeder separately. As the crusher was switched on, blocks were fed continuously to the feeder and immediately impacted by the moving hammers inside the crusher. Each crushing trial was carried out with a feed weight of 42±2 kg in the feeder and at three different crushing speeds (620 rpm, 527 rpm and 434 rpm). Circular-shaped outlet sieve (30 mm or 60 mm) was provided at the lower side of the crusher to prevent oversized crushed aggregates from passing through. A summary of the different parameters used for the study is shown in Table 1.

The percentage of material recovered and crushing capacity for the impact crusher were also calculated using Equations 1 and 2, respectively. The crushing capacity is defined as the mass of material in kg/h.

$$Material\ recovered\ (\%) = \frac{Material\ mass\ output}{Material\ mass\ input} \quad (1)$$

$$Crushing\ capacity = \frac{Average\ mass\ after\ crushing}{Average\ time\ taken\ to\ crush} \quad (2)$$

Figure 1. Chemical composition of fly ash
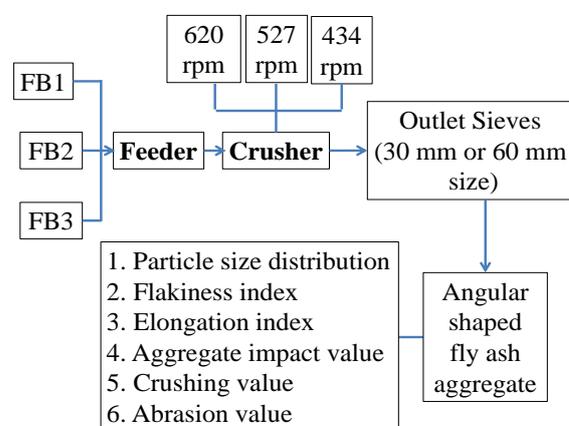
Figure 2. Process flow sheet for studying the effect of crusher parameters in the laboratory

TABLE 1. Combinations of different crusher parameters

Trial No.	Feed size	Number of blocks	Feed weight (kg)	Crusher speed (rpm)	Outlet sieve size (mm)
		20	42.5	620	
T1	FB1	20	42.3	527	30
		20	42.7	434	
		20	42.5	620	
T2	FB1	20	42.8	527	60
		20	42.7	434	
T3	FB2	40	42.1	527	60

**TABLE 2.** Grading requirement for Granular Sub-base (GSB) materials (21)

IS Sieve size (mm)	Percentage by weight passing the IS sieve (Grading I)
75	100
53	80-100
26.5	55-90
9.5	35-65
4.75	25-55
2.36	20-40
0.85	-
0.425	10-15
0.075	<5

Sieve analysis of obtained fly ash aggregates was carried out in dry conditions. The sieve sizes mentioned in MoRTH [21] for the granular sub-base (GSB) layer were used. Three samples were tested for each study of sieving and an average of three was reported. Table 2 summarises the sieves used for particle size distribution. Flakiness and elongation index were investigated for each trial to study the effect of crusher parameters on the shape and size of fly ash aggregates. The tests were conducted as per IS 2386-Part 1 (22).

Aggregates should have sufficient toughness, strength and hardness to resist their disintegration due to upcoming impact load, gradually applied compressive load and surface wear caused by friction, respectively. Mechanical properties such as aggregate impact value, crushing value and Los Angeles abrasion value were determined as per IS 2386-Part 4 (23). Each test was performed thrice for each sample. The aggregate impact and crushing value were determined for aggregates of size 10-12.5 mm. During the crushing test, the load in the compression testing machine was applied at the rate of 4 tons per minute until it reached a maximum load of 40

tonnes. Then, the crushed sample was passed through a 2.36 mm IS sieve. The grade A aggregate (40 mm to 10 mm in size) was used in the Los Angeles abrasion test.

4. RESULTS AND DISCUSSION

4. 1. Effect of Crusher Speed and Outlet Sieve Size on the Particle Size Distribution   In T1 and T2 trials, the samples with feed size FB1 were crushed at three different speeds (434 rpm, 527 rpm and 620 rpm) for two different outlet sieve sizes. Figure 3 shows the effect of three crusher speeds on particle size distribution for 30 mm and 60 mm outlet sieve sizes. A higher percentage finer for both outlet sieves can be observed for higher crushing speeds. Reducing crushing speed produces a coarser product (24). Higher crushing speeds can lead to more frequent and intense particle collisions within the crushing chamber. These particle-to-particle interactions can cause more breakage and fragmentation, resulting in higher finer particles. The particle size distribution curve shifted towards well gradation when the crushing speed was reduced. These results are consistent with the previous study carried out by Fladvad and Onnela (24) for crushing stones. The reduction in the percentage finer for all particle sizes was observed when the size of the outlet sieve was increased from 30 mm to 60 mm. In trial T1, 85.30%, 90.30% and 94.20% of particles lesser than 26.5 mm and 31.90%, 44.48% and 52.37% lesser than 4.75 mm particle size can be observed for crushing speed of 434 rpm, 527 rpm and 620 rpm, respectively. In trial T2, 74.5%, 84.1% and 88.5% of particles lesser than 26.5 mm and 24.1%, 35.2 % and 49.1% lesser than 4.75 mm particle size can be observed for crushing speed of 434 rpm, 527 rpm and 620 rpm, respectively.

It can be seen in Figure 3 that particle size distribution is not within the limits specified in MoRTH (21) for the GSB layer, as some of the particle sizes are either on the
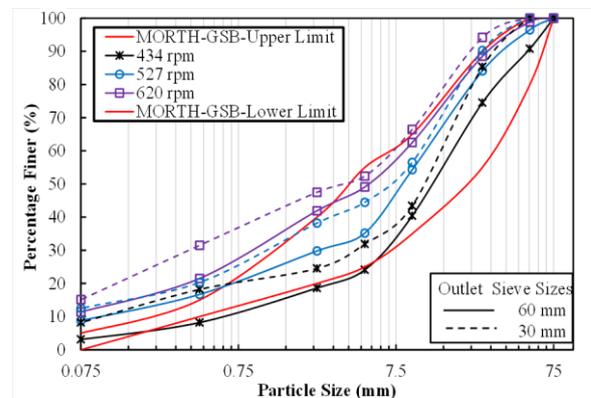
Figure 3. Effect of crusher speed and outlet sieve size on the particle size distribution

higher or lower side of the limits. In Figure 3, the percentage finer for the 30 mm outlet sieve size, corresponding to 4.75 mm particle size, was found to be higher than that of the 60 mm outlet sieve size. When a 30 mm outlet sieve was used, multiple crushing of larger particles (>30 mm) led to the production of smaller particles as smaller particles (<30 mm) were only allowed to pass through 30 mm. However, when the outlet sieve size is set to 60 mm, the impact crusher may produce particles that are, on average, slightly larger. A particle size greater than 53 mm was also obtained in the 60 mm outlet sieve. It can be seen in Figure 3 that the particle size distribution of 527 rpm crushing speed and 60 mm outlet sieve is better than that of other crusher speeds and outlet sieve sizes. In order to improve the particle size distribution, the feed block size was varied for further investigation while maintaining a crusher speed of 527 rpm and an outlet sieve size of 60 mm.

4. 2. Effect of Feed Block Size on the Particle Size Distribution
Figure 4 shows the effect of feed block size on particle size distribution for a 60 mm outlet sieve at 527 rpm crushing speed. On reducing the feed block size, improvement in particle size distribution can be seen in Figure 4. When the feed block size is larger, there is a higher chance of producing oversized particles that cannot pass through the outlet sieve of the crusher. These oversize particles may circulate within the crusher, undergoing multiple impact cycles, which can produce more finer particles. 64.8%, 67.8% and 71.8% aggregates were found to be retained on a 4.75 mm sieve for a crushing speed of 527 rpm and feed block size of FB1, FB2 and FB3, respectively. The production of oversized particles is minimized by reducing the feed block size. This leads to an improvement in particle size distribution. Particle size distribution for a feed block size of FB3 is within the limits specified in MoRTH (21) for the GSB layer.
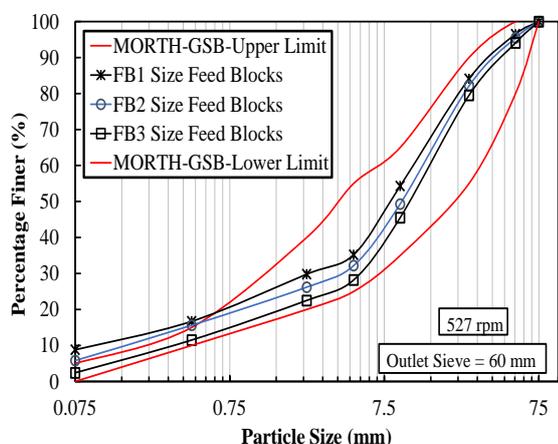
Figure 4. Effect of feed block size on the particle size distribution

4. 3. Effect of Crusher Speed and Feed Block Size on the Flakiness-elongation Index
The effect of crusher speed on flakiness and elongation index was also studied after crushing FB1, FB2 and FB3 sizes HSFB and using an outlet sieve of 60 mm. The variation of flakiness and elongation index with the change in crusher speed and feed block size can be seen in Figures 5 and 6, respectively.

The maximum flakiness index of 6.6%, 5.9%, 5.8% for FB1 size feed block; 5.9%, 5.4%, 5.5% for FB2 size feed block and 5.4%, 4.8%, 5.5% for FB3 size feed block were found corresponding to the size range of 10-6.3 mm for crushing speed of 434 rpm, 527 rpm and 620 rpm, respectively. The maximum elongation index of 4.9%, 4.2%, 4.1% for FB1 size feed block; 4.2%, 3.5%, 3.5% for FB2 size feed block and 3.6%, 3.2%, 3.1% for FB3 size feed block were found corresponding to the size
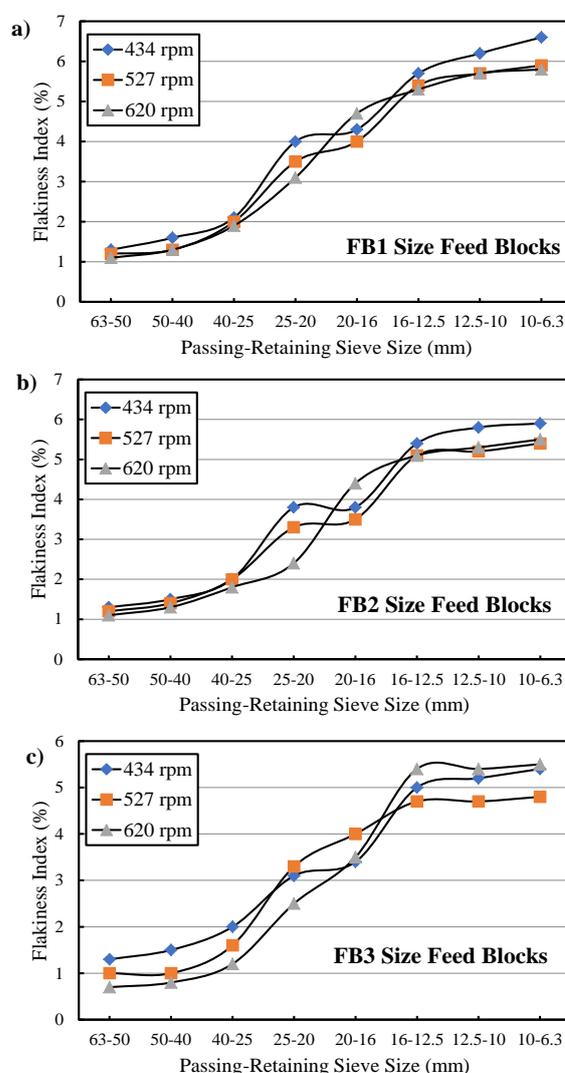

Figure 5. Effect of crusher speed and feed block size on the flakiness index
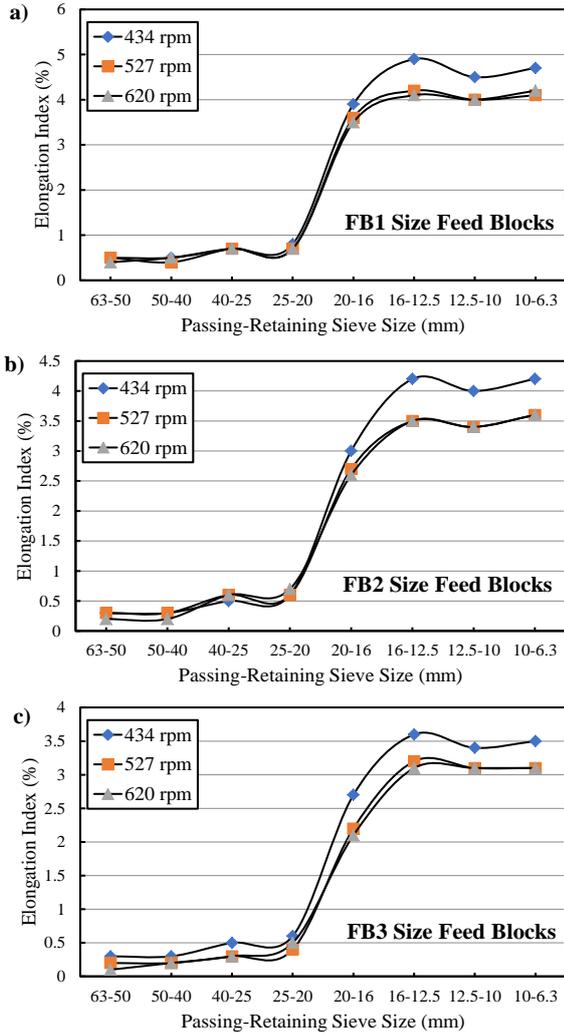
Figure 6. Effect of crusher speed and feed block size on the elongation index

range of 16-12.5 mm for crushing speed of 434 rpm, 527 rpm and 620 rpm, respectively. The flakiness and elongation indices were found to be lower for larger particles and higher for decreased particle size. Similar results were reported by Fladvad and Onnela (24) for crushing stones in a jaw crusher. Larger particles tend to travel through the crusher more quickly due to their higher weight and are less likely to experience multiple impacts. This results in lower elongation and flakiness. Smaller particles may undergo more collisions and impacts, leading to higher flakiness.

Lower flakiness and elongation indices were found for crushing speeds of 434 rpm and 527 rpm compared to 620 rpm. Lower crushing speed allows the material to spend more time inside the crusher, increasing the chances of re-crushing already crushed particles. This re-crushing process can flatten and elongate the particles, increasing their flakiness and elongation index.

Reduction in flakiness and elongation index with smaller feed block size can be observed in Figures 5 and 6, respectively. Fladvad and Onnela (24) also reported that coarser feed material in a jaw crusher results in more flaky crushing stones. Less elongated or flaky particles were likely to form because smaller size HSFB were more quickly and effectively broken down into smaller particles. When the feed block size is smaller, it allows for more efficient and uniform impact forces to be applied to the material. This results in a greater likelihood of fracturing the HSFB along its natural boundaries, leading to reduced flakiness and elongation.

The variation of combined flakiness and elongation index (FI+EI) with the change in crusher speed for different feed block sizes is also presented in Figure 7. The FI+EI was found to be highest for 434 rpm crushing speed. FI+EI for crushing speeds of 620 and 527 rpm are almost the same. Reduction in FI+EI with lower feed
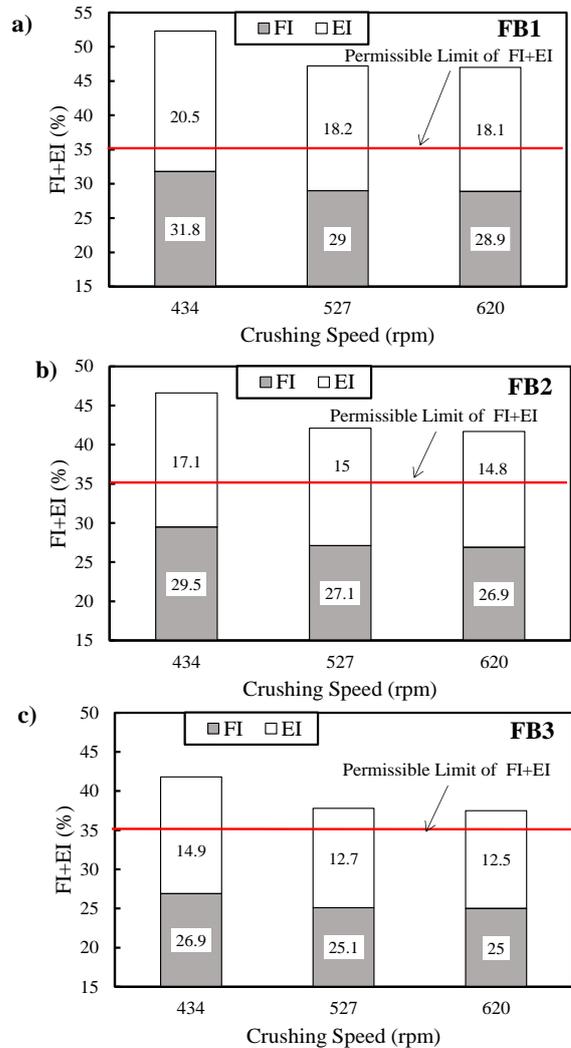
Figure 7. Comparison of combined flakiness-elongation index for different crusher speeds and feed block sizes

block size can also be observed in Figure 7. FI+EI of 47.2%, 42.1% and 37.8% were found after crushing FB1, FB2 and FB3 sizes at a speed of 527 rpm for aggregates of 6.3 to 63 mm. The FI+EI was found to be near the permissible limit of 35% as per MoRTH (21) after crushing FB3 size HSFB at 527 rpm.

Based on the above results of particle size distribution and flakiness-elongation index, well-graded fly ash aggregates with good particle shape (less flaky and less elongated) were produced after crushing FB3 size HSFB in impact crusher at a speed of 527 rpm and outlet sieve of 60 mm.

4. 4. Mechanical Properties

Mechanical properties of angular fly ash aggregate obtained after crushing FB3 size HSFB at different speeds using an outlet sieve of 60 mm are presented in Table 3. It was found that there is not much variation in the mechanical properties of aggregates with crusher parameters. The mechanical properties of a material mainly depend on its intrinsic composition and structure; in this case, FB1, FB2 and FB3 had the same composition and structure except for the size. Ranges of 24.2-25.1%, 27.4-28.3% and 35.3-36.5% were found for impact, crushing and abrasion values at different crushing speeds. Values are within the permissible limit of MoRTH (21) for the GSB layer and IS 9142 (Part 2) for lightweight aggregate.

4. 5. Crushing Capacity

Table 4 shows the crushing time and material mass recovery results for different crusher parameters. It was found that the impact crusher used in the present study takes a minimum time of 5.3 minutes to crush the HSFB, with a 98.81% recovery rate for FB3 feed size, 527 rpm speed and 60 mm outlet sieve size. On average, 41.61 kg of aggregate was collected after crushing 42.40 kg bricks in 5.6 minutes. Only about 1.87% is lost on average during the crushing operation.

This loss may be due to the formation of dust during crushing and aggregates retained inside the crusher. Crushing capacity in the range of 373.1 to 498.0 kg/h was achieved for the present impact crusher.

TABLE 3. Mechanical properties of angular fly ash aggregate for different speeds

Properties	620 rpm	527 rpm	434 rpm	MoRTH (21)	IS 9142-Part 2
Impact value (%)	25.1	24.5	24.2	≤40 for sub-base ≤30% for base	≤40
Crushing value (%)	28.3	28.0	27.4	-	≤45
Abrasion value (%)	36.5	36.1	35.3	≤40 for base	≤40

TABLE 4. Crushing time and material mass recovery

Crusher speed (rpm)	Feed size	HSFB Mass (kg)	Outlet Screening size	Time Taken (min)	Mass of aggregates (kg)	Material recovered (%)
620	FB1	42.50	30	5.5	41.03	96.54
527	FB1	42.30	30	6.0	41.31	97.66
434	FB1	42.70	30	6.8	42.28	99.02
527	FB1	42.80	60	5.5	42.06	98.27
527	FB2	42.10	60	5.3	41.45	98.46
527	FB3	42.00	60	5.0	41.50	98.81

5. CONCLUSIONS

The present study leads to the following conclusions:

- Higher crushing speeds in the impact crusher resulted in a higher percentage of small-size fly ash aggregates. This may be due to increased impact forces between crushing surfaces and materials with speed. A crushing speed of 527 rpm in a laboratory-scaled impact crusher was found suitable for obtaining quality fly ash aggregate.
- The particle size distribution of produced fly ash aggregate was observed better with a 60 mm size outlet sieve than with a 30 mm one. The percentage of small-size fly ash aggregate was obtained higher in the output of a 30 mm size outlet sieve, resulting in poor particle size distribution.
- On varying crusher parameters, insignificant changes in the mechanical properties of the produced fly ash aggregate were found because mechanical properties mainly depend on the composition and structure of the material. In the present study, all feed blocks used for producing fly ash aggregates had the same composition and structure.

Based on the investigation, well-graded fly ash aggregates with good particle shape (less flaky and less elongated) for the subbase layer of the road were produced after crushing HSFB of one-third size (feed size) in a laboratory-scaled impact crusher at a crushing speed of 527 rpm and an outlet sieve of 60 mm. The findings of the present study are helpful for optimizing single-stage crushing in terms of impact crusher operation and fly ash aggregate quality on a large scale. The study was performed for a laboratory-scaled impact crusher. The results may differ for different types of crusher. Future studies using different crushers in the field or laboratory may be carried out for producing high-quality fly ash aggregate.

6. REFERENCES

1. Bakare M, Pai R, Patel S, Shahu J. Environmental sustainability by bulk utilization of fly ash and GBFS as road subbase materials. Journal of Hazardous, Toxic, and Radioactive Waste. 2019;23(4):04019011.   https://doi.org/10.1061/(asce)hz.2153-5515.00004502

2. Turkane S, Chouksey S. Partial replacement of conventional material with stabilized soil in flexible pavement design. International Journal of Engineering, Transactions B: Applications.   2022;35(5):908-16. https://doi.org/10.5829/ije.2022.35.05b.07

3. Patel S, Shahu J. Comparative study of slags stabilized with fly ash and dolime for utilization in base course. Journal of Materials in   Civil   Engineering.   2017;29(10):04017168. https://doi.org/10.1061/(asce)mt.1943-5533.0002017

4. Widodo S, Alfirahma R, Prawiranegara A, Amir MF, Dewi A. Development of Eco-friendly Self-compacting Concrete Using Fly Ash and Waste Polyethylene Terephthalate Bottle Fiber. Civil Engineering   Journal.   2023;9(2):437-52. https://doi.org/10.28991/CEJ-2023-09-02-014

5. Bakare M, Shahu J, Patel S. Complete substitution of natural aggregates with industrial wastes in road subbase: A field study. Resources, Conservation and Recycling. 2023;190:106856. https://doi.org/10.1016/j.resconrec.2022.106856

6. Rangan PR, Tumpu M, Mansyur M, Mabui D. Assessment of Fly Ash-Rice Straw Ash-Laterite Soil Based Geopolymer Mortar Durability. Civil Engineering Journal. 2023;9(06):1456-70. https://doi.org/10.28991/CEJ-2023-09-06-012

7. Singh S, Patel S. Development of angular-shaped lightweight coarse aggregate with low calcium fly ash using autoclave curing-Experimental and microstructural study. Journal of Building Engineering.   2023;79:107860. https://doi.org/10.1016/j.jobe.2023.107860

8. Al-Hindawi LAA, Al-Dahawi AM, Sh J Al-Zuheriy A. Use of Waste Materials for Sustainable Development of Rigid Pavement. International Journal of Engineering, Transactions A: Basics,. 2023;36(10):1919-31.
    https://doi.org/10.5829/ije.2023.36.10a.16

9. Nistratov AV, Klimenko NN, Pustynnikov IV, Vu LK. Thermal regeneration and reuse of carbon and glass fibers from waste composites.   Emerg   Sci   J.   2022;6:967-84. https://doi.org/10.28991/ESJ-2022-06-05-04

10. Singh S, Patel S. Potential Use of Fly Ash for Developing Angular-shaped Aggregate. International Journal of Engineering, Transactions   C: Aspects.   2023;36(6):1114-20. https://doi.org/10.5829/ije.2023.36.06c.09

11. Joshi AR, Patel S. Application of Class C Fly Ash and Quarry Dust Mix for Utilization as Subbase Material in Flexible Pavement. International Journal of Engineering, Transactions C: Aspects.   2023;36(9):1597-604. https://doi.org/10.5829/ije.2023.36.09c.02

12. Bijen J. Manufacturing processes of artificial lightweight aggregates from fly ash. International Journal of Cement Composites and Lightweight Concrete. 1986;8(3):191-9. https://doi.org/10.1016/0262-5075(86)90040-0

13. Shahane HA, Patel S. Influence of curing method on characteristics of environment-friendly angular shaped cold bonded fly ash aggregates. Journal of Building Engineering. 2021;35:101997. https://doi.org/10.1016/j.jobe.2020.101997

14. Terefe TO, Tefera GA. Design of impact stone crusher machine. Int J Sci Eng Res. 2019;10:904-9.

15. Räisänen M, Mertamo M. An evaluation of the procedure and results of laboratory crushing in quality assessment of rock aggregate raw materials. Bulletin of engineering geology and the environment. 2004;63:33-9. https://doi.org/10.1007/s10064-003-0218-1

16. Eloranta J. Influence of crushing process variables on the product quality of crushed rock: Tampere University of Technology; 1995.

17. Briggs C, Evertsson CM. Shape potential of rock. Minerals Engineering. 1998;11(2):125-32. https://doi.org/10.1016/S0892-6875(97)00145-3

18. Bengtsson M, Evertsson CM. An empirical model for predicting flakiness in cone crushing. International Journal of Mineral Processing.   2006;79(1):49-60. https://doi.org/10.1016/j.minpro.2005.12.002

19. Concrete ACC-o, Aggregates C. Standard specification for coal fly ash and raw or calcined natural pozzolan for use in concrete: ASTM international; 2013.

20. Standard I. Determination of water content-dry density relation using heavy compaction. 1983.

21. Transport IMoR, Highways, editors. Specifications for road and bridge works2013: Indian Roads Congress.

22. IS. Methods of test for aggregates for concrete. Indian Standard, Bureau of Indian Standards New Delhi, India; 1963.

23. BIS. IS 2386 (Part 4): Methods of test for aggregates for concrete–mechanical properties. BIS New Delhi, India; 1963.

24. Fladvad M, Onnela T. Influence of jaw crusher parameters on the quality of primary crushed aggregates. Minerals Engineering. 2020;151:106338.
    https://doi.org/10.1016/j.mineng.2020.106338

Persian Abstract

چکیده

تقاضا برای مصالح ساختمانی مهندسی عمران در بازار زیاد است. استفاده گسترده از خاکستر بادی برای تولید خاکستر بادی بهترین راه حل پایدار برای برآوردن تقاضای کل و استفاده از خاکستر بادی استفاده نشده است. خرد کردن یک مرحله ضروری برای تولید سنگدانه های زاویه ای است. در این مقاله، یک مطالعه تجربی با استفاده از یک سنگ شکن ضربه ای در مقیاس آزمایشگاهی به منظور بررسی تاثیر پارامترهای فرآیند خرد کردن (اندازه بلوک خوراک، سرعت سنگ شکن و اندازه غربال خروجی) بر کیفیت (توزیع اندازه ذرات، شاخص پوسته پوسته شدن–طولانی و) انجام شد. خواص مکانیکی سنگدانه های خاکستر بادی زاویه ای شکل که پس از خرد کردن بلوک های خاکستر بادی با استحکام بالا تولید می شوند. توزیع اندازه ذرات و شاخص پوسته پوسته شدن با پارامترهای خرد کردن تغییر یافتند. سرعت خرد شدن بیشتر منجر به ایجاد دانه های خاکستر بادی با اندازه کوچک شد. توزیع اندازه ذرات بهتر دانه های خاکستر بادی خرد شده با استفاده از الک خروجی ۶۰ میلی متر در مقایسه با ۳۰ میلی متر تولید شد. سنگدانه های خاکستر بادی خوب با شکل ذرات خوب (کمتر پوسته پوسته شدن و کمتر کشیده) برای لایه زیرپایه جاده پس از خرد کردن بلوک های خاکستر بادی با اندازه خوراک یک سوم در یک سنگ شکن ضربه ای مقیاس آزمایشگاهی با سرعت خرد کردن ۵۲۷ به دست آمد. دور در دقیقه و غربال خروجی ۶۰ میلی متر. خواص مکانیکی (مقادیر ضربه، خرد شدن و سایش) دانه‌های خاکستر بادی تحت تأثیر پارامترهای فرآیند خرد کردن قرار نگرفت. یافته های این مطالعه به بهینه سازی عملیات خرد کردن سنگ شکن ضربه ای صنعتی برای تولید سنگدانه های خاکستر بادی زاویه ای شکل با کیفیت بالا در مقیاس بزرگ کمک می کند.

International Journal of Engineering

Gate Oxide Thickness and Drain Current Variation of Dual Gate Tunnel Field Effect Transistor

S. Howldar, B. Balaji*, K. Srinivasa Rao

Department of Electronics and Communication Engineering, Koneru Lakshmaiah Education Foundation, Green Fields, Vaddeswaram, Andhra Pradesh, India

A B S T R A C T

Two-dimensional analytical modelling of Dual Material Gate Tunnel Field Effect Transistor with change in variation of gate oxide thickness (DMG-UOX-TFET) is proposed in this work. This proposed device employs dielectric materials such as hafnium oxide and silicon dioxide, with distinct oxide thicknesses. This device was invented using a technology-aided computer design tool in 10 nm (0.01 µm) technology. This work investigates the impact of gate oxide thickness on the electrical characteristics of the proposed device, with a particular focus on drain current variation. The extensive simulations and key performance parameters of the proposed device were analyzed regarding gate oxide thickness. The various gate oxide thicknesses and their effects on the device subthreshold slope, On- current, Off- current, and on-off-current ratio were analyzed. The proposed device incorporates n-type operations within the gate overlap region, effectively mitigating the corner effect and the detrimental band-to-band tunneling that can degrade the on/off ratio. Through careful optimization of the doping concentration in the gate overlap region, achieved a remarkable ~4.8 time enhancement in the on-current, while simultaneously reducing the average subthreshold swing from 91.3 mV/dec to 52.8 mV/dec.

doi: 10.5829/ije.2024.37.03c.09

Graphical Abstract
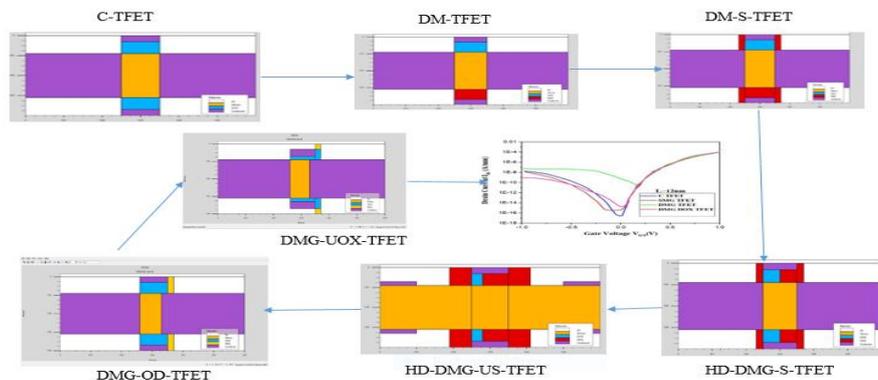
NOMENCLATURE

N_d	Doping concentration	W_f	Gate work function
t_{si}	Thickness of silicon dioxide	*The*	Thickness of low k material
T_{hk}	Thickness of high k material	V_{gs}	Gate to source voltage
I_{on}	On state current (A/µm)	t_{ox}	Oxide thickness (nm)

*Corresponding Author Email: vahividi@gmail.com (B. Balaji)

1. INTRODUCTION

The Metal Oxide Semiconductor Field Effect Transistor (MOSFET), stands as one of the foundational building blocks of modern electronics. Since its invention in the 1960s, the MOSFET has played a pivotal role in revolutionizing the semiconductor industry and enabling the advanced research and rapid speed of technology growing. This versatile and highly adaptable transistor has become the cornerstone of integrated circuits, powering everything essential to have circuits with nanooptimized scaling area for circuit analysis and to operate with the high frequency processing speed concerning low power consumption (1). At its core, the MOSFET is a solid-state electronic device that controls the flow of electrical current through a semiconductor channel via an electric field generated by a gate electrode. Its unique operation is based on the principle characteristics of field-effect modulation, distinct from the bipolar junction transistor (BJT) and which relies on control the on current (2). This fundamental difference gives the MOSFET several advantages, including lower power consumption, fast switching speeds, and scalability for integration into densely packed semiconductor chips (3).

The heart of the MOSFET is its gate terminal, separated from the semiconductor channel by a thin insulating layer typically made of silicon dioxide (SiO_2). By applying a voltage to the gate, the MOSFET can either allow or block the flow of current between its sources and drain terminals (4). This voltage-controlled behavior makes it an ideal choice for digital logic and analog signal processing applications.The MOSFET structure has three terminals gate, source, and drain; which are in nm. The source is the terminal from which the current enters the device, while the drain is where it exits. The gate terminal controls the flow of current between the source and the drain (5).

The CMOS technology is a widely used implementation of MOSFETs. CMOS circuits consume minimal power when idle and are commonly found in digital logic and microprocessor designs. Over the years, MOSFETs have scaled down in size, following Moore's Law, which states that the number of transistors and size on a chip doubles approximately every two years. Smaller transistors allow for higher packing densities and improved performance. MOSFETs find applications in a vast array of electronic devices, including computers, smartphones, power amplifiers, voltage regulators, and more in low power. They are essential components in digital integrated circuits, leading to the miniaturization and increased efficiency of electronic systems (6).

The structure of Tunnel Field Effect Transistor (TFET) is an advanced semiconductor device in the industry that has gained significant attention in recent years for its potential performanc to overcome some of the limitations of traditional MOSFET over the semiconductor industry. TFETs operate on a fundamentally different principle, leveraging quantum mechanical tunneling effects to control the flow of charge through a semiconductor intrinsic channel (7). This unique operation makes them promising devices for various applications, including low-power electronics and high-frequency analog circuits. TFETs are continuous rely on the quantum tunneling phenomenon where charge carriers can pass through a thin insulating barrier even when they do not possess enough energy to overcome the barrier in classical physics. In TFETs, this tunneling occurs between the source and drain terminals through a thin channel region. One of the most significant advantages of TFETs is their ability to achieve subthreshold slopes much steeper than those of traditional MOSFETs (8). This results in extremely low leakage currents when the TFET is in the off-state, making them highly energy-efficient devices.

The TFETs are particularly well suited for low-power applications because they can operate at lower supply voltages and exhibit reduced off-state leakage current. This property makes them attractive for use in battery-powered devices and energy-efficient integrated circuits (9). The performance of TFETs is highly dependent on the choice of semiconductor materials and their bandgap characteristics. Materials with narrow bandgaps are often preferred for TFETs to enhance tunneling effects and improve device performance. TFETs have the potential to impact a wide range of applications, including digital logic circuits, low-power processors, radio-frequency amplifiers, and analog circuits (10). They are especially promising for Internet of Things devices, where energy efficiency is critical. Despite their promise, TFETs face challenges such as low on-state current, fabrication complexity, and sensitivity to process variations. Researchers are actively working to address these issues and unlock their full potential (11).

The Single Gate TFET (SG-TFET), is an emerging semiconductor device that has attracted considerable attention in recent years for its potential to address some of the energy efficiency and performance challenges faced by conventional transistors (12, 13). It is a type of TFET that operates based on quantum mechanical tunneling phenomena, offering a steep subthreshold slope and reduced power consumption. The SG-TFET has exploit quantum tunneling, a quantum mechanical phenomenon where charge carriers can pass through an energy barrier that they classically should not be able to overcome (14). This property allows SG-TFET to exhibit subthreshold slopes well below the fundamental limit of traditional transistors. SG-TFET are controlled by a single-gate electrode, just like traditional MOSFETs (15). This simplicity in control makes the TFET more compatible with existing semiconductor manufacturing processes. One of the most significant advantages of SG-

TFET is their ultra-low subthreshold leakage current. This property makes them highly energy-efficient, particularly in applications where the device spends a significant portion of its operation in standby mode and semiconductor materials play a critical role in SG-TFET performance (16, 17). Narrow bandgap materials are often preferred as they facilitate the quantum tunneling effect.SG- TFETs offer remarkable advantages in terms of subthreshold slope and power efficiency, there are challenges to overcome, such as achieving high on-state current and ensuring device reliability (18).

The Dual Material Gate Tunnel Field-Effect Transistor (DMG-TFET) is a cutting-edge semiconductor device that has gained prominence in recent years for its potential to push the boundaries of energy efficiency and performance in the field of electronics. DMG-TFETs represent an evolution of the traditional TFET by employing a unique dual-material gate structure that enhances their electrostatic analysis control over the semiconductor channel. The most distinctive feature of DMG-TFETs is their gate structure, which combines two different materials in the gate stack (19). Each material is chosen for its unique properties and compatibility with the device's operation. This dual-gate design allows for precise control of the electric field within the transistor channel (20).

The proposed device offers several potential improvements over the traditional TFET design being better control over the tunneling barrier between the source and the channel. This increased control can potentially reduce leakage currents and improve the overall performance of the transistor. The sub-threshold Swing is a key parameter indicating how efficiently a transistor can switch between on and off states. Dual gates can potentially reduce the sub-threshold swing in DG-TFETs compared to SG-TFET, leading to improved energy efficiency and it becomes possible to independently control the threshold voltages of the two gates.

2. DEVICE STRUCTURE AND SIMULATION PARAMETERS

Figure 1 shows a two dimensional cross-sectional view of proposed DMG-UOX-TFET device in 10nm. In this illustration, L1 and L2 represent the channel length and tunneling gate, respectively, while tsi, tox, and thk denote the thickness of silicon, oxide, and high-k dielectric layers in the device, respectively. The relevant device simulated parameters are presented in Table 1. This gate-engineered hetero-junction structure incorporates SiO_2 as the source material and silicon in both the channel and drain regions, thereby creating a hetero-junction within the tunneling region. Two distinct gate materials are employed with work functions, denoted as ϕ M1 and ϕ
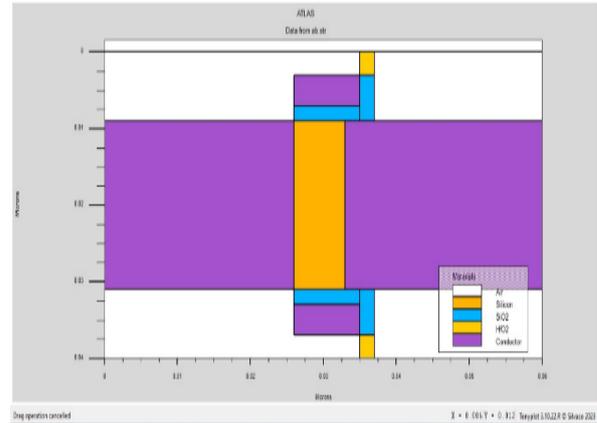
Figure 1. Proposed DMG-UOX-TFET device with differential gate oxide thickness of 1.5nm and 2nm

TABLE 1. Utilized Parameter for the simulation

Utilized Parameters	Proposed device
Thickness of SiO_2	2nm
Thickness of HfO_2	3nm
Metal Gate-1 Work Function (W_F)	4.8eV
Metal Gate-2 Work Function (W_F)	4.2eV
Device Length (W_L)	60 nm
Gate Length (L_G)	10 nm
Source Length (L_S)	25nm
Drain Length (L_D)	25nm
Channel Length (L_C)	10nm
Doping of Source (N_S)	1×10^{20} cm^{-3}
Doping of Drain (N_D)	1×10^{18} cm^{-3}
Doping of Channel (N_C)	1×10^{17} cm^{-3}

M2, set at 4.2eV and 4.8eV, respectively in the device, for the tunneling region, control region, and auxiliary region. The operation of this proposed device relies on the gate bias voltage. In the case of an n-type DMG TFET, achieving the ON state depends on increasing the positive voltage applied to the gate. This action narrows the energy barrier between the SiO_2 source and the intrinsic region. Consequently, the energy band diagram within the intrinsic region are pushed down, facilitating the tunneling of electrons from the valence band of the p-doped silicon source to the conduction band within the intrinsic SiO_2 body, a process known as band-to-band (BTB) tunneling. Subsequently, these electrons move toward the n-doped drain region through drift diffusion (21).

The structure of proposed device implemented using reduced nano dimensions has been simulated in ON and OFF state and correspondingly mesh structure, electric

field distribution, and potential distributions employed using Silvaco TCAD ATLAS tool shown in Figures 2, 3 and 4, respectively. In literature, some models have suggested using a channel length of less than 100 nm to mitigate short-channel effects in electronic devices (22). To comprehensively consider all effects in the nanoscale range, and employed the BTBT model within the ATLAS simulator due to its superior convergence properties. In this work, silicon was chosen as the source and channel material, and the gate dielectric was utilized as SiO_2 and hafnium oxide (HfO_2). The source doping level is set to $Ns = 5 \times 10^{18} cm^{-3}$, and the drain doping level was $Nd = 5 \times 10^{19} cm^{-3}$ and assessed the performance of the proposed device using Silvaco TCAD numerical simulator (23).

The advantages of the proposed devices are enhanced control over tunneling, improved electrostatic control, optimized threshold voltages, potential reduction in drain-induced barrier lowering, and improved current ON/OFF ratio. The disadvantages of this device are the complex fabrication process and increased design complexity.
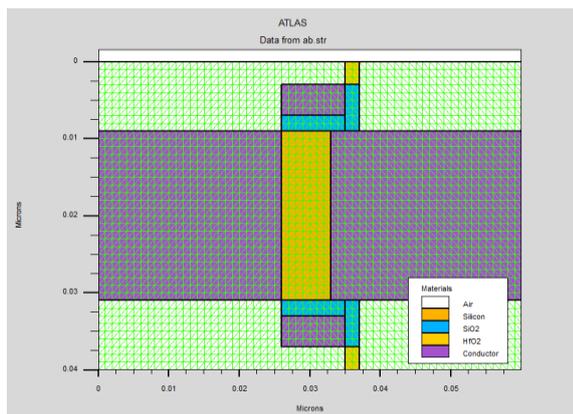
Figure 2. Mesh structure with differential gate oxide hickness of 1.5nm and 2nm
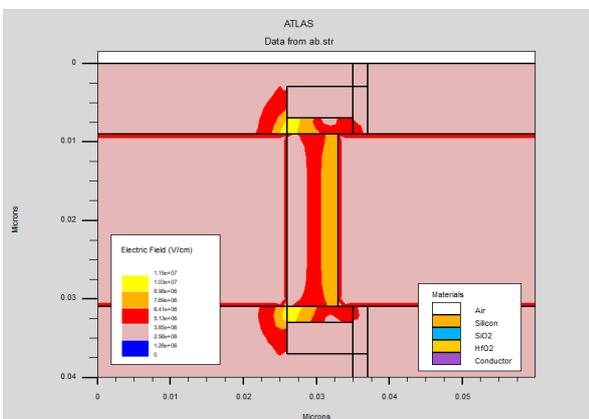

Figure 3. Electric field distribution with differential gate oxide hickness of 1.5nm and 2nm
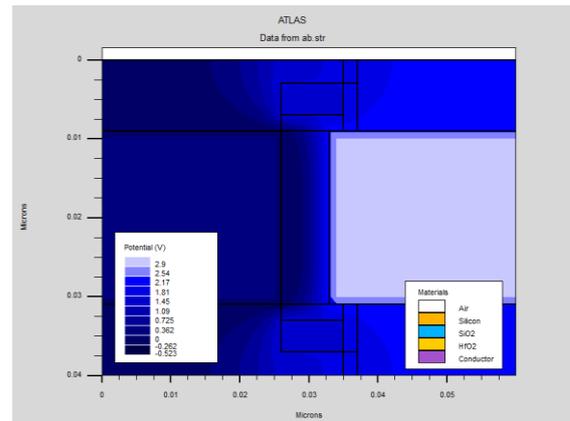
Figure 4. Potential distribution with differential gate oxide hickness of 1.5nm and 2nm

The proposed device controls the current over the two gates. This dual-gate architecture offers enhanced flexibility in tuning device characteristics and allows for precise control over the gate oxide thickness. This control can contribute to optimized tunneling band to band barrier characteristics, potentially reducing leakage currents and improving overall device performance. The DG-TFET provides improved electrostatic control over the intrinsic channel, offering the potential for reduced subthreshold swing and enhanced carrier concentration.

3. RESULTS AND DISCUSSION

3. 1. Drain current Characteristics   The peak drain current for both the conventional device and the proposed structure is achieved under zero gate voltage conditions while operating in depletion mode. This is evident in the case of proposed devices in a 10nm technology, as shown in Figure 5. The graph illustrates a substantial increase in drain current as the gate oxide thickness overlaps with a constant gate voltage (VG=0) (24). In the TFET, it is imperative to deplete the upper region of the intrinsic channel through gate channel bias. Consequently, the carriers near the bottom of the channel experience a lateral movement, resulting in the flow of drain current. Consequently, the improved drain current predominantly flows in the lower region of the channel (25, 26). Consequently, the proposed device exhibits several advantages, including maximum velocity, the highest electron density, an effective channel depth, and optimal drain current flow in the channel. The drain current characteristics of the proposed dielectric material structure, maintain fixed device dimensions within a 32nm technology and a channel length (Lg) of 10nm. This configuration outperforms the conventional device, as evidenced by the simulation results. The drain current experiences a significant boost as device dimensions are minimized, along with a reduction in channel length.
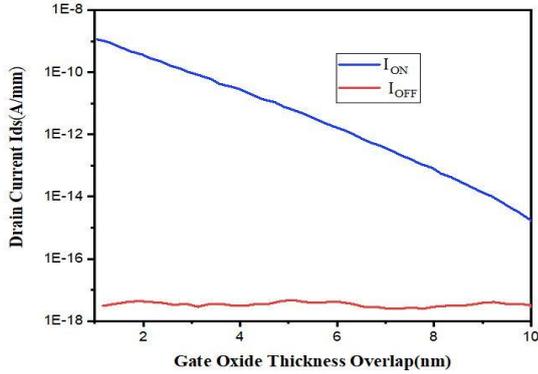
Figure 5. Drain current with gate oxide thickness overlap of the proposed device at 12 nanometer

**Figure 6.** Drain current with gate oxide thickness overlap of the proposed device at 10 nanometer

The drain current is derived by analyzing the drain voltage while varying the gate oxide material. It is crucial to achieve an enhanced drain current. The saturated drain current (Ids) is determined by varying the gate voltage (Vgs) using different materials for the gate oxide. As the device dimensions and channel length decrease, there is a significant increase in drain current. The maximum drain current for the proposed device is attained at Vg=0.6V and Vg=2V. The increase in drain current is associated with a rise in drain voltage, facilitating the movement of electrons within the channel.

Figure 6 illustrates the relationship between Drain current and gate oxide thickness for the proposed device at a fixed Vds of 2V. When the separation between the drain and the channel is substantial, the gate primarily exercises control over channel carriers. This advanced structure exhibits the potential for enhancing drain current while maintaining a balance in the nano scale device performance (27). As depicted in the figure, an incremental increase in drain current corresponds to a decrease in off current. This behavior is attributed to the electric field crowding effect, which is more pronounced near the gate close to the drain. Consequently, there is a higher concentration of electric field compared to conventional devices. The proposed high-k structure intensifies this electric field concentration compared to the electric field distribution in Silicon Carbide (28, 29). In the drift region, the HfO_2 material necessitates a higher electric field for breakdown, resulting in the occurrence of a high electric field at elevated drain voltages (Vd). Applying a higher drain voltage in this proposed structure leads to an increased breakdown voltage within the SiO_2 structure in 10nm technology. Consequently, the electric field diminishes at the interface between the channel and the drain (30).

The on-state current and off-state current of the proposed device at various doping concentrations, gate lengths are shown in Table 2 and gate lengths of 12 nanometers and 10 nanometers node regime are tabulated

and compared with conventional TFET, SG- TFET and double gates are shown in Tables 3, 4, 5 and 6.

3. 2. Drain Current with Gate Oxide Thickness

Figure 7 illustrates the drain current characteristics of the proposed structures developed in the context of 10nm technological innovations. These structures exhibit a reduced electric field concentration on the drain side. Notably, in the 10nm technology setting, the newly devised device demonstrates a higher peak electric field distribution. Consequently, an improved breakdown voltage is achieved by mitigating the electric field around the gate (G) and drain (D) regions. The simulation of the proposed TFET involves the use of three different materials. The performance analysis reveals that the HfO_2 material outperforms the other materials, yielding more favorable performance parameters. The utilization of HfO_2 material leads to an increase in drain current, indicating its superior suitability for the device. Therefore, the proposed device lies in its application for low-power applications (31).

3. 2. Drain Current Comparison at 10nm Node

Figure 8 shows the drain current (Id) as a function of gate voltage (Vg) while varying the oxide thickness (Tox) in a TFET. The proposed device dimensions and material properties, except for the oxide thickness. The oxide thicknesses range from 2 nm to 5 nm, with increments of

TABLE 2. On current and off current at different doping concentrations

Doping Concentration $N_D(cm^{-3})$	Ion (A/μm)	Ioff (A/μm)	Ion/ Ioff
1X10^18	$1.14e^{-09}$	$3.09407e^{-18}$	368332465.5
5X10^18	$1.192e^{-06}$	$4.00396e^{-18}$	$2.97749e^{+11}$
1X10^19	$1.173e^{-05}$	$1.44904e^{-12}$	8093753.993

TABLE 3. On current and off current at Nd= 1×10^{18} cm^{-3} at gate length of 12 nano meter

Device	Ion (A/µm)	Ioff (A/µm)	Ion/ Ioff
C TFET	1.20529	1.94599e^{-17}	1.05495e^{+13}
SMG TFET	1.22274	1.15327e^{-10}	1931345.624
DMG TFET	1.1575	6.64446e^{-12}	23703910.57
DMG DOX TFET	0.17263	2.59633e^{-14}	6649056142

TABLE 4. On current and off current at Nd= 1×10^{18} cm^{-3} at gate length of 10 nano meter

Device	Ion (A/µm)	Ioff (A/µm)	Ion/ Ioff
C TFET	1.22271	2.36543e^{-16}	9.41521e^{11}
SMG TFET	1.174301	2.42382e^{-11}	7191177.358
DMG TFET	1.204597	3.69445e^{-10}	553796.2365
DMG DOX TFET	1.148494	1.68717e^{-13}	880136435.3

TABLE 5. On current and off current at Nd= 5×10^{18} cm^{-3} at gate length of 12 nano meter

| Device	Ion (A/µm)	Ioff (A/µm)	Ion/ Ioff
C TFET	1.114425	7.12968e^{-12}	16049074.76
SMG TFET	1.106412	8.31917e^{-12}	12791162.02
DMG TFET	1.114425	3.98511e^{-09}	28713.09448
DMG DOX TFET	9.80641e^{-05}	2.79177e^{-13}	351261053.9

**TABLE 6.** On current and off current at Nd= 5×10^{18} cm^{-3} at gate length of 10 nano meter

Device	Ion (A/µm)	Ioff (A/µm)	Ion/ Ioff
C TFET	1.355803	2.93691e^{-08}	12114.90464
SMG TFET	1.505557	1.59643e^{-08}	31667.9536
DMG TFET	1.10405	5.92953e^{-08}	1754.769188
DMG DOX TFET	1.250409	8.75488e^{-10}	286022.3694

1 nm. The TFET with a thinner oxide exhibited a lower sub-threshold voltage (Vth), which implies that it can turn on at lower gate voltage. The drain current increased more rapidly with gate voltage for TFETs with thinner oxides, indicating improved on-current performance (32). The sub-threshold slope, representing the steepness of the Id-Vg curve, was smaller for thinner oxide TFETs for better-switching characteristics. In a single-gate TFET, increasing the gate voltage typically increases the drain current, as it controls the tunneling of electrons or holes through the tunnel junction. However, this effect is usually nonlinear due to the unique band structure of TFETs shown in Figure 9. The oxide thickness can influence the TFET's performance by affecting the tunneling probability and the sub-threshold slope. A
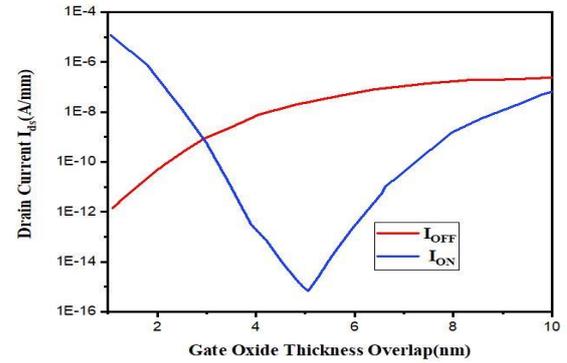
Figure 7. Drain current with gate oxide thickness overlap of the proposed device with Nd= 5×10^{18} cm^{-3} at gate length of 10 nanometer
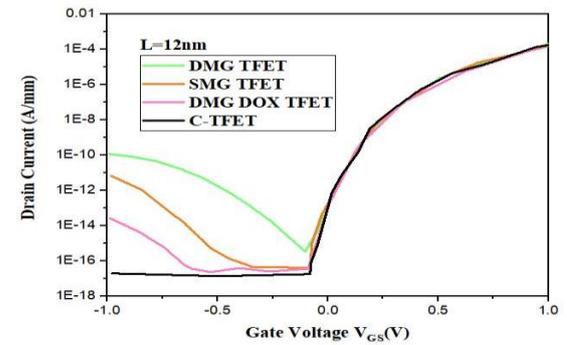
Figure 8. Drain current with gate voltage of various structures at 12 nanometer node

thinner oxide layer generally results in better tunneling and lower sub-threshold slope, leading to higher drain currents. In dual gate TFETs, there are two gate voltages Vg1 and Vg2. Vg1 controls the tunneling barrier and impacts the drain current similarly to a SG-TFET. Vg2 often called the modulation gate, allows for additional control over the tunneling and can further enhance the drain current. A thinner oxide layer still tends to improve performance, but the dual gate TFET will provide more opportunities for control and optimization. Oxide thickness indirectly affects the TFET performance by influencing the gate voltage needed to achieve a certain drain current. Thinner oxide layers generally require lower gate voltages to control tunneling effectively. Lower oxide thickness tends to result in better TFET performance, with lower sub-threshold slopes and higher drain currents as shown in Figure 10.

The proposed device exhibits a drain conductance related to 6H-SiC and SiO$_2$ dielectric materials. This superiority in drain conductance contributes to the device achieving the highest packing density, attributed to the enhanced current flow within the device. Consequently, this structural advantage of the proposed device results in a notable improvement and improved characteristics of
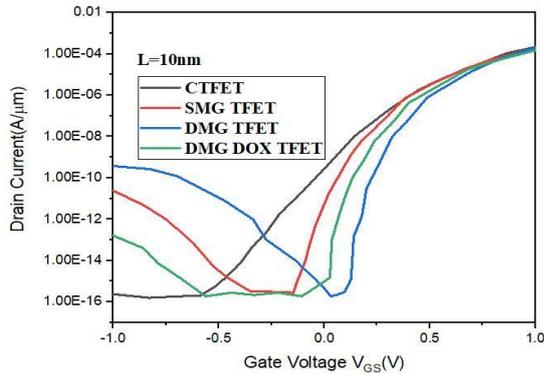
Figure 9. Drain current with gate voltage of various structures at 10 nanometer node
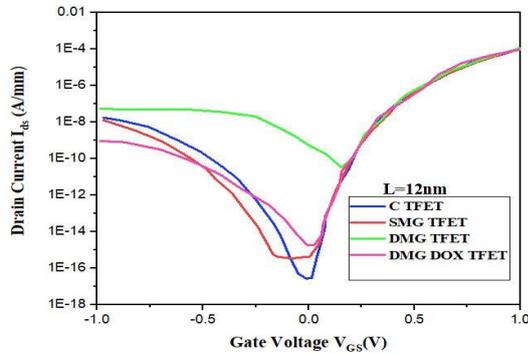
Figure 10. Drain current with gate voltage of various structures at 12 nanometer node at a different doping concentration

transconductance. A high transconductance is imperative for achieving proper device gain. However, the reduction in subthreshold slope, while desirable, leads to increased off-current and power dissipation within the device.

4. CONCLUSION

The performance analysis of DMG-UOX-TFET with variation of oxide materials is analysed using TCAD ATLAS simulator in 10nm node . This device features a hetero-junction formed by combining silicon materials and hafnium oxide in the drain-channel junction. Additionally, it utilizes a hetero-dielectric gate stack comprising SiO_2 and HfO_2 where HfO_2 holds substantial promise as a semiconductor material for high-voltage and high-frequency applications, including cosmic cells and energy devices. The proposed structure, designed for 10nm innovations and employing Silvaco TCAD, exhibits notable enhancements in electrical properties such as On current (Ion), Off current (Ioff), Ion/Ioff ratio, as well as RF properties like drain conductance (Gd) and

On resistance (Ron). Therefore, this proposed structure is well suited for low-power applications.

5. REFERENCES

1. Howldar S, Balaji B, Srinivasa Rao K. Design and Analysis of Hetero Dielectric Dual Material Gate Underlap Spacer Tunnel Field Effect Transistor. International Journal of Engineering, Transactions C: Aspects. 2023;36(12):2137-44. 10.5829/ije.2023.36.12c.01

2. Venkatesh M, Suguna M, Balamurugan N. Influence of germanium source dual halo dual dielectric triple material surrounding gate tunnel FET for improved analog/RF performance. Silicon. 2020;12:2869-77. http://link.springer.com/article/10.1007/s12633-020-00385-6

3. Raju V, Sivasankaran K. Performance analysis of double gate Junctionless tunnel field effect transistor: RF stability perspective. International Journal of Advanced Computer Science and Applications. 2019;10(11). https://doi.org/10.1456/IJACSA.2019.010117

4. Madan J, Pandey R, Sharma R, Chaujar R. Impact of metal silicide source electrode on polarity gate induced source in junctionless TFET. Applied Physics A. 2019;125(9):600. https://doi.org/10.1007/s00339-019-2900-6

5. Musalgaonkar G, Sahay S, Saxena RS, Kumar MJ. A line tunneling field-effect transistor based on misaligned core–shell gate architecture in emerging nanotube FETs. IEEE Transactions on Electron Devices. 2019;66(6):2809-16. https://doi.org/10.1109/TED.2019.2910156

6. Zare M, Peyravi F, Hosseini SE. Impact of hetero-dielectric ferroelectric gate stack on analog/RF performance of tunnel FET. Journal of Electronic Materials. 2020;49:5638-46. https://doi.org/10.1007/s11664-020-08315-3

7. Meshkin R. An Extended-Source Tunneling-FET with Gate-Overlapped n+-Doped Pocket. Journal of Electronic Materials. 2023:1-7. https://doi.org/10.1007/s11664-023-10524-5

8. Radhamma E, Vemana Chary D, Krishnamurthy A, Venkatarami Reddy D, Sreenivasa Rao D, Gowthami Y, et al. Performance analysis of high-k dielectric heterojunction high electron mobility transistor for rf applications. International Journal of Engineering, Transactions C: Aspects. 2023;36(9):1652-8. 10.5829/ije.2023.36.09c.09

9. Gowthami Y, Balaji B, Srinivasa Rao K. Performance Analysis and Optimization of Asymmetric Front and Back Pi Gates with Dual Material in Gallium Nitride High Electron Mobility Transistor for Nano Electronics Application. International Journal of Engineering, Transactions A: Basics 2023;36(7):1269-77. 10.5829/ije.2023.36.07a.08

10. Keighobadi D, Mohammadi S, Mohtaram M. Recessed gate cylindrical heterostructure TFET, a device with extremely steep subthreshold swing. Transactions on Electrical and Electronic Materials. 2021:1-7. https://doi.org/10.1007/s42341-021-00321-4

11. Wangkheirakpam VD, Bhowmick B, Pukhrambam PD. Investigation of a dual MOSCAP TFET with improved vertical tunneling and its near-infrared sensing application. Semiconductor Science and Technology. 2020;35(6):065013. https://doi.org/10.1088/1361-6641/ab8172

12. Gowthami Y, Balaji B, Rao KS. Design and performance evaluation of 6nm hemt with silicon sapphire substrate. Silicon. 2022;14(17):11797-804. https://doi.org/10.1007/s12633-022-01900-7

13. Kumar PK, Balaji B, Rao KS. Performance analysis of sub 10 nm regime source halo symmetric and asymmetric nanowire MOSFET with underlap engineering. Silicon. 2022;14(16):10423-36. https://doi.org/10.1007/s12633-022-01747-y

14. Howldar S, Balaji B, Srinivasa Rao K. Design and Qualitative Analysis of Hetero Dielectric Tunnel Field Effect Transistor Device. International Journal of Engineering, Transactions C: Aspects 2023;36(6):1129-35. 10.5829/ije.2023.36.06c.11

15. Anvarifard MK, Orouji AA. Enhancement of a nanoscale novel Esaki tunneling diode source TFET (ETDS-TFET) for low-voltage operations. Silicon. 2019;11(6):2547-56. https://doi.org/10.1007/s12633-018-0043-6

16. Dixit A, Gupta N. A compact model of gate capacitance in ballistic gate-all-around carbon nanotube field effect transistors. International Journal of Engineering, Transactions A: Basics. 2021;34(7):1718-24. 10.5829/IJE.2021.34.07A.16

17. Raj A, Singh S, Priyadarshani KN, Arya R, Naugarhiya A. Vertically Extended Drain Double Gate S i 1− x G ex Source Tunnel FET: Proposal & Investigation For Optimized Device Performance. Silicon. 2021;13:2589-604. https://doi.org/10.1007/s12633-02000603-1

18. Chakrabarty R, Roy S, Pathak T, Kumar Mandal N. Design of Area Efficient Single Bit Comparator Circuit using Quantum dot Cellular Automata and its Digital Logic Gates Realization. International Journal of Engineering, Transactions C: Aspects. 2021;34(12):2672-8. 10.5829/ije.2021.34.12c.13

19. Gopal G, Varma T. Simulation-based analysis of ultra thin-body double gate ferroelectric TFET for an enhanced electric performance. Silicon. 2022;14(12):6553-63. https://doi.org/10.1007/s12633-021-01428-2

20. Roy A, Mitra R, Kundu A, editors. Influence of channel thickness on analog and RF performance enhancement of an underlap DG AlGaN/GaN based MOS-HEMT device. 2019 Devices for Integrated Circuit (DevIC); 2019: IEEE.

21. Gedam A, Acharya B, Mishra GP. Junctionless silicon nanotube TFET for improved DC and radio frequency performance. Silicon. 2021;13:167-78. https://doi.org/10.1007/s12633-020-00410-8

22. Mehrabani AH, Fattah A, Rahimi E. Design and Simulation of a Novel Hetero-junction Bipolar Transistor with Gate-Controlled Current Gain. International Journal of Engineering, Transactions C: Aspects 2023;36(03):433. 10.5829/ije.2023.36.03c.01

23. Rafiee A, Nickabadi S, Nobarian M, Tagimalek H, Khatami H. Experimental investigation joining al 5083 and high-density polyethylen by protrusion friction stir spot welding containing nanoparticles using taguchi method. International Journal of Engineering, Transactions C: Aspects. 2022;35(6):1144-53. 10.5829/ije.2022.35.06c.06

24. Alassery F, Khan AI, Shaik MS. Implementation of Advanced Tunnel Field Effect Transistor (DP-TFET) for High Power Switching Applications. Silicon. 2022;14(15):9589-93. https://doi.org/10.1007/s12633-021-01647-7

25. Sahu SA, Goswami R, Mohapatra S. Characteristic enhancement of hetero dielectric DG TFET using SiGe pocket at source/channel interface: proposal and investigation. Silicon. 2020;12(3):513-20. https://doi.org/10.1007/s12633-019-00159-9

26. Balaji B, Srinivasa Rao K, Girija Sravani K, Bindu Madhav N, Chandrahas K, Jaswanth B. Improved drain current characteristics of hfo2/sio2 dual material dual gate extension on drain side-tfet. Silicon. 2022;14(18):12567-72. https://doi.org/10.1007/s12633-022-01955-6

27. Kumar PK, Balaji B, Rao KS. Halo-Doped Hetero Dielectric Nanowire MOSFET Scaled to the Sub-10 nm Node. Transactions on Electrical and Electronic Materials. 2023:1-11. https://doi.org/10.1007/s42341-023-00448-6

28. Emami N, Kuchaki Rafsanjani M. Extreme learning machine based pattern classifiers for symbolic interval data. International Journal of Engineering, Transactions B: Applications. 2021;34(11):2545-56. 10.5829/IJE.2021.34.11B.17

29. Fouladinia F, Gholami M. Decimal to excess-3 and excess-3 to decimal code converters in QCA nanotechnology. International Journal of Engineering, Transactions C: Aspects. 2023;36(9):1618-25. 10.5829/ije.2023.36.09c.05

30. Gowthami Y, Balaji B, Rao KS. Design and Analysis of a Symmetrical Low-κ Source-Side Spacer Multi-gate Nanowire Device. Journal of Electronic Materials. 2023;52(4):2561-8. https://doi.org/10.1007/s11664-023-10217-z

31. Rani CSH, Bagan KB, Roach RS. Improved drain current characteristics of germanium source triple material double gate hetero-dielectric stacked TFET for low power applications. Silicon. 2021;13:2753-62. https://doi.org/10.1007/s12633-020-00556-5

32. Mehrabani AH, Fattah A, Rahimi E. Design and Simulation of a Novel Hetero-junction Bipolar Transistor with Gate-Controlled Current Gain. International Journal of Engineering, Transactions C: Aspects. 2023;36(03):433. 10.5829/ije.2023.36.03c

---

Persian Abstract

چکیده

مدلسازی تحلیلی دو بعدی ترانزیستور اثر میدانی تونل دروازه دوگانه با تغییر در تغییر ضخامت اکسید گیت (DMG-UOX-TFET) در این کار پیشنهاد شدهاست. این دستگاه پیشنهادی از مواد دی الکتریک مانند اکسید هافنیوم و دی اکسید سیلیکون با ضخامت های اکسید متمایز استفاده می کند. این دستگاه با استفاده از یک ابزار طراحی کامپیوتری به کمک فناوری در فناوری ۱۰ نانومتر (۰.۰۱ میکرومتر) اختراع شد. این کار تاثیر ضخامت اکسید گیت را بر ویژگیهای الکتریکی دستگاه پیشنهادی، با تمرکز ویژه بر تغییرات جریان تخلیه بررسی میکند. شبیهسازیهای گسترده و پارامترهای عملکرد کلیدی دستگاه پیشنهادی با توجه به ضخامت اکسید گیت تحلیل میشوند. ضخامتهای مختلف اکسید گیت و تأثیرات آنها بر شیب آستانه فرعی دستگاه، نسبت جریان روشن، جریان خاموش و نسبت جریان خاموش، تحلیل میشوند. دستگاه پیشنهادی عملیاتهای نوع n را در ناحیه همپوشانی دروازه ترکیب میکند، که به طور موثر اثر گوشه و تونلزنی مضر نوار به باند را کاهش میدهد که میتواند نسبت روشن/خاموش را کاهش دهد. از طریق بهینهسازی دقیق غلظت دوپینگ در ناحیه همپوشانی دروازه، به افزایش قابلتوجه ۴.۸ زمان در جریان پیوسته دست یافت، در حالی که به طور همزمان میانگین نوسان زیرآستانه را از ۹۱.۳ mV/dec به ۵۲۸ mV/dec کاهش داد.

International Journal of Engineering

Journal Homepage: www.ije.ir

Presenting a Model to Detect the Fraud in Banking using Smart Enabling Tools

M. Karbasiyan[1,2], H. Hamidi*[1,2]

[1] Information Technology Group, K. N. Toosi University of Technology, Tehran, Iran
[2] Department of Industrial Engineering, Information Technology Group, K. N. Toosi University of Technology, Tehran, Iran

ABSTRACT

In recent years, with the increase of access to customer data and the improvement of data analysis capabilities through intelligent methods, various activities have been carried out to analyze customer behavior; it is in the detection of bank frauds. Currently, bank frauds have a wide range of results, other than material and financial losses to the bank, customers and banks. After using smart tools to use different algorithms, the two selected algorithms XGBoost and LightGBM, according to the high ROC in the obtained models were selected step by step. At the same time, it has been used in final tests with the reduction of false samples labeled as fraud (FP). This model is developed using real development data and gives very acceptable results in card-to-card fraud detection. This model can significantly improve the security of the banking system and be used as a tool to reduce financial crimes.

doi: 10.5829/ije.2024.37.03c.10

Graphical Abstract

Conclusion: In this research, an advanced method for detecting fraud in transactions was presented. There are two main steps in this method. The XGBoost algorithm is used to identify frauds by entering transaction information after preprocessing. Only the transactions that received the fraud label in the first step are included after filtering the output of this algorithm. To enhance fraud detection accuracy, the filtered information is fed into the LightGBM algorithm in the second step. The accuracy of fraud detection is significantly increased by this step. The results show that by combining XGBoost and LightGBM algorithms with two stages of fraud detection, the speed and accuracy of fraud detection are significantly increased. This method can be used in banking and financial transaction systems that face various types of fraud.

1. INTRODUCTION

Fraud, which is a multi-million-dollar business worldwide, has become a significant problem nowadays.

The development of new technologies has resulted in the creation of new ways to commit fraud. The creation of a new information system, in addition to its advantages and benefits, can create additional opportunities for

*Corresponding Author Email: h_hamidi@kntu.ac.ir (H. Hamidi)

criminals. In addition to detecting fraud and fraud in organizations, fraud detection techniques and intelligence tools aim to predict future behavior and reduce the risk of fraud by understanding user and customer behavior. Banks and financial institutions are striving to speed up the process of identifying fraudsters due to the high costs of fraud (1-3). It is against the law to commit fraud in electronic banking and electronic money transfer. Fraudsters are encouraged and incited to enter this field due to the large volume of monetary and financial transactions and transfers conducted on the Internet and electronic platform (4-6). To provide electronic services, it is crucial and important to recognize the identity of individuals. The purpose of this study was to uncover fraud in the banking system and develop an optimal method for analyzing information from the One of the State banks of Iran using intelligence tools and model evaluation. The focus of this research is to review the latest fraud detection methodologies and tools. The propose of this is to develop the framework for the fraud detection mechanism, as well as the use of the Python language to implement the developed model. In the following, according to the research literature and the background of the research, there is an introduction about the previous studies and different methods of fraud detection, in the next part, the proposed research plan and research methodology, and then the analysis of the information and the research results are given.

2. LITERATURE REVIEW

An introduction to fraud and fraud detection methods is provided in this preliminary section, based on previous studies. The increase in communication technologies and online transactions has led to an increase in financial frauds. One of the most common and dangerous forms of financial fraud is credit card fraud. Machine learning algorithms and neural networks can be used to detect patterns and anomalies related to fraud in mobile banking transactions (7-10). Artificial intelligence-based systems are able to detect and prevent fraud in real time due to the increasing number of financial frauds in the banking industry and the significant financial losses caused to banks and their customers, which is a significant advantage over traditional fraud detection methods. Real-time performance is what all AI-based systems have in common. Using machine learning algorithms and neural networks, these systems are capable of identifying fraudulent patterns and behaviors in mobile banking transactions and taking preventive measures if fraud is detected. Fraud detection systems can model customer behavior patterns based on past transaction history and other factors like location, time, and type of transactions. Then, if anomalous behavior or suspicious transactions are detected, the system activates an alert. To review and verify the transactions, the bank or customer can receive

this alert as a text message or notification (11-15).

The detection and identification of fraudulent activities in credit card transactions can be achieved through the use of machine learning and data mining methods. The importance of this issue is because the use of credit cards in payments is increasing worldwide. Fraud detection is done in all three classical, online, and commercial fields through data mining and machine learning (16-19). Banking and other related industries face a significant challenge in detecting and preventing fraud. Companies use data analysis and machine learning algorithms to identify patterns and suspicious behaviors. There is no complete and effective solution for fraud detection in banking and e-commerce yet, and there are problems like false positive results and reduced system accuracy (20-23). Advanced fraud detection models can be very effective in dealing with fraud in e-commerce. As an intelligent system, these models are capable of identifying fraud patterns and recognizing suspicious transactions. Using advanced methods like machine learning and artificial intelligence can improve fraud detection and prevent financial and credit losses caused by fraud in e-commerce (24-26). The financial industry has been able to use better and more effective fraud detection methods; thanks to the development and advancement of various technologies and their combination with big data analysis and artificial intelligence. The detection and prevention of fraud in the financial industry can be significantly improved by integrating these methods and using expert teams. Algorithms, machine learning models, artificial neural networks, data analysis techniques, and process automation tools are used in banking intelligence. Banking uses these tools to identify fraudulent patterns and trends, predict fraudulent behavior, quickly detect fraud, and improve banking security and control systems (27-31). In banking, fraud detection is done through the use of artificial intelligence and machine learning algorithms. These algorithms can identify patterns and anomalies that suggest fraud by analyzing large volumes of data from various sources, like transaction records, customer information, and network logs, which include unauthorized access, unusual transaction patterns, and suspicious behavior. Using algorithms and computational methods; machine learning can directly extract the required information from the data for fraud detection. These methods are capable of learning information from data without the need for default equations (32, 33).

3. SUGGESTED DESIGN

The proposed plan to detect suspicious behaviors in card transactions is presented in Figure 1, based on various studies conducted in the field of credit card fraud detection and utilizing examples from related articles.

A strong and accurate model for predicting fraud is created using the combination of XGBoost and LightGBM algorithms in this model.

3. 1. Exploratory Data Analysis

The fraud detection process begins with the extraction and loading of exploratory data from the bank's database. For optimal algorithm performance, this step involves transforming features, filling in empty values, removing duplicate data and noise, and using other methods such as transformation, normalization, and standardization. The data preprocessing operation is complete.

3. 2. Features Engineering

Feature engineering and the opinion of expert experts are used to select important and influential data at this stage. PCA algorithms can be utilized to select the best features.

3. 3. Data Training

The pre-processed data is randomly split into two training and experimental groups, with 80% belonging to training data and 20% belonging to experimental data. Then, different algorithms that were assumed to be important and reliable in previous fraud detection studies are trained in different stages using training data, so that different models of each algorithm are ready to be evaluated.

3. 4. Sampling by Smote METHOD

In this step, the Smote method is used to address the problem of unsatisfied classes in the data. By generating artificial samples from existing samples, Smote can increase the number of minority class samples.

3. 5. Testing Data

Different built models are used to test the data of the experimental group, and a confusion matrix of the results for each algorithm is prepared for use in step evaluating models.

3. 6. Evaluating Models

The F criterion and AUC criterion are calculated for each of the confusion matrices in this step.

3. 7. Determining A Machine Learning Model

First, determine the number of algorithms for which the highest F criterion was measured after reviewing the criteria calculated in step evaluating models. The number of selected algorithms is decreased based on the amount calculated for the AUC criterion. XGBoost and LightGBM algorithms were chosen after completing this stage based on the statistical population of this research and the criteria mentioned. Due to its shorter execution time compared to LightGBM, the XGBoost algorithm will be prioritized for model execution in the main stages to reduce the execution time to a suitable extent.

3. 8. New Transaction

The bank's database is used to extract card-to-card transaction information for fraud detection operations at this stage.

3. 9. Preparing Data

The pre-processing of the extracted information in step new transaction is done similarly to step features engineering.

3. 10. Predicting Fraud Using the Xgboost Algorithm

The main fraud detection procedure commences at this point, with the use of the XGBoost algorithm. The XGBoost algorithm is a powerful machine learning algorithm that can accurately predict various data.

3. 11. Improving Fraud Detection Accuracy with The Lightgbm Algorithm

In this step, the output information of step predicting fraud using the Xgboost algorithm is filtered and only the information related to the transactions that have been labeled fraudulent by the XGBoost algorithm are entered as input to the LightGBM algorithm. When it comes to dealing with large and complex datasets, the LightGBM algorithm, which is based on gradients, performs better. By using this combined algorithm, the goal is to reduce the number of false positives (FN) and increase model accuracy.

3. 12. A Caution to The Bank

In the final stage, the forecast information is checked, and fraudulent transactions are notified to the bank with a warning. This process is repeated to check new transactions. By using the proposed scheme, it is possible to conduct a more detailed analysis to detect fraud in card-to-card transactions. To predict transaction information for the One of the State banks of Iran and other banks. Figure 1 shows the proposed hybrid model.

4. METHODOLOGY

The focus of this research has been on examining and discussing an important and research topic. The primary objective of this research is to investigate and analyze a particular problem or challenge and suggest innovative and appropriate solutions to resolve it. Various research methods and techniques have been employed to achieve this goal, which are described below:

The method of this research is the case study method because it specifically focuses on an Iranian state bank and an European bank.

a) The research is practical in terms of its purpose, as its results are used to inform bank managers and the task force to discover Bank Fraud and send the required reports to the Central Bank of J.A.

b) In terms of location, the research is conducted on the internet and field type. The data of the European Bank are collected through the website www.kaggle.com,

Figure 1. Suggested Design

while the data of the One of the State banks of Iran are collected through the field and legally stored in the bank's data storage unit.

c) By predicting the fraud label using transaction information from both banks within a certain period of time, the research is predictive.

d) In terms of the nature of the data, the research employs a qualitative approach. For feature engineering, this method is utilized to obtain expert opinions, views, opinions, and experiences from experts, data warehouse specialists, and individuals related to the subject under study.

4. 1. Collecting Data   The first data set of the research includes credit card transactions made by a European bank for two days in 2013. The second data set includes card-to-card transactions made by the Tose'e Ta'avon bank for one month. For the Tose'e Ta'avon bank, the selected features include various variables such

as age group, job, economic sector, customer membership type, terminal type, day and time and transaction amount, number and amount of daily and monthly card transactions as source and destination. if in the reviewed studies, the calculation features of the number and amount of card transactions have not been used in other time periods.

4. 2. Data Sample Quantity   In the first data set, out of a total of 284,807 transactions, only 492 are fraudulent transactions and 284,315 are non-fraudulent transactions, and in the second data set, out of a total of 4,139,607 card-to-card transactions, which are related to one month, the number is 5. 161 cases have already been identified as fraudulent transactions.

4. 3. Tools For Collecting Data   The information related to the first data set was received from the website www.kaggle.com and the information of the second data

set was directly compiled and engineered by the experts of the bank's data warehouse unit. Feature engineering and initial pre-processing of this educational data is also done by Oracle sql development software.

Also, the implementation of the model with machine learning algorithms and its evaluation has been done by Python coding tool and PyCharm 2021.3.3 IDE.

5. DATA ANALYSIS

In this section, the proposed design is used to analyze statistical data set information. The introduced algorithms have been used because of their power, good performance, and wide applications. In the following, the evaluation criteria of the algorithms were examined and then the algorithms were evaluated on sample data from the European Bank in order to provide a suitable solution to detect fraud in the real data of the Tose'e Ta'avon bank and an optimal process to increase its speed and accuracy.

The Xgboost Algorithm is a powerful machine learning algorithm based on gradient boosting and provides better performance than other algorithms by exploiting the power of hardware computing.

The Decision Tree (Dt) Algorithm is used for classification and regression and makes a decision by building a decision tree based on the features and conditions of the segmentation.

The Random Forest Algorithm operates based on the concept of a set of decision trees and makes decisions by combining their results.

Nearest Neighbors Algorithm is based on nearest neighbors and uses labels of neighboring samples to predict labels.

Isolation Forest Algorithm is a method to detect rare and unusual defects in data. This algorithm tries to separate defects from other data by building random trees and simulating the random process.

The Local Anomaly Factor (Lof) Algorithm uses a method to detect defects and local anomalies in the data.

Lightgbm Algorithm is a gradient boosting based machine learning algorithm developed by Microsoft. This algorithm is used for classification and regression. LightGBM is commonly used in large datasets due to its high speed and low memory consumption.

5. 1. The Criteria for Evaluation
The algorithms are evaluated against sample data from the European Bank using the specified criteria, and a suitable solution is provided to detect fraud in the data, increasing the speed and accuracy of the analysis process.

Accuracy: The ratio of the number of correctly classified data to the total number of data.

Precision: The ratio of the number of true positive data that are correctly detected to the total number of detecting positive data.

Recall: The ratio of the number of true positive data correctly recognized to the total number of true positive data.

Measurement (F1 score): F1 is a measure that combines accuracy and readability and is used to compare algorithms.

Operating characteristic curve (ROC curve): A graph that shows the ratio between the correct detection rate and the false detection rate of the algorithm.

5. 2. Comparing the Results of Different Algorithms and Selecting Suitable Algorithms
The performance of the algorithms is evaluated by dividing the dataset into two parts: training and testing. The training data set is utilized for algorithm training, while the test data set is utilized for evaluating their performance. The calculation and reporting of accuracy, recall, F-score, and ROC-AUC scores for each algorithm was done.

According to the results obtained in Table 1, the following four algorithms are selected as the best algorithms according to the record of the highest value of the F function:

XGBoostSmoted,XGBoost,LightGBM,Smoted LightGBM

In the next step, the following two algorithms are selected according to the record of the highest ROC-AUC criterion: Smoted XGBoost, Smoted LightGBM.

Finally, considering the higher processing time of the Smoted LightGBM algorithm and the large number of input data, we arrange the algorithms in such a way that the data processing takes place in the following two steps:

TABLE 1. Evaluation results with different methods in the European Bank

Algorithm	Smote	F Score	Time training (s)	ROC-AUC
XGBoost	NO	0.9996	28.60	0.8928
XGBoost	YES	0.9996	91.16	0.9285
Decision Tree	NO	0.9994	8.76	0.8928
Decision Tree	YES	0.9982	110.83	0.8027
Random Forest	NO	0.9996	2683.57	0.8928
Random Forest	YES	0.9995	5135.88	0.9234
KNN	NO	0.9984	0.07	0.6570
KNN	YES	0.9708	0.19	0.7867
Isolation Forest	NO	0.9510	4.804	0.9092
Isolation Forest	YES	0.9924	8.407	0.6295
LOF	NO	0.9442	54.466	0.7378
LOF	YES	0.9380	244.241	0.6379
LightGBM	NO	0.9998	131.685	0.9030
LightGBM	YES	0.9998	343.914	0.9183

First, the data is processed by the XGBoost algorithm and fraud label prediction is done.

In this step, the output of the previous step is filtered, only the data that includes the label Class=1 are entered into the Smoted LightGBM algorithm as input, and these data are re-predicted as primary data with the corresponding Class.

Once the data has been processed, it's crucial to pay attention to these points:

- Due to the greatly reduced amount of data in the input of the second stage, the prediction operation can be performed at a higher speed in the second stage.
- FP cases pertain to transactions that are not fraudulent, but the first algorithm (XGBoost) recognizes them as fraud, and the second algorithm (LightGBM) significantly decreases the model's accuracy.

Figure 2's ROC diagram shows that the two selected algorithms are better than the other reviewed algorithms. Two algorithms, XGBoost and LightGBM, are chosen to optimize the model and detect fraud in card transaction information in the European Bank dataset.

5. 2. Testing the Model and Its Results on the Real Data of the Tose'e Ta'avon Bank   First, using the XGBoost algorithm, the data of Tose'e Ta'avon bank is divided into two parts, training and testing, in such a way that the training data includes a small portion of the whole data. The Smote algorithm is used to balance the training data since the data with label 1 is very limited and much less than the data with label 0, and the data set is unbalanced.

Because the prediction is based on the type of fraud detection, the goal is to first increase the number of fraud cases correctly detected and then decrease the number of non-fraud cases that are falsely detected to increase

accuracy. The training data is used for supervised learning, and then the entire bank transaction information is tested. The confusion matrix of Figure 3 is obtained as a result. According to the analysis and evaluation results of the XGBoost hybrid algorithm using Smote, it can be seen that this algorithm performed very well with 99.76% accuracy. The confusion matrix shows that out of a total of 4,144,892 samples, approximately 4,139,607 were correctly identified as negative samples, and only 8,285 were identified as false positive samples. Also, the accuracy of positive and negative predictions is 99.96% and 29.64%, respectively. The recall rates are 99.80% and 67.64%, and the F score is 0.9988 for negative samples and 0.4122 for positive samples. Also, the area under the ROC-AUC chart equal to 0.8372 shows that the algorithm has a good ability to distinguish between the two categories. The XGBoost algorithm's performance has been improved by the use of the Smote technique, and the processing time was approximately 388.23 seconds. Equation 1 is the equivalent of the total number of fraudulent transactions.

$$\text{Count}([\text{Class}]==1) = \\ \text{TP} + \text{FP} = 3491 + 1670 = 5161 \tag{1}$$

The total number of cases was 5,161, but only 3,491 were correctly identified. But the number of 8,285 cases was also wrongly labeled as fraud, which is considered a new data set to solve this issue in the continuation of the transactions in relation 2.

$$\text{TP} + \text{FN} = 3.491 + 8.285 = 11.776 \tag{2}$$

The number of 11,776 transactions is entered as input to the LightGBM algorithm, and again the supervised learning steps are performed on the training data of the filtered dataset, and then data testing is performed on all 11,776 transactions, and finally the results are according to the matrix The confusion of Figure 4 is obtained.
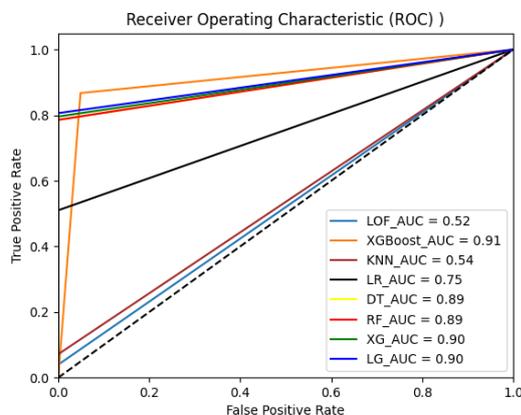
Figure 2. ROC graph for different algorithms without using Smote technique
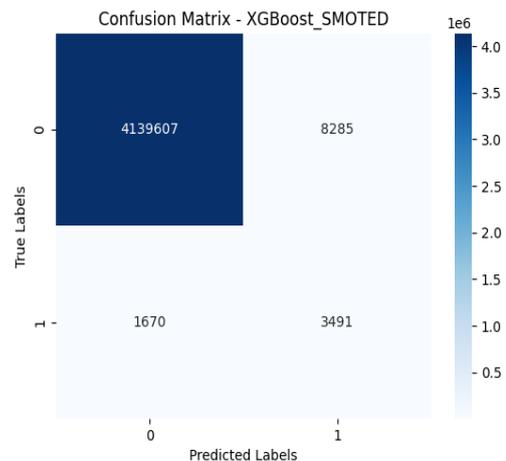
Figure 3. Confusion matrix of XGBoost algorithm with Smote on real data of Tose'e ta'avon bank
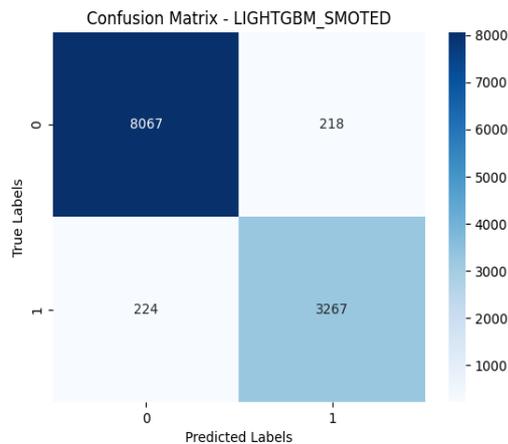
Figure 4. Confusion matrix of LightGBM algorithm with Smote on real data of Tose'e ta'avon bank after filtering

The combined algorithm's analysis and evaluation results indicate that it has a good performance with a 96.25% accuracy. The confusion matrix indicates that among 8,776 samples, approximately 8,067 were correctly identified as negative samples, while only 218 were identified as false positive samples. Also, the accuracy of positive and negative predictions is 97.30% and 93.74%, respectively. The recall results are 97.37% and 93.58%, with the F score being 0.9733 for negative samples and 0.9366 for positive samples. The algorithm's ability to distinguish between the two categories is demonstrated by the 0.9548 area under the ROC-AUC chart. The algorithm's performance on the test data is demonstrated by the ROC-AUC score of 0.9562 on the test set.

According to equation 3, it is evident that the model decreases the items related to FN by keeping TP and enhances the accuracy of the output.

$$TN + TP + FP + FN = 8.067 + 3.267 + 224 + 218 = 11.776$$
$$FN1 = 8.285, FN2 = 218 \tag{3}$$
$$TP1 = 3491, TP2 = 3267$$

Therefore, the model is also optimized by selecting two algorithms XGBoost and LightGBM to detect fraud in card transaction information in the Tose'e Ta'avon bank dataset.

6. CONCLUSION

According to comprehensive analyses and tests, the proposed model was developed to detect fraud in the transaction information of the Tose'e Ta'avon bank, using XGBoost and LightGBM algorithms. The objective of this algorithm combination is to detect defects and anomalies in data with high speed and accuracy. The experiments demonstrate that this model with high

accuracy can correctly detect defects and provide reliable information about the data's state. Using the existing knowledge and experience in the field of data analysis and machine learning, it is certain that this model with the combination of XGBoost and LightGBM has the ability to detect fraud in the information of The Tose'e Ta'avon bank well and can be used as a powerful tool in detecting fraud. In this research, an advanced method for detecting fraud in transactions was presented. There are two main steps in this method. The XGBoost algorithm is used to identify frauds by entering transaction information after preprocessing. Only the transactions that received the fraud label in the first step are included after filtering the output of this algorithm. To enhance fraud detection accuracy, the filtered information is fed into the LightGBM algorithm in the second step. The accuracy of fraud detection is significantly increased by this step. The results show that by combining XGBoost and LightGBM algorithms with two stages of fraud detection, the speed and accuracy of fraud detection are significantly increased. This method can be used in banking and financial transaction systems that face various types of fraud. The proposed method in the current research provides a reliable and accurate solution to detect fraud in Tose'e Ta'avon bank transactions. This method can significantly improve the speed and accuracy of fraud detection and can be used in financial and banking transaction systems.

7. REFERENCES

1. Merryta D, Tuga M. Artificial Intelligence Model as an Early Warning System for Fraudulent Transactions in Mobile Banking. ICIC Express Letters Part B: Applications. 2023;14(07):747. https://doi.org/10.24507/icicelb.14.07.747

2. Madhuri TS, Babu ER, Uma B, Lakshmi BM. Big-data driven approaches in materials science for real-time detection and prevention of fraud. Materials Today: Proceedings. 2023;81:969-76. https://doi.org/10.1016/j.matpr.2021.04.3232214-7853/_

3. Mytnyk B, Tkachyk O, Shakhovska N, Fedushko S, Syerov Y. Application of Artificial Intelligence for Fraudulent Banking Operations Recognition. Big Data and Cognitive Computing. 2023;7(2):93. https://doi.org/10.3390/bdcc7020093

4. Ogundokun RO, Misra S, Ogundokun OE, Oluranti J, Maskeliunas R, editors. Machine learning classification based techniques for fraud discovery in credit card datasets. Applied Informatics: Fourth International Conference, ICAI 2021, Buenos Aires, Argentina, October 28–30, 2021, Proceedings 4; 2021: Springer.

5. Seeja K, Zareapoor M. Fraudminer: A novel credit card fraud detection model based on frequent itemset mining. The Scientific World Journal. 2014;2014. http://dx.doi.org/10.1155/2014/252797

6. Padhi B, Chakravarty S, Biswal B, editors. Anonymized credit card transaction using machine learning techniques. Advances in Intelligent Computing and Communication: Proceedings of ICAC 2019; 2020: Springer.

7. Moradi R, Hamidi H. A New Mechanism for Detecting Shilling Attacks in Recommender Systems Based on Social Network

Analysis and Gaussian Rough Neural Network with Emotional Learning. International Journal of Engineering, Transactions B: Application. 2023;36(2):321-34. https://doi.org/10.5829/ije.2023.36.02b.12

8.   Sharma D, Kang SS, editors. Hybrid model for detection of frauds in credit cards. 2022 4th International Conference on Advances in Computing, Communication Control and Networking (ICAC3N); 2022: IEEE.

9.   Zhang Y, Chen X, Li J, Wong DS, Li H, You I. Ensuring attribute privacy protection and fast decryption for outsourced data security in mobile cloud computing. Information Sciences. 2017;379:42-61. https://doi.org/10.1016/j.ins.2016.04.015

10. Timothy DP, Santra AK, editors. A hybrid cryptography algorithm for cloud computing security. 2017 International conference on microelectronic devices, circuits and systems (ICMDCS); 2017: IEEE.

11. Hashemi SK, Mirtaheri SL, Greco S. Fraud Detection in Banking Data by Machine Learning Techniques. IEEE Access. 2022;11:3034-43.

12. Nkomo BK, Breetzke T, editors. A conceptual model for the use of artificial intelligence for credit card fraud detection in banks. 2020 Conference on Information Communications Technology and Society (ICTAS); 2020: IEEE.

13. Pham VVH, Liu X, Zheng X, Fu M, Deshpande SV, Xia W, et al., editors. PaaS-black or white: an investigation into software development model for building retail industry SaaS. 2017 IEEE/ACM 39th International Conference on Software Engineering Companion (ICSE-C); 2017: IEEE.

14. Aljawarneh S. Cloud security engineering concept and vision: Concept and vision. Cyber security and threats: Concepts, methodologies, tools, and applications: IGI Global; 2018. p. 93-101.

15. Khan N, Al-Yasiri A. Cloud security threats and techniques to strengthen cloud computing adoption framework. Cyber security and threats: Concepts, methodologies, tools, and applications: IGI Global; 2018. p. 268-85.

16. Khosravi S, Kargari M, Teimourpour B, Eshghi A, Aliabdi A, editors. Using Supervised Machine Learning Approaches To Detect Fraud In The Banking Transaction Network. 2023 9th International Conference on Web Research (ICWR); 2023: IEEE.

17. Balagolla E, Fernando W, Rathnayake R, Wijesekera M, Senarathne A, Abeywardhana K, editors. Credit card fraud prevention using blockchain. 2021 6th international conference for Convergence in Technology (I2CT); 2021: IEEE.

18. Bahrami L, Safaie N, Hamidi H. Effect of motivation, opportunity and ability on human resources information security management considering the roles of attitudinal, behavioral and organizational factors. International Journal of Engineering, Transactions C: Aspects. 2021;34(12):2624-35. https://doi.org/10.5829/ije.2021.34.12c.07

19. Kirar JS, Kumar D, Chatterjee D, Patel PS, Yadav SN, editors. Exploratory Data Analysis for Credit Card Fraud Detection. 2021 International Conference on Computational Performance Evaluation (ComPE); 2021: IEEE.

20. Alghushairy O, Alsini R, Ma X, editors. An Efficient Local Outlier Factor for Data Stream Processing: A Case Study. 2020 International Conference on Computational Science and Computational Intelligence (CSCI); 2020: IEEE.

21. Hamidi H, Rafebakhsh M. Analyzing factors influencing mobile social media marketing acceptance among customers. International Journal of Engineering, Transactions C: Aspects. 2022;35(6):1209-16. https://doi.org/10.5829/ije.2022.35.06c.13

22. Hamidi H, Seyed Lotfali S. Analysis of role of cloud computing in providing internet banking services: Case study bank melli iran. International Journal of Engineering, Transactions B: Application. 2022;35(5):1082-8. https://doi.org/10.5829/ije.2022.35.05b.23

23. Daliri S. Using harmony search algorithm in neural networks to improve fraud detection in banking system. Computational Intelligence and Neuroscience. 2020;2020. https://doi.org/10.1155/2020/6503459

24. Esmail FS, Alsheref FK, Aboutabl AE. Review of Loan Fraud Detection Process in the Banking Sector Using Data Mining Techniques. International journal of electrical and computer engineering systems. 2023;14(2):229-39. https://doi.org/10.32985/ijeces.14.2.12

25. Handa A, Dhawan Y, Semwal P. Hybrid analysis on credit card fraud detection using machine learning techniques. Handbook of Big Data Analytics and Forensics. 2022:223-38. https://doi.org/10.1007/978-3-030-74753-4_15

26. Hamidi H. A combined fuzzy method for evaluating criteria in enterprise resource planning implementation. Intelligent systems: Concepts, methodologies, tools, and applications: IGI Global; 2018. p. 639-70.

27. Nilchi AN, Vafaei A, Hamidi H, editors. Evaluation of security and fault tolerance in mobile agents. 2008 5th IFIP International Conference on Wireless and Optical Communications Networks (WOCN'08); 2008: IEEE. 10.1109/WOCN.2008.4542509

28. Parekh P, Rana C, Nalawade K, Dholay S, editors. Credit Card Fraud Detection with Resampling Techniques. 2021 12th International Conference on Computing Communication and Networking Technologies (ICCCNT); 2021: IEEE. 10.1109/ICCCNT51525.2021.9579915

29. Patil S, Nemade V, Soni PK. Predictive modelling for credit card fraud detection using data analytics. Procedia computer science. 2018;132:385-95. https://doi.org/10.1016/j.procs.2018.05.199

30. Sharma U, Sharma M, Rana A, editors. Experimental Analysis of Anomaly Detection Algorithms on Banking data. 2021 9th International Conference on Reliability, Infocom Technologies and Optimization (Trends and Future Directions)(ICRITO); 2021: IEEE.

31. Rambola R, Varshney P, Vishwakarma P, editors. Data mining techniques for fraud detection in banking sector. 2018 4th International Conference on Computing Communication and Automation (ICCCA); 2018: IEEE.

32. Hamidi H, Vafaei A, Monadjemi SA. Evaluation and checkpointing of fault tolerant mobile agents execution in distributed systems. Journal of Networks. 2010;5(7):800.

33. Hamidi H, Moradi S. Analysis of consideration of security parameters by vendors on trust and customer satisfaction in e-commerce. Journal of Global Information Management (JGIM). 2017;25(4):32-45. 10.4018/JGIM.2017100103

Persian Abstract

چکیده

در سال‌های اخیر، با افزایش دسترسی به داده‌های مشتریان و توانایی‌های پیشرفته تحلیل داده‌ها با استفاده از روش‌های هوشمند، برای تحلیل رفتار مشتریان اقدامات مختلفی صورت گرفته است. یکی از این اقدامات، استفاده از سیستم‌های هوشمند برای کشف تقلب در بانکداری است. تقلبات بانکی در حال حاضر گستره وسیعی دارند و باعث آسیب‌های مالی و غیرمالی جدیدی به بانک‌ها و مشتریان آن‌ها شده‌اند. با توجه به اهمیت موضوع، در این تحقیق یک مدل هوشمند برای کشف تقلب در بانکداری طراحی شده است. پس از استفاده از ابزارهای هوشمندسازی برای بررسی الگوریتم‌های مختلف یادگیری ماشین ، دو الگوریتم XGBoost و LightGBM به دلیل برتری معیارهای F و ROC در مدل مورد نظر انتخاب شدند. این الگوریتم‌ها به صورت مرحله‌ای در آزمایشات نهایی استفاده شدند تا همزمان با دقت بالا، تعداد نمونه‌های نادرست با برچسب تقلب (FP) را کاهش دهند. این مدل با استفاده از داده‌های واقعی یک بانک دولتی آزمایش شده و نتایج بسیار قابل قبولی در تشخیص تقلب در تراکنش‌های کارت به کارت ارائه می‌دهد. این مدل می‌تواند بهبود چشمگیری را در امنیت سیستم بانکی فراهم کند و به عنوان ابزاری موثر در کاهش جرایم مالی استفاده شود.

International Journal of Engineering

Enhancing Book and Document Digitization from Videos: A Feature Fusion-Based Approach

G. Buddhawar*[a], K. Jariwala[a], C. Chattopadhyay[b]

[a] Computer Science and Engineering Department, Sardar Vallabbhai National Institute of Technology, Surat, Gujarat, India
[b] School of Computing and Data Sciences, FLAME University, Pune, Maharashtra, India

P A P E R I N F O	*A B S T R A C T*
	In an age where preserving knowledge and information from books and documents is crucial, traditional manual scanning methods are tedious and error-prone. It involves a lot of human intervention and, as a result, sometimes results in erroneous digitization, which makes the downstream tasks, such as optical character recognition, difficult. Therefore, innovative techniques are required to be proposed that not only reduce human effort in terms of digitization but also give highly accurate results over the recently proposed state-of-the-art techniques. We proposed a novel computer vision-based algorithm that combines Gray-Level Co-occurrence Matrix (GLCM) features with Thepade's 10-ary texture features (TSBTC) for video frame classification. This hybrid approach significantly enhances frame selection accuracy, ensures high-quality digitization, and accommodates multiple languages and document types. We also proposed a dataset of 54,000 diverse images to demonstrate our algorithm's effectiveness in real-world scenarios and compare it to existing methods, making a valuable contribution to document digitization. The proposed dataset can be utilized for several document image analysis tasks. *doi: 10.5829/ije.2024.37.03c.11*

Graphical Abstract
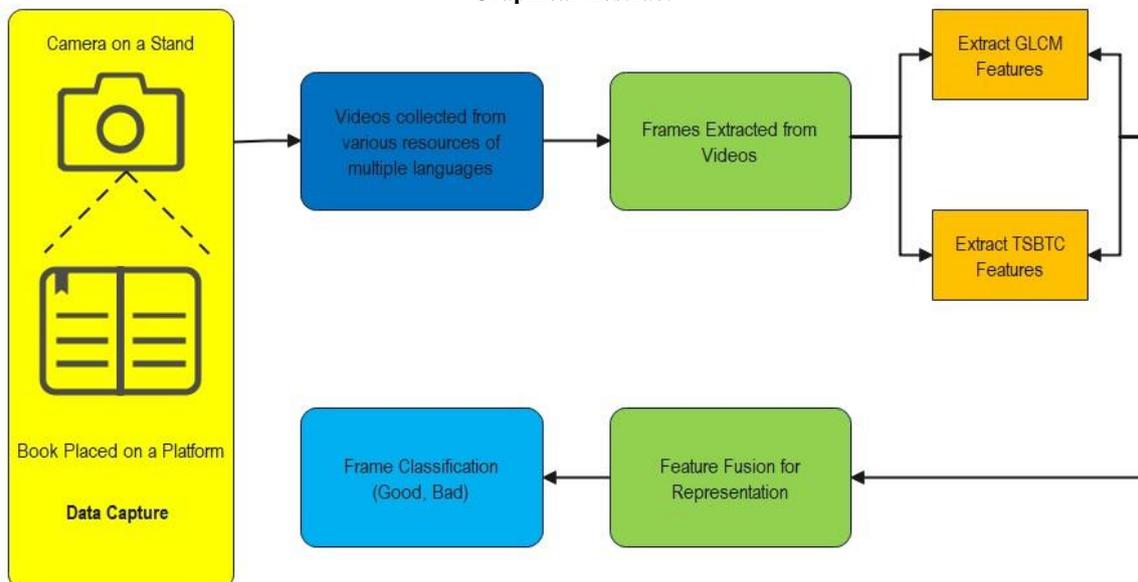
*Corresponding author email: d18co005@coed.svnit.ac.in (G. Buddhawar)

1. INTRODUCTION

Books and documents are valuable sources of information and knowledge that need to be preserved and accessed for various purposes. Digitizing books and documents are the processes of converting them from physical to digital form, which enables easier storage, retrieval, analysis, and dissemination of their content. However, digitizing books and documents is not a trivial task, as it involves several challenges, such as dealing with different languages, formats, layouts, fonts, and the quality of the original documents. Moreover, digitizing books and documents can also bring many benefits, such as enhancing their readability, accessibility, searchability, and usability. One of the common methods for digitizing books and documents is manual scanning, which is a tedious, costly, and error-prone process. A more efficient and convenient way is to record a video of the book and later extract the pages, but this requires a robust and accurate computer vision-based algorithm to perform the digitization. Therefore, developing efficient and effective methods for digitizing books and documents is an important and relevant problem.

Several methods have been proposed for digitizing books and documents from video recordings (1-3). These methods can be broadly classified into two categories: frame-based and video-based. Frame-based methods treat each frame of the video as an independent image and apply image processing techniques to extract the document content. Video-based methods exploit the temporal information of the video and use motion analysis techniques to track the document regions and capture the optimal frames. Frame-based methods are simpler and faster, but they are more sensitive to noise, blur, and distortion in the frames. Video-based methods are more robust and accurate, but they are more complex and computationally intensive. A detailed literature survey of these methods will be provided in section 2.

In this paper, we proposed a novel computer vision-based algorithm to automatically digitize books and documents from video recordings. Our algorithm is a feature-fusion based approach that combines two methods and achieves high accuracy in identifying the optimal frames to capture from the video, avoiding flipping instances, and ensuring high-quality digitization. Our algorithm can handle multiple languages and various types of documents, such as books, magazines, newspapers, and reports. We also introduce a new dataset of 5400 document images in different languages, which we used to train and evaluate our algorithm. We demonstrate the effectiveness of our algorithm on various real-world scenarios and compare it with existing methods.

Digitized documents can be used for various applications of information extraction and retrieval (4-8). Information extraction is the process of automatically extracting structured information from unstructured documents (8). Information retrieval is the process of finding relevant and useful information from large collections of documents (4). Some examples of information extraction and retrieval techniques are indexing, searching, summarizing, categorizing, and analyzing the document content (4-6). These techniques can help users find the information they need, as well as discover new insights and patterns from the document data. However, the quality and accuracy of information extraction and retrieval depend on the quality and accuracy of digitization (5, 6). Therefore, our algorithm can facilitate these tasks and improve their performance by providing high-quality digitization of books and documents from video recordings.

Based on the purpose mentioned in the previous paragraph, the current version of the paper makes the following key research contributions:
- A Dataset of 54000 Frames with their Ground Truth.
- A novel hybrid algorithm for video frame classification that combines GLCM features with Thepade's 10-ary texture features.
- Performance comparison with existing methods.

The rest of the paper is organized as follows: Section 2 provides a literature survey of the existing methods. Section 3 describes the details of the new dataset, while the proposed algorithm and its components in detail are given in section 4. Section 5 presents the experimental results, while section 6 concludes the paper and suggests some directions for future work.

2. LITERATURE SURVEY

Digitizing books and documents from video recordings are a challenging but valuable task, involving the extraction and reconstruction of textual and graphical content to enhance information accessibility. This task can be useful for various applications, such as digital libraries, e-learning, cultural heritage preservation, and personal archiving (7-9). However, it also faces several difficulties (10). To address these challenges, various methods have been proposed in the literature (11-13) that can be broadly classified into two categories: frame-based and video-based methods. Frame-based methods operate on individual or selected frames of the video, while video-based methods exploit the temporal information and redundancy of the video sequence.

Frame-based methods assume that the video frames contain sufficient information to reconstruct the document content and typically consist of three steps: frame selection, frame rectification, and frame stitching (14). Brown et al. (15) proposed a minimal solution for panoramic stitching based on homography estimation. Chhajed and Gargb (16) developed a smartphone-based system for book digitization using frame selection and

rectification. Bouguet (17) implemented a camera calibration toolbox for frame rectification.

A two-level semi-supervised clustering method (3)incorporates labelled and unlabelled data simultaneously on various documents. A dictionary-independent method (6) for text language identification was proposed and tested on 31000 texts from 31 different languages. Fadaei (7) proposed a new dominant color descriptor to improve accuracy. The authors use a GAN-based resolution network (8) for face recognition. Parnak et al. (10) proposed the forgery detection mechanism for the extraction of features from the image using Benford's law as a benchmark and on CASIA datasets. Rashno and Fadaeib (14) also proposed an image restoration model based on the convex set feature of the images. Chhajed and Gargb (16) proposed the work related to binary images in based on a histogram-based decision tree that performs better with applications like steganography and watermarking. Charoqdouz and Hassanpour (18) proposed an approach for face images on documents.

Video-based methods are based on the idea that the video sequence contains redundant and complementary information that can be exploited to improve document reconstruction. These methods typically consist of four steps: video segmentation, video rectification, video mosaicing, and video enhancement (11). The advantages of video-based methods are their ability to handle camera motion and illumination variation, to reduce the number of frames required to cover the whole document, and to produce high-resolution and high-quality document images. However, they also have some disadvantages, such as being complex, time-consuming, and prone to errors in video segmentation and mosaicing. Charoqdouz and Hassanpour (18) proposed a robust book page extraction algorithm using boundary growing, and Chen et al. (19) developed a robust text detection method using edge-enhanced maximally stable extremal regions. Ulges

et al. (20) presented a document capture system using stereo vision. Edge-based methods were also proposed by Kantarcıoğlu et al. (21), Firouzi et al. (22), Dixit and Shirdhonkar (23). We summarize their main features, advantages, and disadvantages in Table 1.

Understanding the textual component of a natural scene (24) is useful for various applications, such as navigation and translations. It faces challenges such as complex background, low resolution, varying font, size, color, orientation, and style of text, occlusion, and distortion (25). The methods for this task can be classified into two categories: top-down and bottom-up methods. Top-down methods (26, 27) use global cues to locate and segment the text regions, while bottom-up methods use local cues to group and merge the text components or characters. Table 2 summarises some of the key research in this domain. Based on the literature survey, we found that the drawbacks of the methods discussed require an innovative way to digitise books and documents from video recordings. We suggest an innovative approach and overcome their drawbacks in the following part. Our approach and its experimental findings are described.

3. DATASET PREPARATION

The first step in this research is to prepare a dataset for book flip recognition. The proposed dataset has 54000 frames (.jpeg images) with their ground truth (good and bad frames marked). We have scanned these textbooks and documents in Hindi, English, and Marathi. Book Scanner with a mobile stand was used to perform the above operation. Frames are extracted from the recorded video using the ffmeg tool. Each image is 1024x768 pixels. All the images are saved as colour images with

TABLE 1. Comparison of frame-based and video-based approaches

Method	Features	Advantages	Disadvantages
Frame-based	- Frame level - Consist of frame selection, frame rectification, and frame stitching	- Simple, efficient, - Robust to occlusion and page curling	- Require many frames - Sensitive to camera motion and illumination - Produce artifacts or inconsistencies
Video-based	- Video segmentation, - Video rectification, - Video mosaicing, - Video enhancement	- Handle motion and illumination - Require fewer frames - Produce high-resolution and quality images	- Complex and slow - Prone to errors in segmentation and mosaicing

TABLE 2. A summary of state-of-the-art algorithms, datasets, and performance metric available in the literature in the said domain

Sr.no	Algorithm	Dataset	Metric
1	Deep Learning-Based Optical Character Recognition (9)	MNIST	Character Recognition Accuracy
2	Document Layout Analysis (13)	COCO text	Word recognition accuracy
3	Document Analysis Systems (28)	IAM handwriting dataset	Text detection metric
4	Attention-Based Models for OCR (29)	Synthetic dataset	layout analysis metrics
5	Sparse Coding and Dictionary Learning (30)	Books magazines and newspaper	End to End evaluation metric

RGB channels. Figure 1 depicts some of the extracted frames, where the odd numbers ((i), (iii), and (v) represent the good frames, while the even number frames, i.e., (ii), (iv), and (vi), are the bad frames. The dataset is used to evaluate the proposed approach for improving the performance of machine learning classifiers and will be made publicly available for research purposes.

4. PROPOSED APPROACH

In this section, we are going to describe the proposed approach in detail. Figure 2 depicts a block diagram of the proposed approach. The proposed approach is discussed in the following sub-sections.

4. 1. TSBTC Algorithm in Book Digitization
Thepade's Sorted Block Truncation Coding (TSBTC) algorithm (12) performs complex procedures to identify the key frames from a set of video frames captured in a controlled or uncontrolled scenario. Initialising frame counts for "bad" and "good." A 500x9 grid-based multidimensional array is initialised. This array stores frame colour component average values. A video stream picture, 'A,' is processed during frame processing. Red (R), Green (G), and Blue (B) values are carefully retrieved from this picture. Colour components are key to the frame's aesthetic character. These extracted values are listed in ascending order. Then, mean values for each component are calculated and placed in the array.

A key feature of the TSBTC algorithm is its ability to distinguish between good and bad frames. A threshold-

based mean colour value evaluation distinguishes this. If the estimated mean values for R, G, and B components fall below a threshold, the frame is considered "good" and the count is increased. However, if the mean values are above the threshold, the frame is considered "bad", and the count of "bad" frames is increased. In the TSBTC algorithm, the RGB got divided. Simultaneously, to find out the feature vector again, the frame values were divided into 10 parts. Per part, the centroid is calculated. Equations 1 to 4 in Table 3 show the criteria for the R value and it is the same for the remaining colors. The feature vector size is calculated using TSBTC 10-ary.
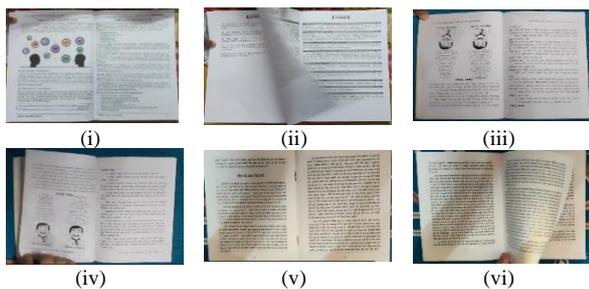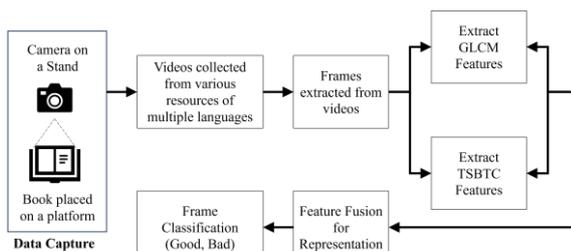
4. 2. GLCM Feature Extraction in Book Digitization
The use of Gray-Level Co-occurrence Matrix (GLCM) feature extraction is pivotal in the proposed book digitization process. It effectively captures visual characteristics, especially during sequential page flipping recorded in curated videos. GLCM computation utilizes advanced statistical techniques to reveal spatial correlations among grayscale pixel intensity pairs in image 'e1'. It visually represents intricate patterns and textural details in digital book pages by capturing frequency distributions of pixel pairings at various distances and angles. The process includes preprocessing steps like converting 'q1' to grayscale 'w1' and resizing 'e1' to a 128x128-pixel resolution, improving efficiency and uniformity. Equations 5 to 8 in Table 4 demonstrate how to compute the GLCM features. The systematic transformation of dynamic video data into statistical co-occurrence matrices enables spatial correlation analysis among pixel intensities.

4. 3. Synergistic Fusion of TSBTC and GLCM Approaches in Book Digitization
The breakthrough in the domain of book digitization is achieved through the combination of TSBTC and GLCM feature extraction. Algorithm 1 presents the broader steps of the proposed hybrid approach.

The initialization of 'good' and 'bad' frame counters initiates this procedure. A multidimensional array, 'arr,' records mean color values from the Red (R), Green (G),

Figure 1. Sample images of the proposed dataset

Figure 2. Block diagram of the proposed approach

TABLE 3. Equations used to calculate red component values in the TSBTC technique.

Feature	Formula	
lR	$\left[\frac{4}{m \times n}\right] \times \sum_{i=1}^{\frac{m \times n}{4}} sortedSDR(i)$	(1)
muR	$\left[\frac{4}{m \times n}\right] \times \sum_{i=\frac{(m \times n)}{4}+1}^{\frac{m \times n}{4}} sortedSDR(i)$	(2)
mlR	$\left[\frac{4}{m \times n}\right] \times \sum_{i=(m \times n)/2+1}^{\frac{m \times n}{4}} sortedSDR(i)$	(3)
uR	$\left[\frac{4}{m \times n}\right] \times \sum_{i=(m \times n \times 3)/4+1}^{\frac{m \times n}{4}} sortedSDR(i)$	(4)

TABLE 4. Equations used to calculate the feature extraction using GLCM features

Feature	Formula	
Contrast	$\sum_{i=1}^{N} \sum_{j=1}^{N} (i-j)^2\, P(i,j)$	(5)
Entropy	$-\sum_{i=1}^{N} \sum_{j=1}^{N} P(i,j) \lg P(i,j)$	(6)
Correlation	$\dfrac{\sum_{i=1}^{N} \sum_{j=1}^{N} (i-\bar{x})(j-\bar{y})\, P(i,j)}{\sigma_x\, \sigma_y}$	(7)
Energy	$\sum_{i=1}^{N} \sum_{j=1}^{N} P(i,j)^2$	(8)

and Blue (B) components of each frame's color channels. The algorithm processes each frame iteratively, extracting colour values and calculating their mean. The frame is then classified based on predefined thresholds for each colour component. Frames falling within the defined thresholds are considered 'good,' while those exceeding the thresholds are labelled as 'poor.'

The inclusion of GLCM feature extraction enhances the algorithm's ability to identify complex textual patterns. This is accomplished by calculating the 'r1' gray-level co-occurrence matrix. During this phase, the algorithm processes the grayscale representation 'w1,' derived from the video dataset frame 'q1'. Resizing the image to a standard size of 128 by 128 pixels ensures computational consistency.

The 'r1' is generated through sophisticated statistical computations and stores the gray-level co-occurrence matrix from w1. This matrix represents the frequency distribution of pixel intensity pairings within the 'e1' image and captures textural patterns. This characterizes pixel relationships in terms of spatial proximity and orientation, yielding a nuanced understanding of the textual complexities of digitized book pages.

The amalgamation of TSBTC and GLCM enables the algorithm not only to classify frames based on color attributes but also to explore intricate textural nuances. By uniting these techniques, the algorithm not only enhances the preservation of book content but also reveals new insights into the textual and visual essence of the original material.

4. 3. 1. The Proposed Hybrid Approach
The algorithm merges TSBTC and GLCM, their individual attributes combining synergistically. Initially, TSBTC classifies frames into 'excellent' or 'poor' quality using color attributes. Concurrently, GLCM's texture analysis computes the gray-level co-occurrence matrix 'r1,' capturing nuanced textural patterns in frames. Each step contributes to this orderly process by learning from its predecessor. Our earlier rationale serves as the foundation for this handcrafted feature engineering, which embodies a holistic approach that transcends particular methodologies by combining the best of both the features. Such feature engineering allows the proposed algorithm to capture both visual aspects and the

---

Algorithm 1: Hybrid Approach

```
# Step 1: Extract intensity values and color components
    image = load_image(image_path)
    color_comps = extract _components(image)
# Step 2: Create feature vectors
    feature_vec = create_feature_vec(color_comps)
# Step 3: Sort feature vectors
    sorted_vec = sort_feature_vect(feature_vec)
# Step 4: Divide sorted feature vectors
    parts = divide_feature_vecs(sorted_vec,
desired_variation="ternary")
# Step 5: Compute representative values
    repr_val = compute_representative_values(parts)
# Step 6: Create comprehensive feature vector
    feature_vec = create_comp_feature_vec(repr_val)
# Step 7: Compute GLCM features
    GLCM_features = compute_GLCM (feature_vec)
# Step 8: Compute texture measures
    txtr_msr = comp_txtr_meas(GLCM_features)
# Step 9: Create GLCM features array
    GLCM_array = create_GLCM_array(txtr_msr)
# Step 10: Extract key frames
    key_frames = extract_key_frames(GLCM_array)
    return key_frames
```

essence of textural patterns in digitized book pages, aligning seamlessly with our study's core goals.

5. EXPERIMENTAL RESULTS AND DISCUSSION

The findings of this study provide an approach for finding the representative frame of the Open Page Image (OPI) and removing unwanted frames from the video stream of the book being flipped. The code was executed on a Jupiter notebook, and the use of GPUs is done extensively. Hyperparameters in GLCM, like the number of gray levels and offset or distance, are used, while in TSBTC, the intensity value is used.

5. 1. Quantitative Results
In this section, we present the quantitative results of our comprehensive analysis, depicting the performance of various approaches across different classifiers. It is very common to use the F1 measure for binary classification. The mathematical formulation of the performance metric is given in the following set of equations:

$$Accuracy = \left(\frac{TP+TN}{TP+TN+FP+FN}\right) * 100 \qquad (9)$$

$$F_1 = \left(\frac{TP}{TP+0.5(FP+FN)}\right) \qquad (10)$$

where,

TP => True Positives (Good Frame predicted as Good)
TN => True Negatives (Bad Frames predicted as Bad).
FP => False Positives (Bad Frames predicted as Good)
FN => False Negatives (Good Frames predicted as Bad)

TABLE 5. Performance Comparison of the accuracy of all digitization techniques with various classifiers

Classifier	Features		
	TSBTC (%)	GLCM (%)	Hybrid (%)
ZeroR	**85.32**	**77.66**	**58.21**
Attribute Select Classifier	96.17	99.79	100
Bayes Net	95.31	99.68	99.88
Naïve Bayes	94.31	95.76	77.13
Naïve Bayes Multinomial	77.66	94.62	57.99
Logistic	88.23	99.06	87.21

The results are presented in Table 5, with approaches represented as columns and classifiers as rows. Notably, the best performing values, highlighted in *italics*, offer valuable insights into the efficacy of each approach. Within this context, our findings shed light on the enhanced performance of the hybrid model, further affirming its superiority. Additionally, we have experimented with Convolutional Neural Network (CNN) based on the LeNet-5 design (18) to measure the performance. There were 2,500 labelled good frames and 12,750 bad frames used for training set. The training process aimed to minimize the binary cross-entropy loss, and model accuracy was a key evaluation metric. A comparison between the performance of CNN and the proposed method is shown in Table 6.

5. 2. Qualitative Results   The qualitative results of our study are depicted in Figure 3, where a 2x2 grid
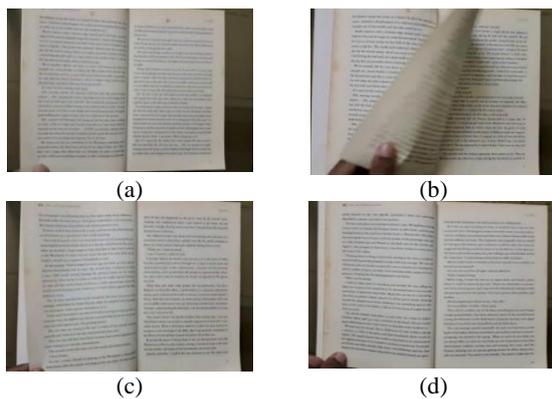
Figure 3. Qualitative results of the key frame extraction using the proposed hybrid approach

TABLE 6. Performance Comparison between the proposed model and CNN

Sr. No	Approach	% Accuracy
1	CNN	95%
2	Proposed Method	99%

format encapsulates the results at different stages of processing. Each quadrant of the grid presents a distinct image, showing a specific stage. Figure 3(a) portrays the 'good' frame, embodying the desired outcome. Figure 3(b) provides a glimpse of a 'half-flipped' frame, while Figure 3(c) delves into a 'twisted' representation that signifies an unwanted deviation. Lastly, Figure 3(d) resurfaces the ideal 'good' frame. Notably, the best-performing result will be the one where a page is completely flipped open and the textual portion of the page is completely visible, thereby making the visual comprehension of effectiveness seamless. It can be observed that Figures 3(a) and 3(d) satisfy these criteria. Although in both cases a part of the thumb is visible, however, it is not obstructing the text. To be more critical, Figure 3(a) can be considered as best among these four frames, as the portion of the thumb is the minimum in that frame. This shows that the proposed approach is able to achieve the desired result efficiently.

5. 3. Applications and Limitations   The proposed work has valuable real-life applications in digitizing books and documents from videos, benefiting fields such as education, research, and preservation. Examples of potential downstream real-life applications of the proposed include digitizing historical documents, archival research, education and eLearning, content indexing, work for the visually impaired and protecting fragile documents. However, it faces limitations related to video quality, text recognition accuracy, language support, and legal considerations. Examples of such limitations are the quality of source videos, variability of text, distorted images, multiple language text, copyrights and permissions from various book authors, managing a large digital document, the privacy of data, and digitization process. Addressing these limitations and ensuring the quality and ethical use of digitized content are essential in the future.

6. CONCLUSION AND FUTURE SCOPE

This paper presents a computer vision-based system that identifies key frames from video of a book being flipped under the field of view of a camera. The system fuses two algorithms (TSBTC and GLCM) to select the best frames and avoid page flipping, achieving high accuracy. The system supports many languages and document types and is evaluated on a new dataset of 54,000 images. The system outperforms existing methods and opens up new possibilities for digitizing textual resources. Future work can concentrate on refining the algorithm's precision, optimising its computational efficiency, and integrating advanced techniques such as deep learning to further enhance its accuracy. By improving the algorithm, we foresee a future in which digitization becomes more accessible, efficient, and accurate.

8. REFERENCES

1. Obiora KU, Okeke IE, Onwurah B. Digitization of library resources in university libraries: A practical approach, challenges and prospects. 2015. 10.1109/ETTLIS.2015.7048210

2. Azim N, Mat Yatin S, Jensonray R, Ayub Mansor S. Digitization of records and archives: Issues and Concerns. International Journal of Academic Research in Business and social sciences. 2018;8(9):170-8. 10.6007/IJARBSS/v8-i9/4582

3. Sadjadi S, Mashayekhi H, Hassanpour H. A two-level semi-supervised clustering technique for news articles. International Journal of Engineering, Transactions C: Aspects. 2021;34(12):2648-57. https://doi.org/10.5829/ije.2021.34.12C.10

4. HS C, Shenoy MK. Advanced text documents information retrieval system for search services. Cogent Engineering. 2020;7(1):1856467. 10.1080/23311916.2020.1856467

5. Lillis D, Scanlon M, editors. On the benefits of information retrieval and information extraction techniques applied to digital forensics. Advanced Multimedia and Ubiquitous Engineering: FutureTech & MUE; 2016: Springer. 10.1007/978-981-10-1536-6_83

6. Hassanpour H, AlyanNezhadi M, Mohammadi M. A Signal Processing Method for Text Language Identification. International Journal of Engineering, Transactions C: Aspects. 2021;34(6):1413-8. 10.5829/ije.2021.34.06c.04

7. Fadaei S. New dominant color descriptor features based on weighting of more informative pixels using suitable masks for content-based image retrieval. International Journal of Engineering, Transactions B: Applications. 2022;35(8):1457-67. 10.5829/ije.2022.35.08b.01

8. Shahbakhsh MB, Hassanpour H. Empowering face recognition methods using a gan-based single image super-resolution network. International Journal of Engineering, Transactions A: Basics. 2022;35(10):1858-66. 10.5829/ije.2022.35.10a.05

9. Buddhawar G, Jariwala KN, Chattopadhyay C, editors. Some Aspects of Text Recognition from Video Document in Education 4.0. 2021 Emerging Trends in Industry 40 (ETI 40); 2021: IEEE. 10.1109/ETI4.051663.2021.9619427

10. Parnak A, Baleghi Damavandi Y, Kazemitabar S. A Novel Image Splicing Detection Algorithm Based on Generalized and Traditional Benford's Law. International Journal of Engineering, A: Basics; 2022;35(4):626-34. 10.5829/ije.2022.35.04a.02

11. Kumar V. Region completion in a texture using multiresolution transforms. International Journal of Engineering, Transactions B: Applications; 2014;27(5):747-56. 10.5829/idosi.ije.2014.27.05b.10

12. Kekre H, Thepade SD, Lohar AT, editors. Image retrieval using block truncation coding extended to color clumps. 2013 International Conference on Advances in Technology and Engineering (ICATE); 2013: IEEE. 10.1109/ICAdTE.2013.6524769

13. Binmakhashen GM, Mahmoud SA. Document layout analysis: a comprehensive survey. ACM Computing Surveys (CSUR). 2019;52(6):1-36. 10.1145/3355610

14. Rashno A, Fadaei S. Image restoration by projection onto convex sets with particle swarm parameter optimization. International Journal of Engineering, Transactions B: Applications; 2023;36(2):398-407. 10.5829/ije.2023.36.02b.18

15. Brown M, Hartley RI, Nistér D, editors. Minimal solutions for panoramic stitching. 2007 IEEE conference on computer vision and pattern recognition; 2007: IEEE. 10.1109/CVPR.2007.383082

16. Chhajed G, Garg B. Novel Scheme for Data Hiding in Binary Images using Cover Pattern Histogram. International Journal of Engineering, Transactions B: Applications; 2023;36(11):2124-36. 10.5829/ije.2023.36.11b.16

17. Bouguet J-Y. Camera calibration toolbox for matlab. http://www vision caltech edu/bouguetj/calib_doc/. 2004. 10.22002/D1.20164

18. Charoqdouz E, Hassanpour H. Feature Extraction from Several Angular Faces Using a Deep Learning Based Fusion Technique for Face Recognition. International Journal of Engineering, Transactions B: Applications; 2023;36(8):1548-55. 10.5829/ije.2023.36.08b.14

19. Chen H, Tsai SS, Schroth G, Chen DM, Grzeszczuk R, Girod B, editors. Robust text detection in natural images with edge-enhanced maximally stable extremal regions. 2011 18th IEEE international conference on image processing; 2011: IEEE. 10.1109/ICIP.2011.6116200

20. Ulges A, Lampert CH, Breuel T, editors. Document capture using stereo vision. Proceedings of the 2004 ACM symposium on Document engineering; 2004. 10.1145/1030397.1030434

21. Kantarcıoğlu M, Xi B, Clifton C. Classifier evaluation and attribute selection against active adversaries. Data Mining and Knowledge Discovery. 2011;22:291-335. 10.1007/s10618-010-0197-3

22. Firouzi M, Fadaei S, Rashno A. A new framework for canny edge detector in hexagonal lattice. International Journal of Engineering, Transactions B: Applications; 2022;35(8):1588-98. 10.5829/IJE.2022.35.08B.15

23. Dixit U, Shirdhonkar M. An Improved Fingerprint-based Document Image Retrieval using Multi-resolution Histogram of Oriented Gradient Features. International Journal of Engineering, A: Basics; 2022;35(4):750-9. 10.5829/IJE.2022.35.04A.15

24. Mishra A, Alahari K, Jawahar C, editors. Top-down and bottom-up cues for scene text recognition. 2012 IEEE conference on computer vision and pattern recognition; 2012: IEEE. 10.1109/CVPR.2012.6247990

25. Roy S, Roy PP, Shivakumara P, Louloudis G, Tan CL, Pal U, editors. HMM-based multi oriented text recognition in natural scene image. 2013 2nd IAPR Asian Conference on Pattern Recognition; 2013: IEEE. 10.1109/ACPR.2013.60

26. Shivakumara P, Bhowmick S, Su B, Tan CL, Pal U, editors. A new gradient based character segmentation method for video text recognition. 2011 International conference on document analysis and recognition; 2011: IEEE. 10.1109/ICDAR.2011.34

27. Singh M, Kaur A, editors. An efficient hybrid scheme for key frame extraction and text localization in video. 2015 International conference on advances in computing, communications and informatics (ICACCI); 2015: IEEE. 10.1109/ICACCI.2015.7275784

28. Hamdan M, Cheriet M. ResneSt-Transformer: Joint attention segmentation-free for end-to-end handwriting paragraph recognition model. Array. 2023:100300. 10.1016/j.array.2023.100300

29. Xiao Z, Nie Z, Song C, Chronopoulos AT. An extended attention mechanism for scene text recognition. Expert Systems with Applications. 2022;203:117377. 10.1016/j.eswa.2022.117377

30. Gao F, Deng X, Xu M, Xu J, Dragotti PL. Multi-modal convolutional dictionary learning. IEEE Transactions on Image Processing. 2022;31:1325-39. 10.1109/TIP.2022.3141251

Persian Abstract

چکیده

در عصری که حفظ دانش و اطلاعات از کتاب ها و اسناد بسیار مهم است، روش های اسکن دستی سنتی خسته کننده و مستعد خطا هستند. این کار مستلزم مداخلات انسانی زیادی است و در نتیجه گاهی اوقات منجر به دیجیتالی شدن اشتباه می شود که کارهای پایین دستی مانند تشخیص کاراکترهای نوری را دشوار می کند. بنابراین، باید تکنیک‌های نوآورانه‌ای پیشنهاد شود که نه تنها تلاش انسان را از نظر دیجیتالی کردن کاهش می‌دهد، بلکه نتایج بسیار دقیقی را نسبت به تکنیک‌های پیشرفته اخیر ارائه می‌دهد. ما یک الگوریتم جدید مبتنی بر بینایی کامپیوتری را پیشنهاد کردیم که ویژگی‌های ماتریس هم‌وضعیت سطح خاکستری (GLCM) را با ویژگی‌های بافت ۱۰-اری Thepade (TSBTC) برای طبقه‌بندی فریم‌های ویدئویی ترکیب می‌کند. این رویکرد ترکیبی به طور قابل توجهی دقت انتخاب فریم را افزایش می دهد، دیجیتالی شدن با کیفیت بالا را تضمین می کند و چندین زبان و انواع سند را در خود جای می دهد. ما همچنین مجموعه داده‌ای از ۵۴۰۰۰ تصویر متنوع را برای نشان دادن اثربخشی الگوریتم خود در سناریوهای دنیای واقعی و مقایسه آن با روش‌های موجود پیشنهاد کرده‌ایم که سهم ارزشمندی در دیجیتال‌سازی اسناد دارد. مجموعه داده پیشنهادی را می توان برای چندین کار تجزیه و تحلیل تصویر سند مورد استفاده قرار داد.

International Journal of Engineering

J o u r n a l   H o m e p a g e :   w w w . i j e . i r

Design and Optimization of High-gain Series and Parallel-fed Array Antennas for Enhanced Gain and Front-to-back Ratio in X-Band Applications

T. P. S. Kumar Kusumanchi*, L. Pappula

Department of Electronics and Communication Engineering, Koneru Lakshmaiah Education Foundation, AP, India

P A P E R I N F O	*A B S T R A C T*

This study presents a comprehensive analysis of the design of a high-performance meta-material loaded square patch antenna arrays specifically tailored for X-band applications. To enhance the gain and front to back ratio (FTBR), a novel 1×3 series-fed linear array configuration that integrates solitary series-fed elements with metamaterial-based square patches at X-band frequencies is introduced. Later, parallel-fed 1×2 and 1×4 antenna arrays are designed by considering the series-fed antenna array as a single element for further enhancement of gain and FTBR. The single element 1×3 series fed array is fabricated with dimensions of $\lambda \times 3.5\lambda \times 0.028\lambda$, whereas the respective 1×2 and 1×4 parallel fed antenna arrays has the dimensions of $2.86\lambda \times 3.8\lambda \times 0.028\lambda$ and $2.86\lambda \times 4.3\lambda \times 0.028\lambda$, respectively. The Taconic substrate is chosen as the dielectric material, exhibiting a dielectric constant of 2.2 and a loss tangent of 0.0025. The empirical data presented substantiates the superior performance of the 1×4 parallel fed configuration. This is evident through the remarkable reflection coefficient of -25dB, the wide bandwidth spanning 47MHz, the substantial gain of 17.8dBi, and the FTBR of 30.7. The metrics serve to highlight the array's capacity in guaranteeing a superior level of signal fidelity, encompassing a wide frequency spectrum, amplifying incoming signals, and directing transmissions towards specific orientations. These metrics unequivocally validate its potential for advanced X-band applications.

doi: 10.5829/ije.2024.37.03c.12

Graphical Abstract
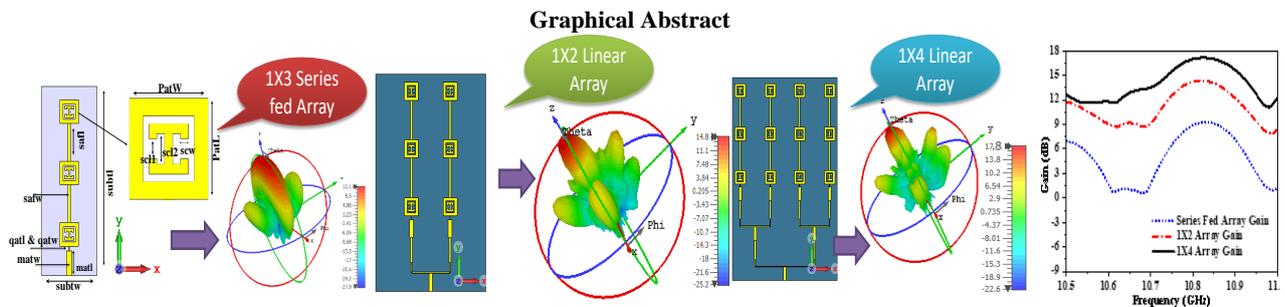
1. INTRODUCTION

The X-band, encompassing frequencies spanning from 8.0 GHz to 12.0 GHz, assumes a pivotal role within the electromagnetic spectrum, occupying a distinct position that facilitates its utilization across diverse domains such as radar systems, satellite communications, remote sensing, and scientific inquiry. In order to optimize the utilization of X-band technology, it is crucial to prioritize the advancement of antenna systems. The primary instantiation of remote sensing entails the application of satellite communication systems, contingent upon the condition of an atmosphere devoid of cloud cover, to acquire data of utmost quality. The effectiveness of

---

Corresponding Author Email: satishkumar8421@gmail.com (T. P. S. Kumar Kusumanchi)

satellite communication systems has been observed to be constrained during periods of reduced illumination, unfavorable meteorological circumstances such as storms, and in areas distinguished by high levels of vegetation coverage.

The central constituent of the x-band communication system is the sensing module, more precisely denoted as the Antenna module. In contemporary times, the escalating occurrence of perilous meteorological phenomena on a worldwide scale has instigated a notable upsurge in scholarly attention towards the investigation of economically viable and compact synthetic aperture radar (SAR) systems deployed in space (1). These technological systems exhibit significant promise in the realm of monitoring and evaluating natural disasters, encompassing a wide range of events such as tsunamis, typhoons, landslides, and volcanic eruptions. Their efficacy is particularly noteworthy in nations that are susceptible to these catastrophic occurrences (2). The antenna demonstrates multi-band functionality, accommodating both horizontal and vertical polarizations, thus serving as a vital constituent in synthetic aperture radar (SAR) systems. Both co-polarization and cross-polarization are essential elements in enabling the Synthetic Aperture Radar (SAR) antenna to efficiently capture and acquire data with exceptional detail (3). There is an imperative to alleviate the complexity associated with SAR antenna design, while also minimizing its physical dimensions, mass, and costs. This must be achieved while ensuring that the antenna meets the specified requirements for enhanced gain, multiple frequency bands, and dual polarizations. Owing to the exorbitant financial expenditure, considerable mass, and cumbersome physical proportions of the antennas utilized in synthetic aperture radar (SAR) applications. The X-band synthetic aperture radar (SAR) demonstrates a notable level of appropriateness for reconnaissance and disaster monitoring purposes, primarily due to its remarkable spatial resolution capabilities. Therefore, it is considered the most suitable option for the purpose of surveillance (4).

The effectiveness of systems undergoes degradation as a result of multiple factors, specifically side-lobe level, cross-polarization, co-polarization, front-to-back ratio, and half power beam width (HPBW) (5). In this particular instance, the radar antenna proficiently acquired the echo signal through the utilization of the back lobe or side lobe, facilitated by the presence of numerous reflections. Likewise, the transmission signals experienced scattering in a similar manner. This phenomenon leads to the detection of inaccuracies within the designated data, consequently leading to the manifestation of erroneous alerts. Microstrip antenna arrays, colloquially referred to as MSA arrays, manifest substantial promise across diverse domains, encompassing radar systems, satellite communications,

and wireless communication networks. The reduced mass, cost-effectiveness, and seamless compatibility with the feed network are key attributes of the aforementioned (6, 7). Arraying is a widely utilized technique in long-distance communication networks for the purpose of amplification enhancement. Arrays can be categorized into two discrete classifications based on their feeding methodology, specifically parallel-fed arrays and series-fed arrays (8).

The design of the feed network plays a pivotal role in configuring arrays of microstrip antennas (MSAs). In the context of microstrip arrays, employing a series feed mechanism that seamlessly integrates with each radiating element facilitates achieving in-phase excitation while ensuring consistent amplitude across these elements. However, this approach leads to increased side lobe levels (SLL) and heightened losses in the feedlines. The utilization of a technique referred to as series-feed has been implemented to address the issue of signal leakage and reduce losses in the feedline. This methodology presents the benefit of occupying a diminished physical space while efficiently tackling the aforementioned concerns. Furthermore, it is pertinent to highlight that array antenna configurations employing printed circuit boards (PCBs) exhibit distinctive attributes, including a reduced physical footprint and a lightweight construction. The aforementioned attributes render them exceptionally well-suited for implementation in millimeter-wave (MMW) scenarios, outperforming preceding metal-based configurations such as four quadrant horn arrays with reflectors and waveguide slot arrays (9, 10). Numerous comprehensive research studies have explored microstrip arrays, employing both parallel and series feed techniques (11-16), plate slot arrays (17), and substrate integrated waveguide (SIW) slot arrays (18-22).

Significant attention has been directed towards microstrip arrays, primarily due to their relatively simplified manufacturing process in comparison to substrate integrated waveguide (SIW) structures. Furthermore, these arrays offer improved convenience in achieving desired radiation patterns through various configurations of constituent elements and feed networks (23). The investigation employed a configuration comprising of six series-fed microstrip linear subarrays, as elucidated in the reference (24). The implemented configuration featured a distribution of tapered patch widths. The integration of the subarrays was accomplished by employing a single-end connecting Substrate Integrated Waveguide (SIW) parallel feed network. The configuration was intricately designed to manipulate geometric formations in both the horizontal and vertical cross-sectional planes. The investigation carried out by Zhao et al. (25) employed a set of patches featuring gradually decreasing widths and impedance transformers to construct a planar microstrip array that

was specifically engineered for the task of long-range automobile radar detection. Remarkably, an admirable accomplishment was observed in achieving an optimal first side lobe level (FSLL) of approximately -20 dB in both the E and H planes. Furthermore, the previously mentioned by Kothapudi and Kumar (26, 27) elucidated the execution of a 6-port 3 × 3 series-fed planar array and a 4-port 2 × 2 series-fed planar array, correspondingly. Both of these designs integrated excitations originating from two orthogonal directions, employing a chosen configuration to confer dual-polarized characteristics upon the arrays. The aforementioned attribute rendered them exceedingly suitable for integration into X-band airborne synthetic aperture radar (SAR) systems. Moreover, a K-band linear array comprising ten series-fed rectangular patches was postulated by Bayderkhani and Hassani (28).

This paper introduces a novel approach by incorporating series feeding, along with the utilization of a parallel feeding in the design. The results demonstrate the ability to accommodate a greater number of radiating elements in confined space, leading to the achievement of high gain. In contrast to conventional designs employing normal square patches, this study utilizes metamaterial square patches. The use of metamaterials allows for the creation of antenna elements with unique electromagnetic properties, facilitating miniaturization and enabling features such as Frequency Selectivity, Steerable, and Reconfigurable Antennas. The primary objective of this research is to design and fabricate a compact series-fed linear array tailored for X-band applications. The developed antenna prototype ensures optimal functionality at a frequency of 10.76GHz, placing it within the X-band spectrum.

This investigation employed Taconic TLY-5 as the substrate material due to its capacity to offer a diverse range of impedance bandwidth, peak gain, and high radiation efficiency. The final iteration of the antenna prototype features physical dimensions of 80×50×0.8mm³, operating at a frequency of 10.76 GHz. To optimize gain and FTBR (Front-to-Back Ratio), linear array configurations, specifically a 1×2 and a 1×4 parallel fed linear array, were implemented. These arrays exhibit minimal mutual coupling among their constituent elements, resulting in enhanced overall performance. The system demonstrated a notable improvement in amplification, making it well-suited for applications in the X-band.

The main objective of the paper is to present the design of a high gain and FTBR series-fed antenna arrays at X band frequencies. To realize, we introduced a novel unique 1×3 series-fed linear array configuration that integrates solitary series-fed elements with metamaterial-based square patches. Later, parallel-fed 1×2 and 1×4 antenna arrays are designed by considering the series-fed antenna array as a single element for further enhancement

of gain and FTBR.

The geometry of the proposed 1×3 series-fed antenna array with metamaterial-loaded rectangular patches is discussed in section 2. The selection mechanism of the proposed antenna array parameters is discussed in section 3. Section 4 presents elaborate discussions on the measured results of the proposed antenna array. In section 5, the design of parallel-fed 1×2 and 1×4 antenna arrays for further enhancement of gain and FTBR is discussed by considering the series-fed antenna array as a single element. The complete discussion of the proposed arrays' radiation characteristics is discussed in section 6. Section 7 summarizes the final conclusions of the article.

2. DESIGN OF BASIC 1×3 SERIES-FED ANTENNA ARRAY

Microstrip patch antennas are fabricated utilizing a dielectric substrate, which is encased by a conductive layer on both sides. In contrast, the upper surface of the substrate is incompletely covered, serving as the exclusive location for the patch elements and feeding line. The substrate material utilized in this investigation is Taconic TLY5, which possesses a dielectric constant of 2.2 and a loss tangent of 0.002. The substrate possesses a vertical dimension of 31 mil and is furnished with a copper cladding of 1 oz on each of its surfaces.

Antenna arrays combine multiple radiating elements, and feeding methods are critical in their architecture. Series feeding connects the primary feed line to all elements, while series feeding links components sequentially. In linear fed arrays, the primary element emits radiation, cascading feed power to subsequent elements.

The basic antenna configuration comprises a metamaterial loaded square patches are connected in series with a 50-Ω microstrip line, with a quarter-wave transformer etched onto the substrate's top surface. The matching between the radiating square patch and the 50-Ω microstrip line is achieved through a quarter-wave transformer. The current research endeavors to examine the stimulation of this sequence of elements by employing a unique feed port that has been meticulously designed to function at a precise frequency of 10.73 gigahertz. The array is stimulated directly via a microstrip feed line, wherein the series feeding of the array elements is situated at the uppermost region of the substrate. The terrestrial surface, conversely, is situated in the lowermost stratum of the substrate.

The Square patch width 'W' and length 'L' are calculated from the following expressions 1& 2.

$$W = \frac{(2M+1)}{\sqrt{\frac{\varepsilon_r+1}{2}}} \times \frac{\lambda_0}{2} \tag{1}$$

$$L = \frac{(2N+1)}{\sqrt{\varepsilon_{eff}}} \times \left(\frac{\lambda}{2}\right) - 2 \times \Delta L \qquad (2)$$

where M and N are non-negative integers (in our present design M=N=1).

The feedline width calculated by using below Equation 3.

$$W = \frac{7.48 \times h}{e^{\left(Z_0 \frac{\sqrt{\varepsilon_r+1.41}}{87}\right)}} - 1.25 \times t \qquad (3)$$

where h is height of the substrate t is the thickness of the copper.

The diagram depicted in Figure 1 showcases the geometric arrangement of a 1×3 series-fed square patch linear array, which includes a single RF antenna port. The process of optimizing a finite set of parameters at the resonant frequency of 10.76 gigahertz results in the attainment of the most advantageous reflection coefficient. The series-fed square patch linear array, possessing dimensions of 1×3, was efficiently fed by employing a matching transformer and a λ/4 impedance transformer. Both the matched transformer and the λ/4 impedance transformer are employed to optimize impedance matching between the radiating array and the feed. The establishment of a direct or series connection between the square elements is accomplished by utilizing microstrip lines with precise dimensions of safl and safw. The impedance characteristics of the matched transformer, quarter-wavelength impedance transformer, and matched feedlines interconnecting the patches are dependent on the dimensional attributes of the corresponding feedlines. The dimensional parameters of the matched transformer and λ/4 impedance transformer are denoted as matl, matw, qatl, and qatw, correspondingly.

Optimization techniques are utilized in order to augment the operational efficacy of the array, thereby facilitating the attainment of utmost gain and enhanced impedance matching. The present array is comprised of a solitary RF antenna port exhibiting a return loss characteristic. The array under consideration

demonstrates an impedance bandwidth spanning from 10.70 GHz to 10.74 GHz, with a bandwidth of 40 MHz.

Figure 2 depicts the surface current distribution, as well as the impact of the electric field (E-field) and magnetic field (H-field), for a 1×3 series-fed square patch linear array. This array is equipped with a single radio frequency (RF) antenna port, and the simulation was conducted using CST simulation software. The simulation was carried out with carefully optimized parameters. The specified dimensions for the optimized construction of the proposed 1×3 series -fed square patch linear array antenna are presented in Table 1.

3. SELECTION OF OPTIMAL PARAMETERS

The goal of the study was to determine the best parameters for a single RF antenna to analyze the
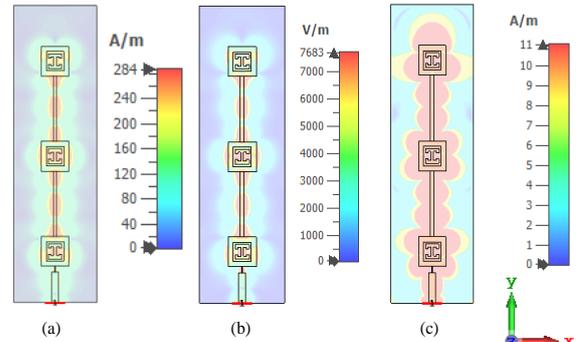
Figure 2. a) surface current, b) magnitude of E-field c) magnitude if H-field of the basic 1×3 series fed antenna array

TABLE 1. Geometrical Parameters of Antenna Array

Parameter	Parameter Description	Value (mm)
PatL	Square patch Length	10
PatW	Square patch Width	10
qatl	λ/4 impedance transformer Length	2
qatw	λ/4 impedance transformer Length Width	0.28
matl	Impedance Matching Transformer Length	10.25
matw	Impedance Matching Transformer Width	2.46
safl	Length of the series-fed line	22
safw	Width of the series-fed line	1.9
subtl	Antenna Substrate Length	80
subtw	Antenna Substrate Width	50
subth	Antenna Substrate Heigh	0.787
scw	Slot width	1
sc11	Slot1 small length	2
scl2	Slot1 long length	3

Figure 1. Construction and fabricated model of the basic 1×3 series fed antenna array

reflection coefficient of a proposed 1×3 series-fed square patch linear array. The matched transformer, λ/4 impedance transformer, and serried feedline dimensions are optimized, and the effect of their variation on return loss is investigated. The parameters that have been optimized include matw, matl, qatw, qatl, safw, and safl. The process of optimization entailed optimizing each parameter one at a time, holding the other parameters constant. Best results and improved impedance matching were found at qatl=2.8mm, qatw=0.5, matl=12mm, matw=3mm, safl=11mm, and safw=1.5mm using simulation software. Figure 3(a-e) presents a visual representation of the optimization results related to the suggested antenna.

3. 1. Varying Qatl   Figure 3a depicts the impact of varying the length of the λ/4 impedance transformer, with precise adjustments made in 0.2mm increments within the range of 1.5 to 5mm. Other parameters (qatw, matw, matl, safw, and safl) remain constant throughout the experiment. Superior impedance matching was achieved at 2.8 millimeters, resulting in favorable resonance at a frequency of 10.736GHz. The simulation indicated the antenna's operation within the X-band frequency range, specifically between 10.70GHz and 10.74GHz.

3. 2. Varying qatw   In Figure 3b, the impact of varying the width of the λ/4 impedance transformer is illustrated, with precise adjustments made using a 0.03mm step size within a range of 0.3mm to 1.5mm. Remaining parameters (qatl, matw, matl, safw, and safl) were held constant. Optimal impedance matching was achieved at a width of 0.5 millimeters. Simulation results showed resonance at 10.736 GHz, indicating excellent impedance matching, and the antenna functioned within the 10.70GHz to 10.74GHz X-band frequency range.

3. 3. Varying matl   Figure 3c illustrates the impact of varying the length of the matched transformer, systematically adjusted within the range of 5mm to 15mm with a 0.1mm step size. Parameters qatw, matw, qatl, safw, and safl are held constant. Enhanced impedance matching was observed at a length of 12 millimeters. Simulation results revealed resonance at 10.736GHz, indicating commendable impedance matching, and the antenna operated within the X-band frequency range, specifically between 10.70GHz and 10.74GHz.

3. 4. Varying matw   Figure 3d demonstrates the impact of varying the width of the matched transformer, systematically adjusted within the range of 2 to 4mm with a 0.1mm step size. Parameters qatw, mqatl, matl, safw, and safl are held constant. Superior impedance matching was achieved at a width of 3 millimeters. Simulation results indicated resonance at 10.736 GHz, showcasing

commendable impedance matching, and the antenna operated within the X-band frequency range, specifically between 10.70GHz and 10.74GHz.

3. 5. Varying Safw   In Figure 3e, the impact of varying the width of the series feedline connecting the patches is depicted, systematically adjusted within the range of 0.5mm to 3.5mm with a 0.2mm step size. Parameters qatw, matw, matl, qatl, and safl are held constant. Enhanced impedance matching was observed at a width of 1.5 millimeters. Simulation results indicated resonance at 10.736GHz, demonstrating commendable impedance matching, and the antenna operated within the X-band frequency range, specifically between 10.70GHz and 10.74GHz.

4 TEST RESULTS OF BASIC 1×3 SERIES FED ANTENNA ARRAY

The 1×3 series-fed square patch linear array, designed for X-band operation, has been fabricated and measured to validate simulation results. Figure 1 illustrates the fabricated prototype. Both simulated and measured data juxtaposition at the operational frequency range within the X-band. Figure 4a presents a comparison of simulated and fabricated reflection coefficients and it's demonstrates an impedance bandwidth of 40MHz, ranging from 10.70 GHz to 10.74 GHz, with a gain of 12.8dB. The electrical field the series fed array oriented perpendicular to the surface of the radiating patch, defining it as a vertically polarized antenna array. This
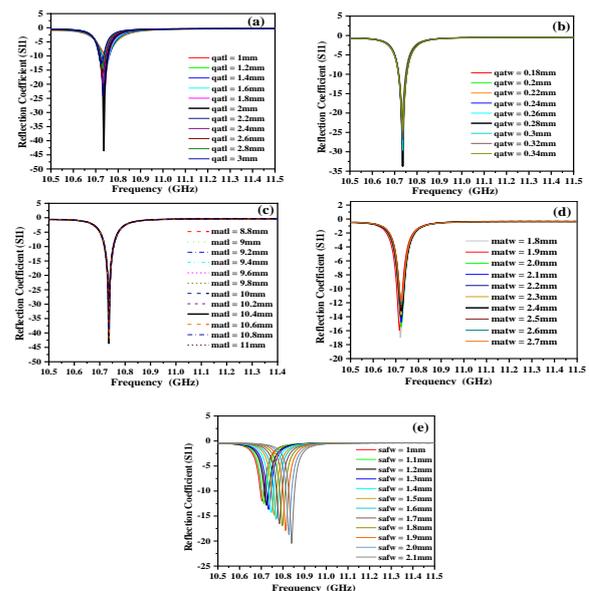
Figure 3. Reflection Coefficient of proposed antenna with various parameters a) qatl, b) qatw, c) matl, d) matw & e) safw

characteristic underscores the array's alignment for effective vertical polarization in its radiation pattern.

Figure 4(b & c). represents 2D Co and cross polarization graph of the proposed series fed element at 10.73 GHz. The outcome indicates that the radiation patterns exhibit directive characteristics, are vertically polarized, and have minimal sidelobe levels.

5. DESIGN OF PARALLEL FED 1×2, ANF 1×4 ANTENNA ARRAY IMPLEMENTATION

High gain antennas are essential for efficient signal propagation over long distances. Increasing antenna gain often involves using an array of elements rather than a single one. The cardinality of the array, or the number of elements, directly correlates with the antenna's gain. The signal feed network, distributing power across branches, is crucial in high-gain antenna construction. Variations in power divider arm length and width impact signal amplitude and phase, leading to changes in the angular range of beam scanning.

The array configuration employs parallel feeding with microstrip transmission lines for power division between the primary port and radiating elements. Linear power dividers (LPDs) are fabricated using a simple arrangement, dividing a single microstrip transmission line into two to bifurcate power into separate paths. The 1×4 parallel fed power divider arrangements, as depicted in Figure 5.
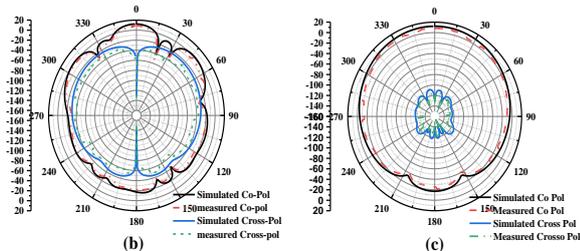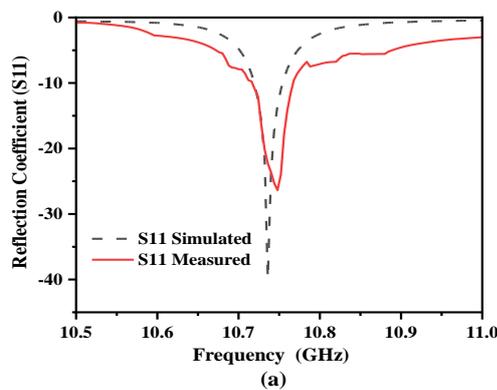
The selection was made to utilize the parallel or corporate feed methodology for the purpose of dividing the power into two distinct transmission lines. The proposed configuration involves the fabrication of a 1 x 2 array structure, accomplished by spatially segregating two 1×3 series-fed square patch linear arrays. The intentional setting of the separation distance between the individual elements is half of the wavelength.

The rationale behind this design decision is to effectively address the issue of gating lobes, which have the potential to negatively affect the overall performance of the array. The integration of a Stranded T-Junction power divider has been successfully incorporated into the corporate feed network design for the 1×2 parallel fed array. The Maximum Power Transfer Theorem is a fundamental principle widely utilized in the field of electrical engineering to facilitate the attainment of impedance matching. To augment the antenna gain, a configuration is deployed whereby two 1×2 corporate feeding networks are interconnected consecutively, leading to the establishment of a 1×4 parallel fed array. Through the utilization of a quarter-wave transformer, the transmission lines possessing an impedance of 100Ω are efficiently transformed into transmission lines exhibiting an impedance of 70.7Ω. Following this, the aforementioned lines are subsequently aligned with an inset feed configuration possessing an impedance of 50 Ω. The diagram illustrated in Figure 6 represents a unidimensional array with a size of 1×2. In contrast, the structure depicted in Figure 7 exemplifies a
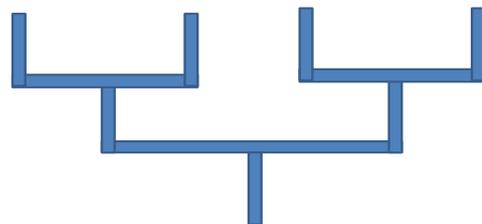

Figure 5. 1×4 parallel fed Power Divider

**Figure 4.** (a)Reflection Coefficient of proposed antenna (b) Gain theta Co and Cross polarization, (c) Gain Phi Co and Cross polarization
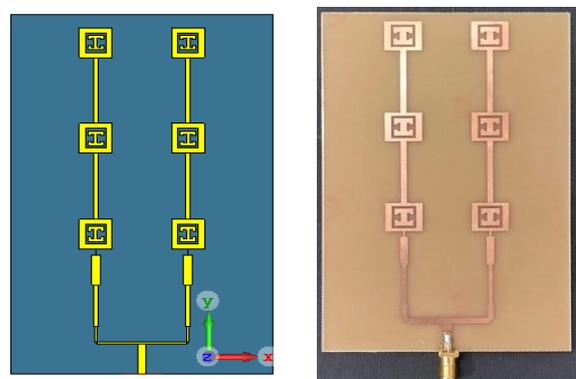
Figure 6. Simulated and fabricated model of 1×2 parallel fed antenna array

unidimensional array characterized by dimensions of 1×4 parallel fed antenna array.

6. RESULTS AND DISCUSSION

6. 1. Return Loss   Figures 8a and 8b depict the S11 parameters, which represent the reflection coefficient of the 1×2 and 1×4 parallel fed antenna arrays. The single-element patch antenna resonates at 10.732 GHz with a reflection coefficient of -34 dB and a bandwidth of 40 MHz. In the 1×2 parallel fed antenna array configuration, the antenna shows a return loss of -26.99 dB and a bandwidth of 37 MHz, peaking at a resonant frequency of 10.74 GHz. The 1×4 array antenna displays a reflection coefficient of -25.76 dB and a broader bandwidth of 47 MHz.

6. 2. Directivity   The directivity of a single element, 1×2, and 1×4 parallel fed antenna array at a frequency of 10.74 GHz was measured to determine the level of radiation intensity. The measured directivity was found to be 17.8dBi, which quantifies the amount of radiation emitted by the antenna. The directivity values for the single element, 1×2, and 1×4 parallel fed antenna array configurations are recorded as 13.52 dBi, 16.50 dBi, and 17.9 dBi, respectively. The directivity of a 1 x 4 array of

serried fed linear array exhibits superior performance in comparison to that of a single element antenna and a 1 x 2 array antenna.

6. 3. Gain   Figure 9 illustrates the Gain plot of a single element, 1 x 2, and 1 x 4 array antenna operating at a frequency of 10.74 GHz. The Gain plot exhibits a gain value of 17.8 dBi. The 1×3 series fed single element, 1×2, and 1×4 parallel fed antenna array configurations have achieved gains of 12.1 dBi, 14.9 dBi, and 17.8 dBi, respectively. The performance of a 1×4 parallel fed linear array exhibits superior gain when compared to that of a 1×3 series fed single element antenna and a 1×2 parallel fed antenna antenna.

6. 4. Co and Cross Polarization   Figure 10 (a & b) depicts the two-dimensional co-polarization and cross-polarization characteristics of the 1×2 parallel fed antenna array operating at a frequency of 10.74 GHz and Figures 11a, and 11b represents the two-dimensional co-polarization and cross-polarization characteristics of the array antennas operating at a frequency of 10.74 GHz. Based on the obtained results, it can be observed that the radiation patterns exhibit a directive characteristic. The current antenna arrays' Co and cross polarization graphs indicate that they possess cross polarization levels within acceptable limits and exhibit minimal side lobe levels (SLL). Figures 12a,12b, and 12c are represent the 3-dimensional gain of the 3 proposed arrays.
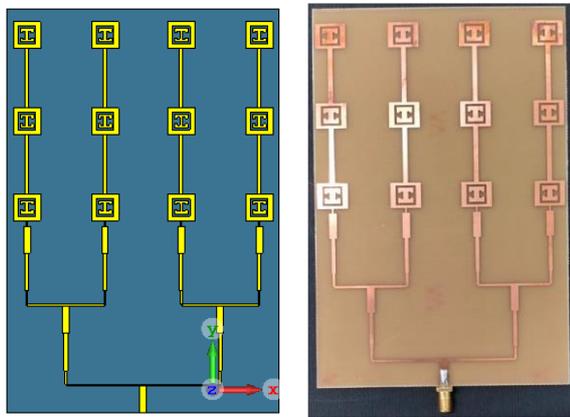
Figure 7. Simulated and fabricated model of 1×4 parallel fed antenna array

**Figure 9.** Gain Comparison between the Proposed 1×3 series fed, 1×2 and 1×4 parallel fed antenna arrays

Figure 8. a & b Simulated and Fabricated Reflection coefficient of 1×2 and 1×4 parallel fed antenna array
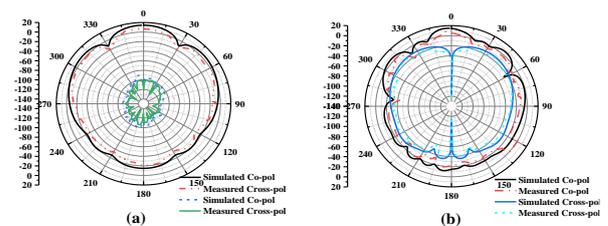
Figure 10. a & b 1×2 parallel fed array gain phi & theta co and cross polarization
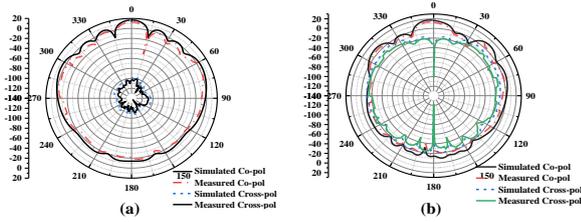
Figure 11. a & b 1×4 parallel fed array gain phi & theta co and cross polarization
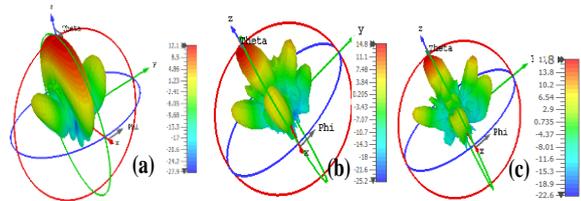
Figure 12. 3-Dimentional gain a)1×3 series fed b) 1×2 parallel fed, & c) 1×4 parallel fed antenna array

The performance characteristics of a single 1×3 series-fed, 1×2 parallel fed, and 1×4 parallel fed Microstrip patch antenna array are presented in Table 2.

Table 3 provides a thorough comparison of crucial parameters, encompassing antenna size, antenna gain, sidelobe levels, efficiency and FTBR, across the various designs proposed. This in-depth analysis aims to underscore the merits of the proposed antenna array designs, spanning from the 1×3 series-fed array to the 1×4 parallel fed linear array. The comparison specifically emphasizes the advantages such as substantial gain improvement, favorable FTBR.

A high FTBR in this context signifies that the proposed array exhibits maximum gain radiation in a specific direction, accompanied by low sidelobes. It serves as a key indicator of the array's effectiveness in focusing its radiation in the desired direction. However, it's essential to acknowledge a limitation of the proposed array, which lies in its suitability primarily for narrow-band applications.

TABLE 2. Comparison between the 3 proposed antenna arrays

Parameter		1×3 Series Fed antenna array	1×2 parallel fed antenna array	1×4 array parallel fed antenna array
Bandwidth		10.719-10.754 GHz (35MHz)	10.74-10.77 GHz (37MHz)	10.739-10.78 6GHz (47MHz)
Resonant Frequency		10.736GHz	10.76GHz	10.76GHz
Gain		12.1dB	14.8dB	17.8dB
Radiation Efficiency		82%	84%	86%
E-plane	SLL(dB)	-10.6dB	-9.5	-11.4
	HPBW(deg)	16.5	15.2	12.6
	Cross Pol(dB)	-24.2	-13.2	-10.7
	FTBR	30	25.6	30.7
H-plane	SLL(dB)	-10.6dB	-9.5	-11.4
	HPBW(deg)	16.5	15.2	12.6
	Cross Pol(dB)	-92	-90.2	-96.7
	FTBR	30	28.6	30.7

TABLE 3. Comparison of proposed work with previous series fed arrays

Ref no	No.of patches	Size (mm)	Working band	Gain	SLL	FTBR
(11)	2×2 patch array	50x42	X	12.4	-19	30
(12)	21×4 patch array	240 dia	X	22.4	-15	NA
(13)	4×4 patch array	210x210	C	18.4	-12	NA
(16)	Radial wave guide slot array	80 dia	X	18.1	-14.9	NA
(22)	3×3	80x80	K	12.2	-25.4	31
(23)	1×10	100x15	K	17.4	-26.3	37
(24)	6×6	150x150	X/K	17.2	-15	37
(8)	2×2	77x24	C	13.95	NA	NA
(11)	2×2	84x45	X	13.4	-19	NA
This work	**Series fed(1×3)**	**80x50**	**X**	**12.1**	**-10.6**	**٣٠**
This work	**1×2 parallel fed antenna array**	**120x100**	**X**	**14.8**	**-11.5**	**28.6**
This work	**1×4 parallel fed antenna array**	**150x120**	**X**	**17.4**	**-15**	**30.7**

7. CONCLUSION

A unique 1×3 series-fed linear array setup that integrates individual series-fed elements with square patches based on metamaterials at X-band frequencies is developed and discussed in this article. Furthermore, parallel-fed 1×2 and 1×4 antenna arrays are designed by considering the series-fed antenna array as a single element is designed. The outcomes of this design process encompass essential parameters such as the reflection coefficient, bandwidth, directivity, gain, and front-to-back ratio for all three proposed designs. The gain and FTBR are significantly increased while operating at the desired frequencies around 10.76 GHz. For example, it has been determined that the parallel fed 1×4 linear array is resonated with a bandwidth of 47 MHz at 10.76 Ghz. The measured gain is 17.8dBi, signifies the array's capacity to augment the received signal by amplifying its strength and enhancing its overall quality. It produced FTBR of 30.7 and radiation efficiency of 86%. All the designed arrays are vertically polarized. These obtained metrics offer a superior level of signal fidelity, amplify incoming signals, and direct transmissions towards specific orientations. The potential of the proposed arrays for advanced X-band applications is unequivocally confirmed by these metrics.

8. REFERENCES

1. Ravindra V, Akbar PR, Zhang M, Hirokawa J, Saito H, Oyama A. A Dual-Polarization $ X $-Band Traveling-Wave Antenna Panel for Small-Satellite Synthetic Aperture Radar. IEEE Transactions on Antennas and Propagation. 2017;65(5):2144-56. 10.1109/TAP.2017.2676760

2. Mao C-X, Gao S, Tienda C, Rommel T, Patyuchenko A, Younis M, et al. X/Ka-band dual-polarized digital beamforming synthetic aperture radar. IEEE Transactions on Microwave Theory and Techniques. 2017;65(11):4400-7. 10.1109/TMTT.2017.2690435

3. Rabideau DJ, Parker P, editors. Ubiquitous MIMO multifunction digital array radar. The Thrity-Seventh Asilomar Conference on Signals, Systems & Computers, 2003; 2003: IEEE.

4. Kuo F-Y, Hwang R-B. High-isolation X-band marine radar antenna design. IEEE Transactions on Antennas and Propagation. 2014;62(5):2331-7. 10.1109/TAP.2014.2307296

5. Skolnik MI. Radar handbook. 1970.

6. Li M, Tian S, Tang M-C, Zhu L. A compact low-profile hybrid-mode patch antenna with intrinsically combined self-decoupling and filtering properties. IEEE Transactions on Antennas and Propagation. 2021;70(2):1511-6. 10.1109/TAP.2021.3111638

7. Chang L, Liu H. Low-profile and miniaturized dual-band microstrip patch antenna for 5G mobile terminals. IEEE Transactions on Antennas and Propagation. 2021;70(3):2328-33. 10.1109/TAP. 2021.3118730

8. Wang B, Zhao Z, Sun K, Du C, Yang X, Yang D. Wideband Series-Fed Microstrip Patch Antenna Array With Flat Gain Based on Magnetic Current Feeding Technology. IEEE Antennas and Wireless Propagation Letters. 2022;22(4):834-8. 10.1109/LAWP.2022.3226461

9. Ling C, Rebeiz GM. 94 GHz integrated horn monopulse antennas. IEEE transactions on antennas and propagation. 1992;40(8):981-4. 10.1109/8.163437

10. Soltan A, Neshati M. Design and Development of High Gain, Low Profile and Circularly Polarized Cavity-backed Slot Antennas Using High-order Modes of Square Shaped Substrtae Integrated Waveguide Resonator. International Journal of Engineering, Transactions C: Aspects. 2017;30(12):1840-7. 10.5829/ije.2017.30.12c.04

11. Khatami SA, Meiguni J, Elahi AA-e, Rezaei P. Compact via-coupling fed monopulse antenna with orthogonal tracking capability in radiation pattern. IEEE Antennas and Wireless Propagation Letters. 2020;19(8):1443-6. 10.1109/LAWP.2020.3005023

12. Kumar H, Kumar G. Broadband monopulse microstrip antenna array for X-band monopulse tracking. IET Microwaves, Antennas & Propagation. 2018;12(13):2109-14. 10.1049/iet-map.2018.5332

13. Lamultree S, Phalla M, Kunkritthanachai P, Phongcharoenpanich C. Design of a Circular Patch Antenna with Parasitic Elements for 5G Applications. International Journal of Engineering. 2023;36(9):1686-94. 10.5829/ije.2023.36.09c.13

14. Fakharian M. A wideband fractal planar monopole antenna with a thin slot on radiating stub for radio frequency energy harvesting applications. International Journal of Engineering, Transactions B: Applications 2020;33(11):2181-7. 10.5829/IJE.2020.33.11B.08

15. Atamanesh M, Abbasi Arand B, Zahedi A. Wideband microstrip antenna array with simultaneously low sidelobe level in both sum and difference patterns. IET Microwaves, Antennas & Propagation. 2018;12(5):820-5. 10.1049/iet-map.2017.0494

16. Contreras A. Objective Functions for the Optimization of an Ultra Wideband Antenna. International Journal of Engineering. 2021;34(7):1743-9. 10.5829/ije.2021.34.07a.19

17. Aliasgari J, Atlasbaf Z. A novel compact monopulse parallel-plate slot array antenna. IEEE Antennas and Wireless Propagation Letters. 2015;15:762-5. 10.1109/LAWP.2015.2472462

18. Ying F, Ahmed F, Li R. A multiband multiple-input multiple-output antenna system for long term evolution and wireless local area networks handsets. International Journal of Engineering, Transactions B: Applications 2016;29(8):1087-93. 10.5829/idosi.ije.2016.29.08b.08

19. Cheng YJ, Hong W, Wu K. 94 GHz substrate integrated monopulse antenna array. IEEE transactions on antennas and propagation. 2011;60(1):121-9. 10.1109/TAP.2011.2167945

20. Dashti H. Design investigation of microstrip patch and half-mode substrate integrated waveguide cavity hybrid antenna arrays. International Journal of Engineering, Transactions B: Applications 2015;28(5):686-92. 10.5829/idosi.ije.2015.28.05b.06

21. Li W, Liu S, Deng J, Hu Z, Zhou Z. A compact SIW monopulse antenna array based on microstrip feed. IEEE Antennas and Wireless Propagation Letters. 2020;20(1):93-7. 10.1109/LAWP.2020.3041485

22. Yang T, Zhao Z, Yang D, Liu X, Liu Q-H. A single-layer SIW slots array monopulse antenna excited by a dual-mode resonator. IEEE Access. 2019;7:131282-8. 10.1109/ACCESS.2019.2940635

23. Menzel W, Moebius A. Antenna concepts for millimeter-wave automotive radar sensors. Proceedings of the IEEE. 2012;100(7):2372-9. 10.1109/JPROC.2012.2184729

24. Xu J, Hong W, Zhang H, Wang G, Yu Y, Jiang ZH. An array antenna for both long-and medium-range 77 GHz automotive radar applications. IEEE transactions on antennas and propagation. 2017;65(12):7207-16. 10.1109/TAP.2017.2761549

25. Zhao J, Zou L, Jiang R, Wang X, Gao H. Hybrid antenna arrays with high angular resolution for 77 GHz automotive radars. IEICE Electronics Express. 2020;17(2):20190687-. 10.1109/TAP.2017.2761549

26. Kothapudi VK, Kumar V. A 6-Port Two-Dimensional 3×3 Series-Fed Planar Array Antenna for Dual-Polarized X-Band Airborne Synthetic Aperture Radar Applications. Ieee Access. 2018;6:12001-7. 10.1109/ACCESS.2018.2810233

27. Kothapudi VK, Kumar V. Compact 1×2 and 2×2 dual polarized series-fed antenna array for X-band airborne synthetic aperture radar applications. Journal of electromagnetic engineering and science. 2018;18(2):117-28. 10.26866/jees.2018.18.2.117

28. Bayderkhani R, Hassani HR. Wideband and low sidelobe slot antenna fed by series-fed printed array. IEEE Transactions on Antennas and Propagation. 2010;58(12):3898-904. 10.1109/TAP.2010.2078437

Persian Abstract

چکیده

این مطالعه یک تجزیه و تحلیل جامع از طراحی آرایه‌های آنتن مربعی بارگذاری شده با متا مواد با کارایی بالا ارائه می‌کند که به طور خاص برای کاربردهای باند X طراحی شده است. برای افزایش بهره و نسبت جلو به عقب ((FTBR، یک پیکربندی جدید آرایه خطی با تغذیه سری ۳×۱ که عناصر تغذیه‌شده سری منفرد را با تکه‌های مربعی مبتنی بر فرا‌ماده در فرکانس‌های باند X معرفی می‌کند. بعدها، آرایه های آنتن ۲×۱ و ۴×۱ با تغذیه موازی با در نظر گرفتن آرایه آنتن سری به عنوان یک عنصر واحد برای افزایش بیشتر بهره و FTBR طراحی می شوند. آرایه تغذیه سری ۳×۱ تک عنصری با ابعاد ۰.۰۲۸λ×۳.۵λ×λ ساخته شده است، در حالی که آرایه های آنتن ۲×۱ تغذیه موازی و ۴×۱ دارای ابعاد ۰.۰۲۸λ×۳.۸λ×λ۲.۸۶ و ۲.۸۶. λ×۴.۳λ×۰.۰۲۸λ است. بستر Taconic به عنوان ماده دی الکتریک انتخاب می شود که ثابت دی الکتریک ۲.۲ و مماس تلفات ۰.۰۰۲۵ را نشان می دهد. داده های تجربی ارائه شده، عملکرد برتر پیکربندی تغذیه موازی ۴×۱ را اثبات می کند. این امر از طریق ضریب بازتاب قابل توجه dB۲۵–، پهنای باند وسیع ۴۷ مگاهرتز، بهره قابل توجه dBi۱۷۸ و FTBR 30.7 مشهود است. معیارها برای برجسته کردن ظرفیت آرایه در تضمین سطح برتر از وفاداری سیگنال، شامل طیف گسترده فرکانسی، تقویت سیگنال های دریافتی، و هدایت انتقال به سمت جهت گیری های خاص هستند. این معیارها به صراحت پتانسیل آن را برای برنامه های باند X پیشرفته تایید می کند.

International Journal of Engineering

An Investigation to Reduce the Cutting Force in CNC Slot Milling Operation by Forecasting Optimum Process Parameters and Develop Precise Mathematical Model for It

L. S. Patel*[a], V. P. Parekh[b], A. S. Vagh[c]

[a] Mechanical Engineering Department, Government Engineering College Sura, Gujarat Technological University, Gujarat, India
[b] Mechanical Engineering Department, SVIT-Vasad, Gujarat Technological University, Gujarat, India
[c] Liquid Terminal Department, Adani Hazira Port Limited, Surat, Gujarat, India

ABSTRACT

Industries frequently encounter several difficulties during milling operations, especially with cutting forces. Slot milling involves the machining of slots in materials using a milling cutter, and the challenges related to cutting forces can significantly impact the efficiency and quality of the milling process. CNC milling is widely used for machining of different types of materials in the manufacturing industry. Therefore, it is required to study process parameters and its behavior on materials which is not only to enhance the process but also make an effective and efficient path in metal cutting process. This research includes the effect of three input parameters i.e. feed rate, cutting speed and depth of cut on cutting force for Mild Steel. An empirical study gives the significant behavior of process or input parameter on machining properties. A mathematical study viz. ANOVA (Analysis of variance) gives the correlation in-between input or process parameters and machining or output properties for Mild Steel. It is also developed an equation for cutting force using a Regression model for the prediction of feed, speed and depth of cut. Values obtained from the mathematical models and Regression model was found to be very close to the data obtained from the experimental studies. The lowest cutting forces were obtained at high cutting speed and low feed rate and depth of cut.

doi: 10.5829/ije.2024.37.03c.13

Graphical Abstract
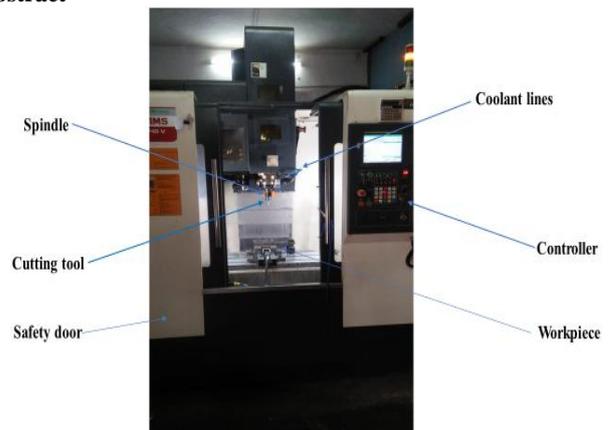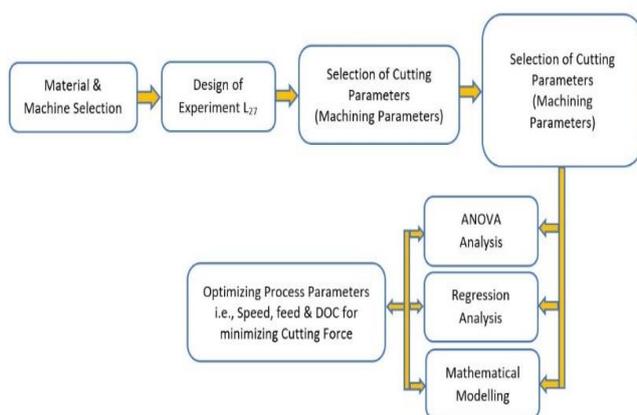
*Corresponding author email: lspatel82rp@gmail.com (L. S. Patel)

1. INTRODUCTION

Milling operations frequently cause problems for industries, such as tool wear, increased energy use, and shorter tool life. Excessive cutting forces can cause vibration and chatter during slot milling, leading to poor surface finish, dimensional inaccuracies. Controlling the cutting forces is essential to minimize vibrations and ensure smooth and accurate machining. The cutting forces can impose limitations on the material removal rate, restricting the efficiency and productivity of the slot milling process. Manufacturing sectors try to provide high-quality goods at a cheaper rate in order to retain competitive advantages in the market. A variety of metal cutting processes, such as turning, drilling, milling, boring, and others are used to make these items. Among these approaches, milling stands out as a commonly adopted metal cutting process used to manufacture planar surfaces with effectively material removal and high surface quality (1). Milling includes passing a workpiece through a revolving cylindrical tool fitted with several cutting blades (2). The main purpose of the art of metal cutting is to solve practical problems connected to the efficient and exact removal of metal from a workpiece. Achieving trustworthy and measurable forecasts of different technical performance metrics, preferably in the form of equations, is vital for creating optimization methods when determining cutting parameters during process design. By applying the technique of milling, machine components with specified dimensional precision and surface quality may be created on planar, obliquely, circular in shape and varied profile surfaces. The method is very profitable owing to the work of cutting instruments with several inserts. Surface quality is crucial for material for engineering, and surface roughness is a good measure of how well-surfaced a material is after it has been machined. It is impacted by elements including the workpiece's properties, the cutting environment, the material of the tool, and the shape (3). The significance of cutting forces in cutting processes cannot be overstated, as they directly influence several critical cutting performance factors. These factors include surface precision, tool wear, tool damage, cutting temperature, self-driven and forced vibrations, and others. The forces generated during metal cutting processes lead to deflections in the workpiece, tool, or machine structure, imparting energy to the machining system, which can lead to unstable vibrations or elevated temperatures. Hence, understanding and managing cutting forces are essential for optimizing the overall cutting process and achieving desired outcomes. In milling, excessive cutting pressures are undesirable because they lead to poor surface smoothness, dimensional errors, and more tool wear. The machinability of various materials is compared using measured cutting forces, which are also used for

continuous control and monitoring of cutting operations, tool wear, and failures. Calculating cutting forces is useful for establishing fixture design, bearing loads, and machine power needs (4). In order to achieve good machinability indices, the machining force is crucial (5). To attain the highest level of machining process efficiency throughout the last ten years, the metal cutting operation has seen substantial increase. The main goal in achieving this efficiency is often to provide the optimal machining parameters, which calls for the creation and use of efficient process control via parameter optimization (6). The behavior of the forces of cutting and their connection to chip production and machining damages in orthogonal cutting of composites made from fibers have been thoroughly investigated in another research (7). Numerous variables, such as tool shape, cutting settings, temperature, and tool wear, have an impact on the cutting process. Tool geometry parameters are one of them that significantly affect the surface product's quality (8, 9). However, milling presents unique difficulties for process modeling when compared to other machining techniques. Accurately describing a cutting-edge geometry is one such problem. It is challenging to establish a general geometric model that accurately describes milling tools due to the large range of tool forms. As a consequence, creating milling model for each unique cutter shape has been the traditional technique in the literature. Additionally, cutting forces and the creation of chips are significantly influenced by the geometry of the cutting edge and the method employed to prepare it (10). Target precision in machining processes necessitates thorough analysis of the best circumstances, taking into account things like resource conservation, cutting conditions, and the impact on the environment (11-14). Minimizing cutting power in slot milling is an exciting goal in addition to guaranteeing surface quality. Analysis of surface quality and energy utilization in dry cutting milling of austenitic stainless steel has been the topic of certain investigations (15). In order to determine cutting power and force at the tool tip in slot milling processes analytically, Liu et al. devised a model (16). By using mathematical structures, mathematical models may be used to represent important features of reality. When compared to alternative ways of collecting the fundamental understanding about reality, they are more cost- and convenience-effective (17, 18). A "model" is a collection of equations that explain and connect all the variables and parameters that comprise a physical system or process. The process of "modeling" entails determining suitable equations that can be solved for a system of variables and parameters used in a process. These remedies, also known as simulations, imitate the actions of real systems and processes. Modeling is widely used in the physical sciences and engineering fields, sometimes referred to as "Applied Mathematics." Additionally, it has found use in fields

like management science, finance, and economics that do not just focus on physical processes (19). In particular for slot milling on mild steel, this work proposes an effective mathematical model for calculating cutting forces and assessing cutting parameters in the milling process. The goal is to increase cutting force estimation's precision. After analyzing the literature, it is clear that this research makes a unique addition that may improve machining techniques since no other work of its like has been discovered. To avoid numerical integration, the model relies on curve fitting-based cutting force estimates. By using this model, the suggested ideal cutting circumstances are tested, and the optimal and nearly-optimal values of cutting parameters are identified based on optimum responses. The findings that have been provided might be useful for regional and global automotive businesses that work with related material families. The bulk machining and home metal cutting sectors both have comparable setups, making the study's conclusions valuable and helpful. In the context of this study, the development of an effective mathematical model for slot milling on mild steel opens up new possibilities for enhancing machining techniques and optimizing cutting processes. The proposed model's reliance on curve fitting-based cutting force estimates offers a more streamlined and accurate approach compared to traditional numerical integration methods. By using this model, researchers and engineers can gain deeper insights into the cutting forces involved in the milling process, leading to more informed decision-making and improved machining outcomes.

The use of appropriate cutting tools, optimizing cutting parameters, putting in place efficient cooling and lubrication systems, using the right workpiece fixturing, and utilizing advanced machining technologies, such as computer numerical control (CNC) and adaptive control systems, are just a few of the strategies and techniques that industries frequently use to address these challenges.

Moreover, the study's focus on slot milling on mild steel holds great significance for a wide range of industries, particularly those involved in automotive manufacturing, aerospace, and general machinery production. Mild steel is a commonly used material in these sectors due to its excellent mechanical properties, weldability, and affordability. Therefore, the findings of this research have the potential to impact numerous applications and contribute to advancements in various manufacturing processes. Furthermore, the optimization of cutting parameters based on the model's optimum responses can lead to substantial cost savings and resource conservation for companies. With the ability to identify optimal cutting conditions, manufacturers can reduce waste, minimize energy consumption, and extend the lifespan of cutting tools, ultimately increasing overall productivity and profitability. In addition to its practical implications, this study also advances the theoretical understanding of metal cutting processes, particularly in

the context of milling. By considering tool geometry parameters and their impact on surface quality, researchers can devise improved cutting tool designs that enhance material removal rates and minimize surface roughness. As the manufacturing industry continues to evolve, the demand for sustainable and environmentally-friendly processes becomes increasingly critical. The proposed mathematical model, along with its focus on resource conservation and energy utilization, aligns with the broader goal of achieving greater sustainability in manufacturing operations. Manufacturers can use the model's results to optimize cutting conditions and minimize energy-intensive processes, contributing to an eco-friendlier approach to production. Overall, the unique contribution of this research lies in its combination of mathematical modeling, cutting force estimation, and optimization techniques in the context of slot milling on mild steel. By enhancing machining efficiency, surface quality, and resource utilization, this study can empower manufacturers to stay at the forefront of innovation and maintain a competitive edge in today's fast-paced global market. The proposed mathematical model for slot milling on mild steel presents a promising approach to address the challenges and complexities of metal cutting processes. Through accurate cutting force estimation and optimization of cutting parameters, this research offers valuable insights and practical solutions for enhancing manufacturing techniques. As industries strive for greater efficiency and sustainability, the findings of this study have the potential to drive positive change, benefiting both businesses and the environment. With continuous research and application, the pursuit of excellence in metal cutting and machining will undoubtedly lead to further advancements in the field of manufacturing.

2. EXPERIMENTAL SETUP & METHODOLOGY

The slot milling experiments were conducted using a state-of-the-art CNC vertical machining center (VMC-ACE Micromatic), equipped with a powerful spindle capable of delivering up to 30 kW of power and reaching a maximum speed of 8000 rpm. This machining center provided the necessary precision and stability required to carry out the slot milling process with optimal control over cutting parameters. Figure 1 shows the general idea map to calculate the milling cutting force model. Figure 2 and Figure 3 shows experimental setup and slot milling machining process.

For the milling process, Tungsten Carbide milling inserts were carefully selected due to their excellent wear resistance and high cutting performance. These inserts are known for their ability to withstand the demanding conditions of metal cutting, ensuring prolonged tool life and consistent machining results.

To quantify and analyze the cutting forces during the
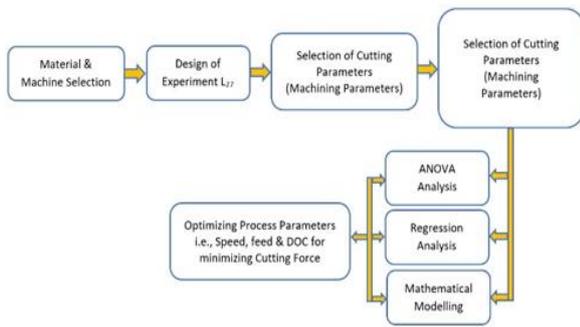
Figure 1. General idea map to calculate the milling cutting force model
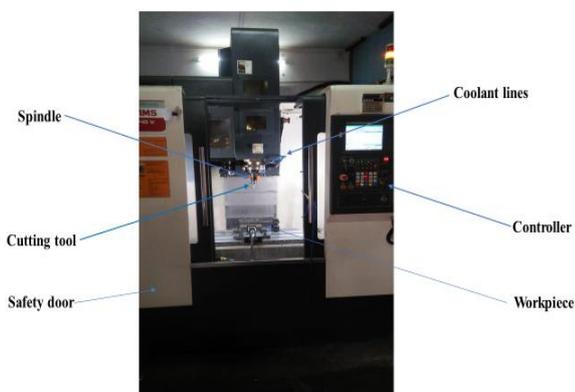
Figure 2. Experimental Setup for Slot milling operation

Figure 3. Machining Process

slot milling process, a mechanical dynamometer was employed. The dynamometer allowed for real-time measurement and recording of the cutting forces experienced during the milling operation. This data served as critical input for evaluating the machining performance and validating the mathematical model proposed in this study.

In order to efficiently design the experiments and analyze the collected data, the well-established Taguchi method was employed. Taguchi methodology is widely used in experimental design and optimization, offering robustness and efficiency in handling multiple variables simultaneously. The MINITAB Design of Experiment

(DOE) software, a reliable and widely accepted tool for conducting statistical analyses, was utilized for implementing the Taguchi method.

A Taguchi L27 Orthogonal array, chosen based on its optimal arrangement of experimental runs, was employed for conducting the slot milling experiments. This design enabled the systematic variation of cutting parameters, such as cutting speed, feed rate, and depth of cut, within a controlled and efficient experimental framework. The use of orthogonal arrays minimizes experimental errors and reduces the number of required experimental runs, making the process time-effective and resource-efficient.

The data obtained from the Taguchi experiments were then used to develop a regression model. This model established a mathematical relationship between the cutting parameters (speed, feed, and depth of cut) and the cutting forces experienced during the slot milling process. By analyzing the regression model (20), researchers gained valuable insights into the impact of each parameter on cutting forces, enabling them to identify the optimal combination of cutting conditions for achieving desired machining outcomes.

The combination of advanced machining equipment, precise measurement techniques, and the systematic Taguchi experimental design showcases the meticulousness and rigor employed in this research. The comprehensive approach adopted in this study ensured that the results and findings are reliable, repeatable, and applicable in real-world manufacturing scenarios.

The utilization of Tungsten Carbide milling inserts, in conjunction with the CNC vertical machining center, demonstrated the practicality and industry relevance of the research. The proposed mathematical model, backed by experimental validation, promises to enhance the understanding and control of slot milling on mild steel, leading to improved machining efficiency and surface quality.

Overall, this chapter's experimental setup and methodology embody the pursuit of scientific excellence and the commitment to optimizing metal cutting processes. The combination of innovative technology, robust experimental design, and advanced statistical analysis sets a solid foundation for the subsequent analysis and discussion of results, which can contribute to advancements in manufacturing practices and benefit various industrial sectors.

Table 1 shows the different variable factors and their levels for experimentation work.

3. RESULT AND DISCUSSION

3. 1. ANOVA for Cutting Force   From the response diagram in Figure 4, It is observed that if speed is increased, cutting force getting increased. If feed is increased then cutting force also get increased. Similarly

with increase in depth of cut, cutting force get increased. This analysis is carried out using an experimental data in Table 2.

In ANOVA analysis first of all S/N ratio is considered. The values of S/N ratios are given in Table 3.

TABLE 1. Variable Factors and their levels

Factors level	Speed (m/min)	Feed (mm/min)	Depth of cut (mm)
	A	B	C
1	10	6	1
2	13	9	1.5
3	16	12	2

Figure 4. Response diagram for cutting forces

TABLE 2. Experimental data for depth and cutting force

Sr. No.	Doc (mm)	Feed (mm/min)	Speed (m/min)	Cutting Force (N)
1	1	6	10	33.18
2	1	6	13	32.71
3	1	6	16	40
4	1	9	10	37.17
5	1	9	13	34.99
6	1	9	16	33.19
7	1	12	10	40.28
8	1	12	13	36.75
9	1	12	16	34.02
10	1.5	6	10	35.75
11	1.5	6	13	33.18
12	1.5	6	16	31.25
13	1.5	9	10	39.66
14	1.5	9	13	36.11
15	1.5	9	16	34.39
16	1.5	12	10	42.55
17	1.5	12	13	39.27
18	1.5	12	16	37.21
19	2	6	10	35.96
20	2	6	13	33.71
21	2	6	16	32.08
22	2	9	10	42.04
23	2	9	13	40.15
24	2	9	16	34.45
25	2	12	10	48.08
26	2	12	13	42.63
27	2	12	16	37.56

TABLE 3. S/N ratios cutting force

Experiment No.	Cutting Force		S/ N Ratio
	Set 1	Set 2	
1	3.17	3.60	-10.61
2	3.62	3.67	-11.24
3	3.82	3.52	-11.30
4	3.52	4.06	-11.60
5	3.88	4.21	-12.15
6	4.34	4.24	-12.65
7	3.73	4.49	-12.31
8	4.4	4.28	-12.75
9	5.11	4.70	-13.82
10	3.3	3.29	-10.47
11	3.42	3.35	-10.59
12	3.64	3.24	-10.75
13	3.41	3.73	-11.06
14	3.64	3.73	-11.33
15	4.10	4.09	-12.25
16	3.59	3.91	-11.49
17	4.05	3.96	-12.05
18	4.62	4.08	-12.79
19	3.29	3.03	-10.01
20	3.23	3.15	-10.08
21	3.43	3.12	-10.31
22	3.32	3.45	-10.60
23	3.43	3.59	-10.91
24	3.70	3.53	-11.17
25	3.41	3.54	-10.81
26	3.85	3.75	-11.59
27	4.04	3.63	-11.68

3. 1. 1. CALCULATIONS FOR SIGNAL TO NOISE (S / N) RATIO

The S/N ratio, as described below, is utilized to evaluate the machining quality characteristic of force, which follows the principle of "smaller the better" (21).

$$\eta = -10 \log \left[\sum_{u=1}^{Ni} \frac{y_u^2}{Ni} \right] \tag{1}$$

Table 2 presents the data for the machining characteristic (force) and the corresponding S/N ratios, which were calculated using Equation 1 in the repeated trial condition. The trials were performed n times, and the responses for each trial, denoted as y1, y2, ..., yn, were used in the calculations. There are a total of 27 trials represented in the table, showcasing the resulting S/N ratios alongside the raw force data.

3. 1. 2. Response Table for Cutting Force

The sum of S/N ratios for different levels is done which is given in Table 4. Cutting force is being smaller the better characteristics. From the Table 4, it is observed that A1-B3-C3 is an optimum combination of parameters. It means Speed of 10 m/min; Feed of 12 mm / min & Depth of cut of 2mm is an optimum combination of parameters to obtain minimum cutting force.

Now,

$$M = (1/27) \sum_{i=1}^{3} A_i = \left(\frac{1}{27}\right) * (-3019.702) = -111.841 \tag{2}$$

3. 1. 3. Analysis of Variance (ANOVA) for Cutting Force

ANOVA is utilized to examine the processes that have a significant impact on the quality characteristics. The details are mentioned in Table 4. The calculations are performed using the following Equations3, where the readings for factor A at each level are utilized to demonstrate the calculations. The calculations for factors B and C are mentioned in Table 5.

Sum of square SS for factor A can be calculated by:

$$\text{Sum of square SS} = 3 * [(M_{A1} - M)^2 + (M_{A2} - M)^2 + (M_{A3} - M)^2] = 279.667 \tag{3}$$

Similarly SS for factors B and C can be calculated. Then,

TABLE 4. Level Totals for S/N ratios

Factors	A	B	C
Levels	Speed	Feed	D.O.C.
1	-1068.99	-927.52	-981.66
2	-1004.56	-1023.51	-1007.29
3	-946.15	-1068.67	-1030.75
Total	-3019.70	-3019.70	-3019.70

Mean Square MS = SS/ Degree of Freedom =
279.667/2= 139.883 $\tag{4}$

Similarly MS can be calculated for factors B and C.

Table 6 summarized the ANOVA analysis for cutting force.

Aforementioned table represents ANOVA for cutting force analysis; it is observed that "feed" is the most significant parameter affecting cutting force with 54% significance. The significant of speed and depth of cut is found to be 39% and 6%, respectively.

In the current case, the error variance or error mean square is determined by dividing the sum of squares (SS) with the lowest value by its degree of freedom.

$$\text{Error Variance } \sigma_e^2 = \frac{Sum\ of\ Squares\ due\ to\ error}{Degree\ of\ freedom\ due\ to\ error} = \frac{44.665}{2} = 22.33 \tag{5}$$

The F-Test (21, 22) is employed to identify the process parameters that have a substantial impact on the quality characteristics. The variance ratio denoted by F is given by $F = MS / \sigma_e^2$. A higher value of F indicates that the factor's effect is significantly greater compared to the error variance. When a particular factor contributes more to the total sum of squares, it has a greater ability to influence η. This influence is expressed as a percent contribution (%P), which is calculated as follows

$$\%P = SS / \text{Total sum of SS} \tag{6}$$

3. 1. 4. Contour Plot Analysis for Cutting Force

Graphs are useful tools for visualizing the response surface of a variable. However, when there are more than two independent variables, it becomes challenging or nearly impossible to represent the response surface graphically due to the limitations of three-dimensional visualization. For better understanding contour plots are developed using MINITAB 14.0 software.

TABLE 5. Average η by factor level

Factors	A	B	C
Levels	Speed	Feed	D.O.C.
1	-118.78	-103.06	-109.08
2	-111.62	-113.72	-111.92
3	-105.13	-118.74	-114.53

TABLE 6. ANOVA for cutting force analysis

Factors	SS	DF	MS	F	%P
Speed	279.67	2	139.83	6.26	39.43
Feed	384.89	2	192.44	8.62	54.27
D.O.C.	44.66	2	22.332	1	6.3
Total	709.22	6	354.61	-	100.00

As shown in Figure 5 for higher speed and lower feed, cutting force value is smaller and as feed is increase, cutting force would increase. As illustrated in Figure 6 for lower depth of cut and higher speed, force would be decrease, and as D.O.C. is increased, cutting force would increase as well.

As shown in Figure 7 for lower feed and depth of cut, cutting force is less. As feed and D.O.C. are increase; cutting force would also increase.

3. 1. 5. Co-Relation of Process Parameters
The co relations between the factors cutting speed, feed, depth of cut, cutting force are obtained by multiple linear regression analysis. The quality characteristic used for

the force is 'smaller the better'. The regression equations are obtained from MINITAB software 14.0. The regression equations are given in Equation 7 as below. The regression equation is

$$\text{Force} = 33.1 - 0.917S + 1.10\,f + 3.71\,d_c \tag{7}$$

where, S= Speed, f = Feed, d_c = Depth of cut

4. EMPIRICAL MODELING FOR CNC MILLING PROCESS PARAMETERS

4. 1. Modeling for Cutting Force
To develop an empirical model, the depth of cut is kept constant and its value will remain 1 for different values of feed and speed mentioned in Table 7. The quadratic graph as shown in Figure 8 of force vs speed for different values of feed, as shown in quadratic graph, if cutting speed is increase, cutting force would decrease. And from graph three quadratic equations are obtained.

As shown in Figure 8, three equations are obtained in the form of Force=aS^2+bS+c. Here a, b and c are constants and S represent speed. Values of the constants are separated from the equations and mentioned them in below Table 8 for future reference.

Now in the second step, from the constants vs feed graph, again three equations are obtained for depth of cut = 1mm.These equations are in the form of Force, speed and Feed [17]. For DOC=1mm, values of constants are mentioned in below Table 9. Tables 10 to13 summarized experimental data for different D.O.C. Table 4 stated the Values of constant related to feed.

Figure 5. contour plot of cutting forces vs speed, feed
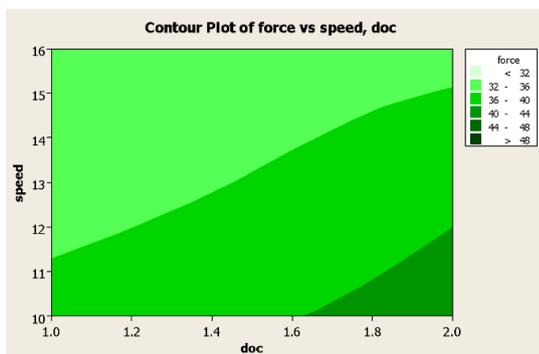
**Figure 6.** Contour plot of cutting forces vs speed, D.O.C
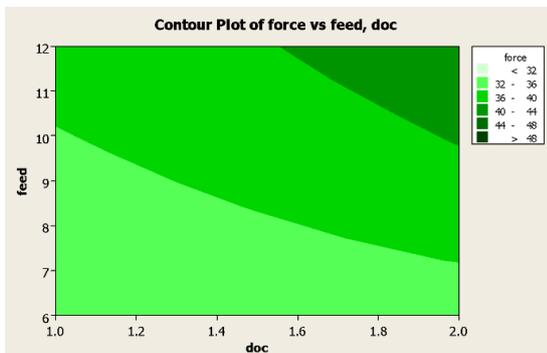
Figure 7. contour plot of cutting forces vs Feed, D.O.C

TABLE 7. DOC= 1mm

| Speed (m/min)	10	13	16	Feed (mm/min)
Force (N)	33.18	32.77	30.99	6
Force (N)	37.17	34.99	33.19	9
Force (N)	40.28	36.75	34.02	12
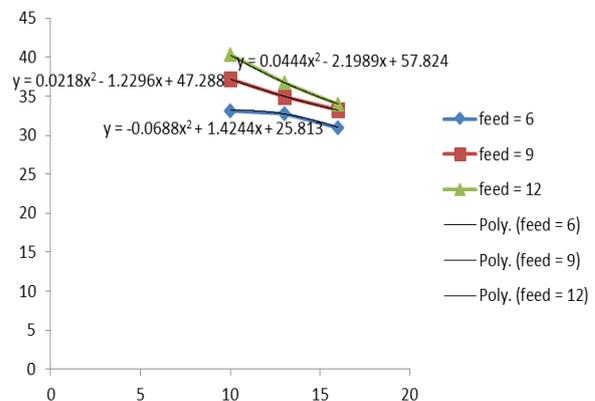
Figure 8. Plot of force Vs Speed at constant DOC = 1 mm

TABLE 8. Values of the constants related to feed

Feed	6	9	12
A	-0.068	0.021	0.044
B	1.424	-1.229	-2.198
C	25.81	47.28	57.82

TABLE 9. D.O.C. = 1mm

Constant	1	1.5	2
d	-0.003	-	-
e	0.084	-	-
g	-0.444	-	-
h	0.093	-	-
I	-2.287	-	-
j	11.78	-	-
k	-0.607	-	-
l	16.26	-	-
m	-49.92	-	-

TABLE 10. D.O.C. = 1.5 mm

Speed	10	13	16	Feed (mm/min)
Force	35.75	33.18	31.25	6
Force	39.66	36.11	34.39	9
Force	42.55	39.27	37.21	12

TABLE 11. D.O.C. = 1.5 mm

Feed	6	9	12
a	0.035	0.101	0.067
b	-1.674	-3.521	-2.652
c	48.93	64.71	62.29

TABLE 12. D.O.C. = 1, 1.5 mm

Constant	1	1.5	2
D	-0.003	-0.005	-
E	0.084	0.105	-
G	-0.444	-0.397	-
H	0.093	0.15	-
I	-2.287	-2.879	-
J	11.78	10.16	-
K	-0.607	-1.011	-
L	16.26	20.42	-
M	-49.92	-37.23	-

TABLE 13. D.O.C. = 2 mm

| Speed	10	13	16	Feed (mm/min)
Force	35.96	33.71	32.08	6
Force	42.04	40.15	34.45	9
Force	48.08	42.63	37.56	12

Figures 9 shows the plot of constant Vs Speed at constant DOC = 1 mm. Figure 10 illustrates the plot of force Vs feed at constant DOC = 1.5 mm. The plot of constants Vs feed at constant DOC = 1.5 mm is shown in Figure 11.

Figure 12 shows the plot of force Vs Speed at constant DOC = 2 mm. The plot of constants Vs feed at constant DOC = 2 mm is shown in Figure 13. The plot of constants Vs DOC is shown in Figure 14. The below Table 15 shows the different values of constants for depth of cut 1, 1.5 and 2 mm.

The quadratic graph as shown in below of constants vs different values of depth of cut.

Finally, from above graph below equation is obtained in the form of speed, feed, depth of cut and force.
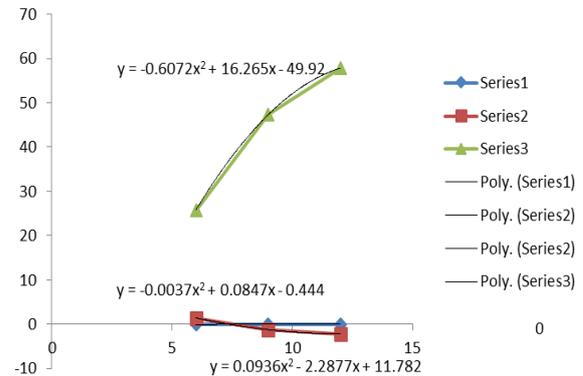
Figure 9. Plot of constant Vs Speed at constant DOC = 1 mm
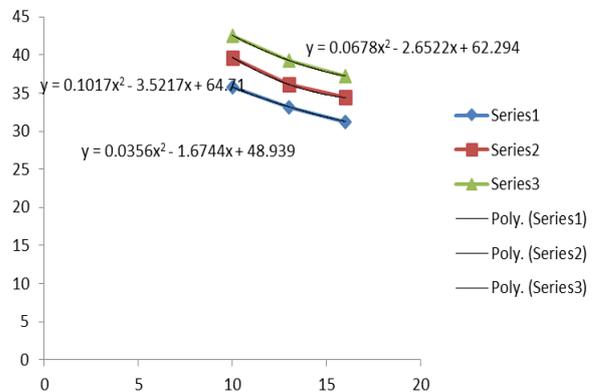
**Figure 10.** Plot of force Vs feed at constant DOC = 1.5 mm
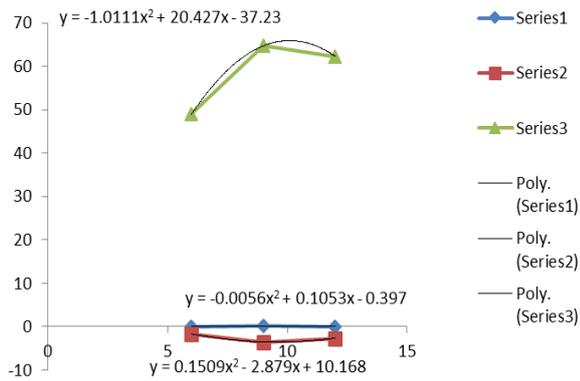
Figure 11. Plot of constants Vs feed at constant DOC = 1.5 mm

TABLE 15. D.O.C. =1, 1.5, 2 mm

Constant	1	1.5	2
D	-0.003	-0.005	0.026
E	0.084	0.105	-0.479
G	-0.444	-0.397	1.955
H	0.093	0.15	-0.684
I	-2.287	-2.879	12.19
J	11.78	10.16	-50.06
K	-0.607	-1.011	4.182
L	16.26	20.42	-71.77
M	-49.92	-37.23	327.9
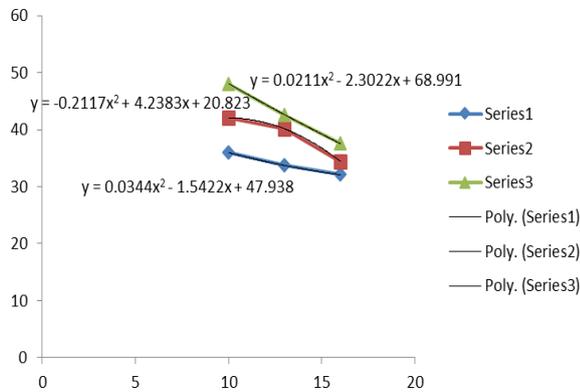
Figure 12. Plot of force Vs Speed at constant DOC = 2 mm
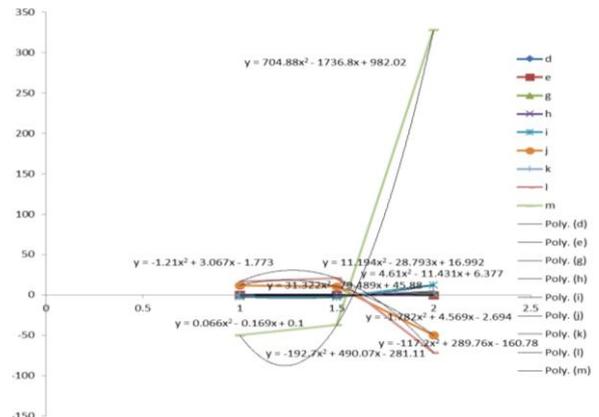
Figure 14. Plot of constants Vs DOC

TABLE 14. Values of constant related to feed

Feed	6	9	12
A	0.034	-0.211	0.021
B	-1.542	4.238	-2.302
C	47.93	20.82	68.99

Cutting force = $[(0.066d_c^2 – 0.169d_c + 0.1)$ $f^2 + (-1.21d_c^2 + 3.067d_c – 1.773)$ f $+ (4.61d_c^2 – 11.43d_c + 6.377)]S^2 + [(-1.782dc2 + 4.569d_c – 2.693)$ $f^2 + (31.32d_c^2 – 79.48d_c + 45.88)$ f $+ (-117.2d_c^2 + 289.7d_c – 160.7)]$ S $+ [(11.19d_c^2 – 28.79d_c + 16.99)f^2 + (-192.7d_c^2 + 490d_c – 281.1)f + (704.8d_c^2 – 1736d_c + 982)]$ (8)

where, S= Speed, f = Feed, d_c = Depth of cut

Figure 13. Plot of constants Vs feed at constant DOC = 2 mm

5. CONCLUSION

This study presents the results of an experimental investigation that examines how the feed rate, cutting speed, and depth of cut impact the cutting force in mild steel. It is found from the ANOVA (Analysis of variance), cutting force would be decreased with the increase of speed, and it would be increased with increase in feed and depth of cut. Thus, higher cutting speed is desired for minimizing cutting force requirement. By using an empirical & regression model, an equation has been developed for force to predict feed, speed and depth of cut. The validation equation has been checked by

putting experimental data and similar values are obtained from all equations for Force. This approach can be utilized to quickly determine the optimal cutting parameters during machining, especially in situations where there is limited time for extensive experimental analysis.

6. REFERENCES

1. Qehaja N, Jakupi K, Bunjaku A, Bruçi M, Osmani H. Effect of machining parameters and machining time on surface roughness in dry turning process. Procedia Engineering. 2015;100:135-40. https://doi:10.1016/j.proeng.2015.01.351

2. Giridharan R, Kumar P, Vijayakumar P, Tamilselvan R. Experimental investigation and design optimization of end milling process parameters on monel 400 by Taguchi method. Int J Mech Eng Technol. 2017;8(2):113-22.

3. Özel T, Karpat Y. Predictive modeling of surface roughness and tool wear in hard turning using regression and neural networks. International journal of machine tools and manufacture. 2005;45(4-5):467-79. https://doi.org/10.1016/j.ijmachtools.2004.09.007

4. Kalidass S, Ravikumar TM. Cutting force prediction in end milling process of aisi 304 steel using solid carbide tools. International Journal of Engineering-Transactions A: Basics. 2015;28(7):1074-81. https://doi.org/10.5829/ije.2022.35.06c.08

5. Prasanth I, Ravishankar D, Manzoor Hussain M. Analysis of milling process parameters and their influence on glass fiber reinforced polymer composites (research note). International Journal of Engineering. 2017;30(7):1074-80. https://doi.org/10.5829/ije.2017.30.07a.17

6. Zainal Z, Rusli N, Shuaib N. Effect of Cutting Environment and Swept Angle Selection in Milling Operation. International Journal of Engineering. 2021;34(12):2578-84. https://doi.org/10.5829/ije.2021.34.12c.02

7. Sheikh-Ahmad J, El-Hofy M, Almaskari F, Kerrigan K, Takikawa Y. The evolution of cutting forces during slot milling of unidirectional carbon fiber reinforced polymer (UD-CFRP) composites. Procedia CIRP. 2019;85:127-32. https://doi.org/10.1016/j.procir.2019.09.043

8. Gao X, Cheng X, Ling S, Zheng G, Li Y, Liu H. Research on optimization of micro-milling process for curved thin wall structure. Precision Engineering. 2022;73:296-312. https://doi.org/10.1016/j.precisioneng.2021.09.015

9. Venkata Vishnu A, Sudhakar Babu S. Mathematical modeling & multi response optimization for improving machinability of alloy steel using RSM, GRA and Jaya algorithm. International Journal of Engineering. 2021;34(9):2157-66. https://doi.org/10.5829/ije.2021.34.09C.13

10. Denkena B, Biermann D. Cutting edge geometries. CIRP annals. 2014;63(2):631-53. https://doi.org/10.1016/j.cirp.2014.05.009

11. Lu Q, Zhou G, Zhao F, Ren Y, Li L, Luan X, et al. Topology optimization of oilstone components considering carbon emissions associated with honing processes. Journal of Cleaner Production. 2019;225:181-95. https://doi.org/10.1016/j.jclepro.2019.03.273

12. Camposeco-Negrete C, de Dios Calderón-Nájera J. Optimization of energy consumption and surface roughness in slot milling of AISI 6061 T6 using the response surface method. The International Journal of Advanced Manufacturing Technology. 2019;103:4063-9. https://doi.org/10.1007/s00170-019-03848-2

13. Zhou G, Lu Q, Xiao Z, Zhou C, Tian C. Cutting parameter optimization for machining operations considering carbon emissions. Journal of Cleaner Production. 2019;208:937-50. https://doi.org/10.1016/j.jclepro.2018.10.191

14. Sihag N, Sangwan KS. Development of a multi-criteria optimization model for minimizing carbon emissions and processing time during machining. Procedia Cirp. 2018;69:300-5. https://doi.org/10.1016/j.procir.2017.11.060

15. Muñoz-Escalona P, Shokrani A, Dhokia V, Imani-Asrai R, Newman ST, editors. A surface roughness and power consumption analysis when slot milling austenitic stainless steel in a dry cutting environment. Advances in Sustainable and Competitive Manufacturing Systems: 23rd International Conference on Flexible Automation & Intelligent Manufacturing; 2013: Springer.

16. Liu N, Zhang Y, Lu W. A hybrid approach to energy consumption modelling based on cutting power: a milling case. Journal of Cleaner Production. 2015;104:264-72. https://doi.org/10.1016/j.jclepro.2015.05.049

17. Davis D. Nomography and Empirical Equations. Reinhold. New York/Chapman & Hall, London; 1962.

18. Nguyen VN, Van Cao V. Experimental and Analytical Study on Postfire Reinforced Concrete Beams Retrofitted with CFRP in Flexure and Shear. Civil Engineering Journal. 2023;9(7):1610-29. http://dx.doi.org/10.28991/CEJ-2023-09-07-05

19. Gandhi A, Raval H. Analytical and empirical modeling of top roller position for three-roller cylindrical bending of plates and its experimental verification. Journal of materials processing technology. 2008;197(1-3):268-78. https://doi.org/10.1016/j.jmatprotec.2007.06.033

20. Mohammed AH, Mubarak HM, Hussein AK, Abulghafour TZ, Nassani DE. Punching Shear Characterization of Steel Fiber-Reinforced Concrete Flat Slabs. HighTech and Innovation Journal. 2022;3(4):483-90. http://dx.doi.org/10.28991/HIJ-2022-03-04-08

21. Gupta S. Fundamentals of Statistics: Sixth Revised & Enlarged Edition. Himalaya Publishing House, Delhi, Mumbia pp; 2011.

22. Gupta S. Statistical methods, sultan chand & sons. New Delhi. 2001;21.

<div align="center">Persian Abstract</div>

<div dir="rtl">

چکیده

صنایع اغلب در طول عملیات آسیاب، به ویژه با نیروهای برش، با مشکلات متعددی مواجه می شوند. فرز اسلات شامل ماشینکاری شیارها در مواد با استفاده از فرز برش است و چالش های مربوط به نیروهای برش می تواند به طور قابل توجهی بر کارایی و کیفیت فرآیند آسیاب تأثیر بگذارد. فرز CNC به طور گسترده ای برای ماشینکاری انواع مختلف مواد در صنعت تولید استفاده می شود. بنابراین، بررسی پارامترهای فرآیند و رفتار آن بر روی مواد مورد نیاز است که علاوه بر بهبود فرآیند، مسیری موثر و کارآمد در فرآیند برش فلز ایجاد کند. این تحقیق شامل تأثیر سه پارامتر ورودی یعنی نرخ تغذیه، سرعت برش و عمق برش بر نیروی برش فولاد ملایم است. یک مطالعه تجربی رفتار قابل‌توجهی پارامتر فرآیند یا ورودی را بر روی خواص ماشینکاری نشان می‌دهد. یک مطالعه ریاضی یعنی.) ANOVAتحلیل واریانس) همبستگی بین پارامترهای ورودی یا فرآیند و خصوصیات ماشینکاری یا خروجی را برای فولاد ملایم نشان می دهد. همچنین معادله ای برای نیروی برش با استفاده از مدل رگرسیون برای پیش بینی نرخ تغذیه، سرعت و عمق برش ایجاد شده است. مقادیر به دست آمده از مدل های ریاضی و مدل رگرسیون بسیار نزدیک به داده های به دست آمده از مطالعات تجربی بود. کمترین نیروهای برشی در سرعت برش بالا و سرعت پایین تغذیه و عمق برش به دست آمد.

</div>

International Journal of Engineering

Well-to-wheel Energy Consumption and CO_2 Emission Comparison of Electric and Fossil Fuel Buses: Tehran Case Study

M. Nikzad*[a], R. Khalilzadeh[b], A. Rabiei[c]

[a] Faculty of Engineering, Lorestan University, Khorramabad, Iran
[b] School of Electrical and Computer Engineering, Tarbiat Modares University, Tehran, Iran
[c] Department of Electrical and Computer Engineering, Western University, London, ON, Canada

P A P E R I N F O

A B S T R A C T

The development of public transportation is considered a vital issue in reducing traffic as well as urban pollution. City buses play an important role in the city transportation system. In Iran, due to the high average age of city buses, it is necessary to replace the old buses with new ones, To replace the old buses, diesel and CNG, hybrid, and electric buses are proposed as the main alternatives. Global warming and the energy crisis are now considered as two potential serious threats for the world. Therefore, energy consumption and CO_2 emissions are examined as two outstanding criteria for comparing candidate buses in this paper. To make an accurate comparison, the amount of energy consumption and CO_2 emissions have been calculated based on the well-to-wheel approach. The electric bus well-to-wheel analysis has been done for both electricity generation mix and renewable generation. To perform more accurate calculations and simulations, as a case study, a real driving cycle has been constructed for Tehran. For this approach, a modified micro trip method as a novel solution is presented to synthesize the driving cycle. The results show that due to the high share of fossil power plants (about 92%) in Iran, the use of electric buses in the bus fleet may not have much effect on reducing energy and CO_2 eq emissions. By using renewable power plants, the amount of well-to-wheel energy consumption and CO_2 emissions decrease significantly (about 56% and 93%, respectively) compared to that for the generation mix.

Graphical Abstract
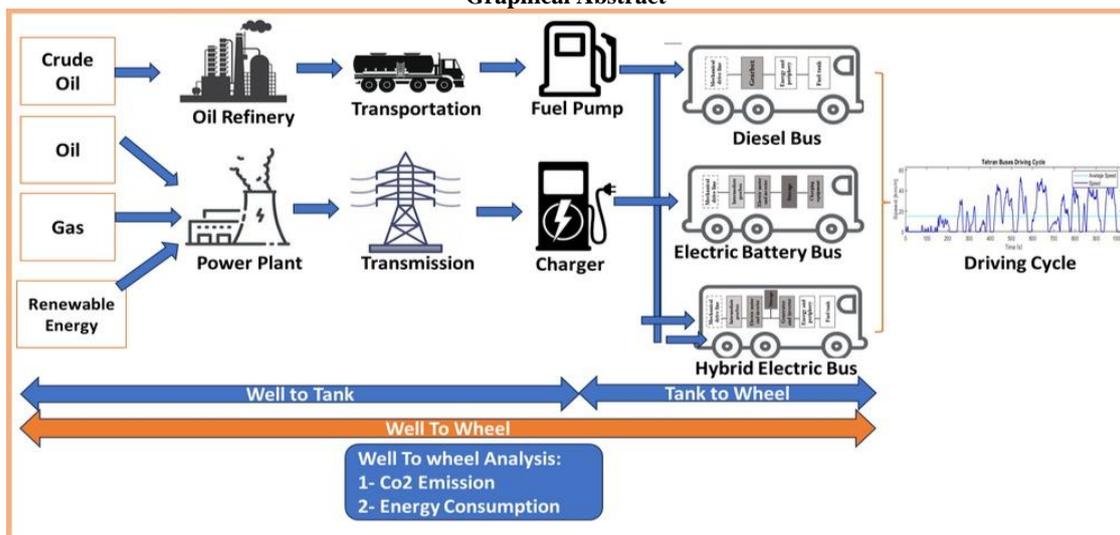
*Corresponding author email: nikzad.m@ut.ac.ir (M. Nikzad)

1. INTRODUCTION

Nowadays, transportation and urban traffic are highly significant challenges for large industrialized cities. The lack of proper development of urban transportation systems may be the cause of many problems in various fields, such as environmental, social, economic, health, and even politics. One of the best solutions to deal with the issue is to develop and strengthen urban public transportation. City buses can play a crucial role in the urban transportation system. Enhancement of city bus fleets can lead to a reduction in the traffic of private cars and decrement in air pollution at a low cost (1, 2).

Furthermore, global warming and the energy crisis are now considered two potential serious threats for the world. Hence, reducing energy consumption and greenhouse gases have become two important requirements while developing the transportation fleet in recent years. The increase in greenhouse gases causes severe crises such as global temperature rise, ocean water level rise, and climate change (3). The importance of this issue has led to the implementation of different international agreements to reduce greenhouse gases and prevent climate change (4, 5).

Regarding energy consumption, a reduction in the transportation sector may be considerable. According to the International Energy Agency, the share of energy consumption in the transportation sector of the total energy consumption is 21% (6).

Tehran is a highly populated city in the world with a population of approximately 12 million, is a good candidate for the evaluation and implementation of fleets for city buses with alternative fuel systems. In the bus fleet of Tehran, which is considered as the case study in this paper, there are about 6000 active city buses. Among these buses, about 3500 are diesel powered, and about 2500 use CNG (7).The average life of Tehran's bus fleet is more than 15 years. Therefore, necessary actions should be taken to purchase new buses and renew the fleet.

Because the replacement of new buses involves a huge investment, the development of the bus fleet should be done with proper consideration. According to the powertrain type, hybrid electric bus (HEB), battery electric bus (BEB), diesel bus, and CNG bus are the most common ones in terms of market share (8-10). A schematic of each bus topology is shown in Figure 1. In this paper, these kinds of buses are considered the best candidate alternatives for replacing conventional old ones.

Different criteria, such as total cost of ownership (TCO) (11-14), local pollution (15, 16), CO_2 emission (17-19) and energy consumption (16, 18, 20) may be considered to select the appropriate powertrain type. Regarding the major mentioned challenges, i.e., emissions and energy usage, in this paper, suitable powertrain architecture for the Tehran bus fleet have been investigated from the two perspectives of reducing CO_2 pollution and energy consumption.

Generally, due to the much higher efficiency of the electric motor compared to the internal combustion engine (ICE), BEB has lower tank-to-wheel (TTW) energy consumption than the other types. Furthermore, the amount of BEB CO_2 emission is zero. However, a well-to-wheel (WTW) approach may reveal the energy consumption and emission release of the whole cycle of power generation, transmission, and usage in the vehicle. This analysis evaluates the benefits of increasing the share of renewable and clean power sources in a country. Electricity generation in fossil fuel power plants consumes energy and emits CO_2. Therefore, to have an accurate study, the amount of energy consumption and CO_2 emission should be computed from the source of energy production to the tailpipe of the bus, which is known as the WTW study. In other words, although the TTW CO_2 emission of BEB is zero, its well-to-tank (WTT) emission is not zero and should be investigated for countries, case by case, based on the source of electric energy.

WTW analysis for vehicles in the literature may be conducted using standard driving cycles (9, 21) or real driving data (22-25). A WTW study for heavy-duty vehicles, where different e-fuels are used for the power generation section, is done (17). The WTT emissions of the e-fuel pathways are calculated using an in-house tool. However, a specific driving cycle is not used for data extraction and simulation. A data-driven approach is used to provide a WTW study for vehicle fleet renovation in Roma, where real traffic data is used (20). The study is carried out for private vehicles and city buses. It is concluded that partial electrification may lead to significant CO_2 reduction. However, as it is stated by the authors, the portion of renewable energy sources is about one-third of total electric power generation in Italy, which is a far different case from that in Iran. Another comparative study for Roma has been conducted between five vehicles with different powertrain types, including ICE, hybrid electric, and battery electric, in terms of WTW energy consumption and CO_2 emission (26). Two driving cycles, i.e., NEDC and WLTC, are considered for the tests, and the results were compared with a real driving cycle test in Roma. It is shown in this paper that the results of real tests may deviate significantly from those of the two mentioned driving cycles for some types of powertrains. Using real-life operational data provided by a waste management company in Berlin, an economical investigation is also performed for diesel-powered and electric waste collections vehicles through calculation of WTW emission costs (27).

In most of the previous works, the standard driving cycles of several specific cities, such as New York (NY) City Bus, Millbrook Westminster London bus (London

city), and Braunschweig City (Germany), have been used in the simulations (9). However, to perform a proper simulation and accurate prediction, a driving cycle similar to the driving behavior of the area under study should be used. In order to obtain more accurate results, a suitable driving cycle for the city buses of Tehran has been modeled in this paper.

In Iran, about 92% of electrical energy is generated by fossil fuel power plants (28). Therefore, electric power production is associated with the emission of a significant amount of carbon dioxide and energy loss.

In order to calculate the energy consumption and the amount of bus emissions, a simulation tool could be used. For this purpose, different simulator packages, which are mainly MATLAB-based tools, such as ADVISOR (advanced vehicle simulator) (29), PSAT (PNGV System Analysis Toolkit) (30) and QSS toolbox (31), have been developed. The simulator performs computations based on a specific driving cycle, which expresses the vehicle's speed over time. Also, the ADVISOR tool, along with MATLAB software, is used for simulation study.

In this paper, in section 2, the driving cycle modeling method is described. In section 3, the WTW energy consumption of different types of powertrains has been investigated case by case. In section 4, the WTW analysis of CO_2 equivalent emission has been done. In both sections 3 and 4, For BEB, Studies have been done for both mix and renewable energy electricity generation. Finally, the results have been discussed and concluded in section 5.

2. DRIVING CYCLE MODEL

Generally, the driving cycle expresses the driving behavior based on a time-speed profile. A precise driving cycle could be used to determine different vehicle parameters, such as sizing components, predicting fuel consumption, emissions, and optimizing the control strategy (32-34). Depending on urban traffic, city size, geographical characteristics, number of highways, and arterial or local routes, the driving cycle of each city is different from other cities (35-37). Therefore, by using the real driving cycle of a city, it is possible to choose the most suitable type of city bus based on the desired criteria, such as the amount of energy consumption and air pollution.

Different methods have been presented in the literature to synthesize a standard driving cycle. These methods could be classified into four categories: Micro trip based, Segment based, Pattern classification, and Markov chain method (32, 35, 37-40).

A micro trip is defined as the path traveled by the vehicle between two starting points (41). In the micro trip-based method, the micro trips of the collected data are extracted, and then according to the average speed

and the percentage of stopping time of each micro trip, the data are divided into different groups. Then, the
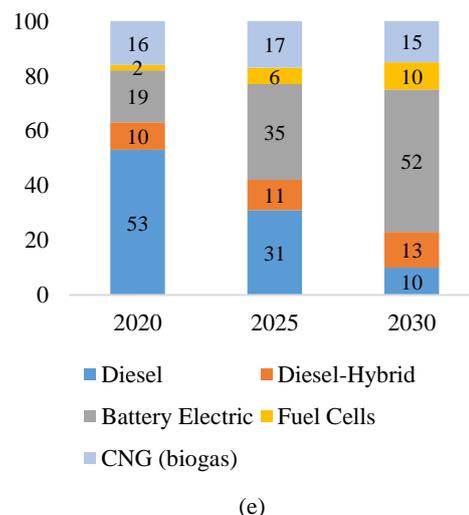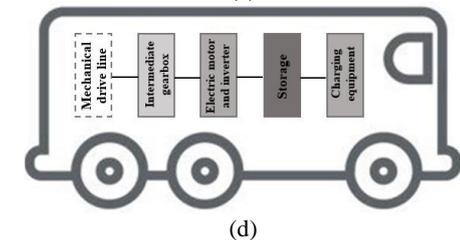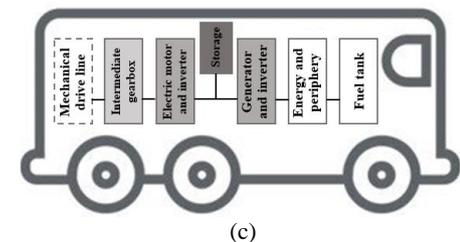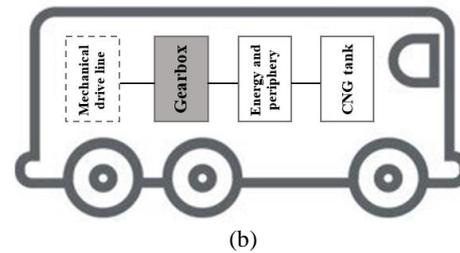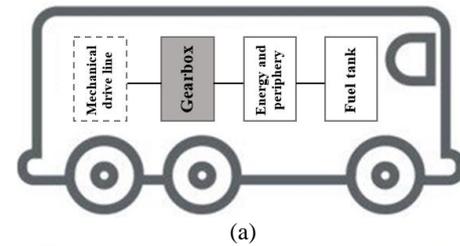
Figure 1. Deposition Different architecture of city busses: a) conventional diesel, b) CNG, c) hybrid electric bus (HEB), d) battery electric bus (BEB) e) market share prediction [10]

driving cycle is made by putting the micro trips together in such a way that the target parameters (population parameters) such as average speed, maximum speed, minimum speed, percentage of stopping time, and any other information according to the purpose of the study are met (41-44). Micro trips are extracted regardless of the conditions of the driving route or Level of Service (LOS) (41, 42). In the modified micro trips-based methods, with the help of micro trip classification algorithms, micro trips are divided into different categories, each of which represents a specific type of driving route or LOS. After categorizing, some micro trips are selected from each category according to the participation percentage. (43, 44). In this way, a driving cycle is obtained by putting the micro trips together.

As mentioned before, in the basic micro trips-based method, the collected data are divided into smaller groups only according to the stops on the route. Therefore, there is no information about the type of route and LOS that the vehicle traveled through. In the segment based method, the accumulative data is divided according to the type of LOS to create a driving cycle. For this purpose, the participation percentage of each LOS in different divisions is used (39, 45).The drawback of the cycle created with this method is that it only looks at the driving cycle from the perspective of the type of route and LOS provided by it. This perspective is not suitable for creating a driving cycle for pollution measurement, because the amount of vehicle pollution depends on parameters such as the percentage of time stopping and average speed (46).

In the pattern classification method, different "kinematic sequences" are used to build a driving cycle. The kinematic sequence is similar to micro-travel, with the difference that many variables are used to define it. For example, in the kinematic sequences used to build a European urban cycle, 20 variables are used, including trip duration, percentage of stop time, trip length, instantaneous speed, effective acceleration of each sequence, standard deviation, maximum speed, etc. (47). Each of these movement sequences is divided into different classes with the help of statistical methods such as principal component analysis (PCA) (48). To construct the driving cycle, these kinematic sequences are put together in a manner that is logical and justifiable in terms of time and statistics. For example, the cycle should start from the inner-city class, and to enter the suburban class, it should enter the arterial class (44). The advantage of this method is that it could obtain the driving pattern with high accuracy and be a real representative of the driving behavior in different areas. However, in this method, a large amount of data is needed to extract the kinematic sequence and categorize the routes, which is time-consuming (35).

In the Markov chain method, every driving pattern in the real world is divided into different modes, such as

increasing speed (positive acceleration), decreasing speed (negative acceleration), cruising (uniform speed) and stopping mode (37, 46, 49). In addition to the average speed and the percentage of stopping time, the amount of vehicle emissions and fuel consumption is also dependent on the change of driving mode (50). As a result, for the two scenarios with the same average speed and percentage of stopping time but with different change of modes, the amount of fuel consumption and emissions are different. Therefore, making a cycle by considering the changes in driving mode has been added to the appropriate methods for making a driving cycle. Because the probability of the event of a driving mode in driving depends only on the previous state, the Markov chain method is used to build the driving cycle in this method.

In this paper, a modified micro trip method is used to stablish the driving cycle. The percentage of stopping time and average speed are considered the two significant parameters to construct the driving cycle. The reason for choosing these two criteria is that most of the pollution produced by the buses depends on these two parameters (36). In the proposed method, first, data related to the micro trips have been collected for nine main routes in Tehran. Then, as shown in Figure 2, the data of each route is sorted based on the two parameters of stopping time and average speed. In the following, the data of all routes are cumulated together, as shown in Figure 3. About 500 micro trips have been sampled in this study. To apply the impact of the type of driving route and LOS, the aggregated data of the micro trips are divided into three categories, each of which represents congested, arterial, and highway routes, respectively. The highway routes have the highest average speed and the lowest stopping time. The congested routes are the routes that have the lowest average speed and the highest stopping time, and the arterial routes have a feature between these two
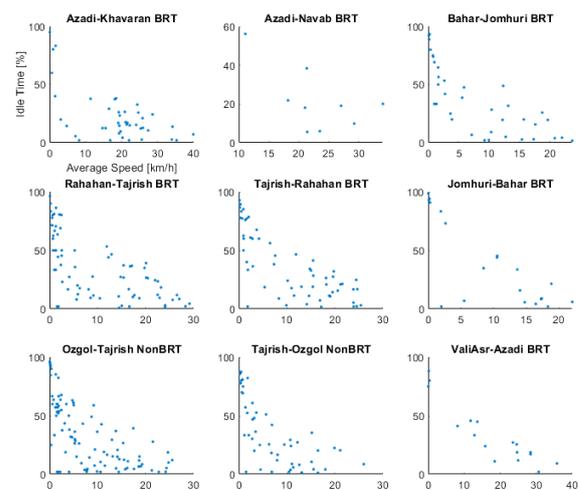
Figure 2. The micro trips characteristics of each route based on stop time and average speed
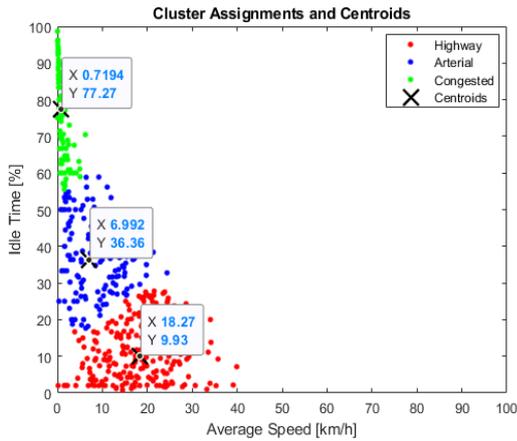
Figure 3. Clustering of the accumulative data using the K-means method

routes. To cluster the data, the k-means method is used in this study. To establish a driving cycle, according to the number of micro trips and their time percentage, some micro trips from each category are randomly selected and placed together. If the average speed and percentage of stopping time and effective acceleration of the constructed cycle have a significant error with those of the cumulative data, the constructed cycle cannot represent the cumulative data. But if this error is small, the constructed cycle is a suitable candidate for expressing the traffic behavior of cumulative data. Figure 4 shows the constructed driving cycle for Tehran. In the following sections, the synthesized driving cycle has been used in simulations to predict the amount of energy consumption and CO_2 emissions of the buses under study.

3. WTW ENERGY CONSUMPTION

In order to have an accurate study and a fair comparison, the energy consumption of each type of bus should be analyzed from WTW. Thus, the amount of energy consumption should be calculated over the entire energy flow process, from the energy source to the tailpipe of the bus . WTW analysis is divided into two parts: WTT and TTW. In fossil fuel buses, WTT analysis is used to
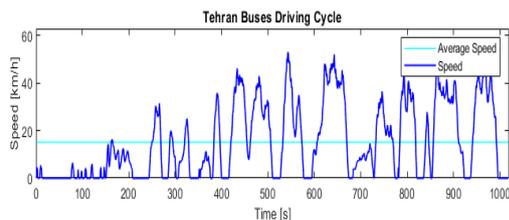
calculate the energy consumption in the processes of extracting, refining, and transferring fuel to the bus. While in an electric bus, the purpose of WTT analysis is to estimate the amount of energy consumed in the processes of electricity generation, transmission, and bus charging at charging stations. Also, in the TTW analysis, the fuel consumption of the bus (fossil or electric) is estimated while driving in the considered route.

3. 1. TTW Analysis   While a bus is moving, the tractive force must overcome the resistance forces that prevent the vehicle movement. Rolling, aerodynamic, and grading are the resistance forces that act on a bus moving up a grade. Therefore, as shown in Figure 5, in according to Newton's second law, the force balance of the moving bus can be written as:

$$F_t = F_r + F_W + F_g + F_a \tag{1}$$

where F_t represent the tractive force, F_r is the rolling resistance of the tires, F_W is the aerodynamic drag, F_g is the grading resistance and Fa is the accelerating force of the bus. Rolling resistance is the force that resists the forward motion of tires. The main reason for the rolling resistance is the hysteresis of the tire material. But other parameters such as the adhesion between road and tires, the gravity and weight of the vehicle affect it. Rolling resistance is calculated as:

$$F_r = Mgf_r \cos \alpha \tag{2}$$

where M is the mass of the bus, g is the gravity, and α is the angle of the ground incline. In addition, fr is the coefficient of rolling resistance, which is a function of the type of road and tire, tire inflation pressure, tire temperature, and some other parameters.
Aerodynamic drag force refers to the air resistance that a bus faces while moving. This force is expressed as:

$$F_W = \frac{1}{2}\rho A_f C_D V^2 \tag{3}$$

Figure 4. Constructed driving cycle for Tehran city bus
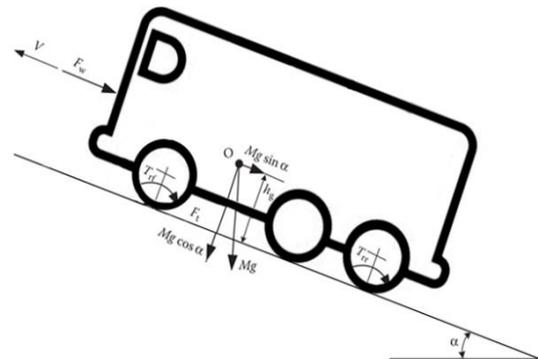
Figure 5. Forces acting on a bus moving up a grade

where V is the bus speed, A_f is frontal area of the bus, ρ is air density, and C_D is the aerodynamic drag coefficient, which is a function of shape and skin friction of the bus.

Grading resistance force opposes the forward motion of the bus during grade climbing, which is calculated as:

$$F_r = Mg \sin \alpha \tag{4}$$

Finally, F_a represents the force required to accelerate or decelerate the bus, which can be expressed as:

$$F_a = \delta M \frac{dv}{dt} \tag{5}$$

where δ is the mass factor that equivalently converts the rotational inertias of rotating components into translational mass.

By using Equation 1, the amount of required power and thus energy consumption of the vehicle could be calculated. It should be noted that the efficiency of powertrain components must be included in the calculations for each operating point.

In this paper ADVISOR software is used to compute the energy consumption. In this software, Equations 1 to 5 are used to model the bus required power. The extracted Tehran city bus driving cycle is considered as the reference in this paper. The specifications of the simulated buses are given in Table 1.

Table 2 shows the computed fuel consumption along with the equivalent energy consumption of each type of bus through simulation. It can be seen that the fuel consumption of the diesel and the CNG buses are higher than the two other types due to the use of low-efficiency ICE. Also, in the case of HEB, because of using the

TABLE 1. The characteristics of the simulated buses (29)

Charactristics	BEB	Diesel	CNG	HEB
Frontal Area	7.9 m²	7.9 m²	7.9 m²	7.9 m²
Weight without passenger	11,945 kg	15,597 kg	11,945 kg	15,597 kg
Length	12.2 m	12.2 m	12.2 m	12.2 m
Wheel radius	500 mm	500 mm	500 mm	500 mm
Aerodynamic coefficient	0.79	0.79	0.79	0.79
Air density	1.23	1.23	1.23	1.23
Rolling resistance	0.008	0.008	0.008	0.008
Gravity	9.81 m/s²	9.81 m/s²	9.81 m/s²	9.81 m/s²
Transmission system efficiency	93%	92%	92%	92%
Maximum power	200 kW	205 kW	209 kW	209 kW
Auxiliary loads	3.5 kW	7.5 kW	3.5 kW	7.5 kW
Battery Capacity	300 kWh	-	-	30 kWh
Battery weight	3,000 kg	-	-	30 kg

TABLE 2. The fuel consumption and the equivalent energy consumption of the simulated buses

Bus Type	Fuel Consumption	Equivalent energy consumption per Km
Diesel[1]	0.59 (L/km)	21.1 MJ
CNG[2]	0.6 (kg/km)	30 MJ
HEB	0.48 (L/km)	17.2 MJ
BEB[3]	1.99 (kWh/km)	7.1 MJ

[1] The energy per liter of diesel is equal to 35.9 MJ (51).

[2] The energy per kilogram of CNG is equivalent to 50 MJ (52).

[3] 1 kWh=3.6 MJ

auxiliary electric motor, less energy is consumed than in the ones of diesel and CNG buses. Finally, as expected, in the BEB, energy consumption is much lower than in other types due to the use of the high-efficiency electric motor in the powertrain.

3. 2. WTT Analysis   In order to WTT analyze of the diesel and the HEB, the energy loss of diesel production and refining processes and the loss of fuel transportation to fueling stations are considered 10% and 2%, respectively (53). For the CNG bus, the energy loss for the extraction, transmission and compression of natural gas, for a gas transmission system with a length of 1000 km is considered 13% (53).

For the case of the BEB, the TTW efficiency is dependent on the power generation method. Based on the data published by the Ministry of Energy of Iran, about 92% of electricity is generated by fossil fuels in Iran (28). The share of different sources in the overall electricity generation in Iran is shown in Figure 6. As shown in the figure, the contribution of electricity generation by combined cycle, steam, gas, Hydroelectric, nuclear, and renewable power plants are 45.9%, 24.8%, 20.9%, 6.4%, and 0.4%, respectively. In addition to the share of each type of power plant, their average efficiency is listed in Table 3 (28). The generation mix efficiency could be calculated according to the portion and the efficiency of the power plants. As shown in Table 3, the efficiency of mixed electricity generation in Iran is about 43.9%. It is clear that the reason for the low mix generation efficiency is the low contribution of renewable sources to the overall electricity mix in Iran.

According to ministry of energy report, the electricity transmission and distribution losses in Iran are 2.8% and 9.5%, respectively (28). Therefore, considering the loss of 6% of the charger, the losses of transmission and charging is 13.2%.

3. 3. WTW Analysis   By including WTT and TTW components the WTW energy consumption of the buses can be computed as:

$$WTW_e\left[\frac{MJ}{km}\right] = WTT_e\left[\frac{MJ}{km}\right] + TTW_e\left[\frac{MJ}{km}\right] \qquad (6)$$

where WTT energy consumption, WTT_e, can be obtained as:

$$WTT_e\left[\frac{MJ}{km}\right] = TTW_e\left[\frac{MJ}{km}\right].WTT_{loss}[\%] \qquad (7)$$

and WTT_{loss} is the total WTT loss.

The WTT, TTW, and WTW energy consumption of each type of city bus is shown in Table 3. The results are also depicted in Figure 6. It can be seen that the WTW energy consumption of the CNG and diesel buses are higher than the other two types due to the higher TTW energy consumption. However, despite the much lower TTW energy consumption in BEB, the amount of the WTW energy consumption is not substantially different from that in the other buses, especially the diesel and HEB. The reason is that the efficiency of generation mix in Iran is low due to the large share of fossil fuel power plants.

Alternatively, it is supposed that instead of fossil fuel, renewable energies are used to supply electricity. Therefore, as seen in Table 4 and Figure 7, the WTT energy consumption and as a result, the WTW energy

TABLE 3. The average efficiency of difference power plant (28)

Type of Power Plant	Share of Generation	Average Efficiency
Combined Cycle	45.9%	46.1%
Steam	24.8%	37.1%
Gas	20.9%	29.7%
Hydroelectric	6.4%	100%
Nuclear	1.6%	33%
Renewable	0.4%	100%
Generation mix efficiency	43.9%	
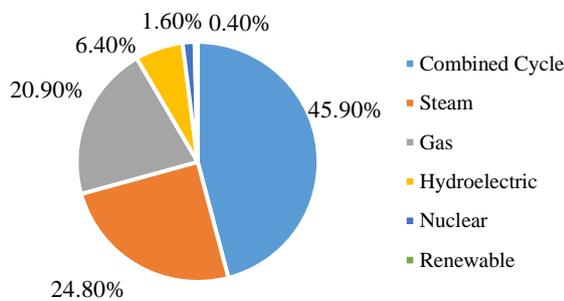
Figure 6. Share of electricity generation of various power plants

TABLE 4. The WTT, TTW, and WWT energy consumption of different buses.

Bus Type	TTW (MJ/km)	WTT (MJ/km)	WTW (MJ/km)
Diesel	21.1	2.8	23.9
CNG	30	4.5	34.5
HEB	17.2	2.3	19.5
BEB With Generation Mix	7.1	11.5	18.6
BEB with Renewable Sources	7.1	1.1	18.6
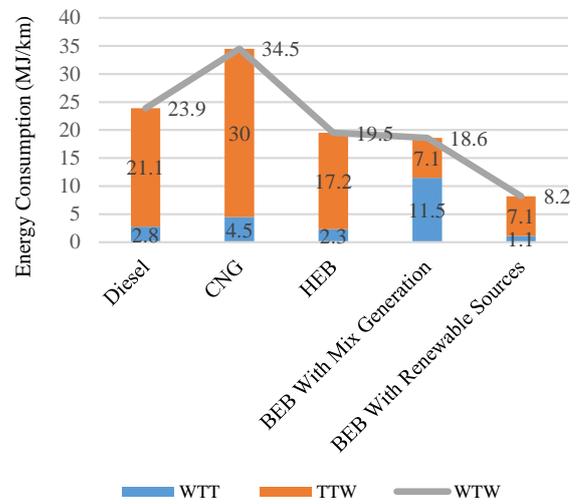
Figure 7. WTT, TTW, and WWT energy consumption of buses

consumption are significantly reduced. In this case, the WTW energy consumption of the electric bus reduces by 56% and provides a significant advantage over the other types of buses.

4. WTW CO$_2$ EMISSION

To analyze the emission of CO$_2$ for each type of powertrain, in addition to the emission of each bus during operation, the amount of CO$_2$ emission in the production process of the energy source (diesel, natural gas, or electricity) should be considered. Therefore, similar to the energy consumption calculations, for an accurate comparison, the CO$_2$ emission should be studied from the production process of the energy source to the bus tailpipe.

As in the previous section, carbon dioxide gas emission calculations should be performed in two stages: 1) WTT, i.e., production and extraction of energy source, and 2) TTW, i.e., during bus operation.

4. 1. WTT Analysis The energy source of the electric bus is the electricity produced in the power plants. Therefore, to study CO_2 emissions during the electricity production process, it is necessary to investigate the electricity production methods in each country. Countries that use more renewable energy in electricity production will have lower CO_2 emissions. The share of power plants in Iran's electricity production, along with the amount of greenhouse gas emissions in each of them, are listed in Table 5 (28).

To consider the effects of various types of greenhouse gases on climate change and their different atmospheric lifetimes, the Intergovernmental Panel on Climate Change (IPCC) has presented the "Global Warming Potential" (GWP) index. According to this index, as stated in Table 6, every greenhouse gas is converted into CO_2 equivalent (54). For example, as listed in the table, the effect of one kilogram of N_2O is equivalent to 298 kilograms of CO_2. In this case, the total of greenhouse gases is considered as a CO_2 equivalent (CO_2 eq).

By using Table 6, the amount of CO_2 eq emission of each type of power plant has been calculated and reported in Table 6. Considering the share of each power plant in electricity production and its CO_2 eq, the amount of CO_2 eq emission of the generation mix is calculated. As shown in Table 6, the CO_2 eq generation mix equals 600 grams. This means that about 600 grams of CO_2 eq is produced per kWh of electricity generation in Iran.

To calculate the WTT emission of the diesel and CNG buses, the CO_2 eq emission from the processes of fuel extraction, refining, and transportation should be considered. Here, taking into account the GREET model

(55), the amount of WTT CO_2 emission for diesel and CNG fuel are 19 (g CO_2 eq /MJ) and 25 (g CO_2 eq /MJ), respectively.

4. 2. TTW Analysis The amount of CO_2 eq emission of each bus after traveling the reference driving cycle is shown in Table 7. As expected, the CO_2 eq emission for the CNG and diesel buses is higher than that for the other two types. Also, due to the use of clean electric energy in the BEB, the CO_2 eq emission of this type of bus is zero.

4. 3. WTW Analysis Using the WTT and TTW of CO_2 eq emissions, the amount of WTW CO_2 eq emissions is calculated as:

$$WTW_{CO_2}[\frac{g\ CO_2\ eq}{MJ}] = WTT_{CO_2}[\frac{g\ CO_2\ eq}{MJ}] + TTW_{CO_2}[\frac{g\ CO_2\ eq}{MJ}] \quad (8)$$

Besides, the WTT CO_2 eq emission, WTT CO_2, is obtained as:

$$WTT_{CO_2}[\frac{g\ CO_2\ eq}{MJ}] = TTW_{CO_2}[\frac{g\ CO_2\ eq}{MJ}].WTT_{Loss}[\%] \quad (9)$$

where WTT_{loss} is the WTT loss.

The calculated values of WTT, TTW, and WTW of the CO_2 eq emission are shown in Table 8 and depicted in Figure 8. As can be seen, despite the zero emissions of the BEB, the WTW of the CO_2 eq emissions is close to that of fossil fuel buses due to the significant contribution of electricity generation from fossil power plants in Iran. However, as stated in Table 8 and Figure 8, if renewable power plants are used instead, the amount of TTW and

TABLE 5. The WTT, TTW, and WWT energy consumption of different buses (28)

Type of Power Plant	CH_4	N_2O	CO_2	CO_2 eq (g/kWh)	Share of Generation (%)	Share of CO_2 eq Emission (g/kwh)
Combined Cycle	0.012	0.002	540.076	540.972	45.9%	243.43
Steam	0.018	0.003	723.798	725.142	24.8%	179.83
Gas	0.017	0.002	837.844	838.865	20.9%	175.32
Hydroelectric	-	-	-	8.22	6.4%	0.52
Nuclear	-	-	-	12.23	1.6%	0.19
CO_2 eq						600

TABLE 6. CO_2 eq for each type of greenhouse gas (54)

Greenhouse Gas	CO_2 eq
1 kg CO_2	1 kg eq CO_2
1 kg CH_4	25 kg eq CO_2
1 kg N_2O	298 kg eq CO_2
1 kg CF_4	7,390 kg eq CO_2
1 kg C_2F_6	12,200 kg eq CO_2

TABLE 7. The Amount of CO_2 eq Emission of the Simulated Buses.

Bus Type	CO_2 eq Emission (g CO_2 eq/km)
Diesel	1,005
CNG	1,092
HEB	784
BEB	0

TABLE 8. The WTT, TTW, and WWT CO_2 eq emission of The Buses

Bus Type	WTT (g CO_2 eq/km)	TTW (g CO_2 eq/km)	WTW (g CO_2 eq/km)
Diesel	466	1,005	1,471
CNG	579	1,092	1,671
HEB	375	784	1,159
BEB With Generation Mix	1,367	0	1,367
BEB with Renewable Sources	95	0	95
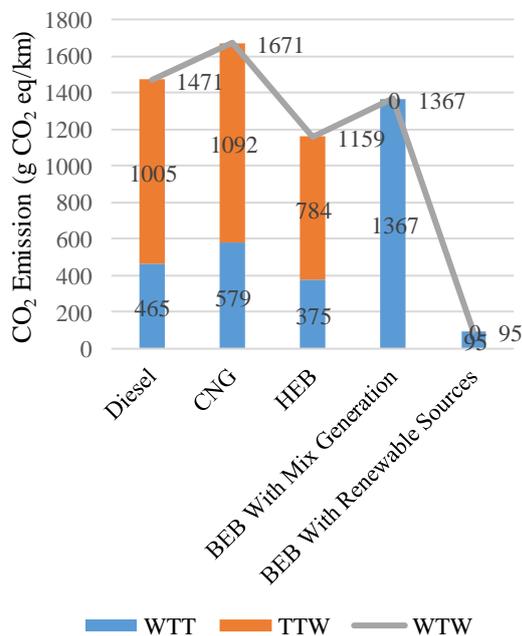
Figure 8. WTT, TTW, WWT CO_2 eq Emission of the Buses

WTW of CO_2 emissions significantly decreased (about 92%) compared to that for the generation mix. In this case, a large difference in CO_2 eq emissions between the BEB and the other types can be observed.

5. CONCLUSION

In this paper, a comparison was made between four types of city buses, including diesel, CNG, hybrid, and electric, to find the best choice for contributing to Tehran, Iran, bus fleet renovation. Energy consumption and CO_2 emissions were considered as two criteria for comparing candidate buses. In order to perform more accurate simulations and calculations, a real driving cycle was derived for Tehran using the micro-trip method. In this method, micro trips were extracted regardless of the driving route conditions and the Level of Service (LOS). Therefore, in the first stage, to apply the impact of the type of driving route and LOS, the accumulated data of the micro trips were divided into three categories, each of which represents congested, arterial, and highway routes, respectively. Then, the k-means method was used to cluster the data.

The energy consumption of the candidate buses was compared. The energy consumption of each type of bus was computed from well-to-wheel (WTW) to have a fair comparison. The WTW analysis was divided into two parts: WTT and TTW. For the fossil fuel buses, WTT analysis was used to calculate the energy consumption in the processes of extracting, refining, and transferring fuel. While for the electric bus, in the WTT analysis, the amount of energy consumed in the processes of electricity generation, transmission, and bus charging at charging stations was estimated. To estimate the WTT energy consumption of the electric bus, the generation mix efficiency was calculated according to the portion and the efficiency of the power plants of Iran. Accordingly, the results show that there is no significant difference between the WTW energy consumption of electric buses and that in the other buses. In addition, according to the results, it can be concluded that if renewable power plants are used, the energy consumption of electric buses reduces by 56% compared to the generation mix.

The WTW CO_2 eq emission comparison was also conducted. The results state that despite the zero pollution of the electric bus, the WTW CO_2 eq emission is not much different from its values for the other bus types due to the major contribution of electricity generation from fossil power plants in Iran. Alternatively, by using renewable power plants, the amount of WTW CO_2 eq emission decreases significantly (about 93%) compared to that for the generation mix.

As a result, considering the high share of fossil power plants (about 92%) in Iran, the use of electric buses in the bus fleet may not have much effect on reducing energy and CO_2 eq emissions. Therefore, to enjoy the advantages of electric buses in Iran, the share of renewable energy production should be increased.

6. REFERENCES

1. Brdulak A, Chaberek G, Jagodziński J. Development forecasts for the zero-emission bus fleet in servicing public transport in chosen EU member countries. Energies. 2020;13(16):4239. https://doi.org/10.3390/en13164239

2. Song Z, Liu Y, Gao H, Li S. The underlying reasons behind the development of public electric buses in China: The Beijing case. Sustainability. 2020;12(2):688. https://doi.org/10.3390/su12020688

3. Hansen J, Sato M, Ruedy R. Perception of climate change. Proceedings of the National Academy of Sciences. 2012;109(37):E2415-E23. https://doi.org/10.1073/pnas.1205276109

4. Delbeke J, Runge-Metzger A, Slingenberg Y, Werksman J. The paris agreement. Towards a climate-neutral Europe: Routledge; 2019. p. 24-45.

5. Fetting C. The European green deal. ESDN report. 2020;53.

6. Tracking Transport 2020. Paris, France: International Energy Agency; 2020.

7. Shafiee M, Lotfi FH, Saleh H. Supply chain performance evaluation with data envelopment analysis and balanced scorecard approach. Applied mathematical modelling. 2014;38(21-22):5092-112. https://doi.org/10.1016/j.apm.2014.03.023

8. Grigoroudis E, Petridis K, Arabatzis G. RDEA: A recursive DEA based algorithm for the optimal design of biomass supply chain networks. Renewable Energy. 2014;71:113-22. https://doi.org/10.1016/j.renene.2014.05.001

9. Al-Ogaili AS, Al-Shetwi AQ, Al-Masri HM, Babu TS, Hoon Y, Alzaareer K, et al. Review of the estimation methods of energy consumption for battery electric buses. Energies. 2021;14(22):7578. https://doi.org/10.3390/en14227578

10. Undertaking HJ. Urban Buses: Alternative Powertrains for Europe: A Fact-based Analysis of the Role of Diesel Hybrid, Hydrogen Fuel Cell, Trolley and Battery Electric Powertrains. 2012.

11. Nurhadi L, Borén S, Ny H. A sensitivity analysis of total cost of ownership for electric public bus transport systems in Swedish medium sized cities. Transportation Research Procedia. 2014;3:818-27. https://doi.org/10.1016/j.trpro.2014.10.058

12. Pihlatie M, Kukkonen S, Halmeaho T, Karvonen V, Nylund N-O, editors. Fully electric city buses-The viable option. 2014 IEEE International Electric Vehicle Conference (IEVC); 2014: IEEE. https://doi.org/10.1109/IEVC.2014.7056145

13. Ally J, Pryor T. Life cycle costing of diesel, natural gas, hybrid and hydrogen fuel cell bus systems: An Australian case study. Energy Policy. 2016;94:285-94. https://doi.org/10.1016/j.enpol.2016.03.039

14. Hamidi H, Tavassolib A. A Model for Scheduling of Electric Vehicles Charging in a Distribution Network using Multi-Agent Model. power. 2023;13(14):20. https://doi.org/10.5829/ije.2024.37.02b.15

15. Stempien J, Chan S. Comparative study of fuel cell, battery and hybrid buses for renewable energy constrained areas. Journal of Power Sources. 2017;340:347-55. https://doi.org/10.1016/j.jpowsour.2016.11.089

16. Torchio MF, Santarelli MG. Energy, environmental and economic comparison of different powertrain/fuel options using well-to-wheels assessment, energy and external costs–European market analysis. Energy. 2010;35(10):4156-71. https://doi.org/10.1016/j.energy.2010.06.037

17. Prussi M, Laveneziana L, Testa L, Chiaramonti D. Comparing e-Fuels and Electrification for Decarbonization of Heavy-Duty Transports. Energies. 2022;15(21):8075. https://doi.org/10.3390/en15218075

18. Sheng MS, Sreenivasan AV, Sharp B, Du B. Well-to-wheel analysis of greenhouse gas emissions and energy consumption for electric vehicles: A comparative study in Oceania. Energy Policy. 2021;158:112552. https://doi.org/10.1016/j.enpol.2021.112552

19. Bhosale AP, Mastud S. Comparative Environmental Impact Assessment of Battery Electric Vehicles and Conventional Vehicles: A Case Study of India. International Journal of Engineering. 2023;36(5):965-78. https://doi.org/10.5829/ije.2023.36.05b.13

20. Liberto C, Valenti G, Orchi S, Lelli M, Nigro M, Ferrara M. The impact of electric mobility scenarios in large urban areas: The Rome case study. IEEE Transactions on Intelligent Transportation Systems. 2018;19(11):3540-9. https://doi.org/10.1109/TITS.2018.2832004

21. Guandalini G, Campanari S, editors. Well-to-wheel driving cycle simulations for freight transportation: battery and hydrogen fuel cell electric vehicles. 2018 International Conference of Electrical and Electronic Technologies for Automotive; 2018: IEEE. https://doi.org/10.23919/EETA.2018.8493216

22. Liberto C, Valenti G, Lelli M, Ferrara M, Nigro M, editors. Evaluation of the impact of e-mobility scenarios in large urban areas. 2017 5th IEEE International Conference on Models and Technologies for Intelligent Transportation Systems (MT-ITS); 2017: IEEE. https://doi.org/10.1109/MTITS.2017.8005701

23. Nizam M, Mujianto A, Triwaloyo H, editors. Comparative analysis well to wheel fuel economy and emission of conventional and alternative vehicle in Surakarta, Indonesia. 2016 2nd International Conference of Industrial, Mechanical, Electrical, and Chemical Engineering (ICIMECE); 2016: IEEE. https://doi.org/10.1109/ICIMECE.2016.7910447

24. Baptista P, Duarte G, Gonçalves G, Farias T, editors. Evaluation of low power electric vehicles in demanding urban conditions: an application to Lisbon. 2013 World Electric Vehicle Symposium and Exhibition (EVS27); 2013: IEEE. https://doi.org/10.1109/EVS.2013.6914794

25. Baert RS, Kort HJ, editors. Real world experience with operating electric vehicles in the Netherlands. 2013 World Electric Vehicle Symposium and Exhibition (EVS27); 2013: IEEE. https://doi.org/10.1109/EVS.2013.6915023

26. Orecchini F, Santiangeli A, Zuccari F. Real Drive Well-to-Wheel Energy Analysis of Conventional and Electrified Car Powertrains. Energies. 2020;13(18):4788. https://doi.org/10.3390/en13184788

27. Schmid F, Taube L, Rieck J, Behrendt F. Electrification of Waste Collection Vehicles: Technoeconomic Analysis Based on an Energy Demand Simulation Using Real-Life Operational Data. IEEE Transactions on Transportation Electrification. 2020;7(2):604-15. https://doi.org/10.1109/TTE.2020.3031072

28. Energy balance. Tehran, Iran: Iran ministry of power; 2020.

29. Bak D-B, Bak J-S, Kim S-Y. Strategies for implementing public service electric bus lines by charging type in Daegu Metropolitan City, South Korea. Sustainability. 2018;10(10):3386. https://doi.org/10.3390/su10103386

30. Hinse PR. Energy use analysis and technology for electric transit buses 2010.

31. Tomar AS, Veenhuizen B, Buning L, Pyman B, editors. Estimation of the size of the battery for hybrid electric trolley busses using backward quasi-static modelling. Proceedings; 2018: MDPI. https://doi.org/10.3390/proceedings2231499

32. Liu X, Ma J, Zhao X, Du J, Xiong Y. Study on driving cycle synthesis method for city buses considering random passenger load. Journal of Advanced Transportation. 2020;2020:1-21. https://doi.org/10.1155/2020/3871703

33. Brady J, O'Mahony M. Development of a driving cycle to evaluate the energy economy of electric vehicles in urban areas. Applied energy. 2016;177:165-78. https://doi.org/10.1016/j.apenergy.2016.05.094

34. Quirama LF, Giraldo M, Huertas JI, Jaller M. Driving cycles that reproduce driving patterns, energy consumptions and tailpipe emissions. Transportation Research Part D: Transport and Environment. 2020;82:102294. https://doi.org/10.1016/j.trd.2020.102294

35. Galgamuwa U, Perera L, Bandara S. Developing a general methodology for driving cycle construction: comparison of

various established driving cycles in the world to propose a general approach. Journal of Transportation Technologies. 2015;5(04):191. http://dx.doi.org/10.4236/jtts.2015.54018

36. BARLOW TJ, Latham S, McCrae I, Boulter P. A reference book of driving cycles for use in the measurement of road vehicle emissions. TRL Published Project Report. 2009.

37. Li Y, Zhai D, Ding H, Islam R. The Construction of Xi'an Urban Bus Driving Cycle: A Case Study. Future Transportation. 2023;3(1):92-107. https://doi.org/10.3390/futuretransp3010006

38. Hongwen H, Jinquan G, Jiankun P, Huachun T, Chao S. Real-time global driving cycle construction and the application to economy driving pro system in plug-in hybrid electric vehicles. Energy. 2018;152:95-107. https://doi.org/10.1016/j.energy.2018.03.061

39. Kivekäs K, VepsäläInen J, Tammi K. Stochastic driving cycle synthesis for analyzing the energy consumption of a battery electric bus. IEEE Access. 2018;6:55586-98. https://doi.org/10.1109/ACCESS.2018.2871574

40. Mohammadbagher A, Torabi S. Multi-Objective Vehicle Routing Problem for a Mixed Fleet of Electric and Conventional Vehicles with Time Windows and Recharging Stations. International Journal of Engineering. 2022;35(12):2359-69. https://doi.org/10.5829/ije.2022.35.12c.12

41. Kamble SH, Mathew TV, Sharma GK. Development of real-world driving cycle: Case study of Pune, India. Transportation Research Part D: Transport and Environment. 2009;14(2):132-40. https://doi.org/10.1016/j.trd.2008.11.008

42. Pouresmaeili MA, Aghayan I, Taghizadeh SA. Development of Mashhad driving cycle for passenger car to model vehicle exhaust emissions calibrated using on-board measurements. Sustainable cities and society. 2018;36:12-20. https://doi.org/10.1016/j.scs.2017.09.034

43. Yuhui P, Yuan Z, Huibao Y. Development of a representative driving cycle for urban buses based on the K-means cluster method. Cluster Computing. 2019;22:6871-80. https://doi.org/10.1007/s10586-017-1673-y

44. Qin D, Zhan S, Qi Z, Chen S. Driving cycle construction using K-means clustering method. Journal of Jilin University (Engineering and Technology Edition). 2016;46(2):383-9. https://doi.org/10.1177/0954407019848873

45. Mayakuntla SK, Verma A. A novel methodology for construction of driving cycles for Indian cities. Transportation research part D: transport and environment. 2018;65:725-35. https://doi.org/10.1016/j.trd.2018.10.013

46. Dai Z, Niemeier D, Eisinger D. Driving cycles: a new cycle-building method that better represents real-world emissions. Department of Civil and Environmental Engineering, University of California, Davis. 2008;570.

47. Andre M, Hickman AJ, Hassel D, Joumard R. Driving cycles for emission measurements under European conditions. SAE transactions. 1995:562-74. https://doi.org/10.2307/44615107

48. Xie H, Tian G, Chen H, Wang J, Huang Y. A distribution density-based methodology for driving data cluster analysis: A case study for an extended-range electric city bus. Pattern Recognition. 2018;73:131-43. https://doi.org/10.1016/j.patcog.2017.08.006

49. Peng J, Jiang J, Ding F, Tan H. Development of driving cycle construction for hybrid electric bus: A case study in Zhengzhou, china. Sustainability. 2020;12(17):7188. https://doi.org/10.3390/su12177188

50. An F, Barth M, Scora G, Ross M. Modeling enleanment emissions for light-duty vehicles. Transportation Research Record. 1998;1641(1):48-57. https://doi.org/10.3141/1641-06

51. Mahmoud M, Garnett R, Ferguson M, Kanaroglou P. Electric buses: A review of alternative powertrains. Renewable and Sustainable Energy Reviews. 2016;62:673-84. https://doi.org/10.1016/j.rser.2016.05.019

52. Erjavec J. Hybrid, electric, and fuel-cell vehicles: Cengage Learning; 2012.

53. JRC RE, HASS H, LARIVÉ J-F, JRC LL, MAAS H, Rickeard D. Well-to-wheels Report Version 4. a JEC Well-to-wheels analysis. Institute for Energy and Transport, Joint Research Centre, Luxembourg: Publications Office of the European Union. 2014;2014.

54. Forster P, Ramaswamy V, Artaxo P, Berntsen T, Betts R, Fahey DW, et al. Changes in atmospheric constituents and in radiative forcing. Climate Change 2007: The Physical Science Basis Contribution of Working Group I to the 4th Assessment Report of the Intergovernmental Panel on Climate Change. 2007.

55. Nylund N-O, Koponen K. Fuel and technology alternatives for buses: Overall energy efficiency and emission performance: VTT Technical Research Centre of Finland; 2012.

Persian Abstract

چکیده

توسعه حمل و نقل عمومی به عنوان یک راه‌حل حیاتی برای کاهش چالش ترافیک و همچنین آلودگی شهری محسوب می‌شود. اتوبوس‌های شهری نقش مهمی در سیستم حمل ونقل شهری دارند. در ایران با توجه به بالا بودن میانگین سن اتوبوس‌های شهری، جایگزینی آن‌ها با اتوبوس‌های جدید ضروری است. بدین منظور اتوبوس‌های دیزلی مدرن، CNG هیبریدی و برقی به عنوان راهکاری جایگزین پیشنهاد شده‌اند. گرمایش جهانی و بحران انرژی به عنوان دو تهدید بالقوه جدی برای جهان در نظر گرفته می‌شود. بنابراین مصرف انرژی و انتشار گازهای گلخانه‌ای (CO_2) به عنوان دو معیار برجسته برای مقایسه اتوبوس های پیشنهادی در این مقاله بررسی می‌شوند. به منظور مقایسه دقیق، میزان مصرف انرژی و انتشار CO_2 براساس رویکرد چاه تا چرخ محاسبه شده است. تجزیه و تحلیل چاه تا چرخ اتوبوس الکتریکی هم برای تولید برق بصورت ترکیبی از انواع نیروگاه‌ها و هم برای نیروگاه های تجدیدپذیر انجام گرفته است. در این مقاله برای انجام محاسبات و شبیه‌سازی ها دقیق تر، به عنوان مطالعه موردی، چرخه رانندگی واقعی برای شهر مدل شده است. برای این هدف، یک روش مبتنی بر روش ریز-سفر اصلاح شده به عنوان یک راه حل جدید برای ساخت چرخه رانندگی ارائه شده است.

AIMS AND SCOPE

The objective of the International Journal of Engineering is to provide a forum for communication of information among the world's scientific and technological community and Iranian scientists and engineers. This journal intends to be of interest and utility to researchers and practitioners in the academic, industrial and governmental sectors. All original research contributions of significant value focused on basics, applications and aspects areas of engineering discipline are welcome.

This journal is published in three quarterly transactions: Transactions A (Basics) deal with the engineering fundamentals, Transactions B (Applications) are concerned with the application of the engineering knowledge in the daily life of the human being and Transactions C (Aspects) - starting from January 2012 - emphasize on the main engineering aspects whose elaboration can yield knowledge and expertise that can equally serve all branches of engineering discipline.

This journal will publish authoritative papers on theoretical and experimental researches and advanced applications embodying the results of extensive field, plant, laboratory or theoretical investigation or new interpretations of existing problems. It may also feature - when appropriate - research notes, technical notes, state-of-the-art survey type papers, short communications, letters to the editor, meeting schedules and conference announcements. The language of publication is English. Each paper should contain an abstract both in English and in Persian. However, for the authors who are not familiar with Persian, the publisher will prepare the latter. The abstracts should not exceed 250 words.

All manuscripts will be peer-reviewed by qualified reviewers. The material should be presented clearly and concisely:

- *Full papers* must be based on completed original works of significant novelty. The papers are not strictly limited in length. However, lengthy contributions may be delayed due to limited space. It is advised to keep papers limited to 7500 words.
- *Research* notes are considered as short items that include theoretical or experimental results of immediate current interest.
- *Technical notes* are also considered as short items of enough technical acceptability with more rapid publication appeal. The length of a research or technical note is recommended not to exceed 2500 words or 4 journal pages (including figures and tables).

Review papers are only considered from highly qualified well-known authors generally assigned by the editorial board or editor in chief. Short communications and letters to the editor should contain a text of about 1000 words and whatever figures and tables that may be required to support the text. They include discussion of full papers and short items and should contribute to the original article by providing confirmation or additional interpretation. Discussion of papers will be referred to author(s) for reply and will concurrently be published with reply of author(s).

INSTRUCTIONS FOR AUTHORS

Submission of a manuscript represents that it has neither been published nor submitted for publication elsewhere and is result of research carried out by author(s). Presentation in a conference and appearance in a symposium proceeding is not considered prior publication.

Authors are required to include a list describing all the symbols and abbreviations in the paper. Use of the international system of measurement units is mandatory.

- On-line submission of manuscripts results in faster publication process and is recommended. Instructions are given in the IJE web sites: www.ije.ir-www.ijeir.info
- Hardcopy submissions must include MS Word and jpg files.
- Manuscripts should be typewritten on one side of A4 paper, double-spaced, with adequate margins.
- References should be numbered in brackets and appear in sequence through the text. List of references should be given at the end of the paper.
- Figure captions are to be indicated under the illustrations. They should sufficiently explain the figures.
- Illustrations should appear in their appropriate places in the text.
- Tables and diagrams should be submitted in a form suitable for reproduction.
- Photographs should be of high quality saved as jpg files.
- Tables, Illustrations, Figures and Diagrams will be normally printed in single column width (8cm). Exceptionally large ones may be printed across two columns (17cm).

PAGE CHARGES AND REPRINTS

The papers are strictly limited in length, maximum 8 journal pages (including figures and tables). For the additional to 8 journal pages, there will be page charges. It is advised to keep papers limited to 3500 words.

Page Charges for Papers More Than 8 Pages (Including Abstract)	
For International Author ***	**$55 / per page**
For Local Author	**100,000 Toman / per page**

AUTHOR CHECKLIST

- Author(s), bio-data including affiliation(s) and mail and e-mail addresses).
- Manuscript including abstracts, key words, illustrations, tables, figures with figure captions and list of references.
- MS Word files of the paper.